FACULTY
OF APPLIED SCIENCES
UNIVERSITY
OF WEST BOHEMIA

DANUBIA ADRIA

36th Danubia Adria Symposium
on
Advances in Experimental Mechanics

EXTENDED ABSTRACTS

September 24–27, 2019
Plzeň, Czech Republic

igitur

DEWESoft®
measurement innovation

About the symposium

Each year since 1984, the Danubia-Adria Symposium on Advances in Experimental Mechanics brings together internationally recognized experts and young researchers in an effort to exchange ideas in different topics having as common link EXPERIMENTAL MECHANICS. The symposium acts also as a platform for establishing connections between different research groups that are trying to establish future scientific collaboration.

The symposium is focused on experimental and measuring methods necessary to deepen the knowledge about the mechanical behavior of materials, mechanical structures, and systems, and to provide the physical bases and verification of numerical or analytical methodologies in engineering design.

Main topics

- Structural analysis – experimental tests, structural health monitoring, system identification, damage assessment, self-adaptive structures
- Materials characterization and testing – smart materials, residual stress, fatigue, fracture, creep
- Practical applications and case-studies
- Biomechanics – biomaterials, biomechanics, medical and orthopedic devices, biofluid mechanics
- Instrumentation – new sensors and actuators, advanced measurement systems, validation and reliability of instrumentation
- Integration of mathematical/numerical methods with experimental mechanics

The symposia are organized jointly by

Danubia-Adria Society on Experimental Methods

and its national member organizations:

Austrian Society of Experimental Strain Analysis (ASESA)

Croatian Society of Mechanics (HDM)

Czech Society for Mechanics (CSM)

German Society of Experimental Structural Analysis (GESA)

Greek Society for Experimental Mechanics of Materials (GSEMM)

Hungarian Scientific Society of Mechanical Engineering (GTE)

Italian Association for Stress Analysis (AIAS)

Polish Committee for Mechanics of the Polish Academy of Sciences (KMPAN)

The Romanian Association for Stress Analysis and Materials Testing (ARTENS)

Serbian Society of Mechanics (SSM)

Slovak Society of Mechanics (SSM)

Slovenian Society of Experimental Mechanics (SSEM)

Scientific committee

Austria: Josef Eberhardsteiner (Vienna), Wilfried Eichlseder (Leoben), Bernhard Pichler (Vienna)

Croatia: Damir Semenski (Zagreb), Lovre Krstulović-Opara (Split)

Czech Republic: Milan Růžička (Prague), František Plánička (Plzeň), Robert Zemčík (Plzeň)

Germany: Werner Daum (Berlin), Martin Stockmann (Chemnitz)

Greece: Stavros Kourkoulis (Athens), Ermioni Pasiou (Athens)

Hungary: Rita Kiss (Budapest), Attila Kossa (Budapest)

Italy: Francesca Cosmi (Trieste), Mario Guagliano (Milano)

Poland: Zbigniew Kowalewski (Warsaw), Paweł Pyrzanowski (Warsaw)

Romania: Dan Mihai Constantinescu (Bucharest), Ştefan Dan Pastramă (Bucharest)

Serbia: Marko Miloš (Belgrade), Miroslav Živković (Kragujevac)

Slovakia: František Nový (Žilina), Eva Tillová (Žilina)

Slovenia: Igor Emri (Ljubljana), Anatolij Nikonov (Novo mesto)

Main organizer

University of West Bohemia
Faculty of Applied Sciences
Department of Mechanics

Univerzitní 8, 301 00 Plzeň, Czech Republic

www.kme.zcu.cz

Local organizing committee

Robert Zemčík
Jan Krystek
Sandra Kaňáková
Tereza Vaňková

Contact: das2019@kme.zcu.cz
Webpage: www.das2019.zcu.cz

Venue

Parkhotel Plzeň Congress Center
U Borského parku 31
301 00 Plzeň
Czech Republic
`www.parkhotel-czech.eu`

Sponsors

The organizers would like to thank the sponsors of the conference.

www.igitur.cz

DEWESoft®
measurement innovation

www.dewesoft.com

Contents

SPECIAL-PURPOSE STRAIN-GAUGE BALANCE FOR ONE WING PANEL OF A WIND TUNNEL MODEL

Dijana DAMLJANOVIĆ[1], Đorđe VUKOVIĆ[1], Jovan ISAKOVIĆ[2], Marko MILOŠ[3]

[1] Military Technical Institute (VTI), Experimental Aerodynamics Department, Ratka Resanovića 1, 11030 Belgrade, Serbia, E-mail: didamlj@gmail.com, vdjole@sbb.rs

[2] Tehnikum Taurunum, College of Applied Engineering Studies, Nade Dimić 4, 11000 Zemun Belgrade, Serbia. E-mail: jisakovic@tehnikum.edu.rs

[3] University of Belgrade, Faculty of Mechanical Engineering, Department of General Machine Design, Kraljice Marije 16, 11120 Belgrade, Serbia. E-mail: mmilos@mas.bg.ac.rs

1. Introduction

Measurements of external aerodynamic load using a wind tunnel balance are based on the behavior of the balance as an elastic system. The balance transfers the load to a fixed support. Deformations of the balance caused by the load are measured using strain gauges applied at convenient measuring stations on the balance body.

Experimental Aerodynamics Department of the Military Technical Institute (VTI) designs, produces, calibrates and uses various strain-gauge-based electromechanical force transducers for measurements in wind tunnel tests (wind tunnel balances). Practical experience in this field has been gained for more than thirty years. A wide range of designs is in use, from one-component to six-componet internal and external balances. The majority of realized designs are monoblock balances, being built from single pieces of high-quality steel.

A special-purpose three-component wind tunnel balance was designed, built, calibrated and used for measurements of aerodynamic forces and moments on a wing panel of a particular wind tunnel model of a missile with slots on the body for storage of folded wings.

2. Design requirements

During balance design certain requirements had to be respected as much as possible:

– Desired load components had to be measured with sufficient accuracy;

– Changes in the angle of attack of the wing, relative to model body, caused by aerodynamic loads acting on the balance, had to be minimized;

– Geometry and location of measuring stations on the balance had to be selected so that sufficiently high levels of output signals could be obtained from measuring bridges; however, relative deformation at any location of a strain gauge was not to exceed 2000 μm/m;

– Satisfactory safety factors, defined as higher than 2 on the basis of equivalent normal stress (von Mises stress) relative to yield strength, had to be established on the critically loaded locations on the balance;

– Deformations of measuring stations caused by primary load components (load components measured at that particular balance stations) had to be more significant than deformations caused by secondary load components;

– If possible, strain gauges had to be applied symmetrically on the measuring stations, in order to provide the highest possible stability;

– The balance was to be calibrated with load configurations as similar as possible to those in the actual test conditions.

3. Wing balance design concept

The three-component strain gauge balance was required to measure normal force *Y*, hinge moment *N* and bending moment *L*, Fig.1, without obstruction to crossflow through the slots.

The relevant load component, for the design of the balance was the normal force, Table 1. The monoblock (single piece) balance concept was selected for the balance. An analysis showed that the use of the Vascomax 350 steel, with high mechanical performances and good machinability was required.

The load range and available space constraints dictated that the balance be of the bending-beam type. Design concept with two parallel load-sensing flexures was selected because the characte-ristic of

this type of the balance is that the angular deflection of the loaded balance around the hinge axis is very small. The two-flexure design also produced little or no obstruction to crossflow through the slots on model body.

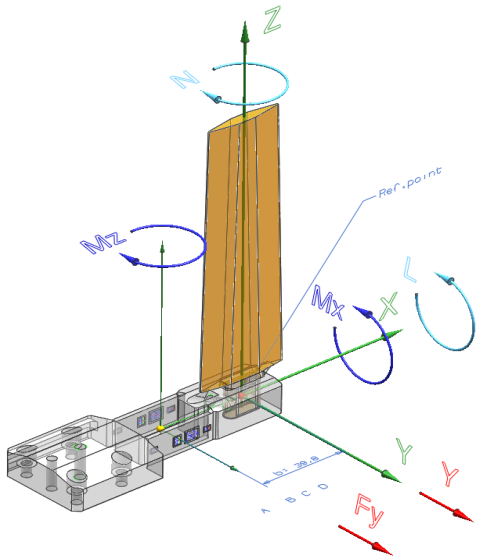

Fig. 1. Aerodynamic load which were measured.

4. Wing balance calibration concept

Any special-built single-use balance is being calibrated at the beginning of the wind tunnel test, usually when the balance is already installed in a model, and connected to the data acquisition system. This procedure ensures that the balance is calibrated in the conditions as similar as possible to the actual test conditions.

The wind tunnel data reduction software in VTI supports primarily the model of the relation between the loads and output signals of a multicomponent balance in which the output signals are expressed as functions of applied loads, [1]. Balances are calibrated using a modern "single-vector" technique that permits simul-taneous application of loads to more than one measuring element (component) of the balance, Fig.2. The idea behind this approach is that the loading configuration during calibration should be representative of the conditions in which the balance will be during a wind tunnel test.

An extensive calibration of the balance was performed, with about 280 datapoints, optimized for load configurations expected in the wind tunnel test. Calibration results confirmed the correct operation of the balance in this configuration. Achieved uncertaintes were very good both in terms of the maximum errors (P.Err.) and in the terms of standard deviations (Std.d.), Table 1 (*Fy*, *Mx* and *Mz* were physical measurement compo-nents, combined to form *Y*, *L* and *N*, while *F*++ and *M*++ were total force and moment loads).

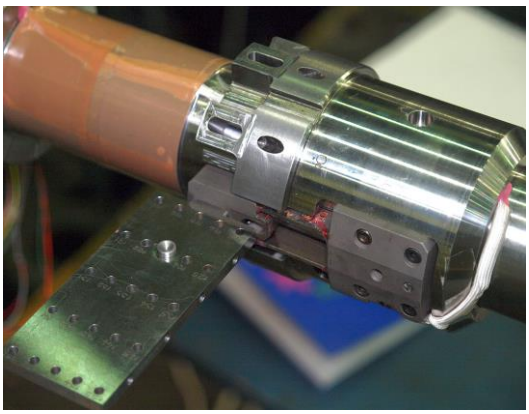

Fig. 2. Calibration of the balance.

Table 1. Summary results of the calibration

BalanceComponent	*Fy*	*Mx*	*Mz*	*F*++	*M*++
Load range,N,Nm	290	18.9	15.7	290	33.2
Applied load,N,Nm	270	17.5	13.4	270	17.5
P.Err.[%]	–0.087	–0.121	0.124	0.087	0.069
Std.d.[%]	0.032	0.044	0.040	0.032	0.025

Achieved accuracies compare well to the current requirements [1] for advanced strain gauge balances, which have been adopted by VTI as the guidelines for evaluating balance quality. The requirements call for standard deviations of the errors, computed from the back calculated calibration data, of approximately 0.05% of full range load for each component under all configurations of loads, which corresponds to an "accuracy" of about 0.1% of full scale design loads. For all components, the balance satisfies these requirements.

5. Conclusions

The balance satisfied the design and calibration requirements. Achieved accuracy, for 95% measurement certainty (equal to 2σ), was better than 0.1%FS for each component (target design accuracy was 0.2%FS). Wind tunnel test campaign confirmed the correct operation of the balance and a very good agreement was noted between test results obtained from the balance and the preliminary CFD calculations.

References

[1] Recommended Practice for Calibration and Use of Internal Strain-Gauge Balances with Application to Wind Tunnel Testing, AIAA Standards, R-091-2003e, 2003

PROPERTIES OF WELDED LOW-ALLOY STEEL AFTER ULTRASONIC IMPACT PEENING APPLICATION

František NOVÝ[1], Libor TRŠKO[2], Otakar BOKŮVKA[1], Michal JAMBOR[1], Filip PASTOREK[2], Miloš MIČIAN[1], Daniel HARMANIAK[1]

[1] University of Žilina. Faculty of Mechanical Engineering, Univerzitná 8215/1, 010 26 Žilina, Slovakia, E-mail: frantisek.novy@fstroj.uniza.sk

[2] University of Žilina, Research Centre of University of Žilina, Univerzitná 8215/1, 010 26 Žilina, Slovakia

1. Introduction

The fatigue of structural materials is the dominant mechanism in the threshold state of material field and is very frequent cause of unexpected structural failures. The reasons of fatigue failures of structural components have been investigated for more than 170 years. The Wöhlers curve incl. fatigue limit (referred to $N = 2\times10^6 \div 10^7$ cycles) is known since year 1858. The strain or stress vs. number of cycles plot ($\varepsilon_a = f(N)$, $\sigma_a = f(N)$) incl. fatigue limit are the main factors used at evaluation of fatigue properties of structural materials [1-3].

The mechanical, metallurgical and environmental variables can influence the fatigue properties of structural materials. The welding is one of them because the weld is a place with highly inhomogeneous microstructure and high residual stresses, which cause that the weld is preferential place for initiation and propagation of fatigue cracks. The fatigue properties are lower due to weld imperfections [4].

The fatigue degradation mechanism in the high-cycle region usually initiate in the place of maximum stress, on the open surface of cyclic loaded components. With regard on this fact, it is important to eliminate the possibility of fatigue degradation mechanisms to take place in the structural materials. The technological surface treatment is possible way. There are the methods which use changes of the chemical composition and microstructure of the surface layers (carburizing, nitriding, hardening or their combination), methods of different coating deposition (CVD, PVD, plasma, metal coating), pre-deformation of static or dynamic repeated loading and methods which mechanically, by deformation, strengthen the surface layers (shot peening, roller burnishing, sand blasting) and so on [3]. Especially shot peening or severe shot peening are the methods used to increase the fatigue properties of structural materials. These methods causes creation of compressive residual stresses in the sub-surface layers of the treated material and mainly increase the time necessary for fatigue cracks initiation and can increase the total fatigue endurance of structural components [5-7].

The High Strength Low-Alloy steels (HSLA) are due to their high mechanical properties and good weldability used in the transportation industry. In the field of transportation are very high requirements on the safety, reliability, economy and ecology of operation, what has direct connection with the increase of fatigue degradation mechanism resistance [8]. One way how increase the fatigue properties of welded HSLA steels is to use methods of ultrasonic impact peening.

In this paper authors publish their own results about mechanical properties of welded HSLA steel after ultrasonic impact peening application with reference to the reliability and safety.

2. Experiments and results

Experimental works (quantitative chemical analysis, tensile tests, ultrasonic impact peening and fatigue tests) were carried out on the HSLA steel Strenx 700 MC. Quantitative chemical analysis (emission spectrometry on an ICP-JY 385 spectrometer) showed following chemical compositions (in weight %), C 0.11, Si 0.093, Mn 0.64, S 0.017, P 0.009, Al 0.017, Nb 0.088, V 0.19, Ti 0.14 and tensile tests (ZWICK Y050 machine) after heat treatment the mechanical properties, Re = 741 MPa, UTS = 823 MPa, A5 = 11.5 %, Re/Rm = 0.90. Specimens for rotating bending fatigue tests (2 sets of 12 pieces, ϕ 7 mm) with welded joint in the middle of the gauge length were treated with ultrasonic impact peening technology (Fig. 1), at impact frequency of f = 20 kHz, displacement amplitude of contact tip ± 10 μm and 85 N contact

force. Fatigue testing was carried out on a rotating bending testing device ROTOFLEX with loading at cycle asymmetry ratio R = -1, frequency f = 20 Hz and temperature T = 21 ± 3 °C. The run – out value was N = 1 × 10^8 cycles and obtained the values of fatigue limit σ_{oc} were σ_{oc} = 370 MPa (welded HSLA steel) and σ_{oc} = 410 MPa (welded HSLA steel + ultrasonic impact peening at 85 N contact force).

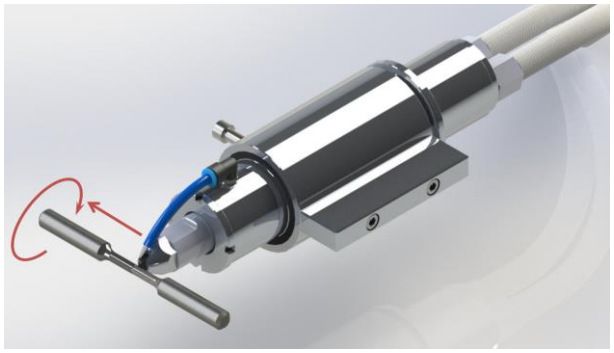

Fig. 1. Ultrasonic impact peening equipment.

The threshold value K_{ath} is very important information used by engineers for an optimal design of structural components. The approximate threshold value K_{ath} of tested HSLA steel was calculated with following equation [9], K_{ath} = -0.052 × UTS + 8.5906 (MPa· $m^{1/2}$), where UTS is the ultimate tensile strength (equation is valid in the region from UTS = 360 MPa to UTS = 1040 MPa). The obtained value was K_{ath} = 4.32.MPa· $m^{1/2}$. Consequently, approximate intrinsic crack lengths a_{01} and a_{02} were calculated for N = 1 x 10^8 cycles of loading using the equation $K_a = 0.656 \times \sigma_o (\pi.a_0)^{1/2}$, (MPa.$m^{1/2}$),

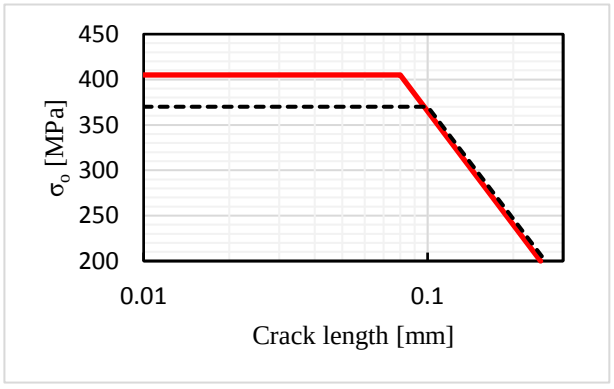

Fig. 2. Kitagawa-Takahashi diagram for welded HSLA steel and welded HSLA steel + ultrasonic impact peening drawn for N = 1×10^8 cycles.

where σ_o is bending stress and a_0 is the intrinsic crack length. The intrinsic crack lengths were a_{01} = 0.10 mm (welded HSLA steel) and a_{02} = 0.08 mm (welded HSLA steel + ultrasonic impact peening at 85 N). The results are shown also in the Fig. 2. The results are in agreement with general conclusions published in works [10-12].

3. Conclusions

With regards to the experimental work carried out on HSLA welded and welded + ultrasonic impact peened steel, can be concluded, that ultrasonic impact peening increased the fatigue limit at N = 1 × 10^8 cycles about 9.45 %.The resistance to crack initiation is the best after ultrasonic impact peening and area of safe loading is more extensive. These facts can be taken into consideration with reference to reliability and safety when designing welded structural components.

Acknowledgements

The research was supported by the project APVV-16-0276 and VEGA No. 1/0951/17.

References

[1] Wöhler, A. Z., Bauw 8,642, 1858; 10,583, 1860; 13,333, 1863; 16,67, 1866; 20,74, 1870. *Engineering 11*, 199, 1871.
[2] Bokůvka, O. et al. *Low and High-frequency Fatigue Testing.* EDIS UNIZA Žilina, SK, 2002.
[3] Bokůvka, O. et al. *Fatigue of Materials at Low and High Frequency Fatigue Loading.* EDIS UNIZA Žilina, SK, 2015.
[4] Michalec, J. et al. *Weld joints fatigue properties of thin carbon steel sheet treated by nitrooxidation.* Techničeski vjesnik, 19 (1), 2012, 65-69.
[5] Miková, K. et al. *Fatigue behavior of X70 microalloyed steel after severe shot peening.* Int. Jour. of Fat., 2013, 55, 33-42.
[6] Trško, L. et al. *Effect of Severe Shot Peening on Ultra-high Cycle Fatigue of Low-alloyed Steel.* Mat. and Design, 2014, 57, 103-113.
[7] Trško, L. et al. *Effect of Severe Shot Peening on the Surface State of AW 5075 Al Alloy.* Kovové materiály – Metalic Materials, 2015, 53, 239-243.
[8] Skočovský, P. et al. *Metal Science*. EDIS UNIZA Žilina, SK, 2014 (in Slovak).
[9] Růžičková, M. et al. *Growth of long cracks at high frequency cyclic loading.* Materials Engiineering, 1999, 6/15, 19-26 (in Slovak).
[10] Ritchie, R. O. *Application of Fracture Mechanics to Fatigue Crack Propagation.* University of California, 1981.
[11] Murakami, Y. *Metal Fatigue: Efects of Small Defects and Nonmetalic Inclusions*. 1st ed. Oxford, Elsewier, 2002.
[12] Klesnil, M., Lukáš, P. *Fatigue of Metalic Materials.* ACADEMIA Praha, CZ, 1980 (in Czech).

MINIATURIZED WEARABLE BROADBAND ENERGY HARVESTERS

Petar GLJUŠĆIĆ [1], Saša ZELENIKA [1], Marina FRANULOVIĆ [1]

[1] University of Rijeka, Faculty of Engineering and Centre for Micro- and Nanosciences and Technologies, Vukovarska 58, 51000 Rijeka, Croatia, e-mail: sasa.zelenika@riteh.hr;

1. Introduction

Low-level ambient energy, gathered and converted into electrical energy using energy harvesting, can be used to power miniaturized devices such as sensors, wearable electronics and Internet-of-Things components. Kinetic energy, due to its presence in all moving systems, is of special interest in wearable technology applications [1-2]. The replacement of batteries with innovative energy harvesting devices (e.g. piezoelectric or electromagnetic) can result in mass and size reduction, favoring ever-increasing miniaturization of wearable devices, as well as drastically increasing their autonomy. Innovative miniaturized broadband wrist-worn kinetic energy harvesting solutions, primarily aimed for powering ultra-low power devices for medical applications (e.g. telemedicine, drug delivery and health monitoring), are proposed in this work [3].

2. Broadband energy harvesting

The proposed energy harvesting devices are based on an optimized piezoelectric bimorph cantilever design. The main issue in this frame is the narrow area of optimal operation around the eigenfrequencies of a specific device. Within this area, a high voltage level is generated, but it rapidly decreases with the variation of the excitation frequency [1]. When kinetic energy from human motion is used, the excitation of the harvester happens across a wide range of frequencies, thus reducing the maximum possible voltage output. Several approaches to solve this problem, i.e., the broadening of the optimal frequency spectrum, have been suggested in recent literature [1-4]:

- changing the conditions around the cantilever free end (e.g. damping control or active tuning),
- changing the geometry of the cantilever (by using complex geometries with bi-stable or nonlinear responses, or a large number of differently tuned cantilevers) and
- "plucking" the free end of a cantilever and letting it oscillate at its eigenfrequency.

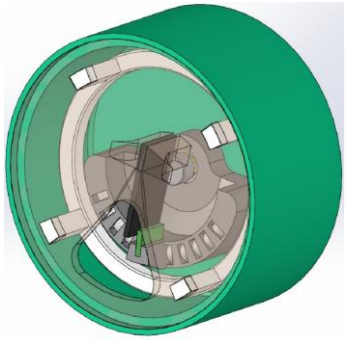

Fig. 1. Piezoelectric energy harvester in a watch-like wearable device [4].

Initial concepts of employing bimorph piezoelectric energy harvesters as wearable power sources, which are studied in collaboration with medical institutions, comprise a watch-shaped device with a flywheel used to transform the energy of hand motion into rotational energy (Fig 1). The attained rotation is used to "pluck" the free end of a bimorph cantilever (or a number of them), thus inducing the excitation of the harvester(s) and generating electrical energy [4]. By modifying the bimorph to an optimized triangular shape (or, due to technological reasons, a more convenient trapezoidal shape), a quasi-uniform stress distribution along its surface can be achieved, thus significantly increasing the specific power output [5]. It was experimentally shown that, by inverting the trapezoidal shape (clamping the cantilever at its narrow end), an even larger increase in specific power can be achieved [5]. In order to overcome the drawbacks of the experimentally validated analytical "coupled modal electromechanical distributed parameter model", the optimization of different cantilever configurations is performed by employing a numerical ANSYS® model, comprising modal and harmonic analyses [2, 4].

3. Geometry optimization and results

In order to increase the specific power output of a bimorph harvester with a predefined maximum surface area of 20 x 40 mm, the conventional rectangular shape (indicated as "R") is divided in two

trapezoidal (A) and an inverted (B) bimorph (Fig. 2). The considered thicknesses of the substrate and piezoelectric layers are equal in all studied bimorphs, while a 0.5 g tip mass is affixed to their free ends. In this frame, it was experimentally shown [5] that the inverted trapezoidal harvester with a narrow clamped end allows achieving a considerable increase of the output power.

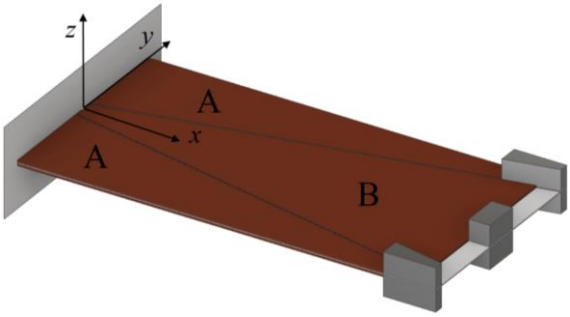

Fig. 2. Optimized usage of the available envelope for the harvester.

As the bimorph is intended to be excited by "plucking", thus allowing each segment to oscillate at its eigenfrequency, the segments are analyzed separately. The optimal load resistance for each segment needs hence to be determined by sweeping through a wide spectrum of load values from 1 kΩ up to 1 MΩ. From the attained data, a power output peak can be observed at a respective optimal load. The specific power output values (Fig. 3) are obtained by normalizing the powers with the segment's surface. It can therefore be concluded that the triangular and inverted shapes result both in higher specific power outputs than the rectangular bimorph. What is more, the optimized configuration allows also matching the maximal power output to a load equivalent to that of a specific wearable sensor, while a variation of the tip mass can be used to vary the respective eigenfrequencies according to the requirements of a specific application.

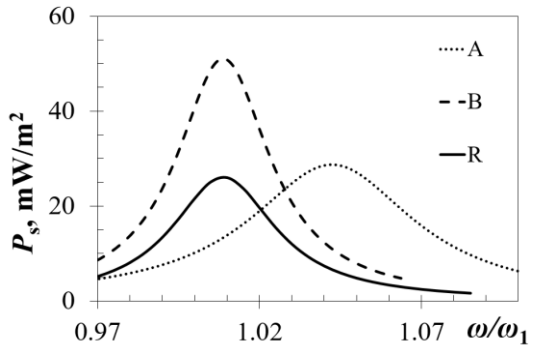

Fig. 3. Specific power output of the analyzed bimorphs.

In order to verify the numerically obtained results, a suitable experimental set-up is developed and will be used next. It is based on a shaker, a piezoelectric accelerometer and a laser Doppler vibrometer. The set-up in interfaced to a LabVIEW-based NI data acquisition system (Fig. 4).

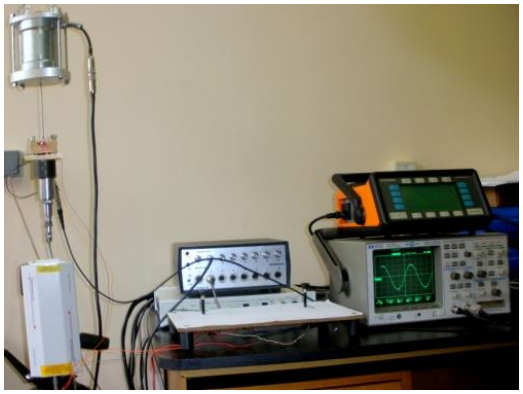

Fig. 4. Experimental set-up.

4. Conclusions and outlook

The specific power output of a wearable piezoelectric harvester can be optimized by varying its shape for a given maximal envelope of the device. By segmenting the conventional rectangular harvester into two trapezoidal and one inverse trapezoidal segment, the power output can thus be significantly increased, providing also a larger flexibility of adapting the performances to the foreseen applications. The segments can hence operate in optimal conditions, maximizing the energy conversion efficiency and, thus, the autonomy of wearable devices. A further experimental optimization of the devised solution is currently being performed.

Acknowledgements

Work supported by the University of Rijeka grant uni-tehnic-18-32 and by using the equipment funded via the ERDF project RC.2.2.06-0001.

References

[1] Prya, S., Inman, D. *Energy harvesting technologies*, Springer: New York, 2009.
[2] Kaźmierski, T.J., Beeby, S. *Energy harvesting systems principles, modeling and applications*, Springer: New York, 2011.
[3] Tan, Y. K. *Energy Harvesting Autonomous Sensor Systems*; CRC Press: Boca Raton, 2013.
[4] Gljuscic, P., Zelenika, S. Coupled electromechanical numerical modelling of piezoelectric vibration energy harvesters, *Proc. 29th DAAAM Int. Sym.*, Vienna, 2018; pp. 0009-0015.
[5] Benasciutti, D. et al. Vibration energy scavenging via piezoelectric bimorphs of optimized shapes. *Microsyst Technol*, 2010, 16(5), 657–668.

DEVELOPMENT OF A CYBER-PHYSICAL SIMULATION ASSISTANCE SYSTEM FOR PARTIALLY AUTOMATED OPTIMIZATION OF THE EXTRUSION PROCESS

Johannes Philipp TERHECHTE[1], Anna-Lena BERSCHEID[2], Ilona HORWATH[3]

[1] Paderborn University, Chair of Automotive Lightweight Design (Technology and Diversity), Warburger Str. 100, D-33098 Paderborn, Germany, E-mail: johannes.terhechte@upb.de

[2] Paderborn University, Chair of Automotive Lightweight Design (Technology and Diversity), Warburger Str. 100, D-33098 Paderborn, Germany

[3] Paderborn University, Chair of Automotive Lightweight Design (Technology and Diversity), Warburger Str. 100, D-33098 Paderborn, Germany

1. Introduction

Regarding the methods of processing polymeric materials, extrusion is one of the most popular methods to manufacture polymer-based products like tubes, pipes, sheets, films, or rods. The increasing number of technological use and the developing market from polymer engineering low-cost products to high-end products reinforces the requirement of quality control and quality assurance. Presently, it is state of the art to detect fluctuating material properties through process monitoring and inline control. The measurements accompany with various parameters during the extrusion process, like pressure, temperature, granules humidity, or cooling velocity. Furthermore, it has been shown that linear product quality control models are not capable to deal with process-related nonlinearities. At the moment, it is nearly impossible to seek out the connection between deviant quality and causal process parameters without years of work experience (Fig. 1).

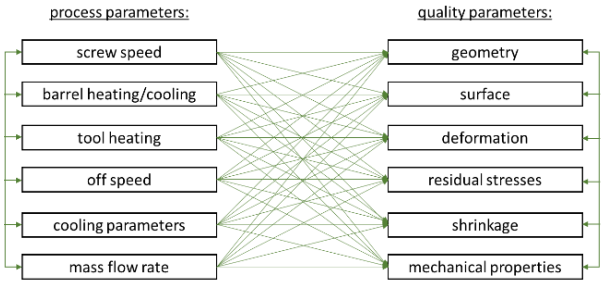

Fig. 1. Linkage between process and quality parameters [4].

In addition, the development of the assistance system provides a solution for the continuous shortage of skilled workforce and the fact that many companies more frequently have to employ untrained personnel as operators for extrusion processes and machines. Moreover, technological improvements should contribute to minimize the process related ubiquitous problems such as long machine downtimes, waste of material, labour and energy to offer multiple economic benefits [2]. In this regard, the development of a cyber-physical assistance system for partially automated optimization of the extrusion process and virtual assistance for unskilled labour force is necessary, to improve productivity, product quality, usability, diversity and working conditions.

2. System Development Process

To feed the cyber-physical assistance system with information from a database of sensor-based live data and an additional availability of expert knowledge regarding the linkage between process parameters and quality parameters, different development steps and information flows are necessary. First of all, the database requires live data from additionally installed sensors at the extruder screw, the assembled tool and the cooling section. Likewise, the data from the main plant control is transferred to the database. The real-time simulation also receives live data from additionally installed sensors and the main system control (Fig. 2). Meanwhile, the simulation software simulates the various process steps online, using the extruder simulation (*REX*), the tool simulation (*Extrude3DPro*) and the simulation of the cooling section (*chillWARE*).

The generated data is stored in a database and flows, combined with the extensive and integrated expert knowledge, into the cyber-physical

assistance system. In case of process deviations, the assistance system activates autonomously the corresponding actuators and supports the machine operator with visualized instructions or assistance for optimized process parameterization.

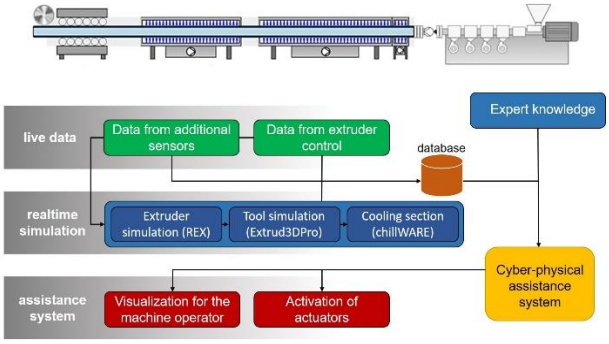

Fig. 2. Cyber-physical assistance system [3].

In order to be able to develop the assistance system in an application-oriented manner, the consideration and implementation of the knowledge of the machine operators and production setters is unavoidable [5]. During the development process, we will be evaluating various stages of the user interface by machine operators and other employees in the plastics industry. As an additional outlook, it is intended to integrate functions, beside the simulation overview, historical data and proposed solutions, as "Optimize" or "Virtual Laboratory". In order to implement the solutions in a user-oriented manner, special scientific methods are necessary.

3. Methodology

For the expertise analysis and the machine operators` requirements, qualitative and quantitative methods are applied. To identify and integrate expert knowledge into the interface between the database and the assistance system, qualitative interviews and observation in different extrusion plants are carried out and translated into social and technical system requirements [1]. These hands-on experiences facilitate to emphasize the actual problems and needs of people who work at the interface of human and machine on an everyday basis and are therefore of great value for a successful development of the assistance system. This approach is based on the fact that organizational work is always embedded in a so called sociotechnical system in which human and machine interact in a productive way. To include the broader expertize of organizations such as companies and works councils, we will complement our qualitative data with the results of a comprehensive survey study.

4. Conclusion

In order to evaluate occurring deviations in the process and in terms of component quality, the connection between process parameters and quality parameters plays the decisive role. The linkage between mechanical parameters and actual process values have to be linked to the online simulation and the expert database. The developed system and the underlying methods will be investigated further and published in the course of the project "ExtrA".

Acknowledgements

The support of this work within the research project "ExtrA - Development of simulation based assistants for extrusion" funded by the European Regional Development Fund (ERDF) is gratefully acknowledged. The project team consists of the companies *SHS plus GmbH*, *IANUS Simulation GmbH*, the *Chair of Plastic Technologies* and the *Chair of Automotive Lightweight Design (Technology and Diversity)* at Paderborn University.

5. References

[1] Holl, H. J., Cojocaru, E. C., Hehenberger, P., Ernst, W., and Horwath, I. Integration of gender in the design process of mechatronic products: an interdiciplinary approach. In *34th Danubia-Adria Symposium on Advances in Experimental Mechanics*.

[2] Kent, R. 2018. *Energy Management in Plastics Processing. Strategies, Targets, Techniques, and Tools*. Elsevier, San Diego.

[3] SHS plus GmbH. 2018. *How you can read data and process parameters from machine controls*. https://extrusion-training.de/en/wie-sie-daten-und-prozessparameter-aus-maschinensteuerungen-auslesen-koennen. Accessed 13 February 2019.

[4] SHS plus GmbH. 2018. *Virtual assistance systems for extrusion – sense or nonsense? | Extrusion Training*. http://extrusion-training.de/virtuelle-assistenzsysteme-fuer-die-extrusion-sinn-oder-unsinn. Accessed 6 September 2018.

[5] Wischmann, S. and Hartmann, E. A., Eds. 2018. *Zukunft der Arbeit - Eine praxisnahe Betrachtung*. Springer Vieweg, Berlin.

TAILORING MECHANICAL PROPERTIES OF POLYAMIDE BY AFFECTING ITS INHERENT STRUCTURE

Barbara ZUPANČIČ[1], Urška FLORJANČIČ[2], Anatolij NIKONOV[2], Igor EMRI[3]

[1] University of Novo mesto Faculty of mechanical engineering, Na Loko 2, 8000 Novo mesto, Slovenia, E-mail: barbara.zupancic@guest.arnes.si

[2] Faculty of industrial engineering Novo mesto, Šegova ulica 112, 8000 Novo mesto, Slovenia, E-mail: anatolij.nikonov@fini-unm.si; urska.florjancic@fini-unm.si

[3] Faculty of mechanical engineering, University of Ljubljana, Aškerčeva ulica 6, 1000 Ljubljana, Slovenia, E-mail: ie@emri.si

1. Introduction

It is known that the macroscopic properties of polymeric materials strongly depend on their inherent structure which may be in general influenced by the initial kinetics (topology of the individual building blocks) and the conditions that material is exposed to during processing and solidification [1]. Therefore, by accordingly adjusting material inherent structure one may tailor desired macroscopic mechanical properties what is of great interest when we want to achieve a particular functionality of products made from this material. Very illustrative examples of this are the polymeric bone implants where it is important that the artificial elements replacing missing part mimic functionality of the gradient bone structures. Besides biocompatibility, it is requested for the material used for the bone implant to possess comparable properties to the natural bone to avoid a phenomena of osteoporosis [2]. From this point of view, one of the most promising polymeric materials to be used for biomedical implant is polyamide (nylon) [3].

The fact above has motivated us to investigate the possibilities of tailoring time-dependent mechanical properties of polyamide 6 (PA6) by affecting its inherent structure via extreme processing conditions.

2. Materials and methods

Polyamide PA6, provided by BASF, with the bimodal mass distribution (distribution has two peaks) as a representative of the new generation of intelligent polyamides was used for this research. Bimodal PA6 has great potential to form different structures under different boundary conditions during processing and solidification due to its complex inherent molecular kinetics, and therefore offer more possibilities to tailor macroscopic properties by modifying the material inherent structure [1].

In order to check the effect of different boundary conditions on the macroscopic time-dependent mechanical properties cylindrical samples were prepared in two ways. Firstly, by the gravimetric casting according to the procedure described in [4]. This was to exclude the effect of processing parameters and consider the effect of inherent kinetics only, since the gravimetric casting is proved to have negligible effect on the formation of structure orientation. Secondly, cylindrical samples were prepared by injection moulding at the extreme pressure of 1600 bar and the temperature 220 °C. Direction of moulding was parallel to the length of cylindrical specimens, and it was expected that the extreme boundary conditions would affect structure orientation (achieving gradient structure).

Macroscopic mechanical properties were examined by measuring the shear creep compliance, $J(t)$, with the apparatus for torsional creep measurements that has been designed and manufactured at the Faculty of mechanical engineering, University of Ljubljana, Slovenia. Torsional creep measurements were performed in segmental form at 8 different temperatures in the temperature range from 30 to 100 °C, under the constant loading torque, which was within the material linear viscoelastic limit. Following the time-temperature superposition principle, the shear creep segments were shifted along the logarithmic time-scale in respect to the segment measured at the reference temperature, $T_{ref} = 40$ °C, to form the shear creep compliance master curve. For more

details on the measuring and the shifting procedure see [4].

Based on the measured shear creep data of the bimodal PA6 the frequency-dependent storage, $J'(\omega)$, and loss, $J''(\omega)$, compliances were calculated by using the interconversion approximation proposed by Schwarzl [5]. As the last step, loss factor was calculated as $\tan\delta(\omega) = J''(\omega)/J'(\omega)$.

3. Results and discussion

In Fig. 1 the shear creep compliance master curves of the gravimetrically casted and injection moulded samples are presented, while Fig. 2 and Fig. 3 show their frequency-dependent behaviour.

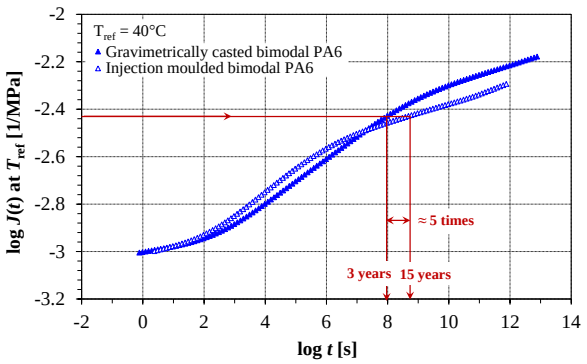

Fig. 1. Time-dependent shear creep compliance vs. time.

It is evident from Fig. 1 that the extreme processing conditions may affect the inherent structure of bimodal PA6 in a way of severely improving its creep time stability (for about 5 times) in the time range relevant for the implant applications.

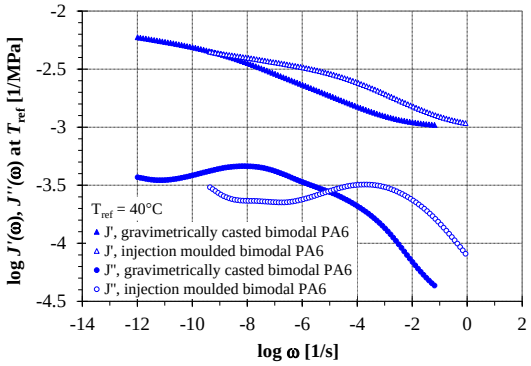

Fig. 2. Frequency-dependent storage and loss compliances vs. angular frequency.

Fig. 2 and Fig. 3 reveal that the extreme processing conditions also affected the frequency-dependent creep properties by finally resulting in the higher magnitude of loss factor (related to the damping capability of a material) and in the shift of its peak closer to the loading frequencies typical for different body functions (e.g., walking, chewing).

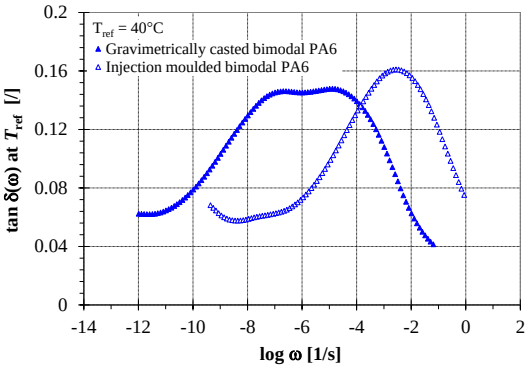

Fig. 3. Loss tangent vs. angular frequency.

4. Conclusions

This research indicates that the ability of different structure formation under particular processing conditions with a consequence of improving macroscopic mechanical properties makes bimodal PA6 to be a perspective implant material. Besides, it exhibits that mechanical testing may be used as a suitable tool to distinguish structural differences via macroscopically detected mechanical responses.

References

[1] Emri, I., von Bernstorff, B. S. The effect of molecular mass distribution on time-dependent behavior of polyamides. *J Appl Mech*, 2006, 73(5), 752–757.

[2] Nagels, J., Stokdijk, M., Rozing, P. M. Stress shielding and bone resorption in shoulder arthroplasty. *J Shoulder Elb Surg*, 2003, 12(1), 35–39.

[3] Rahim, T. N. A. T., Abdullah, A. M., Akil, H. M., Mohamad, D. Comparison of mechanical properties for polyamide 12 composite-based biomaterials fabricated by fused filament fabrication and injection molding. In *AIP Conference Proceedings*, 1791, 2016.

[4] Kubyshkina, G., Zupančič B., Štukelj, M., Grošelj, D., Marion, L., Emri, I. The Influence of Different Sterilization Techniques on the Time-Dependent Behavior of Polyamides. *J Biomater Nanobiotechnol*, 2011, 2, 361–368.

[5] Schwarzl, F. R. The numerical calculation of storage and loss compliance from creep data for linear viscoelastic materials. *Rheol acta*,1969, 8, 6–17.

INFLUENCE OF ROTOR DOWNWASH ON VERTICALLY DISPLACED NANOBOTS IN FLIGHT

Patrick P. NEUMANN[1], Paul HIRSCHBERGER[1], Matthias BARTHOLMAI[1]

[1] Bundesanstalt für Materialforschung und -prüfung (BAM), Unter den Eichen 87, Berlin, Germany,
E-mail: patrick.neumann@bam.de

1. Introduction

Using a swarm of copter-based gas-sensitive aerial nano robots for monitoring indoor air quality is challenging due to, e.g., limited air space in buildings. To avoid an over-regulation of the available indoor air space (e.g., prohibit copters to fly above each other), a safety region around each copter must be defined to guarantee a safe operation of the swarm.

The key contributions of this paper are the realization of experiments that investigate the influence of the rotor downwash on flying vertically displaced nano robots and the development of a model describing the above-mentioned safety region.

2. Robotic Platform

The Crazyflie 2.0 (Bitcraze AB, Sweden) is a flying open-source development platform based on a quadrocopter (Fig. 1, in the following also referred to as nano UAV) [1]. With a take-off weight of 27 g it achieves flight times of up to 7 minutes. The four DC-motors allow a maximum takeoff weight of 42 g, i.e., approx. 15 g remains for additional payload. The diameter of the platform is less than 0.1 m. The nano UAV has a 10 degrees of freedom Inertial Measurement Unit (IMU) and an expansion connector gives access to important interfaces such as I²C, UART, and SPI, as well as PWM, analog in/out, and GPIO. A 2.4 GHz data and control link is used for sending control commands and receiving telemetry and payload data. Via Robot Operating System (ROS) or Python SDK, multiple Crazyflie 2.0 can be controlled simultaneously.

In the current setup, we equipped the nano UAVs with an optical motion detection system (1.6 g), a 3D local positioning system (3.3 g), and a Sensirion SGP30 Multi-Pixel gas sensor. The resulting take-off weight of one copter incl. battery is 35.6 g, which will be further improved to gain longer flight times. Please see [2,3] for further information.

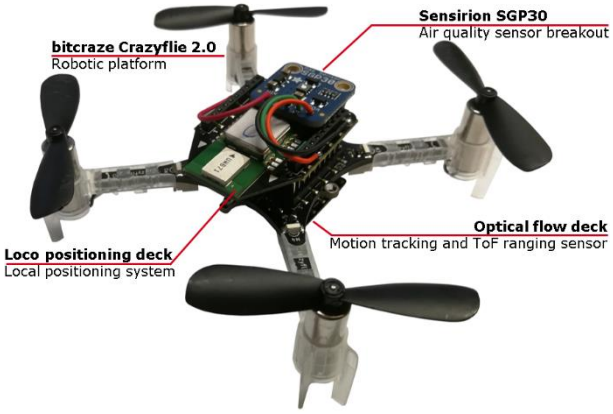

Fig. 1. The Crazyflie 2.0 quadrocopter platform with mounted sensors.

3. Experimental Setup

The time of flight sensor of the optical motion detection system measures the distance to the floor beneath a copter optically. Currently, objects – in this case a second copter – that move into the sensor's field of view are interpreted as the floor resulting in altitude leaps of the copter. To avoid this behavior, we removed the optical motion detection system of the upper flying copter in the experimental setup.

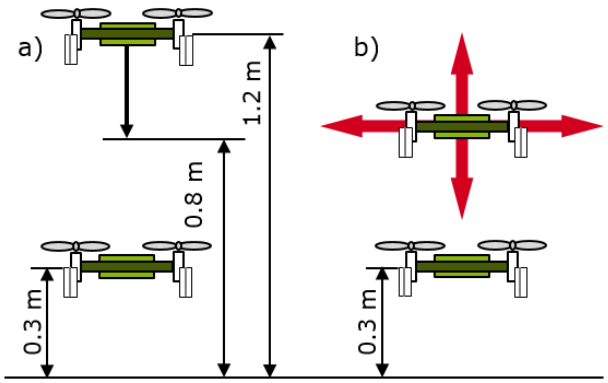

Fig. 2. Experimental setups of a) the minimum vertical distance and b) the horizontal/vertical displacement experiments.

3.1 Minimum Vertical Distance

The experiment was performed with two nano UAVs – one hovering at an altitude of 0.3 m above the ground (CF1), while the second started to descent slowly from an altitude of 1.2 m to 0.8 m (CF4, see Fig. 2(a)). The experiment was stopped, once the flight behavior of CF1 become too unstable or CF1 finally crashed.

3.2 Horizontal/Vertical Displacement

Several flights with two nano UAVs were performed with varying the distance (vertically in 0.1 m and horizontally in 0.05 m steps) to each other, see Fig. 2(b). This was done to study the influence of the rotor downwind of a nano UAV flying above another. Again, the altitude of the hovering copter (CF1) was set to 0.3 m, while the second copter (CF2) was flown to a defined position to examine the hovering performance of CF1. One experiment took 60 s to complete. As performance criteria, we used the combined standard deviation of x, y, and z (σ_{xyz}) of CF1 and the observations we made during the different trials.

4. Experimental Results

In total, we performed 77 trials: one reference trial with a horizontal offset of 1 m between the flying nano UAVs to determine the flight behavior of the copters independently from each other, three trials based on the setup described in Sec. 3.1, and the remaining 73 trials based on Sec. 3.2.

Fig. 3 shows exemplary the resulting trajectories of both nano UAVs of experiment 3.1. As soon as CF4 arrived at its starting position above CF1, the flight behavior of CF1 become more unstable resulting in staggering of the copter, which is comparable to the flight behavior of a copter without installed optical motion detection system. This staggering behavior of CF1 increased during descent of CF4. Finally, CF1 crashed when CF4 reached its minimum vertical distance to CF1 of d_{min} = 0.5 m.

The results of experiment 3.2 can be seen in Figs. 4 and 5. Based on the datasets obtained from the 73 trials, we calculated a map of σ_{xyz}, which is shown in Fig. 5. From this map, three main regions can be identified: a *green* region, where CF2 can fly without having a significant impact on the flight behavior of CF1 (σ_{xyz} < 0.045 m), an *orange* region, where a significant impact on CF1 can be observed (0.045 m ≤ σ_{xyz} < 0.07 m), and a *red* region, where the rotor downwash of CF2 resulted in a crash of CF1 (σ_{xyz} ≥ 0.07 m).

5. Conclusion

In this work, we investigated the influence of the rotor downwash on flying vertically displaced nano robots. From these experiments, we derived the minimum vertical distance between two copters of 0.5 m and a model describing a so-called safety region around each copter allowing a safe operation of the swarm indoors.

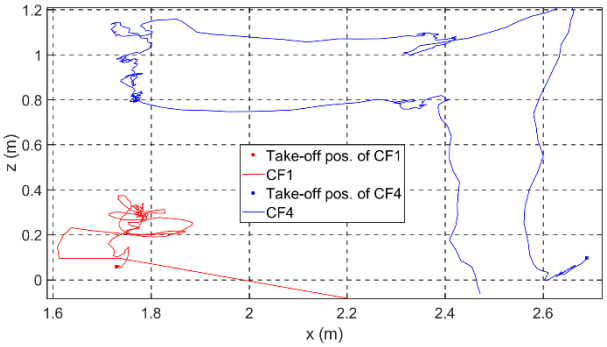

Fig. 3. Result of one vertically displaced flight.

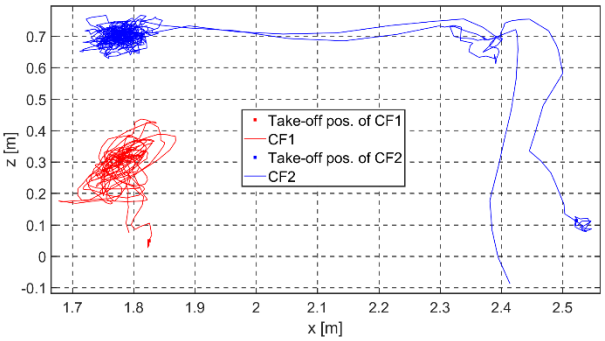

Fig. 4. Result of one flight with a horizontal/vertical displacement of CF2 of 0.15 m and 0.40 m, respectively.

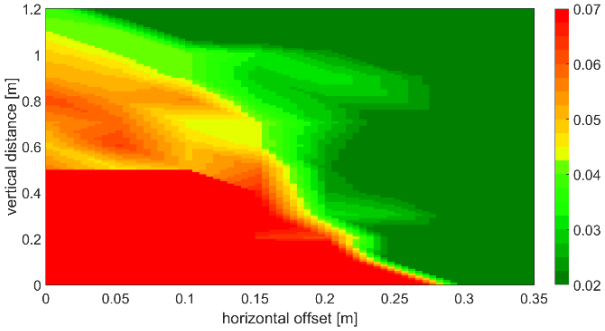

Fig. 5. 2D Map of the combined standard deviation σ_{xyz} of the hovering copter CF1 in [m].

References

[1] https://www.bitcraze.io/
[2] Neumann, P. P., et al., *35th Danubia-Adria Symposium*, Sinaia, Romania, 2018, pp. 139-140.
[3] Neumann, P. P., et al., *2019 ISOCS/IEEE International Symposium on Olfaction and Electronic Nose (ISOEN)*, Fukuoka, Japan, 2019, accepted.

INFLUENCE OF STRAIN RATE ON THE MECHANICAL PROPERTIES OF STEEL

Florin BACIU[1], Aurelia RUSU-CASANDRA[1], Ştefan Dan PASTRAMĂ[1]

[1] Department of Strength of Materials, University Politehnica, Splaiul Independentei 313, sector 6, 060042, Bucharest, Romania, E-mail:{florin.baciu, aurelia.rusu, stefan.pastrama}@upb.ro

1. Introduction

In order to measure strength, elastic constants and other material properties of steel, a number of mechanical tests were developed initially for research purposes and then have been refined and compared to establish if they meet the strict requirements of standardization. A basic and universal engineering test is the tensile test.

Tensile testing procedures have evolved to cover strain rates ranging from static to very high speed. Current tests of tensile properties of various metallic materials may take place in the strain rate range 10^{-6} s^{-1} to 10^{6} s^{-1} on specimens with various gauge length dimensions [1].

While studies of high speed impact situations such as car crashes require high strain rate tests, low strain rate measurements of tensile properties are still widely used for selecting metallic materials for other engineering applications [2].

The purpose of this study was to determine the effect of the strain rates on the mechanical properties and elastic constants of a mild steel under tensile loading.

2. Materials and methodology

The tensile testing methodology fulfills requirements specified in standards ASTM E8-16/ISO 6892-1. Testing was carried out using the universal fatigue testing machine INSTRON 8801 equipped with hydraulic wedge grips and an extensometer (Fig.1).

Five identical sets, each having four identical samples, were cut and machined from a PC52 (0.22%C) steel bar. Specimens had the gauge length of 50 mm and 12.5 mm diameter. Each of the five sets was tested in traction at room temperature and at a specific crosshead speed: 0.1 mm/min; 0.5 mm/min; 1 mm/min; 1.5 mm/min; 2 mm/min. The corresponding strain rates are in the range $3 \cdot 10^{-5}$ s^{-1} – $6 \cdot 10^{-4}$ s^{-1}.

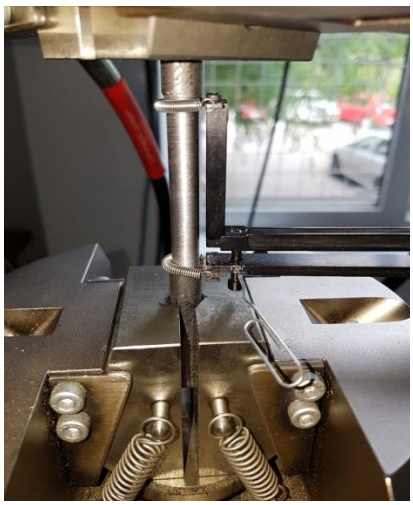

Fig. 1. Fastening of specimen with hydraulic wedge grips.

3. Results

The stress-strain diagrams obtained for the five sets of samples, each tested at a different strain rate, are plotted in Figure 2. Each curve represents the average values obtained from the testing results of the four samples of the set.

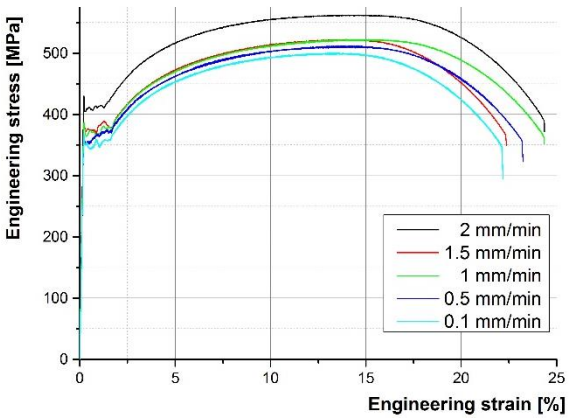

Fig. 2. Stress-strain diagrams for different crosshead speeds.

Figure 3 represents the stress-strain diagrams corresponding to the four specimens tested at a crosshead speed of 1.5 mm/min. The individual

values are very close to the average of the set, in comparison to the rest of the sets.

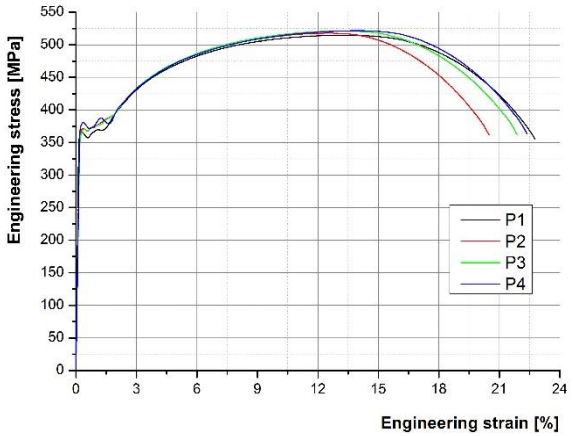

Fig. 3. Stress-strain diagrams for crosshead speed 1.5 mm/min.

Some of the tensile properties measured for the steel specimens at the loading speed of 1.5 mm/min are presented in Table 1.

Table 1. Test results for crosshead speed 1.5 mm/min.

Sample	Yield Strength [MPa]	Tensile Strength [MPa]	Fracture strain (%)	Fracture strength [MPa]
1	355.6	514.8	22.77	354.5
2	368.4	519.2	20.47	360.1
3	366.0	521.2	21.85	361.3
4	368.7	521.3	22.34	363.1

In order to estimate the effect of the loading speed on the statistical distribution of the values of tensile properties measured during testing, the coefficient of variation was calculated according to formula:

$$CV(\%) = \frac{\sigma}{\mu} \cdot 100 \qquad (1)$$

where σ is the standard deviation value and μ represents the mean value. Figures 4 and 5 present the coefficient of variation as a function of the crosshead speed for two of the measured properties, namely yield strength and tensile strength.

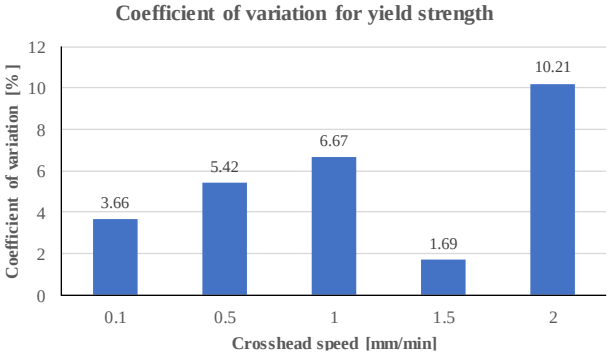

Fig. 4. Coefficient of variation of yield strength.

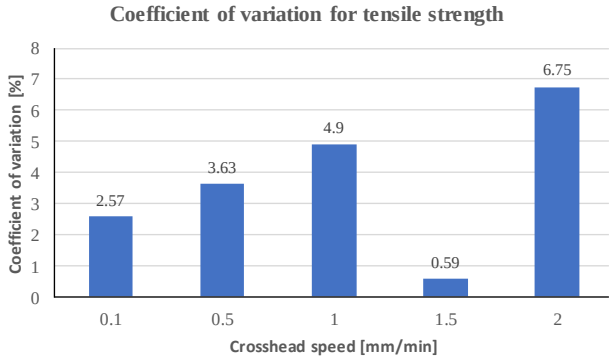

Fig. 5. Coefficient of variation of tensile strength.

4. Conclusions

Tensile properties of steel PC52 have been studied at different loading rates. The results obtained led to the following conclusions:

- Although the strain rates are low, it was noticed that the values of yield strength and tensile strength increase with crosshead speed (Fig.2) in agreement with reference literature [2,3].

- The spread of data of the four stress-strain diagrams (Fig. 3) obtained at loading speed of 1.5 mm/min is the lowest of all rates tested. Therefore, the corresponding values of the coefficients of variation are also the lowest for all tensile properties e.g. 1.69 for yield strength (Fig.4) and 0.59 for tensile strength (Fig. 5), values which are in good agreement with standard ASTM E8/E8M-16. This loading rate should be recommended for tensile test of mild steel PC52.

- The values of the coefficients of variation of tensile properties for other load speeds are higher as a result of a higher spread of measured values.

- The range of these specific low strain rates applied in the study is typical for testing steel used for engineering components in applications such as storage tanks and pressure vessels [1].

References

[1] Wiesner, C.S., MacGillivray, H. Loading Rate Effects on Tensile Properties and Fracture Toughness of Steel. *In 1999 TAGSI Seminar, "Fracture, Plastic Flow and Structural Integrity"* TWI, Cambridge, UK, 29 April, 1999.

[2] Hosford, W. F. *Mechanical Behavior of Materials* Second Edition; Cambridge University Press, New York, 2010.

[3] Dieter G. E. *Mechanical Metallurgy*, McGraw Hill Book Company, New York, USA, 1961.

A NOVEL MULTI-ELEMENT, FOUR-PARAMETER WINDKESSEL MODEL OF THE ARTERIAL TREE

Zdravko VIRAG[1], Fabijan LULIĆ[2], Ivan KORADE[1]

[1] University of Zagreb, Faculty of Mechanical Engineering and Naval Architecture, Ivana Lučića 5, Zagreb, Croatia, E-mail: zdravko.virag@fsb.hr; ivan.korade@fsb.hr;

[2] Pulmonary Disease Clinic, University of Zagreb School of Medicine, Jordanovac 104, Zagreb, Croatia, E-mail: fabijan.lulic@kbc-zagreb.hr;

1. Introduction

Windkessel models of the arterial tree play an important role in clinical practice as well as in prescribing the boundary conditions of one and three-dimensional simulations of blood flow. Such models should describe the main features of the arterial tree (compliance, resistance, inertance and energy dissipation) realistically by using the smallest possible number of parameters. All existing windkessel models consist of a few basic elements modeling inertance, compliance and resistance of the arterial tree, and they can describe the arterial input impedance realistically, but they can model neither the pulse pressure nor flow wave attenuation from the arterial inlet to the capillary outlet.

The goal of this work is to define a novel tree-like structure windkessel model, with only four free parameters which can also model the pressure and flow wave attenuation toward the arterial periphery.

2. Materials and methods

Fig. 1 shows the analog electrical scheme of the proposed windkessel model. Capacitance C_0 and resistance η_0 represent a viscoelastic chamber modeling large arteries. Inertance and resistance in large arteries are modeled by inductance L_0 and resistance r_0. The rest of the arterial tree is modeled by N generations of bifurcating blood vessels. Each generation of blood vessels contains 2^n identical vessels modeled by L_n and r_n while each bifurcation point is a viscoelastic chamber defined by C_n and η_n, where n is the generation number ($n=1,N$). It is assumed:

$$r_n = f_r r_{n-1},\quad C_n = f_C C_{n-1},\quad L_n = f_L L_{n-1},\quad \eta_n = f_\eta \eta_{n-1} \qquad (1)$$

where $f_r = f_\eta = \sqrt[3]{16}$, $f_C = f_L = 1/f_r$. The total peripheral resistance is defined as:

$$R = r_0 + \sum_{n=1}^{N} r_n / 2^n = r_0 \left[1 + \sum_{n=1}^{N} \left(\frac{f_r}{2} \right)^n \right] \qquad (2)$$

The total arterial compliance is defined as:

$$C_{\text{tot}} = C_0 + \sum_{n=1}^{N} 2^{n-1} C_n \qquad (3)$$

It is assumed that the compliance of large arteries ($C_0 + C_1$) is 2/3 of the C_{tot}. Thus, for a given C_0 and taking into account Eq. (1), all other C_n are uniquely defined.

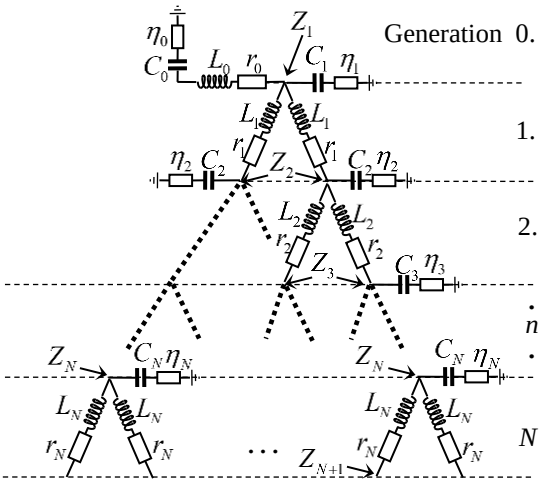

Fig. 1. Electrical analog scheme of the proposed windkessel model.

The impedance of the n-th generation is defined in the frequency domain by:

$$Z_n(\omega) = \left[\frac{sC_n}{1 + sC_n\eta_n} + \frac{2}{sL_n + r_n + Z_{n+1}} \right]^{-1} \qquad (4)$$

where $s = \sqrt{-1}\omega$, and ω is the circular frequency.

Eq. (4) is applied from $n = N$ to $n = 1$, and the input impedance is

$$Z_{\text{in}}(\omega) = \frac{\hat{p}_{\text{in}}(\omega)}{\hat{Q}_{\text{in}}(\omega)} = \left[\frac{sC_0}{1 + sC_0\eta_0} + \frac{1}{sL_0 + r_0 + Z_1} \right]^{-1} \quad (5)$$

where $\hat{p}_{\text{in}}$ and $\hat{Q}_{\text{in}}$ are harmonic phasors of the Fourier series of input pressure and flow, respectively. Free parameters in the model are C_0, η_0, L_0, and r_0.

3. Results and discussion

The model was applied to the systemic arterial tree in a middle-aged man and a pig with available data of input flow and pressure. The model parameters were obtained by minimizing the difference (pressure root mean square error – PRMS) between the measured pressure and pressure calculated from the model using Eq. (5). Figs. 2 and 3 show obtained results in the man, and pig, respectively. In both cases $N = 20$ generations of blood vessels were used.

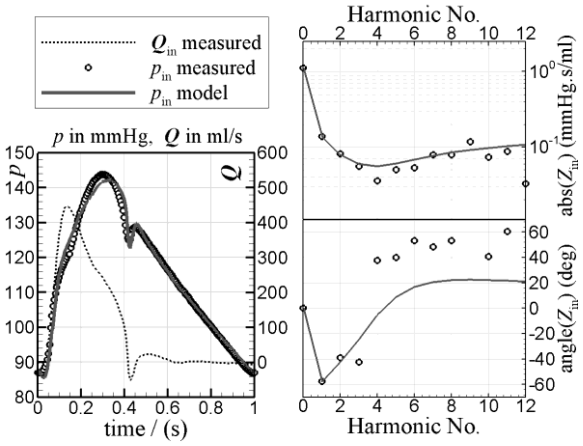

Fig. 2. Results for a middle-aged man, data from [1]. Model parameters: C_0 = 0.717 ml/mmHg, (C_{tot} = 1.238 ml/mmHg), R = 1.15 mmHg·s/ml, L_0=2.62·10^{-3} mmHg·s^2/ml, η_0 =0.141 mmHg·s/ml, achieved PRMS=1.76 mmHg.

In both cases the proposed model describes the arterial input impedance very well. The achieved PRMS is acceptably small. The absolute value of the impedance is minimal at the frequency (or harmonic number) where the angle of the input impedance changes its sign. Westerhof's three element windkessel model (the most frequently used one) can show neither positive values of the angle of Z_{in}, nor local minimum in the absolute value of Z_{in}. This can be seen only in windkessel models with at least five elements (containing at least two capacitors connected by an inductor).

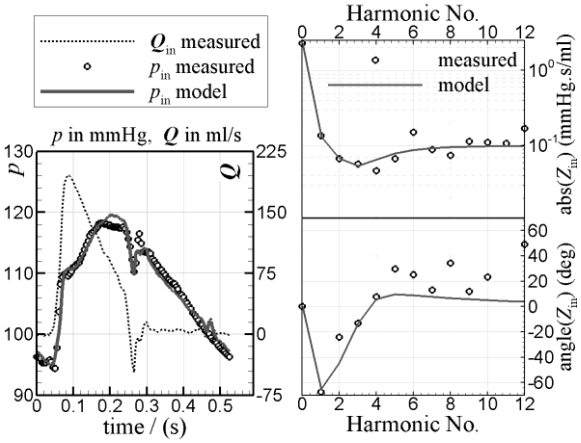

Fig. 3. Results for a pig, data from [2]. Model parameters: C_0 = 0.374 ml/mmHg, (C_{tot} = 0.646 ml/mmHg), R = 2.31 mmHg·s/ml, L_0=2.57·10^{-3} mmHg·s^2/ml, η_0 =0.102 mmHg·s/ml, achieved PRMS=1.25 mmHg.

Fig. 4 shows the fall of the systolic, mean and diastolic pressure in consecutive generations of the pig blood vessels. The generation denoted by zero models the large arteries (let say aorta), and the last generation models arterioles next to the capillaries. A significant reduction in the mean and pulse pressure occurs at the last six generations.

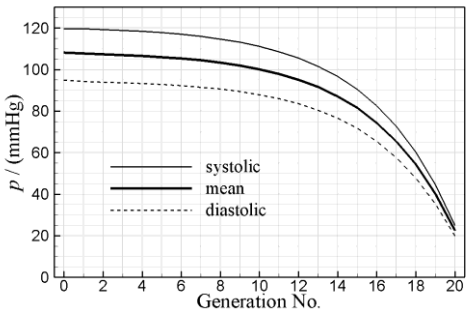

Fig. 4. Attenuation of the pressure pulse.

The proposed model realistically describes the input impedance of the arterial tree as well as the waves attenuation in peripheral small vessels using only four model parameters.

References

[1] Nichols, W.W; O'Rourke, M.F.: McDonald's Blood Flow in Arteries, (5th ed.) Oxford Univ. Press, New York, USA, 2005.

[2] Segers, P., Stergiopulos, N. et al.: Systemic and pulmonary hemodynamics assessed with a lumped-parameter heart-arterial interaction model. J. of Eng. Math., 47, 2003, pp. 185-199.

AN INNOVATIVE METHOD FOR MEASURING YOUNG'S MODULUS OF FLEXIBLE MULTI-LAYERED MATERIALS (TENSILE RING METHOD)

Atsumi OHTSUKI[1]

[1] Department of Mechanical Engineering, Meijo University, Nagoya, Japan,
E-mail: ohtsuki@ccmfs.meijo-u.ac.jp

1. Introduction

In recent years, flexible multi-layered materials with very high performance are used to establish cost-effective processing with regard to long-term performance and reliability. Therefore, Young's modulus of these materials is very important to predict large deformation.

In this study, an innovative mechanical testing method (*Circular Ring Method*) is provided for measuring Young's modulus of each layer in a flexible multi-layered material. By just measuring the vertical or the horizontal displacement of the ring, Young's modulus of each layer can be easily obtained for thin multi-layered materials.

Measurements were carried out on a two-layered wire (Cu: an electrodeposited material + SWPA: a spring steel material).

The method is based on a nonlinear large deformation theory. Exact analytical solutions are obtained in terms of elliptic integrals. Besides the *Circular Ring Method* for a flexible multi-layered material studied here, the *Circular Ring Method* [1], [2], the *Axial Compression Method* [3] for a flexible single-layered material and the *Cantilever Method* [4] for a flexible multi-layered material have already been developed, based on the nonlinear large deformation theory.

2. Fundamental theory

A typical illustration of a deflection shape is given in Fig.1 for a ring, subjected to opposite tensile forces at two points. Denoting the whole arc length of a circular ring by $4L$ and Taking into the boundary conditions $\zeta_{\max}\,(=s_{\max}/L)=1$,$\eta_{\max}=\delta/L$, and, $\xi_{\max}=\lambda/L$, the maximum non-dimensional arc length ζ_{AB}, the maximum non-dimensional vertical displacement η_{AB} and the maximum non-dimensional horizontal displacement ξ_{AB} are obtained as follows.

$$\zeta_{\mathrm{AB}}=1=\frac{F\left(1/k\ ,\ Z_{\mathrm{B}}\right)-F\left(1/k\ ,\ Z_{\mathrm{A}}\right)}{k\sqrt{\gamma}} \tag{1}$$

$$\eta_{\mathrm{AB}}=\delta/L=\frac{\left[\begin{array}{l}\left(2k-1/k\right)\left\{\begin{array}{l}F\left(1/k\ ,\ Z_{\mathrm{B}}\right)\\-F\left(1/k\ ,\ Z_{\mathrm{A}}\right)\end{array}\right\}\\-2k\left\{\begin{array}{l}E\left(1/k\ ,\ Z_{\mathrm{B}}\right)\\-E\left(1/k\ ,\ Z_{\mathrm{A}}\right)\end{array}\right\}\end{array}\right]}{\sqrt{\gamma}} \tag{2}$$

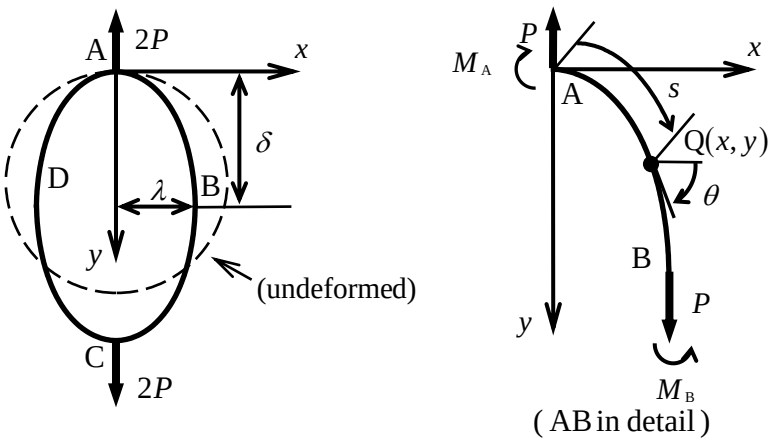

Fig. 1. Schematic illustration of circular ring subjected to opposite tensile forces

$$\xi_{AB} = \frac{\lambda}{L} = \frac{2k\left(\cos\varphi_A - \cos\varphi_B\right)}{\sqrt{\gamma}} \qquad (3)$$

where, $k = \sqrt{\left\{2\lambda + (\alpha + 1/\rho_0)^2/(4\gamma)\right\}}$

$\phi_A = \mathrm{Sin}^{-1}\left[\sqrt{\left\{1/(2k^2)\right\}}\right]$

$\phi_B = \mathrm{Sin}^{-1}(1/k)$

$Z_A = \pi/4, \quad Z_B = \pi/2$

$\gamma = PL^2 \Big/ \sum_{i=1}^{n}(E_i I_i), \quad \alpha = M_A L \Big/ \sum_{i=1}^{n}(E_i I_i)$

I_i : the second moment of area.

The functions $F(1/k, Z_{A,B})$, $E(1/k, Z_{A,B})$ appeared in Eqs.(1), (2) and (3)are elliptic integrals of the first and second kinds, respectively. Using fundamental Eqs.(1)-(3) it is possible to calculate each Young's modulus E_i from the following Eq.(4).

$$\sum_{i=1}^{n}\left(E_i I_i\right) = \frac{PL^2}{\gamma} \qquad (4)$$

One quantity γ (: the non-dimensional load) is required to calculate Young's modulus E_i from Eq. (4). The value of γ is obtained from a chart (Nomograph) of γ -δ relation (δ: the vertical displacement) [Method 1] or γ -λ relation (λ: the horizontal displacement) [Method 2].

3. Experimental investigation

Several experiments were carried out using a two-layered wire [a Copper layer: Cu (0.011mm thick, 500mm long) + a spring steel wire: SWPA (0.38mm diameter, 500mm long)]. Young's moduli of Cu and SWPA obtained by applying Method 2 [Method 1 is omitted here.] are shown in Fig. 2 and 3. The measured values remain nearly constant for a tensile load and the standard deviation (S.D.) is small although the method has a little scattered values.

Acknowledgements

The author thanks to Mr. Noma A, Meijo University, Japan, for assistance in this work.

References

[1] Ohtsuki, A. and Takada, H., A New Measuring Method of Young's Modulus for a Thin Plate/ Thin Rod, *Transactions of Japan Society for Spring Research*, 2002, No.47, pp.27-31. J

[2] Ohtsuki, A., An Innovative Circular Ring Method for Measuring Young's Modulus of Thin Flexible Multi-Layered Materials, Thin Walled Structure, 2011,Vol.1, pp.739-746.

[3] Ohtsuki, A., A New Method of Measuring Young's Modulus Using Postbuckling Behaviours, *Proceedings of the 2006 SEM Annual Conference & Exposition on Experimental and Applied Mechanics*, 2006, *Section* 78, pp.78(1)-78(4). [CD-ROM]

[4] Ohtsuki, A., An Innovative Cantilever Method for Measuring Young's Modulus of Thin Flexible Multi-Layered Materials, *Fifth International Conference on Thin-Walled Structures*, 2008, pp.189-196.

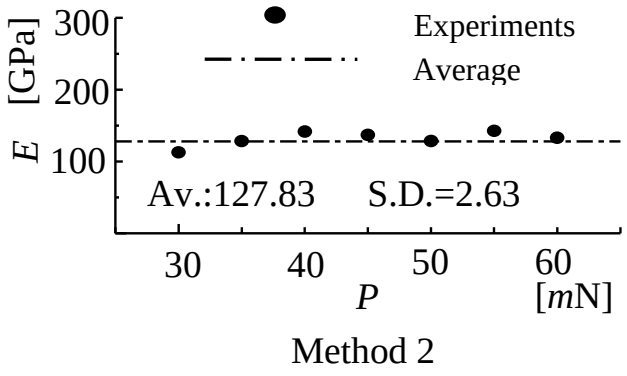

Method 2

Fig. 2. Young's modulus for an electrodeposited material (Cu) [Method 1 is omitted.]

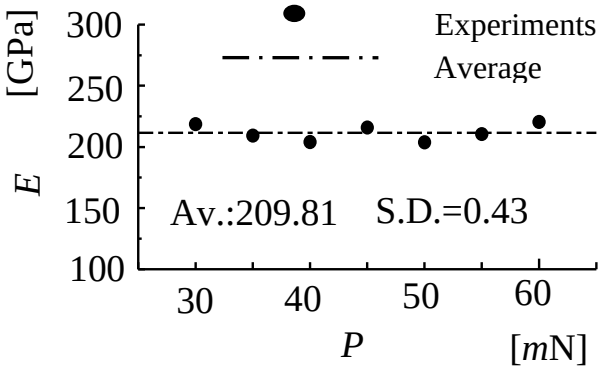

Method 2

Fig. 3. Young's modulus for a steel material (SWPA) [Method 1 is omitted.]

A NEW SOLUTION FOR IMPACT ENERGY DISSIPATION DURING COLLISION OF RAILWAY VEHICLES

Dan Mihail COSTESCU[1], Anton HADĂR[2], Ştefan Dan PASTRAMĂ[2]

[1] Romanian Railway Authority, Calea Griviței nr. 393, Sector 1, Bucharest, Romania,
E-mail: dan@afer.ro
[2] University Politehnica, Splaiul Independenței nr. 313, Sector 6, Bucharest, Romania,
E-mail: {anton.hadar, stefan.pastrama}@upb.ro

1. Introduction

In the railway industry, the necessity of increasing passive safety is a very important task. In order to protect the passengers, train drivers and goods transported on the railway, one of the measures that has to be taken according to the requests of the standard EN 15227:2008+A1:2010 is the controlled absorption of impact energy. In the last 15-20 years, significant progress was noticed on the use of permanent plastic deformation for energy absorption. Witteman [1] showed that the profile with hollow circular section (pipe) should be preferred for energy dissipation, taking into account the energy absorption level and reduced costs. Shakeri et al. [2] described an efficient procedure for impact energy absorption by plastic deformation of a pipe and friction. Another solution, based also on the plastic deformation of a pipe introduced in a tapered ring and on the friction between the pipe and the ring was presented in [3] and [4].

This paper describes the design of a new structural element dedicated to the impact energy absorption for railway vehicles using controlled plastic deformation, as a reliable solution for passive safety during impact of railway cars and locomotives. The energy Q necessary to be dissipated in the plastic collision was established with an average value of 1.1 MJ, for usual maneuvers velocity (10…15 m/s) and for masses between 50 t (cars) and 130 t (heavy locomotives). The relationship used to obtain this energy can be found by writing the equations of conservation of momentum and kinetic energy in plastic collision:

$$m_1\vec{v}_1 + m_2\vec{v}_2 = (m_1 + m_2)\vec{v}\,;\quad \frac{m_1 v_1^2}{2} + \frac{m_2 v_2^2}{2} = \frac{(m_1 + m_2)v^2}{2} + Q$$

where v is the velocity after impact. It should be mentioned also, that a part of the energy Q is absorbed by the buffers and only the remaining part should be dissipated in the newly design absorbers.

2. Design of a new impact energy absorber

A cross section through the new impact energy absorber is shown in Fig. 1. Two absorbers are mounted, one on each buffer. Energy is dissipated in four elements of the structure: 1. The deformable pipe 5 which can expand its diameter with about 24% in case of an impact by being pushed inside the tapered penetrator 6; 2. The penetrator 6 which can absorb energy through friction with the pipe; 3. The support flange 7, on which eight cutting tools are fixed, which cut the deformable pipe and 4. The bending flange used to bend the deformable pipe after cutting.

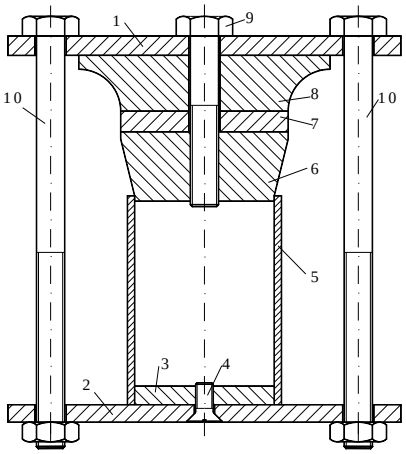

Fig. 1. Section through the impact absorber:
1. Frontal sleeper; 2. Fixing plate; 3. Guiding flange; 4. Fixing screw; 5. Deformable pipe; 6. Tapered penetrator; 7. Cutting support flange; 8 Bending flange; 9. Fixing screw; 10. Pre-stressing screws.

The steel S235JR was used to manufacture the deformable pipe due to its good ductility and toughness. It has a yield limit of 235 MPa and a ultimate strength of 360 MPa. The other elements used to dissipate energy were manufactured from a tougher alloyed steel 45Cr2 (with yield limit 540 MPa and ultimate strength 780 MPa). As indicated in [1], a pipe shaped deformable element was chosen. As stated in standards EN 12663-1/2010 and EN 12663-2/2010, the condition of

plastic deformation only for compression loads higher than 2 MN was imposed in the design process. In order to protect the strength structure of the chassis, a value of 2.5 MN (1.25 MN on each absorber) was considered. Consequently, the length of the element can be inferred from the condition that the dissipated energy U, considered with the average value of 1.1 MJ (0.55 MJ on each absorber) is equal to the mechanical work of the force $W=F\cdot l$. A value l=0.44 m is thus established.

The total length of the deformable pipe was chosen with the value of 500 mm. It's external diameter is 273mm with a wall thickness of 6.3 mm, resulting thus a cross section area A=5278 mm^2 and thus, a normal stress $\sigma=F/A$=236.8 MPa in compression, slightly higher than the yield limit. One end of the pipe is fixed and the other is deformable through the tapered penetrator.

The penetrator (Fig. 2) was designed with an angle of 60° and with a 24mm diameter threaded central hole. The material 45Cr2 was chosen as to ensure only small elastic deformations during collision.

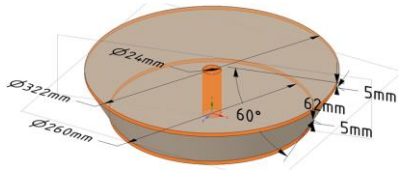

Fig. 2. The tapered penetrator.

The cutting support flange has a radius of 161mm, a height of 10mm and contains eight cutting tools uniformly distributed in the cross section with a 45° angle between them. The width of each tool is 6mm and their length exceeds the maximum diameter of the penetrator with 6mm. Thus, during deformation, they can produce in the pipe eight longitudinal grooves, located symmetrically with respect to the longitudinal axis.

A 3D view of the bending flange, the fourth element used to dissipate the collision energy and which would act in the final stage of the collision if necessary, is shown in Fig. 3.

3. Calculation of the absorbed impact energy

From the entire length of 600 mm, only about 480 mm is the active part of the energy absorber. On this length, a total amount of 1.1 MJ on both elements mounted on the buffers should be dissipated. Based on the dimensions of the elements and the mechanical characteristics of the material, the energy dissipated in each element was calculated as the mechanical work of all forces acting during collision. The results are presented in Table 1.

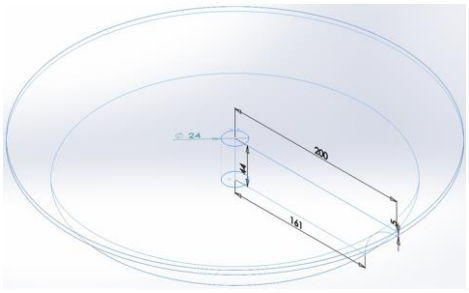

Fig. 3. The bending flange.

Table 1. Energy absorbed in the active elements.

	Expansion of element 5	Friction in element 6	Cutting inside element 7	Bending of element 8	Total
Energy [kJ]	224	252	37.4	47.8	561.2

4. Conclusions

The new energy absorber designed by the authors uses controlled plastic deformation, as a reliable solution for passive safety during impact of cars and locomotives. The calculation of the energy dissipated in all four active elements shows a total amount of 561.2 kJ for each absorber, which is more than the proposed target of 0.55 MN, established based on the common velocities and masses of railway cars and locomotives. Thus, this element can be successfully used as a solution that can diminish the consequences of train collisions. Verification of the obtained results using computer simulations and experiments is to follow as the next step for validation of the proposed structure.

References

[1] Witteman, W.J. Improved Vehicle Crashworthiness Design by Control of the Energy Absorption for Different Collision Situations - Ph.D. Thesis, Technische Universiteit Eindhoven, 1999.

[2] Shakeri, M., Salehghaffari, S., Mirzaeifar, R. Expansion of circular tubes by rigid tubes as impact energy absorbers: experimental and theoretical investigation. *Int J Crashworthiness*, 2007, 12(5), 493-501.

[3] Lučanin, J.V., Tanasković, J.D., Milković, D.D., Golubović, S. Experimental research of the tube absorbers of kinetic energy during collision. *FME Transactions*, 2007, 35(4), 201-204.

[4] Tanasković, J.D., Milković, D.D., Lučanin, J.V., Simić Ž.G. Experimental and numerical determination of tube collision energy absorbers characteristics. *FME Transactions*, 2012, 40(1), 11-16.

LFM CHARACTERIZATION OF TiO_2 FILMS ON A NANOINDENTER

Ervin KAMENAR[1], Marko PERČIĆ[1], Saša ZELENIKA[1], Iva ŠARIĆ[2], Daria JARDAS[2], Petar GLJUŠĆIĆ[1]

[1] University of Rijeka, Faculty of Engineering & Centre for Micro- and Nanosciences and Technologies, Vukovarska 58, Rijeka, Croatia, e-mail: ekamenar@riteh.hr

[2] University of Rijeka, Department of Physics & Centre for Micro- and Nanosciences and Technologies, Radmile Matejčić 2, Rijeka, Croatia

1. Introduction

Thin oxide films are commonly used as coatings in precision devices, where they are often subjected to sliding contacts and friction whose impact can be identified via experimental techniques [1].

An original structured experimental procedure, based on advanced design-of-experiments (DoE) algorithms, allowing to determine the correlation between multiple process parameters and the resulting nanoscale friction, was recently proposed [2]. Such an approach was applied to study, via nanoindentation measurements in the lateral force microscopy (LFM) mode, the effects of the most important influencing parameters on mesoscale friction [1]. In fact, nanoindentation is a valid method to experimentally characterize friction forces in the μN range [3]. LFM measurements performed on a nanoindenter are hence used in this work to assess the properties of a TiO_2 thin-film deposited on an Si substrate. In the space defined by the experimentally determined ranges of sliding velocities and normal forces, the measurement points are determined via DoE routines [2]. Experimental results allow thus establishing correlation functions that can be used as models of the mesoscale frictional behavior of TiO_2 thin films.

2. Materials and methods

The TiO_2 film is deposited on an Si (100) substrate via atomic layer deposition on a Beneq TFS 200 device at 150 °C. A $TiCl_4$ precursor is used for Ti, whereas H_2O is employed as the oxygen source, with the respective pulsing times of 250 and 180 ms, followed by N_2 purging of 3 and 2 s, respectively.

Nanoindentation and nanoscratch measurements are, in turn, carried out on a Keysight Technologies' G200 Nanoindenter, allowing normal and lateral load resolutions of 50 nN and 2 μN, respectively. A fresh Berkovich tip is used to determine the mechanical properties of the sample, whereas LFM tests are performed with a used tip with a slightly "blunter" end. During all the measurements the temperature in the chamber is kept stable at ~ 28 °C.

The mechanical properties of the Si substrate are determined first. The obtained average modulus of elasticity E is 173.4 ± 1.1 GPa, while the average hardness H is 11.9 ± 0.1 GPa. The properties of the TiO_2 film are determined next via a standardized method that enables compensating the influence of the substrate on the results. The average TiO_2 film E value is hence determined to be 144.4 ± 5.2 GPa, while the average H value is 9.5 ± 0.4 GPa.

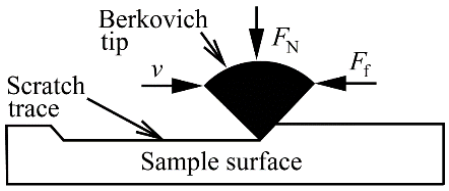

Fig. 1. Scheme of the LFM scratch test.

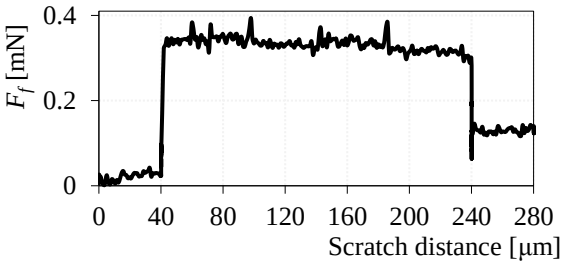

Fig. 2. Typical F_f vs. scratch distance LFM curve.

The second set of experiments is performed by ramping the applied normal load F_N from 0 to 10 mN so as to determine the maximum F_N value for which the displacement of the indenter tip into the surface does not exceed film's thickness (< 150 nm). The F_N range is thus determined to be from 500 μN to 4.5 mN. According to the experimental findings in [1], the range of sliding velocities v is, in turn, from 2 to 50 μm/s. Based on these values, the parameters' design space is sampled by using the Latinized Centroidal Voronoï Tessellation (LCVT) DoE approach [2]. A set of ten $F_N - v$ measurement pairs is hence determined. The

single direction LFM test is used next (Fig. 1) to obtain the values of the friction forces F_f. A single track measurement is repeated 5 times for each $F_N - v$ pair at different locations on the sample, so as to estimate the respective uncertainties. Typical F_f vs. scratch distance graphs are thus obtained (Fig 2).

3. Results and discussion

The mean obtained F_f values for the 10 measurement points are analyzed by using the response surface methodology (RSM), where linear and full quadratic polynomial regression models, whose coefficients are determined iteratively via the Gauss-Newton algorithm, are used [4]. To gain insight into the influence of F_N and v on F_f, the data is statistically analyzed via a correlation matrix (Table 1). It can thus be inferred that F_N has a strong proportional impact on F_f, inducing its growth via tip's penetration into the film (higher plastic deformations). Rising sliding velocities result also in rising F_f values, but the influence of v on F_f is notably smaller than that of F_N.

Table 1. Correlation matrix of experimental data.

	F_N	v	F_f
F_N	1		
v	0.092	1	
F_f	0.964	0.315	1

The derived meta-models have the coefficients of determination R^2 of 0.984 and 0.995, respectively. The linear and full-quadratic meta-models can hence be expressed as [2, 4]:

$$F_f = -0.1055 + 0.1599 \cdot F_N + 0.0032 \cdot v \quad (1)$$

$$F_f = 0.007 + 0.103 \cdot F_N - 0.002 \cdot v + \\ + 0.011 \cdot F_N^2 + 0.0001 \cdot v^2 + 0.0001 \cdot F_N \cdot v \quad (2)$$

Table 2. Average F_f values and respective deviations.

Experimental data				Model predictions			
F_N [mN]	v [µm/s]	Exp. [µN]	St. dev. [%]	Lin. mod. [µN]	St. err. [%]	Full quad mod. [µN]	St. err. [%]
0.6	42	150	8.1	120	14.8	140	1.8
1.1	23	110	5.3	140	30.6	140	24.9
1.4	9	180	2.5	150	20.2	160	11
2	38	330	1.9	340	2.0	310	5.3
2.4	12	310	3.7	320	1.3	310	1.1
2.5	33	370	4.7	400	6.6	370	1.8
3	4	400	1.4	390	4.4	410	0.8
3.5	21	470	6.8	520	11.2	500	7.3
4.1	50	730	1.3	710	2.5	740	1.5
4.2	29	680	7.3	660	3.9	650	4.5

The experimentally and numerically determined F_f values, and the respective deviations, are reported in Table 2. It can be observed that the variance of the experimental F_f values is from 1 to 8 %. When compared to the mean experimental data, the model-derived F_f values induce a standard error e limited to ca. 20 % for the linear and of 10 % for the full quadratic one, except for the second measurement point that shows clearly bigger deviations. Further experimentally obtained F_f values for randomly chosen $F_N - v$ pairs, allow establishing that in all the considered cases e is < 10 % for both models.

4. Conclusions and outlook

The experimentally-derived meta-model of the dependence of mesoscale friction on sliding velocities and normal forces on a TiO_2 thin-film, is described in this work. The measurements, performed by using a nanoindenter in the LFM measurement mode, result in a marked positive correlation of the process parameters on the friction force, although the normal force has clearly a higher impact. The determined polynomial meta-models provide a good fit with the experimental data.

The study will be continued on other thin-film samples (ZnO, MoS_2 and Al). The attained results on the mesoscale shall finally be integrated with performed nano- [2] and macro-scale [5] friction characterization, with the aim of developing a multi-scale friction model to be used in applications aimed at ultra-high accuracy and precision.

Acknowledgements

Work enabled by using the equipment funded via the ERDF project RC.2.2.06-0001 "RISK" and supported by the University of Rijeka grants 4581 and uniri- tehnic- 18- 32.

References

[1] Kamenar, E., Perčić, M., Zelenika, S. From nanometric to meso-scale characterisation of friction using nanoindentation. In *Proc EUSPEN 19th Int Conf*, Bilbao, 3-7 Jun, 2019.

[2] Perčić, M., Zelenika, S., Mezić, I., Peter, R., Krstulović, N. An Experimental Methodology for the Concurrent Characterization of Multiple Parameters Influencing Nanoscale Friction. accepted for publication in *Friction*, 2019.

[3] Carreon, A.H., Funkenbusch, P.D. Material specific nanoscratch ploughing friction coefficient. *Tribol Int*, 2018, 126, 363–375.

[4] Myers, R.H., Montgomery, D.C. *Response Surface Methodology*; Wiley & Sons: New York, 1995.

[5] Kamenar, E., Zelenika, S. Issues in validation of pre-sliding friction models for ultra-high precision positioning. *P I Mech Eng C-J Mec*, 2019, 233(3), 997–1006.

EFFECT OF HEAT TREATMENT AND DIFFERENT AMOUNTS OF Mg ON THE MICROSTRUCTURE AND HARDNESS OF Al-Si-Mg CAST ALLOYS

Lenka KUCHARIKOVÁ[1], Eva TILLOVÁ[1], Mária CHALUPOVÁ[1], Tatiana ORŠULOVÁ[1]

[1] University of Žilina, Department of Materials Engineering, Univerzitná 8215/1, 010 26 Žilina, Slovakia,
E-mail: lenka.kucharikova{eva.tillova, maria.chalupova, tatiana.orsulova}@ftsroj.uniza.sk

1. Introduction

Properties of Al-Si cast alloys are more influencing by morphology, shape and distribution of matrix, Si particles, second phases and defects. These structural features are influenced with the composition, melt treatment conditions, grain refining, modification, solidification rate, casting process, heat treatment, and so on [1-3]. Producers of aluminum casts increase the tensile strength and yield strengths especially with heat-treating.

Precipitation hardening heat treatment is the most commonly used process to obtain the optimal combination of strength and ductility of Al-Si-Mg casts' thanks the Mg addition. Magnesium increases the strength and hardness of the alloys, but especially in castings. The strengthening is ensured with forming the precipitates of Mg_2Si phases during T6 heat treatment. The formation of large Mg_2Si phase of about 4÷8 μm during the solidification of conventional cast alloys is detrimental to the alloys' ductility and impact resistance, too [4-5].

For this reason, the present paper is focused on the effect of precipitation hardening (age hardening) on microstructure and hardness of the production AlSi7Mg0.3 and AlSi7Mg0.6 cast alloy.

2. Experimental materials

The experimental material used in this study was hypoeutectic aluminum-silicon-manganese alloys prepared by gravity die casting to the sound molt in company Uneko. Ltd.

Table 1. The chemical composition of experimental materials, in wt. %.

Alloy	**Si**	**Mg**	**Fe**	**Mn**
A	7.028	0.354	0.123	0.009
B	6.742	0.519	0.128	0.046
Alloy	**Cu**	**Zn**	**Ti**	**Al**
A	0.013	0.036	0.123	balance
B	0.012	0.005	0.108	balance

For comparison, the strengthening effect in such types of materials were used AlSi7Mg materials with 0.3 wt. % of Mg (alloy A) and 0.6 wt. % of Mg (alloy B) for studies (Table 1).

3. Experimental methodology

Experimental materials were age-hardened. The age-hardening (T6) for experimental alloys consist of: solution heat treatment at 525 °C with holding time 6 h, rapid quenching at water for 60 °C, that artificial aging at 175 °C for 6 hours.

After hardening were samples subject for assessment on an optical microscope and a scanning electron microscope (SEM) VEGA LMU II (having both secondary electron (SE). Quantitative analysis (image analysis) were performed with NIS Elements software on optical microscope. Each measured data are average values of min. 60 measured microstructural features. The metallographic samples were prepared according to standard metallographic procedure (wet ground on SiC papers, DP polished with 3μm diamond pastes followed by Struers Op-S). The etcher 0.5 % HF was used for chemical etching. The 3D morphology of eutectic Si, was studied with using scanning electron microscope on samples etched with HCl.

Hardness measurements were performed according to STN EN ISO 6506-1: Brinell hardness tester with a load of 250 kp (1 kp = 9.81 N), 5 mm diameter ball and a dwell time of 15s (HBW 5/250/15) and Vickers hardness tester with a load of 49.02 N and a dwell time of 10s (HV 5/10). The evaluated HBW and HV reflect average values of at least six separately experimental specimens. The hardness of microstructural features was measured with using Vickers microhardness testing machine ZWICK/Roel ZHμ with the evaluation software ZWICK/Roel ZHμ/HD under a 10 g load for 10 s (HV 0.01) on metallographic samples. The evaluated HV 0.01 reflect average values of at least ten measurements on each structural parameters.

4. Results and discussions

The used heat treatment of experimental materials lead to changes in microstructure and hardness. The Si particles in form of small plate (in as-cast state - Fig. 1a) were fragmented and spheroidizated to smaller rod (Fig. 1b) by heat treatment.

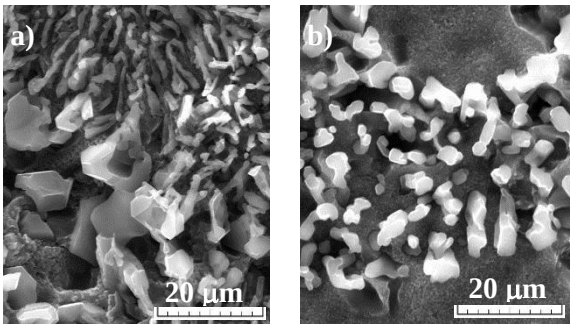

Fig. 1. Morphology of eutectic Si, etch. HCl
a) experimental alloys in as-cast state;
b) experimental alloys after T6.

The metallography observation (Fig. 2) shows changes not only in Si particles but also in other microstructural features: intermetallic phases.

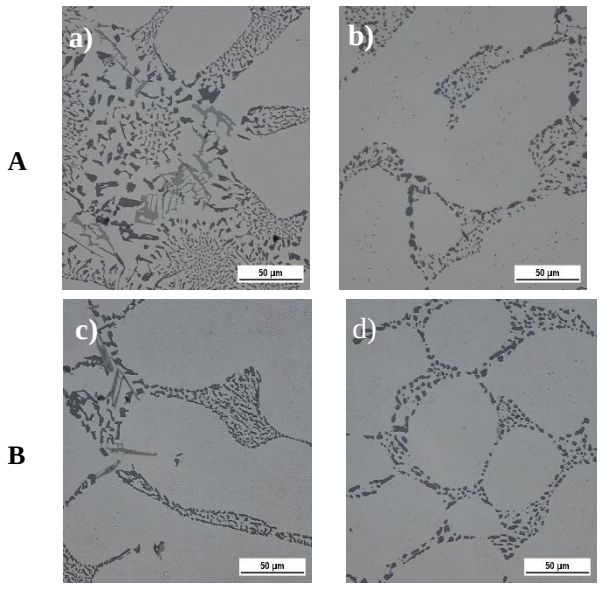

Fig. 2. Microstructure of experimental alloys, etch. 0.5 % HF
a) c) experimental alloys in as-cast state;
b) d) experimental alloys after T6.

The greatest changes were observed in material A in which after age-hardening the intermetallic phases especially Fe-rich phases were fragmented from long skeleton like (Fig. 2a) to small particles (Fig. 2b).

The greatest changes of results of quantitative analysis were also confirmed in material A (Tab. 1). Hardness measurements (Tab. 2) shows that higher hardness have materials after age-hardening which related with formation of Mg_2Si precipitates in substructure of experimental materials. Microhardness of the matrix ($HV0.01^{Al}$) shows greater influence of strengthening with precipitates (Table 2).

Table 1. The results of quantitative analysis.

Alloy	SDAS [µm]	Area fraction of Si [%]	Shape factor of Si	Area fraction of porosity [%]
A	64	6.4	0.845	2.4
A^{T6}	75	8.1	0.921	2.2
B	69	7.9	0.825	2.2
B^{T6}	69	7.0	0.874	2.6

Table 2. The results of hardness measurements.

Alloy	A	A^{T6}	B	B^{T6}
HBW 5/250/15	54.8	93.2	50.8	103
HV 5/10	61	109	58	125.8
$HV0.01^{Al}$	54.3	94.6	49	94

5. Conclusions

The results of this study confirms that higher amount of Mg did not lead to increasing in hardness (materials in as-cast state). Greater influence have age - hardening, which shows with increasing amount of Mg increasing the hardness of materials.

Acknowledgements

This work has been supported by the grant projects Nº 049ŽU-4/2017, Nº 1/0398/19, Nº 012ŽU-4/2019.

References

[1] Tillová, E.,Chalupová, M., Hurtalová, L. Evolution of Phases in a Recycled Al-Si Cast Alloy During Solution Treatment, Rijeka: InTech (2012), Dr. Viacheslav Kazmiruk (Ed.), Scanning electron microscopy, 2012.

[2] Kuchariková, L., Tillová, E., Bokůvka, O. Recycling and properties of recycled aluminium alloys used in the transportation industry *Transport problems*. 11 (2), 117-122 (2016).

[3] Campbell, J. R. A. Harding, Solidification Defects in Castings. TALAT Lecture 3207, EAA - European Aluminium Association, 1994.

[4] Salleh, M.S. Omar, M.Z., Syarif, J. The effect of Mg addition on the microstructure and mechanical properties of thixoformed Al5%Si-Cu alloys. *Journal of alloys and compounds.* 621, 2015, 121-130

[5] Sani A Salihu, Aliyu Isah, Polycarp Evarastics. Influence of Magnesium Addition on Mechanical Properties and Microstructure of Al-Cu-Mg Alloy. *Journal of Pharmacy and Biological Sciences.* 4, 2012, 15-20.

EXPERIMETAL INVESTIGATIONS TO DETERMINE THE DYNAMICAL BEHAVIORS OF THE 3D PRINTED PLA

Peter FICZERE[1], Lajos BORBÁS[2], Gábor SZEBÉNYI[3]

[1] Budapest University of Technology and Economics, Department of Vehicle Parts and Structures Analysis, Stoczek u. 2, ficzere@kge.bme.hu, Budapest, Hungary, H-1111

[2] Budapest University of Technology and Economics, Department of Vehicle Parts and Structures Analysis; and EDUTUS University, Technical Institution, H-2800 Tatabánya, Stúdium tér.: borbas.lajos@edutus.hu

[3] Budapest University of Technology and Economics, Department of Polymer Engineering, Muegyetem rkp. 3., T. bldg. III., Budapest, Hungary, H-111

1. Introduction

The 3D technology nowadays is an everyday technology. Today's applications are carried out not only for marketing and rapid prototyping aims. As individual series production or in small series these products are built into machines [1]. The cost and time of the production equipment can be saved by this technology [2]. To apply as a load-bearing element the load capability of the material must be known. To decide this fact, several numerical simulations must be carried out [3]. In case of cyclic external loading conditions dynamic stresses are developing as well. These are typical vehicle industry applications [4]. For these cases the machine parts must be designed for dynamic conditions where the material characteristics – dynamic and fatigue as well – must be known [5].

From everyday experience it is well known that the external loading conditions act on the machine parts and on the complete machine as a function of time to a small or greater extent. A static load or a load which is constant in time can be interpreted as an idealized limit state. In case of vehicles the service conditions (i.e. in case of off-road condition) change in unsystematic way in their value and frequency as well. Based on these facts the loading conditions can be determined by unsystematic functions. The process can be described by stochastic theories, using statistical parameters. The failure process in the part (material) due to the variable loading conditions essentially differs from the failure process in static case. On the surfaces of machine elements (test specimens) especially in the neighborhood of the notches, peak stress areas make the change, in general the external load starting from the crystalloid grid failures may cause micro cracks. From growth of micro cracks during the fatigue process macro cracks could develop.

During the crack propagation process the cross section decreases, in this way the failure can develop in case of finite cycle number. Starting from this fact, the time-dependent parameters must be determined for the description of the fatigue process. In case of the determination of limit fracture conditions (σ_m=C. mean stress, σ_a=C. amplitude, sinusoidal process) as a result a 3D function is realized $\{\sigma_M ; \sigma_A ; N_t\}$.

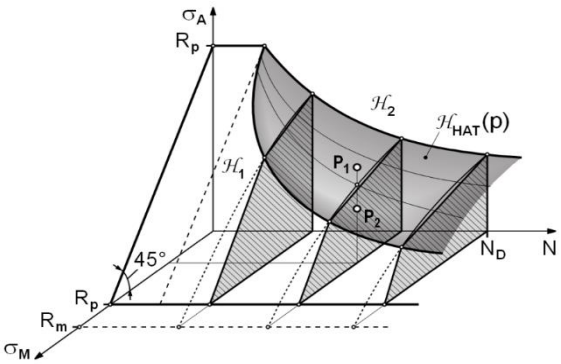

Fig. 1. Limit surface in case of σ_m =C., σ_a =C [6].

In practice the plane-section of the limit condition's area is used for investigation. In case of σ_M =C. the $\{\sigma_A;N\}$ Whöler curve, and in case of N=C. the $\{\sigma_M ; \sigma_A\}$ Haigh diagram is used for investigation [6].

2. Methodology

The fatigue investigation has been realized below the Yield limit as indicated in Fig. 1. To realize this the static material parameters - in our case for PLA material – must be determined. During the fatigue test the alternating load has zero mean value, the push and pull test diagrams must be

determined. In case of a material produced by additive manufacturing technology – because of the layer by layer technology – the properties show anisotropy material properties. That means the material shows different behavior in push and pull direction. It causes other difficulties: the material parameters differ according to the production direction [7], [8], [9].

3. Results

Test specimens have been produced in three different possible production directions, as the results are indicated in Fig 2. and Fig. 3.

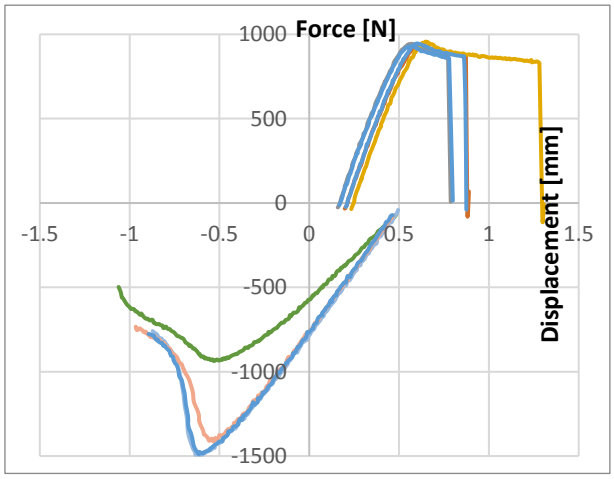

Fig. 2. Force-elongation diagram in "laying" position.

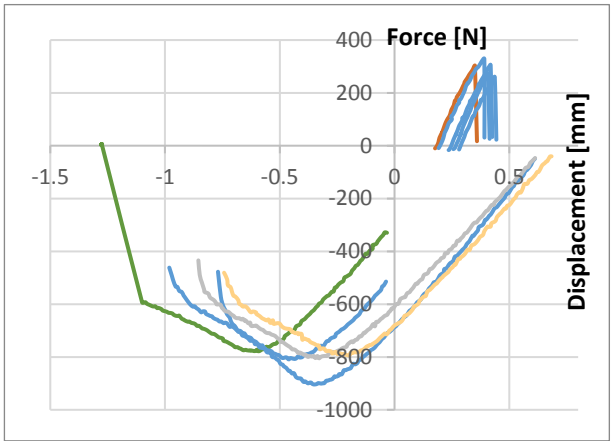

Fig. 3. Force-elongation diagram in "staying" position.

Acknowledgements

This project results have been realized with a subsidy of the National Research Development and Innovation Office from the fund of NKIH. The title of the project is "Development of the New Generation of Production Technology for Individual Medical-Biological Implantation and Tools". Project identification No.: NVKP_16-1-2016-0022, and

Basic research project in the field of Leaser-beam - technologies and energetics Project identification No.: EFOP-3.6.1-16-2016-00009. The elaborators express their thanks for the support.

References

[1] Ficzere, P., Az ipar 4.0 és az egyedi orvosi implantátumok kapcsolata, *GÉP* LXIX. évfolyam : 4 pp. 17-20. , 4 p. (2018)

[2] Ficzere, P., Borbás, L.,Török, Á., Economical investigation of rapid prototyping, *International Journal For Traffic And Transport Engineering* 3 : 3 pp. 344-350. , 7 p. (2013), DOI: 10.7708/ijtte.2013.3(3).09

[3] Győri, M. Ficzere, P. Use of Sections in the Engineering Practice, *Periodica Polytechnica-Transportation Engineering* 45 : 1 pp. 21-24. , 4 p. (2017), https://doi.org/10.3311/PPtr.9144

[4] Székely, P., Ficzere, P., The Examination of Dynamic Effects of Shape Optimized Vehicle Components, *Periodica Polytechnica-Transportation Engineering* 45 : 2 pp. 90-93. , 4 p. (2017), https://doi.org/10.3311/PPtr.9875

[5] Kovács, Á.B., Ficzere, P., Borbás, L., Experimental dynamical analysis of specimens' material properties manufactured by additive technologies, *35th Danubia-Adria Symposium on Advances in Experimental Mechanics*, 25-28 September 2018, Sinaia, Romania, pp 49-50, (2018)

[6] Márialigeti, J.,Devecz, J., Méretezés időben állandó terhelésmodell (nyugvó terhelés) és állandó amplitúdójú és középfeszültségű váltakozó terhelés esetén, *Jármű- és hajtáselemek I.*, Budapest, Magyarország : Typotex Kiadó (2011) , 225 p., ISBN: 9789632795966 BME OMIKK

[7] Ficzere, P., Borbas, L., Falk, Gy., Szebenyi, G., Experimental determination of material model of machine parts produced by Selective laser sintering (SLS) technology, *Materials Today: Proceedings*, Volume 5, Issue 13, Part 2, 2018, pp 26489-26494, ISSN 2214-7853

[8] Ficzere, P., Borbás, L., Török, Á., Usage of rapid prototyping in vehicle manufacturing, In: Stanislaw, Borkowski; Dorota, Klimecka-Tatar (szerk.) *Toyotarity : Elements of the organization's mission* , Dnepropetrovsk, Ukrajna : Yurii V Makovetsky, (2011) pp. 182-193. , 12 p.

[9] Ficzere, P., Borbas, L., Torok, A., Validation of Numerically Simulated Rapid-prototype Model by Photoelastic Coating, *Acta Mechanica Slovaca* 18 : 1 pp. 14-24. , 11 p. (2014)

DESTABILIZATION OF THE COMMINUTED CLAVICLE SHAFT FRACTURE DUE TO BREAKAGE OF THE TITANIUM LOCKING PLATE - MECHANICAL ANALYSIS

Zbigniew L. KOWALEWSKI[1], Grzegorz SZCZĘSNY[2], Tomasz LIBURA[1], Adam BRODECKI[1]

[1] Department of Experimental Mechanics, IPPT, Polish Academy of Sciences, Warsaw, Poland,
E-mail: zkowalew@ippt.pan.pl; tlibura@ippt.pan.pl; abrodec@ippt.pan.pl

[2] Department of Orthopedic Surgery and Traumatology, Medical University, Warsaw, Poland,
E-mail: grzegorz.szczesny@wum.edu.pl

1. Introduction

Implant break off destabilizing the fracture regularly complicates orthopedic procedures. It may be caused by implant's structural defect, its inappropriate usage, or massive overloads exceeding its strength [1, 2].

An analysis of the reason of implant breaking usually brings about troubles coming from limited insight into the incident, as patients often dissemble the genuine circumstances that led to the complication avoiding its responsibility. Especially, when they do not follow postoperative directions. Moreover, implant failure may also be used for clamor of compensation, bringing about several troubles to the manufacturer, to the hospital, and to the surgeon. Hence, recognizing the reason for implant breakings is valuable not only from medical, but also juridical and financial point of view.

The paper presents mechanical analysis of the patient, to whom the locking plate stabilizing comminuted fracture of the clavicle broke destabilizing it at the sixth postoperative week. Circumstances of the incidence were not clear, and therefore, mechanical analyses were made to formulate conclusions that could be helpful for other patients subjected to the similar situations.

2. Problem presentation

33-years old men of 105 kg body weight and 188 cm height was operated on due to comminuted fracture of the shaft of the left clavicle. Fracture was anatomically reduced and stabilized with 2,8 mm Ti-6Al-4V, precontoured, angle stable, locking plate, Fig. 1 ("System 5.0", ChM, Poland) implanted on its superior surface.

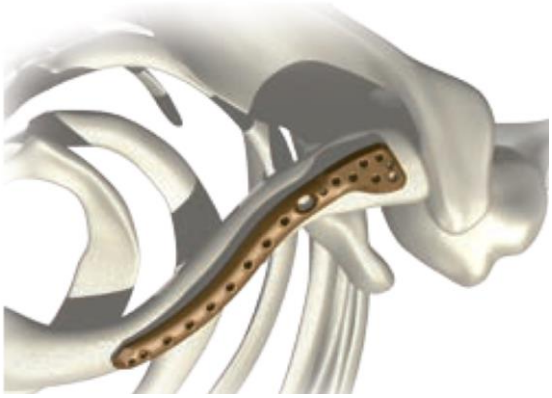

Fig. 1. General view of the locking plate [3].

Both intermediate bone fragments were additionally fixed with titanium cortical screws, Fig.2a. Postoperative wound healed uneventfully and patient was discharged with limb immobilized in shoulder brace for three weeks. After that, patient started rehabilitation, but was recommended to avoid massive physical loads.

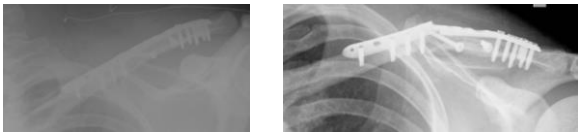

(a) (b)

Fig. 2. Postoperative x-ray (a), and the broken plate evidencing destabilized fracture (b).

At the end of the sixth postoperative week patient reported sudden pain and noticeable click that occurred while closing the trunk lid of the car.

Performed x-ray revealed broken plate and destabilized fracture, Fig.2b. Patient was re-operated and plate was replaced [4].

3. Biomechanical analysis

For biomechanical analysis an analogous plate as the broken one coming from the same manufacturer was used. Ultimate tensile strength and yield point of its alloy (Ti-6Al-4V) were 960 and 850 MPa, respectively. Taking them into account with plate dimensions (length, thickness and width) together with length of clavicle's fragment (necessary for the leverage assessment) it is possible to estimate values of admissible loading under various stress states that cannot be exceeded, thus, protecting plate against the fracture due to overloading.

In order to approximate working conditions of the plate stabilizing broken bone the simple strength tests were carried out (uniaxial tension and simple bending). Assuming an uniaxial tensile conditions (i.e. driving force is acting along the length of the plate) the maximum force should be lower than 11,4 kN to avoid its fracture and lower than 10 kN to protect it against plastic flow processes leading to the permanent deformation of the plate, and thus, in consequence, changes its working conditions (additional components of loadings like bending or torsion may appear). In Fig. 3 the results of uniaxial tensile test supported by digital image correlation (DIC) technique were presented. They confirmed the typical standard parameters of tensile test for the material in question.

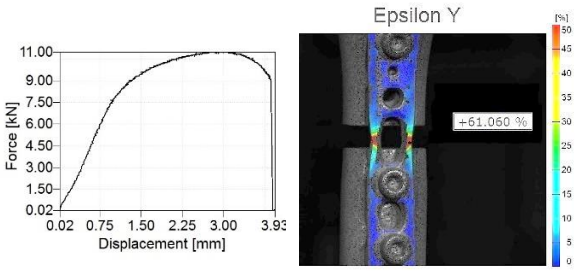

Fig. 3. Tensile characteristic of the plate material (Ti-6Al-4V) and strain distribution just before the fracture of plate.

In vast majority of cases, the clavicle moves in transverse plane forward and backward, bending the plate at its hole, and stretching its posterior branch, whereas the anterior one serves as a hinge. This is much worse working condition of the plate, because even relatively low forces (less than 50N) may lead to the stress value higher than the ultimate tensile strength of the plate.

To analyze an influence of the bending on the plate, the bending plane has to be determined, since for the same bending moment and the cross-section of the plate the maximum stress depends on its orientation.

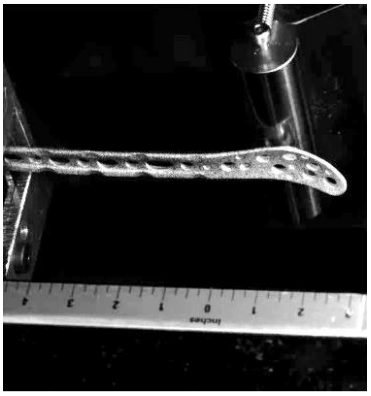

Fig. 4. Experimental setup for bending test of the plate.

For the plate considered here it may differ as much as four times. The lowest stress can be obtained, when the bending force is acting along the width of the plate, the largest if perpendicularly to its thickness. Five simple bending tests were carried out for selected lengths of bending arm: 50; 60; 70; 80 and 90 mm. For the most unfavorable case considered, i.e. simple bending with relatively small force (40 N), but acting over an arm of 90 mm (the distance from the site of the break to the clavico-acromial joint), the moment of the force reached 3,6 Nm, occurring to be sufficient to initiate the permanent deformation of the plate.

4. Conclusions

Superimposing the broken plate on patient's body one can conclude that its fracture had to be caused by a combination of loading that is typical for multiaxial stress, resulting from simultaneous action of tensile force, bending moment and torque. This indicates that patient had not respected postoperative recommendations to avoid any form of overloading.

References

[1] Bostman, O., Manninen, M., Pihlajamaki, H. Complications of plate fixation in fresh displaced mid clavicular fractures. *J Trauma*, 1997, 43, 778–783.

[2] Shin, S.J., Do, N.H., Jang, K.Y. Risk factors for postoperative complications of displaced clavicular midshaft fractures. *J Trauma Acute Care Surg.*, 2012, 72(4), 1046-50.

[3] *Manufacturer's material.* https://chm.eu/uploads/C_5_clavicular_plates.pdf)

[4] Szczęsny, G., Kowalewski, Z. Destabilization of the comminuted clavicle shaft fracture due to breakage of the titanium locking plate - biomechanical analysis. *Clin Surg.* 2018, 3, 2125.

ADHESION OF ELASTIC PUNCH TO CONFINED ELASTIC LAYER

Attila KOSSA[1]

[1] Budapest University of Technology and Economics, Faculty of Mechanical Engineering, Department of Applied Mechanics, Muegyetem rkp. 5., Budapest, 1111 Hungary,
E-mail: kossa@mm.bme.hu

1. Introduction

In nature, several different strategies can be found for temporary and reversible adhesion to various substrates. Animals usually employ various hairy contact structures to ensure the necessary adhesive mechanisms. Among hundreds of animal species, gecko is considered to be one of the most interesting ones in terms of the body weight and its excellent ability to climb on vertical surfaces. Experimental measurements revealed that adhesion ability of gecko is explained by the van der Waals interaction between the contacting substrate and the hairy feet of gecko. Adopting nature's perfect adhesion solution in artificial structures is a primary goal of engineers and scientists in this research field. It is undoubtedly evident that the proper utilization of nature's adhesion mechanism in technological applications could lead to significant improvements in various fields of engineering devices.

Confined elastic layers are widely used in adhesive technologies, including micropatterned adhesives as well [1-4]. In order to properly understand the adhesive behavior of these structures, it is essential to investigate the stress distributions along the contacting interfaces. Furthermore, the classical linear elastic fracture mechanics approach can be used to analyze the variation of the energy release rate if local defect or detachment appears along the interface. Characterization of the stress distributions and the fracture mechanics related behaviors help us in improving the performance of these artificial structures.

The normal stress distribution along the interface of a rigid cylindrical punch and a confined elastic layer was recently characterized in detail for different values of the Poisson's ratio [5]. The variation of the energy release rate for the detachment process was also analyzed and the critical thickness of the layer was found to have stable detachment mechanism [5].

The complete characterization, including the analysis on the variation of the energy rate upon detachment, for the adhesion of an elastic punch to confined elastic layer is not available in the literature. However, its importance in technical applications is evident.

2. Problem description

The investigated axisymmetric problem is depicted in Fig. 1. A linear elastic cylindrical punch is attached to a linear elastic layer, which is considered to be infinite in radial direction. The punch height is L, whereas its radius is denoted by a. The layer thickness is h. The Young's moduli for the punch and the layer are E_1 and E_2 ,respectively. Here, only incompressible case is investigated, thus, the Poisson's ratio is set to 0.5 for both materials.

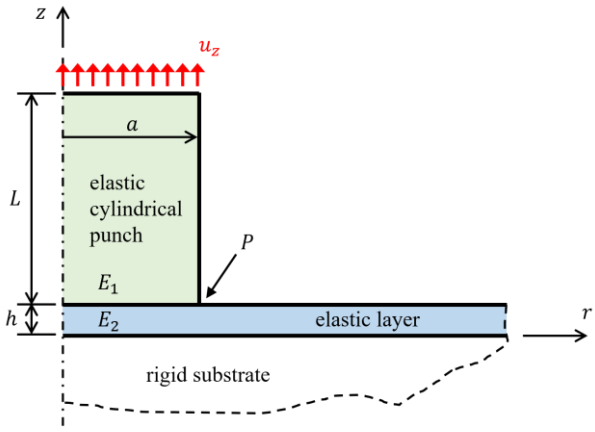

Fig. 1. Geometry of the investigated axisymmetric problem.

The bottom of the layer is perfectly attached to the rigid substrate, no sliding allowed. Perfect bonding is assumed along the interface between the punch and the layer. The loading of the structure is given by the prescribed vertical displacement applied along the top surface of the punch, whereas the radial displacement is not constrained.

It is obvious that stress singularity appears along the perimeter P of the interface in both materials.

The primary goals in the analysis: a) characterization of the stress distribution along the interface b) calculating the energy release rate and its derivative if small radial defect is forming along perimeter P. It must be emphasized that analytical solution for the problem does not exist.

3. Results

The problem is solved using the commercial finite element software ABAQUS version 2019. Eight-noded quadratic axisymmetric hybrid elements were used with full integration scheme. The mesh was extensively refined in the singularity domains.

The derivative of the energy release rate with respect to the defect area along P can be used to check the stability of the detachment. Quantity $\bar{G}'$ measures the normalized dimensionless value of the derivative of the energy release rate with respect to the contact area. If G decreases with the increasing defect area then $\bar{G}'$ is positive, which predicts stable detachment process. The values of $\bar{G}'$ for different layer thickness and for different values of the ratio E_1/E_2 is shown in Fig. 2. One can conclude that the stable domain is a function of the layer thickness and the ratio of the moduli.

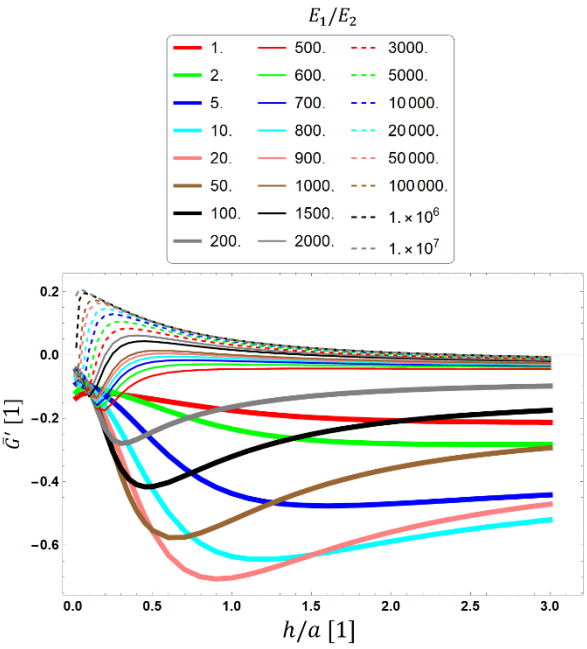

Fig. 2. Variation of the derivative of the normalized energy release rate.

Fig. 3. shows the stability map in the plane of the layer thickness and the ratio of the moduli.

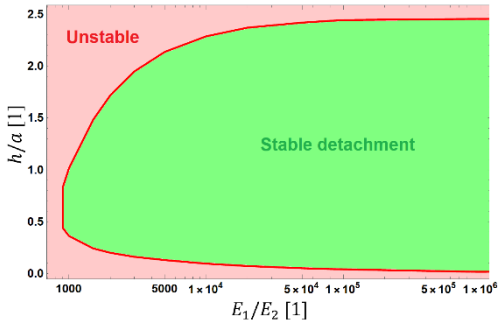

Fig. 3. Illustration of the stable and unstable domains.

The results clearly revealed that the detachment initiation process is unstable for arbitrary layer thickness as long as the ratio E_1/E_2 does not reach a critical value. Higher the value of the ratio of the Young's moduli, larger the stable domain for the layer thickness. Furthermore, the detachment for very thin layers is always unstable if the punch is elastic. The limit case is when the punch is rigid. Then, the process is stable for thin layers as discussed in [5]. For very thick layer the detachment is always unstable for elastic and rigid punches as well.

Acknowledgements

This research has been supported by the ÚNKP-18-4-BME-199 "New National Excellence Program of the Ministry of Human Capacities", Hungary. The support from the National Research, Development and Innovation Office Hungary (Project Identifier: FK 128662) is gratefully acknowledged.

References

[1] Shull, K.R., Ahn, D., Chen, W.-L., Flanigan, C.M., Crosby, A.J. Axisymmetric adhesion tests of soft materials. *Macromol. Chem. Phys.*, 1998, 199, 489–511.

[2] Webber, R.E., Shull, K.R., Roos, A., Creton, C. Effects of geometric confinement on the adhesive debonding of soft elastic solids. *Phys. Rev. E.*, 2003, 68, 021805.

[3] Fischer, S.C.L., Kruttwig, K., Bandmann, V., Hensel, R., Arzt, E. Adhesion and Cellular Compatibility of Silicone- Based Skin Adhesives. *Macromol. Mater. Eng.*, 2017, 302, 1600526.

[4] Bacca, M., Booth, J.A., Turner, K.L., McMeeking, R.M. Load sharing in bioinspired fibrillar adhesives with backing layer interactions and interfacial misalignment. *J. Mech. Phys. Solids*, 2016, 96, 428–444.

[5] Hensel, R., McMeeking, R.M., Kossa, A. Adhesion of a rigid punch to a confined elastic layer revisited. *The Journal of Adhesion*, 2019, 95, 44–63.

BOOSTING THE DISCHARGE OF A HYDROPOWER PLANT

Boris HUBER[1], Reinhard PRENNER[1] and Norbert KROUZECKY[1]

[1] Vienna University of Technology, Institute of Hydraulic Engineering and Water Resources Management, Karlsplatz 13/222 1040 Vienna, Austria. E-mail: norbert.krouzecky@tuwien.ac.at

1. Introduction

1.1 General

The Opponitz power station on the River Ybbs was built in 1922 - 1924 to supply Vienna with electricity, making it one of the oldest hydroelectric power plants of the Austrian capital.

The power plant Opponitz, which is owned by Wien Energie GmbH, carries water with a free surface over an 11.3 km long tunnel system (diameter ca 2.5 m) from Gießling to Opponitz. There, at the end of the tunnel, is a free-surface surge chamber with overflow, where the transition to the penstock down to the powerhouse takes place (drop height = 115 m).

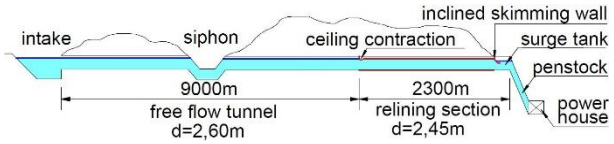

Fig. 1. Sketch of headrace scheme HPP Opponitz.

1.2 Problem

In the course of the renovation of the power plant, the last 2.3 km of tunnels were rehabilitated due to water leaks into the mountain in the so-called "relining" process. Here glass-fibre reinforced plastic (GRP) pipes were drawn into the original tunnel profile and the gap filled. However, due to the reduction in cross-section, which could not be compensated by the smoother tube design, this measure led to a considerable reduction in the maximum turbine quantity of water from the desired 12.7 m³ / sec to about 11 m³ / sec.

Subsequently, Wien Energie GmbH commissioned the Institute of Hydraulic Engineering and Water Resources of the Vienna University of Technology to find a possible solution to this problem. The achievable upgrading of the tunnel was to be demonstrated in the form of physical model experiments.

2. Solution

Since a reduction of the flow resistance of the already relatively smooth GRP pipeline was not technically possible, a proposal was developed for the creation of a suction operation in the relined pipe.

In order to achieve this suction operation, it was necessary to ensure that water occupied the full relined cross-section. For this purpose, an inclined skimming wall was installed in the transition to the open cross-section of the surge chamber. Another skimming wall at the beginning of the relined tube was to prevent the further entry of air from the upstream water in the suction mode. Any air still in the tube was to be sucked out by means of a vacuum pump.

3. Model experiments carried out

3.1 Model set up

The model was scaled according to Froude in order to take into account the inertial and gravitational forces. To keep the deviations in the friction losses low, a very large model scale of about 1:16 was adopted, simulating only a 260m long pipe section. As shown in a preliminary experiment on a smaller scale, the suction operation could be verified in the larger model with a shortened tube length.

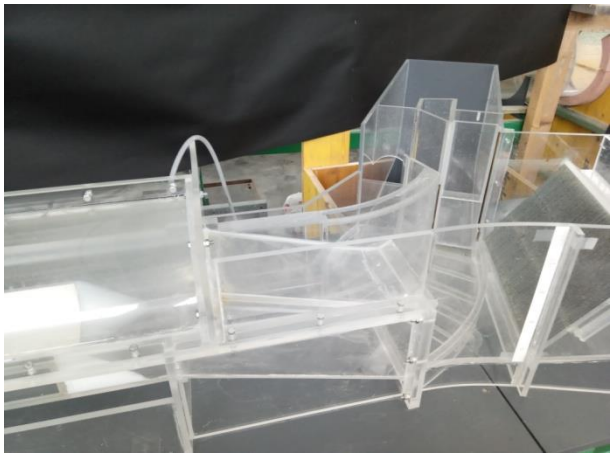

Fig. 2. View of the surge chamber with the inclined skimming wall.

3.2 Data acquisition and measurement technology

The measurement data acquisition and the subsequent analog / digital conversion were carried out with a measuring amplifier "Spider" and the software "Catman" from the company HBM at a measuring rate of 10 Hz. The flow measurement was carried out with a specially calibrated inductive flowmeter from Endress + Hauser (measurement deviation < 0.1%). The pressure or water level measurement was carried out with seven high-precision pressure transducers (measuring accuracy ± 1 mm).

3.3 Experiments performed and lessons learned

The aim of the experiments was to examine both the proposed solution for normal power plant operation and an emergency shutdown of the turbines.

3.3.1 Normal operation

Normal operation of the power plant with free-flowing discharge in the headrace tunnel is possible up to flow rates of approx. 10.7 m3 / sec. It turned out that appropriate ventilation of the relining pipe is to be provided if the water level rises above the lower edge of the upstream ceiling contraction wall.

3.3.2 Start of the suction operation

In order to achieve flow rates greater than 10.7 m³ / s, the water level in the surge chamber had to be lowered accordingly (up to 0.7 m in nature).

Parallel to this, the air evacuation of the tunnel took place. It was found that negative pressures in the pipeline of a maximum of 1 m occurred. This resulted in the first minutes of the suction to a lowering of the water level in the upstream water at the nose by up to 90 cm, while the water level in the surge chamber remained largely constant.

3.3.3 Suction operation

Experiments carried out up to a maximum flow rate of 12.7 m³ / sec with different water levels in the surge chamber showed that the evacuation of the air initiated suction operation can be stably maintained upright.

3.3.4 End of the suction operation

The turbine control allows the discharge to be reduced again (below 10.7 m3 / s) to stop the suction operation by supplying air in the water. The water level in the surge chamber increases accordingly. The water level at the beginning of the relined tunnel rises only slightly.

3.3.5 Emergency shutdown

During an emergency shutdown, the entire turbine water quantity has to be discharged suddenly via sluice gates in the surge chamber, without causing flooding. The experiments showed that this sudden increase in water level in the surge chamber can only be regulated safely with an additional outlet sluice gate.

4. Conclusion

The model tests carried out showed that the proposed hydraulic engineering solution works and allows the desired increase of the discharge up to 12.7 m³ / s.

EVALUATION OF INTERNAL DAMPING ON MAGNESIUM ALLOY DEPENDING ON THE TEMPERATURE USING BY MATHEMATICAL METHODS

Milan UHRÍČIK[1], Peter PALČEK[1], Patrícia HANUSOVÁ[1], Tatiana ORŠULOVÁ[1]

[1] University of Žilina, Faculty of Mechanical Engineering, Department of Materials Engineering, Univerzitná 8215/1, 01026 Žilina, Slovakia, E-mails: milan.uhricik@fstroj.uniza.sk, peter.palcek@fstroj.uniza.sk, patricia.hanusova@fstroj.uniza.sk, tatiana.orsulova@fstroj.uniza.sk

1. Introduction

Effect of gradual storage of mechanical energy in the material results in a change of mechanical and physical characteristics, which can cause degradation of material properties such as: reduction of the machine tools accuracy, initiation of fatigue cracks, generation of noise and vibration in the working environment, changes of material properties, reduction of corrosion resistance, degradation of regulatory devices and sensors, eventually damage of entire device. Measurement of the internal friction allows monitoring the ongoing structural changes and various mechanisms [1]. Analyze of vibrations is important tool for calculation eigen frequencies of the systems and prediction reaction from material to excitation vibrations [2].

As experimental material for study was used a magnesium alloy AZ91 which was manufactured by squeezes casting method and was delivered without heat treatment.

2. Experimental

In experimental measurement was used a resonance method, using by the experimental equipment from Department of Materials Engineering, from University of Žilina. This method is based on continuous excitation of oscillations of the test bar, and the entire apparatus vibrates at a frequency which is close to the resonance.

Ultrasonic resonance system can measure the only at a single resonant frequency. Before the measurement is necessary to adjust the specimen so the resonance frequency of ultrasonic horn with mounted specimen is the same as resonance frequency of the ultrasonic horn by itself.

For the measurement of the decay test specimen was designed so that the resonance frequency with resonance frequency mechanical part. Starting resonance frequency for all measurements was close to f = 20.4 kHz.

In Figure 1 can be seen, that our measured waveform can also be divided into two periods. First interval of temperature from 50 ° C to 200 ° C and the second temperature interval from 200 ° C to 400 ° C, what was the end of the measurement.

During the measurement occurred local maxims of quality factor in a narrow temperature interval. Similar material behavior was also studied in work [3] and the presence of these maxims is still not clear and there is still a discussion about the reason of their creation. According to previous studies [3, 4] the presence of local maxims depends on frequency, temperature and the deformation amplitude.

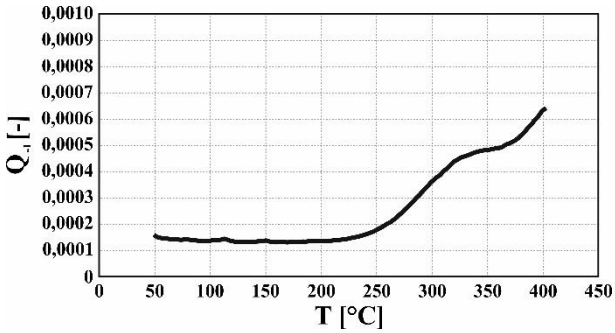

Fig. 1. Temperature depended on internal damping for magnesium alloy.

3. Processing of measured values by mathematical methods

Measurement of the internal damping consists of a large number of measured values of the internal damping depending of temperature. Measuring data contains noisy data, which cannot be presented without necessary adaptations and

without mathematical and physical understanding of the basis of measured data.

The mathematical processing of measured values of the magnesium alloy was used approximation by the least squares method. By numerical experimentation we got the most suitable shapes of functions for the approximation of the measured data. For the measured spectrum of internal damping depending on the temperature (Fig. 1) we looked for a universal linear model. In our case the universal model is a polynomial third degree in the form:

$$y(t) \sim \sum_{i=0}^{3} c_i x^i \qquad (1)$$

whose parameters are: c_0 = 1.304e-004; c_1 = 5.863e-007; c_2 = -7.283e-009; c_3 = 2.251e-011.

From second interval of procedure of the internal damping of a material was derived non-linear exponential model in the form:

$$y(t) \sim c_0 \exp(c_1 t + c_2 t^2 + c_3 t^3) \qquad (2)$$

and represents a relationship which can be linearized by the natural logarithm:

$$lny \sim lnc_0 (c_1 t + c_2 t^2 + c_3 t^3) \qquad (3)$$

Approximation results are shown in Figure 2. The mutual subtracting of regression curves was obtained individual process of the internal damping, which represents the interaction of additive elements with atoms of the parent phase (Fig. 3).

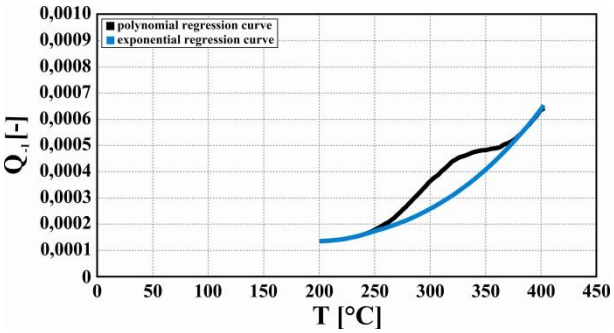

Fig. 2. Regression of the temperature measurement by polynomial and exponential regression curve for magnesium alloy.

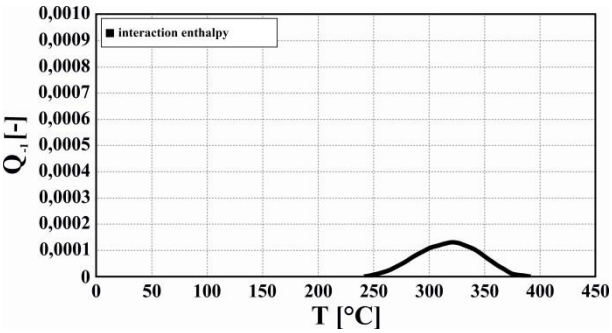

Fig. 3. The separation of the influence of the second mechanism from course of internal damping depending of temperature for magnesium alloy.

4. Conclusions

Based on experimental results from internal damping measurement of magnesium alloy can be stated:

- the internal damping increases with increasing of temperature,
- by increasing the temperature is a lot of energy released by movement of dislocations and the ability of a damping increases in magnesium alloy,
- it can be assumed that the area obtained from peak represents energy used for dissolution of the discontinuous precipitate,
- from curves can be detected the beginning and the end of dissolution and from area can be determined a ratio amount of precipitate in the structure.

Acknowledgements

This work has been supported by Scientific Grant Agency of Ministry of Education of Slovak Republic and Slovak Academy of Sciences, No. 013ŽU-4/2019 and No. 049ŽU-4/2017.

References

[1] Blanter, M. Internal Friction in Metallic Materials, *Springer - Verlag: Berlin Heidelberg*. 2007. pp.539
[2] Seungh, B. High damping Fe – Mn martensitic alloys for engineering applications, In: *Nuclear Engineering and Design*, 2000, 198(3), pp. 241-252
[3] Kasenčák, M. Vnútorné tlmenie zliatin horčíka v závislosti od amplitúdy deformácie, *Dizertačná práca, Žilina: Žilinská Univerzita v Žiline*, 2010, 97 p. (in slovak)
[4] Namašný, A. (2008). Štúdium vlastností horčíkových zliatin meraním vnútorného tlmenia, *Dizertačná práca, Žilina: Žilinská Univerzita v Žiline*, 2008, 90 p. (in slovak).

DEVELOPMENT OF EXPERIMENTAL METHODS FOR DETERMINATION OF RHEOLOGICAL PROPERTIES OF POLYMERIC FILMS

Matic ŠOBAK[1], Ivan JERMAN[1], Anastasiya GOLYADKINA[2], Anatolij NIKONOV[3]

[1] National Institute of Chemistry, Hajdrihova 19, 1000 Ljubljana, Slovenia, E-mail: Matic.Sobak@ki.si, Ivan.Jerman@ki.si;

[2] Faculty of Mechanics and Mathematics, Saratov State University, Saratov, Russia, E-mail: aagramakova@mail.ru

[3] Faculty of Industrial Engineering, Šegova ulica 112, 8000 Novo mesto, Slovenia, E-mail: Anatolij.Nikonov@fini-unm.si

1. Introduction

PVC or poly(vinyl chloride) is one of the most widely used synthetic materials in the world. Its usage ranges from biomedical devices, electrical cable and telecommunication cables and wires, insulation, construction, clothing, non–food packaging, heritage collections, artificial leather for automotive interiors and many other products where rubber can be replaced, e.g. [1]. PVC long-term stability depends on loading conditions. The literature contains reports presenting mechanical and electrical stability studies [2].

Tensile strength is the most often specified property of thermoplastic materials used to indicate the inherent strength of the material [3]. Tensile strength is dependent on the molecular structure and the orientation of the macromolecules within a particular sample. Tensile strength and elongation are also affected by the velocity of deformation to which the samples are exposed [4].

The goal of the research is to perform the experimental analysis on thin films with the aim to provide necessary information for determination of their viscoelastic mechanical properties. In this study, the tensile stress/strain behaviour of PVC consumer thin film materials was characterized using the commercial tensile machine Instron 3342.

2. Experimental

In our work, we observed the influence of different loading velocities on the stiffness of polymer films at room temperature. The test samples were prepared in the shape of strips with an average size of 10 x 70 mm, with a thickness of 0.1 mm. All strips were checked for any imperfections and were measured by a micrometer.

DSC measurements were performed on PVC films to determine T_g and melting temperature of the material. The measurements were performed with the heating rate of 10 K/min under air atmosphere using thermal analyser Netzsch STA 449 F3. For the selected PVC foil, glass transition temperature was T_g = 36 °C, and the melting temperature was 121°C.

The specimens were exposed to axial deformation with a constant rate of deformation using the commercial tensile machine Instron 3342, controlled by a digital controller. Motion of the cross-head measured the change in gage length and hence the strain. A high precision load cell with a resolution of mili-Newton measured force on the test specimens and hence the stress. The measurements were performed at five different constant strain rates. The samples were clamped 5 mm from the edges of the strip using clamping pressure of 2.5 bar for all measured samples. After clamping, the material was left to relax for approximately five minutes. After the samples were preconditioned, the distance between the grips was accurately measured, and the measured values were considered as the initial length of samples (gauge length), from which strain was calculated.

Measurements were conducted at five different loading velocities, i.e. 0.1, 1, 10, 50, and 100 mm/min. All measurements were made at room temperature. The samples were tested five times for every loading velocity, and the average values with corresponding deviations were calculated.

Experimental results show that PVC films exhibit extremely viscoelastic (time-dependent) behaviour at room temperature. Loading velocities significantly affect the viscoelastic response of PVC films subjected to tensile loading. We observed significantly pronounced changes in stiffness at

smaller velocities rather than at higher velocities. This is due to the fact that with increasing strain rate, polymer chains are less susceptible to relaxation mechanism and are less likely to be oriented in the direction of displacement.

3. Results and discussion

In this study, tests were performed at a different range of strain rates. The stress-strain curves at different strain rates under tensile loading conditions are shown in Fig. 1. The observed behaviour of PVC at a wide range of stress rates and is much dependent on loading velocity. We observed higher stiffness of the material for higher loading velocities, and stress relaxation continuously occurs along with deformation. A stress relaxation process randomly orientates coils of polymer chains and aligns them in the displacement direction [3]. As the strain rate increase, polymer chains are less prone to relaxation mechanism and, have less chance to be oriented in the displacement direction resulting in a shorter effective length of polymer chains supporting the load, and the material exhibits a higher tensile modulus (Fig. 2).

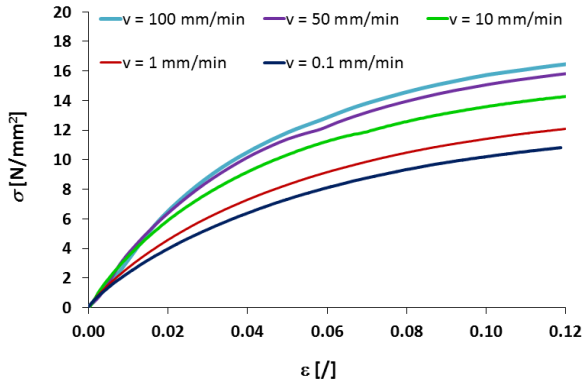

Fig. 1. Stress-strain curves of measured PVC foils at five different velocities.

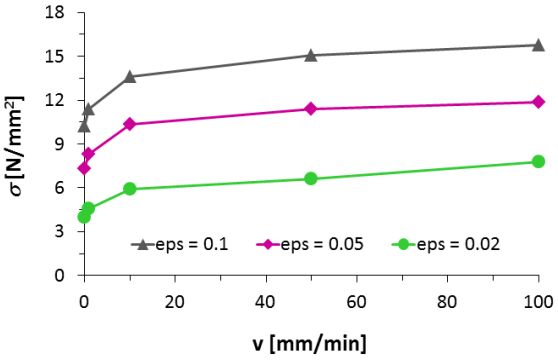

Fig. 2. Stress as a function of loading velocities for PVC foil at three different strains.

4. Conclusions

Prepared PVC samples were exposed to uniaxial tension with five different loading velocities. Uniaxial tension mechanical behaviour of PVC is significantly affected by the strain rate. Increase in strain rate results in higher apparent toughness and higher apparent stiffness. From the obtained results we concluded, that loading velocities have a significant influence on the viscoelastic response of PVC films subjected to tensile loading and that stiffness changes are more pronounced at smaller loading velocities than at higher speeds. The experimental results showed that PVC films exhibit extremely viscoelastic behaviour at room temperature and understanding its rheological properties (viscoelastic moduli) in confined geometries, such as in thin polymeric films, is critical to the stability of structures of many applications.

Acknowledgements

The authors acknowledge the bilateral project BI-RU/16-18-030 which was financially supported by the Slovenian Research Agency.

References

[1] Marceneiro, S., Alves, R., Lobo, I., Dias, I., de Pinho, E., Dias, A.M.A., Graça Rasteiro, M., de Sousa, H.C. Effects of Poly(vinyl chloride) morphological properties on the rheology/aging of plastisols and on the thermal/leaching properties of films formulated using nonconventional plasticizers. *Industrial and Engineering Chemistry Research*, 2018, 57(5), 1454–1467.

[2] Ekelund, M., Edinb, H., Gedde, U.W. Long-term performance of poly(vinyl chloride) cables. Part 1: Mechanical and electrical performances. *Polymer Degradation and Stability*, 2007, 92(4), 617-629.

[3] Mortazavian S., Fatemi, A. Tensile behavior and modeling of short fiber-reinforced polymer composites including temperature and strain rate effects. *Journal of Thermoplastic Composite*, 2017, 30(10), 1414–1437.

[4] Şerbana, D.A., Weber, G., Marşavina, L., Silberschmidt, V.V., Hufenbach, W. Tensile properties of semi-crystalline thermoplastic polymers: Effects of temperature and strain rates. *Polymer Testing*, 2013, 30(2), 413-425.

GAS DISPERSION FLUID MECHANICS SIMULATION FOR LARGE OUTDOOR ENVIRONMENTS

Dino HÜLLMANN[1], Patrick P. NEUMANN[1], Achim J. LILIENTHAL[2]

[1] Bundesanstalt für Materialforschung und -prüfung (BAM), Unter den Eichen 87, 12205 Berlin, Germany, E-mail: dino.huellmann@bam.de

[2] AASS Research Centre, Örebro University, 70182 Örebro, Sweden

1. Introduction

Leaking gases from infrastructure, such as pipelines, industrial plants or landfills, can pose a serious threat to life and our environment. Hence, it is important for both monitoring purposes as well as rescue workers to localise gas leaks efficiently.

Several incidents in the past, such as the gas explosions in Kaohsiung/Taiwan in 2014, have shown that it can be difficult for humans to draw the right conclusions from given gas measurements, because we lack the intuition to interpret the data correctly. To complement this weakness, algorithms can be used that first identify optimal locations to carry out the measurements and in a second step generate gas distribution maps from the measurement data. Given the gas distribution, a human operator or an algorithm can deduce possible leak locations.

However, the development of algorithms for mapping gas distributions and localising gas sources is a challenging task, because gas dispersion is a highly dynamic process and it is impossible to capture ground truth data, especially in outdoor environments. Since experiments are cost-intensive, time-consuming and – most importantly – lack repeatability, fluid-mechanical simulations of the gas dispersion are a suitable way to support the development of algorithms, that can be validated later in real world experiments.

In recent years, some tools for gas dispersion simulation have been developed. Monroy et al. give an overview in [1] and present a new simulator called GADEN. Though this simulator provides more features than its competitors, it is not suitable for simulations of large outdoor environments.

In this paper, we present a concept of how the simulator can be improved to handle both indoor and large outdoor scenarios and give an outlook on future work.

2. Remote gas sensors

In the past, in-situ sensors have been most often used to sense gases. These, however, require direct contact with the gas and are therefore not well suited for scanning large outdoor areas or measuring gas concentrations at elevated locations from the ground. Moreover, moving in-situ sensors through a gas distribution might alter it and thus distort the measured values.

These disadvantages can be avoided by using remote gas sensors based on the Tunable Diode Laser Absorption Spectroscopy (TDLAS). They allow for measuring the concentration of a certain species, for instance methane, by tuning a diode laser from a wavelength, that corresponds to a characteristic absorption line of the species, to a wavelength, that is not affected by the species under measurement. Using the Beer-Lambert law, the concentration can be estimated from the difference of the received signals.

In contrast to their in-situ counterparts, TDLAS sensors cannot measure the gas concentration at a specific point, but provide an integral measurement along their laser beam, as shown in Fig. 1.

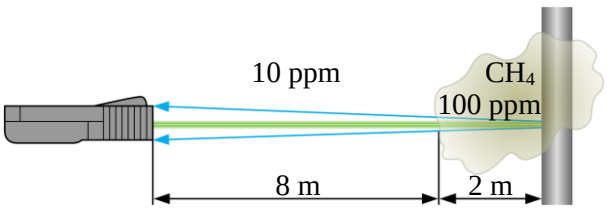

Fig. 1. Remote gas sensors based on the Tunable Diode Laser Absorption Spectroscopy (TLDAS) provide an integral measurement. Here the measurement would read $8\ \mathrm{m} \cdot 10\ \mathrm{ppm} + 2\ \mathrm{m} \cdot 100\ \mathrm{ppm} = 280\ \mathrm{ppm} \cdot \mathrm{m}$.

Often, the laser beam is approximated as a line. However, this does not hold in the real world; instead, the shape of a laser beam can be better described by a cone, which is shown in Fig. 2.

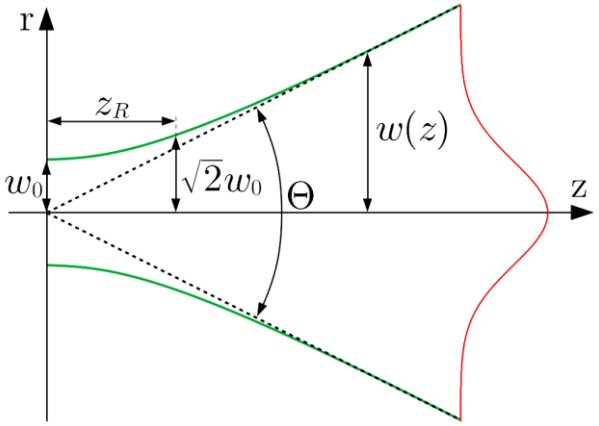

Fig. 2. Parametrisation of a laser beam with a Gaussian intensity profile (red). While Θ denotes the total angular spread of the beam, $w(z)$ is the radial distance at which the intensity drops to $1/e^2$ of its value at the centre.

A typical laser beam of a TDLAS sensor has a total angular spread of about $8.5 \cdot 10^{-3}$ rad and thus yields a spot diameter of 56 cm at a distance of 30 m. Therefore, it can make a significant difference whether the beam is modelled as a line or as a cone, which is also proven in [2]. This fact needs to be considered for the design of the fluid-mechanical simulation.

3. Gas dispersion simulation

The previously mentioned simulator GADEN [1] uses a two-step procedure to simulate a gas dispersion process. In the first step, a wind field is generated using a computational fluid dynamics (CFD) software, for instance OpenFOAM. The shape of the environment, i.e. obstacles from the fluid's point of view, is also taken into account. After this step, the wind field is available as a homogeneously spaced grid.

In the second step, the most relevant gas dispersion effects are used to generate a grid of the same size describing the gas concentration distribution. A typical indoor scenario might have a size of $10\ \text{m} \cdot 4\ \text{m} \cdot 2.5\ \text{m} = 100\ \text{m}^3$ and the grid describing this volume might have a resolution of 0.1 m yielding 100'000 cells, which can be easily handled by off-the-shelf personal computers (PC).

However, this approach aims at rather small indoor environments, because large outdoor areas will simply overcharge the simulator. Given a volume of $100\ \text{m} \cdot 100\ \text{m} \cdot 40\ \text{m} = 400'000\ \text{m}^3$ and a grid resolution of 0.1 m, the simulator would have to deal with $400 \cdot 10^6$ cells. Storing four float values with double precision per cell, i.e. the 3D wind velocity and gas concentration, each with a size of 64 bits / 8 bytes, the whole grid would occupy $4 \cdot 8 \cdot 400\ \text{MB} = 12.8\ \text{GB}$ of memory.

This pushes a currently available off-the-shelf PC to its limit. Moreover, one might want to increase the grid resolution to fully capture the cone shape of the laser beam. By increasing it to 5 cm the grid would occupy already 102 GB of memory.

Since gas distributions often only cover a rather small portion of the environment, one can exploit this fact and store a sparse representation. OpenVDB [3] was explicitly developed for this purpose and stores values on a sparse grid in a B+ tree. Fig. 3 shows an example of a gas plume in an environment measuring $80\ \text{m} \cdot 80\ \text{m} \cdot 30\ \text{m}$. While GADEN uses almost 1 GB to store this plume, the sparse storage using OpenVDB occupies 2.3 MB of memory and therefore allows for simulations of large outdoor environments (as long as the assumption of sparsity holds).

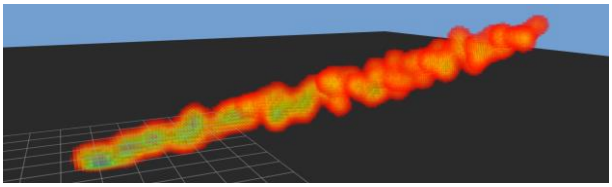

Fig. 3. Gas plume created with GADEN. The plume has a length of approximately 20 m and reaches a diameter of up to 3.5 m. The grid resolution is set to 0.1 m.

4. Conclusion and future work

By exploiting the sparse structure of gas distributions, a simulation of gas dispersion in large outdoor environments becomes possible. However, the description of the wind field still needs to be addressed, since this is affected by the same limitations when the resolution is increased. To some extent, this also applies to the description of the environment. Future work will address both issues and compare the results to well-established CFD software.

References

[1] Monroy, J. et al. GADEN: A 3D Gas Dispersion Simulator for Mobile Robot Olfaction in Realistic Environments. *Sensors*, 2017, 17(7), 1479.

[2] Hüllmann, D. et al. A Realistic Remote Gas Sensor Model for 3-Dimensional Olfaction Simulations. In *IEEE International Symposium on Olfaction and Electronic Nose (ISOEN)*, Fukuoka, 26-29 May, 2019.

[3] Museth, K. VDB: High-Resolution Sparse Volumes with Dynamic Topology. *ACM Transactions on Graphics*, 2013, 32(3), 27.

DEVELOPMENT OF A SHEAR DEVICE FOR PRECISE SHEAR MEASUREMENTS OF RUBBER MATS

Lars KANZENBACH[1], Jörn IHLEMANN[1]

[1] Chemnitz University of Technology, Chair of Solid Mechanics, Reichenhainer Str. 70, 09126 Chemnitz, Germany, E-mail: lars.kanzenbach@mb.tu-chemnitz.de

1. Introduction

For material characterization and model parameter identification simple shear is a very important deformation state [1]. One of the best-known representatives is the cylindrical double-shear-specimen, used at the Tun Abdul Razak Research Centre (TARRC) in Hertford or – in a slightly geometrically modified version – at the "Deutsches Institut für Kautschuktechnologie e. V." (DIK e. V.) in Hannover. The design is based on a cylinder geometry which is vulcanized or glued on the front surface. An advantage is that the shear deformation can be introduced up to a high degree. The disadvantage is that vulcanization or gluing leads to shrinkage or material irritation in the measuring zone [2]. For this, a new shear device with a special fixing design is presented, which enables a uniform initiation of shear deformation for different rubber mats. Furthermore, the shear device is suitable for large shearing, tests with different rubber materials (also fibre-reinforced materials) and tests with pre-stretching [3].

2. Numerical development

The main idea is that the shear load for the rubber mat is initiated via small steel pins (d = 1.0 mm). For this, the shear deformation can be introduced uniformly for the thickness direction. Note that a form fit connection has the advantage that for the load application no high clamping force or high friction coefficient is required. In addition, the disadvantages resulting from vulcanization or gluing can be avoided. On the other hand, one disadvantage can be crack initiation. However, the functional principle shall be tested experimentally. In order to show the potential of the new pin design, a parameter study is conducted for different values of pin size and pin number. Furthermore, a local error measure is defined in such away that the error to the theoretically exact solution of simple shear is indicated. In Fig. 1 the local error (in the range of: $[0, 1]$) is presented.

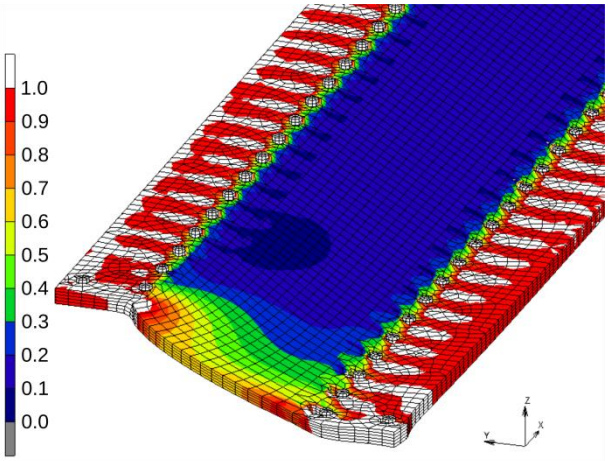

Fig. 1. Local error measure for the new shear specimen.

A nearly homogeneous deformation state in the measuring zone can be seen. Note that a dimension for the rubber mat of 10:1 (length-width-ratio) is recommended to reduce the influence of free edges (see Fig. 1).

3. Experimental setup

Next, the experimental setup for the new shear device with pins is introduced, see Fig. 2.

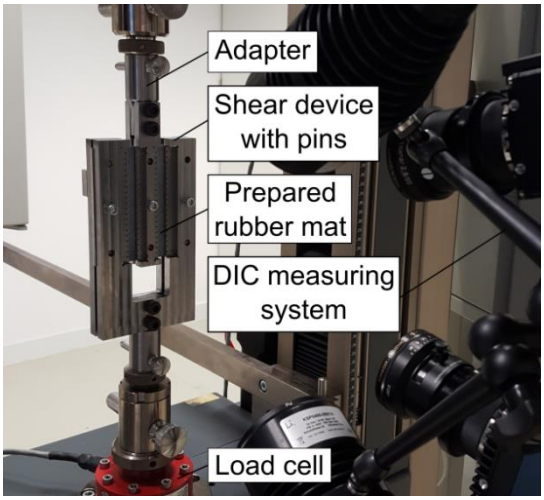

Fig. 2. Experimental setup for the new shear device.

The shearing device can first be divided into a lower and an upper apparatus. The lower part consists of a front and a rear U-profile, which is responsible for the rigid fixation of the rubber mat. The upper part consists of a front and a rear I-profile, which represents the movable fixation on the traverse. The prepared rubber mat is connected to the shearing device via steel pins only. The force was measured by means of a 20 kN load cell and strains were determined using 3D DIC system GOM ARAMIS 4M. A special feature is the vertical test setup of the 3D DIC system. On the one hand, this results in a larger available measuring field and, on the other hand, in a better illumination of the measuring area compared to a horizontal orientation of the DIC system.

4. Experiments and Results

In the following, a double-sided shear test is conducted with the new shear device. In Fig. 3 the "stress-shear value" diagram can be seen for filled EPDM.

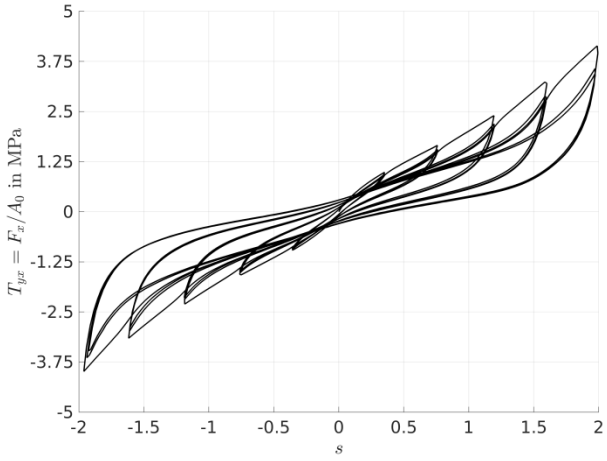

Fig. 3. Double-sided shear test with the new shear specimen.

For this, a nearly point-symmetrical stress-strain curve occurs. The shear value s was calculated via [3]:

$$s = \tan(\varphi)\,. \qquad (1)$$

The value φ describes the shear angle. Furthermore, it can be seen in Fig. 4 that in the middle section of the measuring zone a nearly homogeneous deformation field occurs. Only at the edges where the pins are located, inhomogeneities can be detected. With these first results, the functional principle can be confirmed.

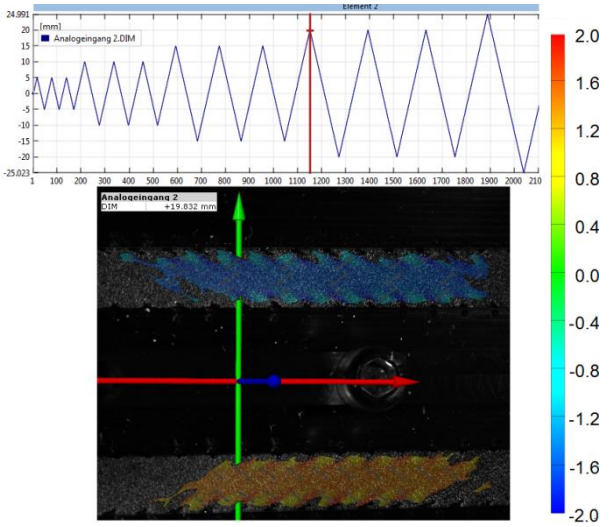

Fig. 4. Presentation of the shear value s for the new shear specimen (evaluation with DIC).

5. Conclusions

In this contribution a new shear specimen is presented, which enables precise shear measurements for large shear values. As pointed out, the special pin design enables a uniform initiation of shear deformation for different rubber thicknesses. The nearly homogeneous deformation field (in the middle section of the shear specimen) is measured and evaluated with a DIC system. Finally, the new shear specimen can be used for the phenomenological investigation of typical rubber properties. A particular focus is on the investigation of anisotropic characteristics.

In further investigations, the new pin design shall be used for the analysis of fibre-reinforced materials.

Acknowledgements

The authors gratefully acknowledge the financial support from Vibracoustic GmbH & Co. KG and Freudenberg Technology Innovation SE & Co. KG.

References

[1] Besdo, D., Ihlemann, J., Kingston, J.G.R., Muhr, A.H. Modelling inelastic stress-strain phenomena and a scheme for efficient experimental characterization. Lisse: Balkema, S. 309-318.
[2] Ballhorn, M. Schadensanalyse an Gummi/Metall-Bauteilen. KGK 60 (5), S. 249-256.
[3] Ihlemann, J. Kontinuumsmechanische Nachbildung hochbelasteter technischer Gummiwerkstoffe. Düsseldorf: VDI-Verlag, 2003.

DESIGN AND IMPLEMENTATION OF AN INEXPENSIVE, HIGH RESOLUTION DISPLACEMENT AND VELOCITY SENSOR

M. STADLER[1], P. PELZMANN[1], F. BLEICHER[1]

[1] Institute of Production Engineering and Photonic Technologies, TU Wien, Getreidemarkt 9, 1060, Vienna, Austria. E-mail: stadler@ift.at

1. Introduction

For axial displacement and velocity measurements of a magnetic levitated rotor a sensor was needed with a relative position accuracy of under 5µm. Maximal propagation delay of the whole sensor system was specified with under 10 µs. The sensor system is placed near a strong magnetic field, therefore systems based on eddy-currents and hall-effect cannot be considered. Commercial displacement and velocity sensors that fulfil the technical requirements are too expensive. Based on the Photosensor EE-SX1070 from OMRON a displacement and velocity measurement system was developed which met the specific demand by negligible costs.

The simplicity of the system allows a broad field of application aside from rotating machines. The measuring range of the displacement sensor is 1 mm.

2. Operating Principle

The EE-SX1070 consists of an emitter, radiating light in the near infrared spectrum (940nm typical) and an optical transistor as detector (see Fig. 1). The transistor has a linear correlation between the detected light and the shaded sensor area. Only at the outermost regions a nonlinear characteristic occurs. The linear range is about ±0.5mm around the optical axis of the transistor.

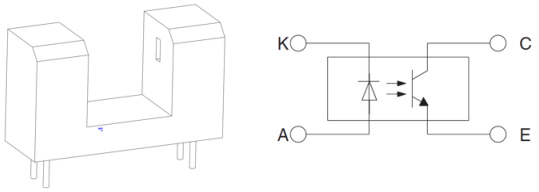

Fig. 1. Photomicrosensor EE-SX1070 [1].

For both, the displacement and velocity measurement the above mentioned transmissive sensor is used. Velocity signals are derived from the displacement values. Fig. 2 shows the arrangement of the displacement (red) and velocity (blue) sensors. The component being measured contains a panel that shades the optical transistor depending on the axial position of the component.

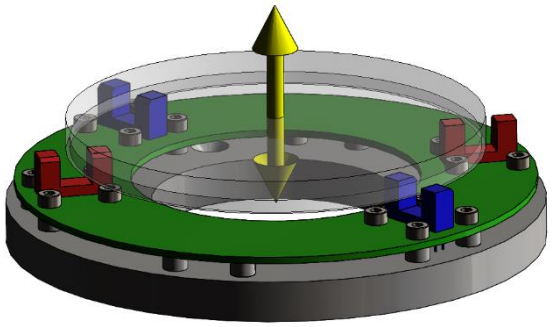

Fig. 2. Sensor configuration.

For error reduction the average of two individually evaluated sensors are used. Due to the separate treatment of the displacement and velocity sensors an error on the displacement signal caused by the differentiators can be excluded.

3. Signal Condition Electronics

The phototransistors are supplied with a constant voltage of 5 volts, therefore the current changes invers proportional to the immersion depth of the moving panel. This current signal is converted back to a voltage by leading it through a shunt resistor and amplifying it to meet the requirements of the following signal processing. A passive low-pass filter of first order with 100 kHz cutoff frequency suppresses high frequency interferences while creating negligible phase shift.

At this point the position signal is ready for further application specific processing (e.g. A/D conversion) or it can serve as a base for analog speed calculation.

To allow measurement of speeds in both directions while using single-supply components, the signal is superimposed with a DC bias voltage.

Due to the nature of the derivation it is essential to suppress high frequency signal noise. Therefore a chebyshev second order low pass filter is used [2]. The cutoff frequency should be adapted to match the highest possible speed of the mechanical system while phase shift has to be kept in an acceptable limit.

Afterwards the speed is calculated from the filtered signal by an enhanced analog differentiator circuit, that is optimized for stable behavior in the given frequency range [3]. The mechanical limitations of the speed serve as a base to set the time constant of the differentiator circuitry in order to avoid signal clipping and hence information loss.

To improve performance it is beneficial to use high oversampling rates when A/D converting the signals. In the given application a sampling rate of 1 MHz with an oversampling rate of 40 is used to achieve 25.000 measurements per second with an accuracy of less than 3.5µm for position and less than 3 mm/s for speed.

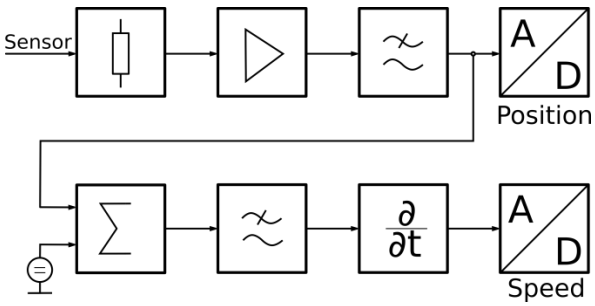

Fig. 3. Signal path.

4. System characteristics

4.1 Propagation Delay

The measuring distance for the displacement sensor includes the low pass filter and the wire between the sensor- and processing unit. In addition the velocity sensor includes the differentiator and the upstream filter. By bridging the diode supply a relative steep voltage drop can be produced (see Fig. 4 solid line). Both voltage curves were measured with a 12-bit digital oscilloscope. The propagation delay is around 5.4 µs for the velocity sensor and 3.2 µs for the displacement sensor due to the missing differentiator and low pass filter.

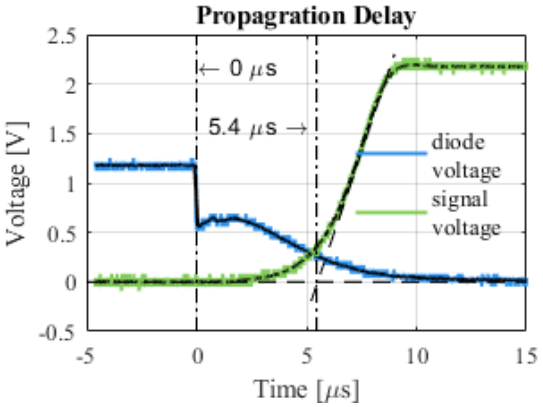

Fig. 4. Propagation delay of the velocity sensor.

4.2 Signal to Noise Ratio (SNR)

The dataset of the signal voltage provided by the propagation delay test (see Fig. 4) is also used to calculate the SNR.

$$SNR=10*\log\left(\frac{u^2_{eff,Signal}}{u^2_{eff,Noise}}\right) \quad (1)$$

Based on Eq. (1) the SNR for the displacement and velocity sensors are listed in Table 1.

Table 1. SNR values.

	$u_{eff,Signal}$ [V]	$u_{eff,Noise}$[V]	SNR[dB]
Displacement	1.86	0.0062	49.5
Velocity	1.28	0.0334	31.67

5. Conclusions and Outlook

The sensor system presented in this paper provides a low cost alternative for contactless displacement and/or velocity measurements with a measuring range of 1mm. It was shown, that the required specifications were comprehensively fulfilled. With little effort, the circuit design can be adapted for different requirements.

By optimizing the electrical shielding and using high accuracy power supply sources the SNR should further increase with consistent propagation delay.

References

[1] Datasheet Photomicrosensor (Transmissive) EE-SX1070, *OMRON*
[2] v. Wangenheim, L. Aktive Filter und Oszillatoren – Entwurf und Schaltungstechnik mit integrierten Bausteinen, *Springer-Verlag Berlin Heidelberg*, 2008
[3] Viehmann, M. Operationsverstärker Grundlagen, Schaltungen, Anwendungen, *Carl Hanser Verlag GmbH & Co. KG*, 2016

POST-IMPACT EVALUATION AT RC PLATES WITH PLANAR TOMOGRAPHY AND FEM

Deborah NERGER[1], Falk HILLE[1], Robabeh MOOSAVI[1], Marcel GRUNWALD[1], Bernhard REDMER[1], Tino KÜHN[2], Marcus HERING[2], Franz BRACKLOW[2]

[1] BAM Federal Institute for Material Research and Testing, Berlin, Germany, deborah.nerger@bam.de

[2] Technical University Dresden, Germany

1. Introduction

Due to the many possible applications, the uncomplicated production and the high application range, reinforced concrete is a widely used building material. This large range of physical material properties still poses an engineering challenge in determining all necessary requirements for predicting dynamic effects under impact load.

Many aspects of impact have already been examined and some correlations have been studied intensively. Examples are the work of Lastunen [1] and Booker [2], who studied the influence of projectile properties on the impact form. Li [3] has also investigated the local effects of an impact. The field of detailed damage analysis has not been in focus so far.

This presentation shows some studies in medium-velocity impact with the focus on post-impact damage evaluation. The impactor is modified so that the test plates show low penetration on the top and scabbing on the bottom. With the unique tomography lab test stand at BAM the plate is scanned after the impact and the damage is analyzed. Cracks and scabbing are made visible with a reconstruction. The comparison of simulation and tomography allows to create prognosis models for damage characterization.

2. Test specimen

Reinforced concrete plates of class C35/45 with the dimensions 1.5 m x 1.5 m were used. The plate thicknesses varied between 0,1 and 0,3 m and 5 plates with different impact speeds were tested for each thickness. Table 1 shows the mean value of the compressive strength (f_c) after 28 days and on the test day, depending on the concrete batch (see series designation). The age of the plate on the test day is shown in brackets.

Table 1. Small overview of the physical properties of the tested plates

plate	thickness [mm]	f_c_28d [MPa]	f_c_test [MPa]
S26/27	200	38,1	66,9 (275 d)
S28	100	33,7	63,9 (230 d)
S29/30	300	39,3	71,9 (214 d)

3. Methodology

The damage properties for the impact loads in the medium-velocity range were investigated. The impact was generated with a cylindrical projectile (diameter d=100mm, weight m=23.34kg) on a reinforced concrete plate. The shape of the impactor has a large influence on the damage [4]. The chosen flat nose shape results in small penetrations on the upper side and scabbing on the underside.

The High Energy X-Ray Lab (HEXYLab) is located at BAM. The plate is investigated with the developed scanning regime. The subsequent reconstruction allows a very detailed examination of the damage of the complete plate with a crack detection algorithm.

Fig. 1 and Fig. 2 show an example of the crack pattern of the surface and also of the interior of the plate (S26P02).

Fig. 1. Crack structure of the underside of S26P02

Fig. 2. Crack structure by planar tomographic investigation

For the development of a prognosis model, the crack structures resulting from the tomography are compared with the computed damage from the numerical simulations. The FE modeling was done using the hydrocode AUTODYN and the material models Drucker-Prager and Riedel-Hiermaier-Thoma.

4. Results

Correlations between bearing force and impact pulse could be determined and can be explained by the degree of damage. Analogous, effects can be seen in the damage volume, cumulating cracks, spalling, scabbing and punching cone (see Fig. 3).

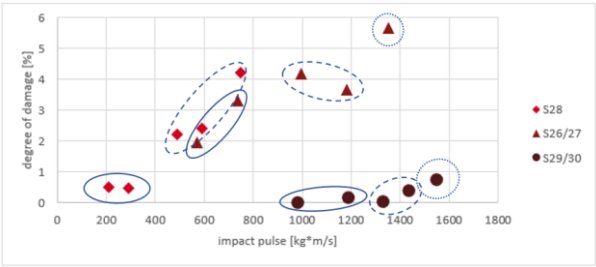

Fig. 3. Degree of damage in % w.r.t. impact pulse. Comparison of the series and their type of damage. Shear cracks (solid line), punching cone (dashed line), punching cone and increased scabbing (dotted line).

Between impact impulse and shear angle an only week correlation could be identified. Comparisons of simulation and experiment show good similarities of the experimental data as well as of the damage characteristics.

5. Conclusions

In the described impact studies with a variation of plate thickness, effects of local damage were detected. Correlations between impact pulse and damage could be determined.

With the help of tomography, the damage analysis can be extended by the examination of the internal crack structures.

Numerical simulation is a useful tool for creating prognosis model of the damage characteristics. Superpositions of FEM, optical scanning and tomographic data indicate similar damage.

Acknowledgements

The underlying research of this publication is sponsored by the Federal Ministry for Economic Affairs and Energy (BMWI). The project executing agency is the Gesellschaft für Anlagen- und Reaktorsicherheit (GRS) gGmbH, project 1501542.

References

[1] Lastunen, A., Hakola, I., Järvinen, E., Calonius, K., Hyvärinen, J. Impact test facility. In *Proceedings of SMIRT19*. 2007; Paper J08/2.

[2] Booker, P. M., Cargile, J. D., Kistler, B. L., La Saponara, V., Investigation on the response of segmented concrete targets to projectile impacts. *Int. J. Impact Eng.*, 2009, 926-939.

[3] Li, Q. M., Reid, S. R., Wen, H. M., Telford, A. R., Local impact effects of hard missiles on concrete targets. *Int. J. Impact Eng.*, 2005, 224-284.

[4] Kühn T., Curbach M. Behavior of RC-slabs under Impact-loading. In *Proceeding of DYMAT 2015, EPJ Web of Conferences 94*, 2015.

EFFECT OF CONTRAST MATERIAL PROPERTIES DURING INJECTION INTO CORONARY BLOOD FLOW

Benjamin CSIPPA[1], Richárd WÉBER[1], Zsolt KŐSZEGI[2], Attila JUHÁSZ[3], György PAÁL[1]

[1] Budapest University of Technology and Economics, Department of Hydrodynamic Systems, Műegyetem rakpart 3, Budapest 1111, Hungary, E-mail:bcsippa@hds.bme.hu
[2] University of Debrecen, Institute of Cardiology, Faculty of Medicine, Móricz Zsigmond körút 22. Debrecen, 4032, Hungary
[3] GE Healthcare Ltd. Pharmaceutical Diagnostics, Pollards Wood, Nightingales Lane, Chalfont St Giles, HP8 4SP United Kingdom

1. Introduction

Coronary arteries are the supplying blood vessels for the heart itself. Ischemic heart disease or coronary artery disease is when a plaque builds up inside the coronary artery and blocks the blood flow. This narrowing can decrease the flow rate of oxygen-rich blood entering the heart muscles that can lead to heart attacks and cardiac arrests. It is the main cause of death according to WHO for at least the last 16 years [1].

In order to enhance the visibility of the vessel during medical imaging an iodinated contrast material (ICM) is injected into the artery. However, another diagnostic purpose exists for ICM injection as well.

The TIMI (Thrombolysis in Myocardial Infarction) [2,3,4] frame-count analysis is a blood velocity measurement method, using the movement of the ICM interface in blood. First, the physician captures the time instant at which the ICM is visible in the images and follows the propagation of the front up to a certain distal marker in the artery. From the recorded time interval between the two instants and the measured length between the two captured points an estimate for the average blood velocity can be made. The goal of this project is to analyze two types of ICMs (Visipaque (iodixanol), Omnipaque (iohexol)) (GE Healthcare AS, Oslo, Norway) with numerical simulations. In this numerical study we investigated the two clinically relevant flow conditions namely the hyperemic state that corresponds to a hyperemic flow condition and the normal state. In both cases the point of interest was to examine the effects of ICM viscosity and density.

2. Numerical methods

We performed numerical simulations on an artificial two-dimensional geometry in order to exclude any non-material property related effect in this part of the investigation. A straight tube (vessel section) with physiologically correct dimensions was taken similarly to [5], so that bends and curves will not affect the simulations (see Fig. 1).

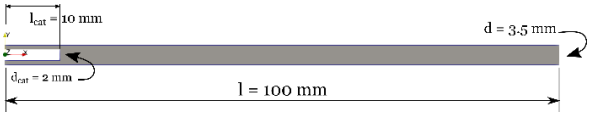

Fig. 1. Model for the two-dimensional simulations.

It consists around 400K cells to ensure proper identification of the contrast-blood front. To address the objectives, the unsteady Navier-Stokes equations were solved numerically in the conserved form with a commercial software suite using the finite volume method. The two-phase flow problem was solved by utilizing the mixture model implemented in ANSYS CFX. The boundary conditions were set to ensure physiological blood flow [6] and clinically applied ICM injection conditions that can be observed in Fig. 2.

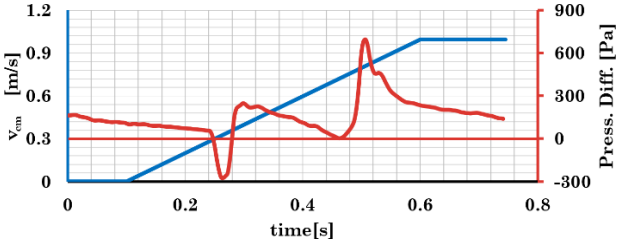

Fig. 2. Boundary conditions: Blood flow inlet condition with red and CM with blue.

The material properties used in the study for the ICMs can be found in Table 1. for the two different temperatures.

Table 1. Material properties.

	Omnipaque (iohexol)	Visipaque (iodixanol)
Density [kg/m^3]@20°C	1406	1356
Viscosity [Pa s]]@20°C	0.0204	0.0254
Density [kg/m^3]@37°C	1406	1303
Viscosity [Pa s]]@37°C	0.0104	0.0114

A total of eight 2D simulations were performed when the injection time instant was kept constant and only the material properties were changed for the normal and hyperemic flow condition.

3. Results

First to inspect the results qualitatively, contour plots of volume fraction distributions were analyzed. Interestingly, the two types of ICMs was observed to behave similarly, both under hyperemic and normal conditions. Comparing the two flow conditions it was observed that under the hyperemic conditions the influence of material properties is negligible (not shown in the abstract). On the other hand, under normal flow conditions perceivable differences were identified, as shown in Fig. 3. but since the effect is not large a more detailed quantitative analysis was performed.

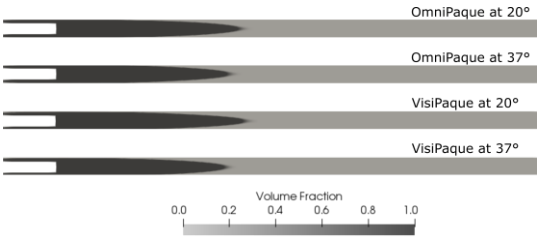

Fig. 3. Volume fraction distributions at a certain time instant under hyperemic condition.

In order to explain the mechanism through which the viscosity affects the front propagation, we plotted the two quantities (flow rate and volume fraction) as the function of time at the inlet boundary depicted in Fig. 4.

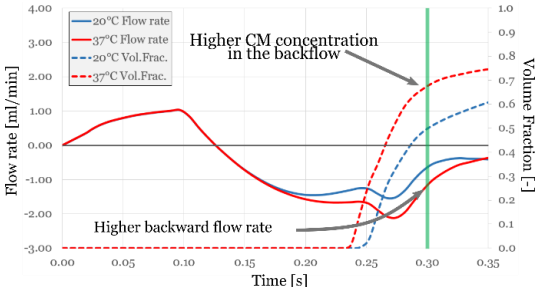

Fig. 4. Volume fraction and flow rate as the function of time on the inlet boundary. The green vertical line shows the above captured time instant.

When the CM was at body temperature (when the viscosity is lower) the ICM concentration was 20% higher in the observed time instant (t =0.3s). Additionally, Figure 4. tells us that more fluid leaves the domain at the inlet than with higher ICM viscosity (when the ICM enters at 20°C). To provide an explanation for this phenomenon one should have a look at Figure 2. Notice that for a short time negative pressures appear from 0.24 s to 0.28 s. During this interval the CM is much slower than the blood, thus the blood still dominates the flow field, thus more CM - with lower viscosity - will "follow" the blood with the back flow. Because of this the higher viscosity ICM phase front is ahead, since the blood can carry the ICM along less.

4. Conclusions

In this study the numerical investigation on the interplay between the contrast materials and blood flow was presented. Based on our results the ICMs of the two examined types (Visipaque, Omnipaque) behave similarly under both hyperemic and normal conditions. Under the hyperemic condition the effect of viscosity is less dominant as inertial forces govern the two-component fluid flow. The effect of not heating up the ICM to body temperature is noticeable, since the viscosity of the ICM at 20°C is two times as much as at 37°C. As a result of this difference, the less viscous the ICM - the ICM viscosity is closer to that of blood viscosity - the more it will adapt to the blood flow velocity.

Acknowledgements

This research was supported by the GE Healthcare, the ÚNKP-18-3 New National Excellence Program of the Ministry of Human Capacities and the BME-Biotechnology FIKP grant of EMMI (BME FIKP-BIO).

References

[1] Global Health Estimates 2016: Death by Cause, Age, Sex, by Country and Region, 2000-2016. *Geneva, World Health Organization*, 2018, 40(4), 739–765.

[2] Gibson, CM., Cannon, CP., Daley, WL., Dodge, JT., Alexander, B., Marble, SJ., McCabe, CH., Raymond, L., Fortin, T., Poole, WK. Timi frame count: a quantitative method of assessing coronary artery flow. *Circulation*, 1996, 93(5), 879–888.

[3] Appleby, MA., Michaels, AD., Chen, M., Gibson, CM. Importance of the timi frame count: implications for future trials. *Trials*, 2000, 1(1), 31.

[4] Stoel, MG., De Cock, CC., Spruijt, HJ., Zijlstra, F., Visser, CA. Corrected timi frame count and frame count velocity, *Neth Heart J*, 2003, 11(3), 109.

[5] Lieber, BB., Sadasivan, C., Hao, Q., Seong, J., Cesar, L. The mixability of angiographic contrast with arterial blood, *Med Phys*, 2009, 36(11), 5064-78.

LUMINESCENCE-BASED EARLY DETECTION OF FATIGUE CRACKS

Falk HILLE[1], Damian SOWIETZKI[2], Ruben MAKRIS[3]

[1] Bundesanstalt für Materialforschung und -prüfung (BAM), Unter den Eichen 87,12205 Berlin, Germany, E-mail: falk.hille@bam.de

[2] MR Chemie GmbH, Nordstraße 61-63, 59427 Unna, Germany, E-mail: sowietzki@mr-chemie.de

[3] as [1], current E-Mail: ruben.makris@beuth-hochschule.de

1. Introduction

At vibrational stressed mechanical components fatigue cracks may be initiated after a certain number of load cycles. This process leads a steady destruction and the residual lifetime of the structure is limited. For safety reasons components under fatigue loading need to be inspected frequently to detect fatigue damage in an uncritical stage.

In dependence of the type and size of the structure and its relevant components, of its anti-corrosion coating and of operational circumstances conventional inspections methods can be unreliable in detecting fatigue cracks. Conventional NDT methods for crack detection such as ultrasonics are not suitable for continuous monitoring of structural parts for they are locally applied. Therefore, the application of these methods requires the information of the crack location in advance which especially for large structures is challenging.

A new method, the so-called crack luminescence, provides an efficient solution for continuous or higher frequent monitoring of structures under fatigue loading. In a cooperative research project between BAM and MR Chemie GmbH different fluorescing and cover coatings were developed and tested on special test devices which allowed the determination of the sensitivity, robustness against mechanical wear and, last not least the applicability of the system.

The present contribution describes the principle of the method and shows its functionality by the means of an exemplary application.

2. Principle and functionality

For crack luminescence, a special coating system is applied on the surface of critical locations regarding possible high stressing, for example weld seams. This coating system consists out of two components, a fluorescing layer and a dark layer which covers the fluorescing one (see Fig. 1) [1].

In case of crack occurrence at the steel's surface the two layers rip open due to its adhesive properties. If then energy-intensive rays (UV) enter the crack, the boundaries of the luminescing layer will emit visible radiation, as schematically illustrated in Fig.2. This luminescence light can easily be seen from distance which allows for an automatized remote damage monitoring using webcams and image recognition software. This can be profitable, especially at locations that are not easy to access as well as in cases, were an interruption of the structure's operation for inspection issues is costly.

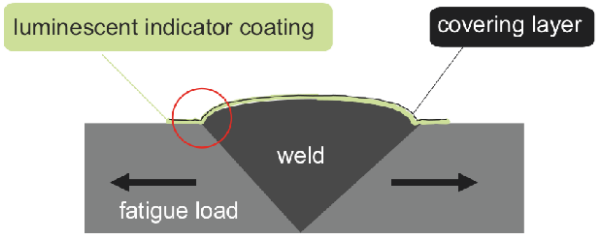

Fig. 1. Application of the crack luminescence coating at a welding seam [1].

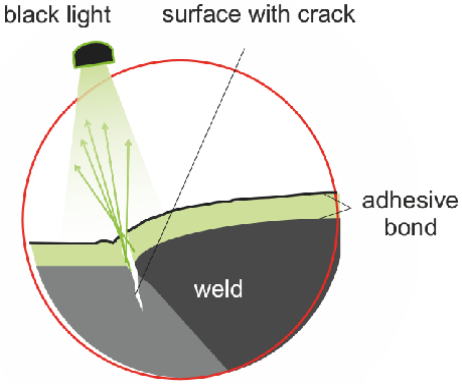

Fig. 2. Case of a crack and the emission of visible radiation [1].

To reproduce thin coatings in a fast and applicable way as well as to ensure a user-friendly handling MR Chemie developed an aerosol can based system. The targeted sprayed layer thickness is 60 to 100 µm. The fluorescing layer makes 50 to 70 % of the total thickness [2].

3. Exemplary application

The crack luminescence method was exemplary tested on butt weld seams [2]. There, fatigue damage was induced by cyclic tensile loading. The tests were monitored by strain gauge measurement and video capture. Fig. 3 shows a butt weld before and after the application of the fluorescing layer.

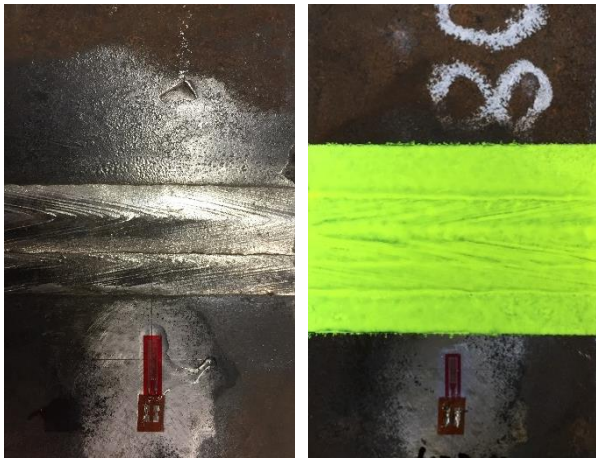

Fig. 3. Butt weld without and with fluorescing coating.

4. Results

Fig. 4. shows the result in form of three pictures of three different stages of the crack formation.

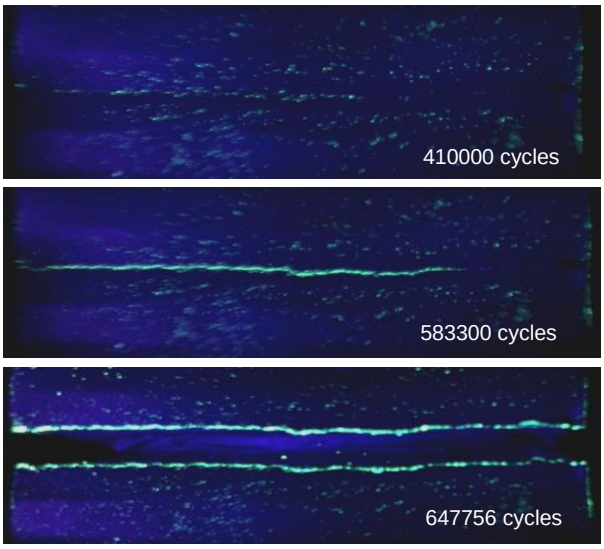

Fig. 4. Evolution of crack formation.

In Fig. 5 the evolution of strain is shown, marking the three specific times, when the pictures were taken. The first mark “a” refers to the point of time (410 000 cycles) when the luminescence-based blinking of the crack started (see Fig. 4). At the same time the maximum strain started to decrease (see Fig. 5). Afterwards, the brightness of the crack's blinking consistently increases. The mark “b” refers to the point of time (583 300 cycles) when the maximum strain has decreased by 5 % (see Fig. 4 and 5). After 647 756 cycles the specimen fractured.

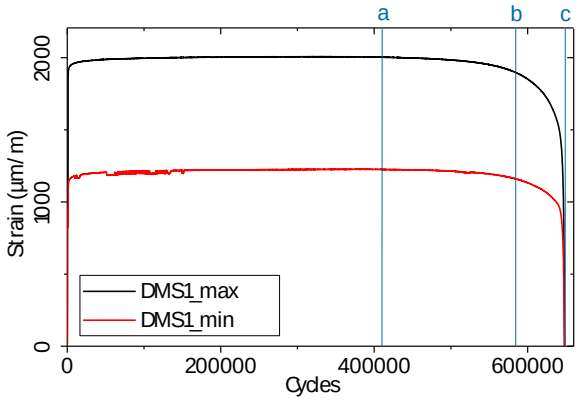

Fig. 5. Evolution of measured strain .

5. Conclusions

The presented study shows a high sensitivity of the crack luminescence and a very good comparability with the strain measurements. It was proved that also without knowledge of the exact location of the crack the method can reliable detect fatigue crack at a butt weld seam. The crack luminescence is a promising approach to support inspections of fatigue-prone structural parts.

Acknowledgements

This work was funded by the German Federal Ministry for Economic Affairs and Energy within the ZIM program; support code ZF2201092ZG4.

References

[1] Mehdianpour, M., Rissluminеszenz – A new method for detection and monitoring of fatigue cracks, VSVI-seminar bridge- and structural engineering, Braunschweig, in German, 2015.
[2] Makris, R., Hille, F., Thiele, M., Kirschberger, D., Sowietzki, D., Crack luminescence as an innovative method for detection of fatigue damage, *J. Sens. Sens. Syst.*, 2018, 7, 259–266.

BOOSTING A LOW-COST SENSOR NETWORK WITH MOBILE HIGH-QUALITY SENSORS

Nicolas P. WINKLER[1], Achim J. LILIENTHAL[2] and Patrick P. NEUMANN[1]

[1] Bundesanstalt für Materialforschung und -prüfung (BAM), Unter den Eichen 87, Berlin, Germany, E-mail: patrick.neumann@bam.de

[2] AASS Research Centre, Örebro University, 70182 Örebro, Sweden

1. Introduction

Occupational health is an important topic, especially in industry, where workers are exposed to airborne by-products (e.g., dust particles and gases). Therefore, continuous monitoring of the air quality in industrial environments is crucial to meet safety standards. For practical and economic reasons, high-quality, costly measurements are currently only carried out sparsely [1], both in time and space, i.e., measurement data are collected in single day campaigns at selected locations only [2].

Recent developments in sensor technology enable cost-efficient gas monitoring in real-time for long-term intervals. This knowledge of contaminant distribution inside the industrial environment would provide means for better and more economic control of air impurities, e.g., the possibility to regulate the workspace's ventilation exhaust locations, can reduce the concentration of airborne contaminants by 50% [3].

This paper describes a concept proposed in the project "Robot-assisted Environmental Monitoring for Air Quality Assessment in Industrial Scenarios" (RASEM). RASEM aims to bring together the benefits of both – low- and high-cost – measuring technologies: A stationary network of low-cost sensors shall be augmented by mobile units carrying high-quality sensors. Additionally, RASEM will develop procedures and algorithms to map the distribution of gases and particles in industrial environments.

2. System Overview

2.1 Stationary Sensor Nodes

A stationary sensor network will be composed out of multiple self-built stationary nodes. Each node will be equipped with various low-cost sensors to assess gas concentration, dust particles, temperature and humidity (as an example see [2]).

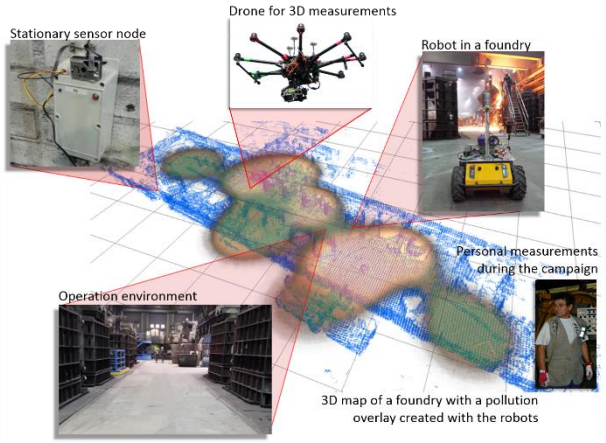

Fig. 1. The key idea of the RASEM project: Dust and gas measurements from stationary sensor nodes in combination with mobile robots and drones to create 3D dust exposure maps in industrial work environments like foundries (adapted from [1]).

The deployed sensor nodes will form a network, whose main tasks are to continuously monitor the dust and gas distribution and identify areas of interest. These areas may be areas with high gradient or noticeable variance.

2.2 Mobile Units

Mobile units (ground and aerial robots) will support the stationary low-cost sensor nodes with high-quality sensors. An aerial unit has the advantage that 3D measurements are possible. Also, it can move fast and independently through an industrial environment. For example, it can monitor a foundry with minimum disturbance for present workers.

While ground-based and aerial robots are fully controllable, the usage of semi-controllable and passive mobile units will be tested: Workers themselves (passive mobility) or forklifts (semi-controllable) can be equipped with portable sensors. The

forklift could suggest the driver to drive in a certain direction, because sensor readings for a specific area are desired.

The mobile units will be equipped with a high-quality, high-cost professional measurement equipment for dust monitoring (e.g., DustTrak II Aerosol Monitor 8532), which can measure three different sizes of dust, namely PM1, PM2.5 and PM10. With this, distribution maps for different particle sizes can be created.

Together with the stationary network, the mobile sensors will complement the distribution maps as stationary sensor nodes cannot cover the whole area. Fully controllable mobile units shall be implemented with a pathfinding algorithm, to also investigate interesting spots, that are identified by stationary nodes. Also, the mobile units – equipped with the high-quality sensors – could be used for cross-calibrating the low-cost sensors.

3. Dust Distribution Maps

One of the main tasks of RASEM will be the development of algorithms to create 3D distribution maps. Distribution maps can display air quality in an intuitive way. The output will be visualized for non-experts (e.g. workers, managers, maintenance) and provide information of dust, gas and airflow.

The algorithms should include time- and event-dependency, e.g., a dependency on periodic events or a smelting process that causes a burst of dust and gas emissions. These dependencies allow extracting temporal patterns from the maps that can be correlated with changes in, e.g., the foundry operation and other seasonal changes (daily shifts, weekends), that enable the detection of abnormal situations with respect to mobility and sensing principle (e.g., excessively high dust level, increased temperature) that may be used to trigger alarms.

Combined with conventional models and exposure assessment methods, risk mitigation measures and human exposure will be estimated to carry out guidelines for the mitigation of health risks in industrial environments.

4. Sensor Planning

RASEM will study and explore approaches on how to effectively combine a dense network of stationary sensor nodes with sparse mobile sensor units. It will build on previous approaches [2] to find optimal positions for sensor nodes to monitor the industrial context.

It is planned to integrate different mobile units in the sensor network. In contrast to fully controllable aerial or ground-based robots, passive (e.g. workers equipped with sensors) and semi-controllable units (e.g. forklift suggesting a route) will be investigated.

5. Conclusion

The proposed concept promises a further examination and usage of recent developments in sensor technology. While low-cost sensors enable the setup of dense sensor networks, they can not deliver the same high-quality data as costly sensor technology can.

The system that is going to be developed in the scope of the RASEM project will be tested under real conditions in multiple industrial sites in Finland. With the cooperation of diverse research institutes and industry partners, it is planned to maximize the insights of how the combination of low-cost and costly sensor technology can enable effective gas/dust distribution mapping.

Acknowledgements

The authors thank the colleagues from Örebro University and Finnish Institute of Occupational Health. Also, the authors express their gratitude to SAF€RA for funding the project in the scope of the 2018 joint call.

References

[1] Schaffernicht, E., et al., *2017 IEEE International Conference on Robotics and Automation (ICRA)*, Singapore, 2017, pp. 2659-2665.

[2] V. H. Bennetts, V.H. et al., *2016 IEEE/RSJ International Conference on Intelligent Robots and Systems (IROS)*, Daejeon, Korea, 2016, pp. 131-136.

[3] Säämänen A., et al., Ventilation 2003, *7th International Symposium on Ventilation for Contaminant Control.* Sapporo, Japan, 2003, pp. 297 – 302.

A FOUR-POINT BENDING TEST APPARATUS FOR MEASUREMENT- AND MODEL-BASED STRUCTURAL ANALYSIS

Cheng-Chieh WU[1], Sven WEISBRICH[2], Mathias BURGER[2], Frank NEITZEL[2]

[1] Bundesanstalt für Materialforschung und -prüfung (BAM), Unter den Eichen 87, 12205 Berlin, Germany, E-mail: cheng-chieh.wu@bam.de;

[2] Technische Universität Berlin, Strasse des 17. Juni 135, 10623 Berlin, Germany

1. Introduction

By means of a small-scale truss bridge, the ability of the Measurement- and Model-based Structural Analysis to detect and localize damage was examined in [1]. Although there was no noteworthy difficulty in detecting damage, it turned out that damage localization responds sensitively to systematic influences, i.e. non-modelled properties of the mechanical model. Therefore, another experiment is being conducted to re-examine the Measurement- and Model-based Structural Analysis. For this purpose, the bending test is carried out as it has been already theoretically respectively numerically discussed in [2]. In this attempt, the systematic influences such as residual stress are kept as low as possible.

2. Specimen and experimental set-up

The specimen is a 1.5 m long slender aluminium beam with a square cross-section of 35 mm by 35 mm, see Fig. 1. The beam was designed with small indentations. They ensure that the applied and reactive forces always act in the same place on the beam specimen. On both ends of the lower side of the beam, there are indentations for the bearings. The notches are located 1 cm from the outer edge of the beam. The bearings consist of a metal chamfer strip glued to a wooden structure. An aluminium profile was used to connect the bearing to the tripod. The tripod was placed on top of a metal star. To prevent the tripod from slipping, the tripod spider was glued to the floor with double-sided adhesive tape. In addition, weights were placed on the stand spider. On the upper side of the beam there are four indentations for attaching weights. Damage is caused by drilling and sawing the beam.

Fig. 1. A six-point bending test apparatus for an aluminium beam specimen.

3. Measurement system

Photogrammetry is used to measure the deformation of the beam. To track the local displacements, in total 34 round target stickers are applied on the surface of the beam (31 markers) as well as on the tripod (three markers). The evaluation software has been developed by the Institute of Geodesy and Geoinformation Science at the Technische Universität Berlin to determine the position of the markers. Accordingly, the camera calibration and distortion corrections were carried out by them.

4. Calibration of the reference state

To adjust the elastic modulus of an undamaged slender beam, twelve experiments were conducted. In each experiment, the deformation behavior of the beam is examined in either unloaded or loaded state. For each beam state, images are taken at short intervals. The exposure time was also considered when determining the intervals. A total of 12 by 300 observations is obtained for each of the 31 markers.

The variance-covariance matrix of the marker position observations is determined by the measurements of the entire experiment. The standard deviation of the displacement in *y*-direction is

$$\sigma_u = 0.003 \text{ mm} \quad (1)$$

and the adjusted elastic modulus is

$$\hat{E} = 67.397 \text{ GPa with } \sigma_{\hat{E}} = 0.009 \text{ mm}. \quad (2)$$

5. Damage detection and localization

In the same way as in [2], the presented approach is followed to detect and localize damage. However, to avoid long computation time, in case where the global test failed to reject the null hypothesis, the standardized residuals NV_ζ of the observed unknown elastic parameters are evaluated. The finite element discretization of the beam specimen is determined in dependence on the attached markers as well as the application points of the forces and bearings. Thus, the finite element model of the beam consists of 36 non-equidistant elements. Considering the two boundary conditions and a linear interpolation of the elastic parameter of each element, a total of 39 unknowns result. Due to the high degree of freedom resulting from the number of unknowns, an incorrect adjustment of the boundary conditions can occur. Eventually, the elastic parameters of the elements can be incorrectly adjusted to counteract the effects of yielding bearings. Therefore, in a first step, all elements share the same elastic modulus. In other words, one Young's modulus and two boundary conditions must be determined from the displacement observations. Then, in the second step, the adjusted boundary conditions are used as fixed values, while the 36 elastic parameters are determined from the displacement observations.

The beam was gradually damaged at a fixed position. The edge-to-edge length of the beam is 1500 mm. The damage was caused at approximately 383 mm, measured from the right edge. The beam length in the finite element model is 1480 mm which corresponds to the distance between the bearings. Thus, the damage position is at approximate 1107 mm. The damage has been successively increased. First, the beam was drilled through with a radius of 4 mm. Six different load experiments were then carried out. The damage was not detected in five out of six cases. And the localization of the fault failed where an alleged damage was detected. The beam was then further damaged. The borehole was extended to 10 mm radius; then two more holes were drilled with 10 mm radius each, and damage was further increased. Again, no damage was noticeably detected. Then, the beam was sawed. Here, it was observed that if the attached weights were large enough, the damage was detected but the localization of the damage failed. Ultimately, the damage was large enough, so that the damage could be detected and localized repeatedly. The damage position is at approximate 1107 mm. Thus, it affects the element node $\zeta = 24$ which is at 1112 mm. However, according to the performed analysis, the damage is located at the element node $\zeta = 22$ which is at 990 mm. This results in an error estimate of 117 mm. In relation to the total length of 1480 mm, the mislocalization is less than 8 percent, (117 mm /1480 mm $\approx$ 0.079).

6. Conclusion

By means of a beam bending experiment, the re-evaluation has shown that the Measurement- and Model-based Structural Analysis can detect and localize damage. However, the likelihood of localizing damage is hampered by systematic influences. Here, in this case, it was observed that ambient light affected the photogrammetric system. Ambient light changes, for example, due to the influence of clouds. As a result, the pixels on the images change their contrasts and thus influencing the adjusting circular position of the marker. It is also inevitable that the markers will become soiled over time. This also impacts an apparent change in the marker position. Subsiding tripods and bearings were also unhelpful in reducing systematic influences during evaluation. The maximum deflection was approximately 1.4 mm and due to the subsiding of roughly 0.1 mm, the elastic parameter was missing 3 GPa at the end of the adjustment. To counteract the subsidence, on the one hand the finite element model had to be extended, on the other hand the attached weight should not become too large. Since the beam was very stiff and it was not possible to attach too much weight, the deflection became too small. But it was necessary that the deflection had to be large enough to overcome the noise and systematic influences of photogrammetry. In the end, there was no other choice but to increase the damage to the beam. This made it possible to achieve consistent damage detection and localization.

References

[1] Wu, C.-C., Kadoke, D., Fischer, M., Kohlhoff, H., Weisbrich, S., Neitzel, F., A small-scale test bridge for Measurement- and Model-based Structural Analysis, In *35th Danubia-Adria Symposium on advances in experimental mechanics*, Sinaia, 25-28 Sep, 2018, PRINTECH, Bucureşti, 2018, pp. 23–24.

[2] Wu, C.-C., Weisbrich, S., Neitzel, F., Integrated structural analysis of hybrid measurement and finite element method for damage detection within a slender beam. In *31st Danubia-Adria Symposium on advances in experimental mechanics*, Kempten, 24-27 Sep, 2014, VDI Verein Deutscher Ingenieure e.V., Düsseldorf, 2014, pp. 191–192.

COMPARISON OF METHODS FOR CALCULATION THE DEFLECTION OF COMPOSITE WOUND TUBES

Tereza ZÁMEČNÍKOVÁ[1], Tomáš MAREŠ[2], Viktor KULÍŠEK[3], Anna MALÁ[4]

[1] Czech Technical University in Prague, Faculty of Mechanical Engineering, Department of Mechanics, Biomechanics and Mechatronics. Technická 4, 166 07 Praha 6, Czech Republic, E-mail: Tereza.Zamecnikova@fs.cvut.cz

[2] Czech Technical University in Prague, Faculty of Mechanical Engineering, Department of Mechanics, Biomechanics and Mechatronics. Technická 4, 166 07 Praha 6, Czech Republic, E-mail: Tomas.Mares@fs.cvut.cz

[3] Czech Technical University in Prague, Faculty of Mechanical Engineering, Department of Mechanics, Biomechanics and Mechatronics. Technická 4, 166 07 Praha 6, Czech Republic, E-mail: Viktor.Kulisek@fs.cvut.cz

[4] Czech Technical University in Prague, Faculty of Mechanical Engineering, Department of Mechanics, Biomechanics and Mechatronics. Technická 4, 166 07 Praha 6, Czech Republic, E-mail: Anna.Mala@fs.cvut.cz

1. Introduction

The aim of this work is to facilitate methods for design of composite wound tubes. The comparison of several analytical methods and FEA methods is performed. This paper is focused on the application of the known methods of computing the deflection of composite beam deformation and on its experimental validation. The three-point bending experiment was implemented on several composite beams. The results and comparisons are presented in this paper.

2. Methods for the Deflection Calculation

The FEM calculations are performed in Abaqus. The model of the composite beam contains the fixed composite tube loaded by the single force at the free end. The geometry of the beam is the same for all models. (Fig.1.). The material constants are entered as parameters of the model.

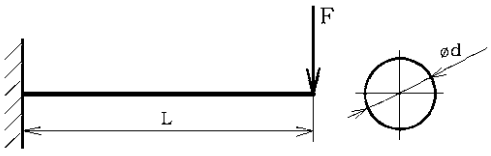

Fig. 1. The geometry of the models.

2.1 Conventional Shell and Continuum Shell

In this model the beam is represented by a shell. The thickness of the shell is specified as a parameter of the model or it is included in ABD matrices which define the stiffness of the beam.

The Continuum Shell is modelled as a solid body. The real thickness of the hollow beam wall is specified as parameter of the model and by the composite layup. The elements are in this model distributed through the whole thickness of the solid body.

The advantage of the Conventional Shell model is the simplicity of the whole model, its preparation and the computational simplicity. The modelled volumes must have the disposition to observing the assumptions for using the shell theory. [1] The Continuum Shell can be stacked. The meshing is more difficult with Continuum Shell because the thickness of the shell must be meshed. Consequently the computation is more difficult too.

2.2 Volume Model

For the calculation using the volume model the full 3-D geometry is specified. Each ply could be created separately as a separate solid body with its own material specification or the composite layup should be assigned to elements by the parameters of the model. This model is most demanding to the preparation and the computation time, but it is more detailed than the other models.

2.3 Analytical methods

The aim to determine the bending stiffness is approached applying the Hooke's law for plane stress state of orthotropic layer under the

assumptions of Bernoulli's beam theory. The compliance matrix of orthotropic material is considered

$$C_{xy} = S_{xy}^{-1} = \begin{bmatrix} \frac{1}{E_x} & -\frac{\nu_{yx}}{E_x} & 0 \\ -\frac{\nu_{xy}}{E_y} & \frac{1}{E_y} & 0 \\ 0 & 0 & \frac{1}{G_{xy}} \end{bmatrix} \quad (1)$$

As the bending stress has the direction of the x-axis the modulus of elasticity E_x from the compliance matrix is used for calculation of the bending stiffness. More details is in [2].

The deflection of the beams is given by Bernoulli's equation

$$w''(x) = -\frac{M_o(x)}{\sum_k E_{x_k} \cdot J_{y_k}(x)} \quad (2)$$

From this equality it is evident that the main problem is the correct determination of the bending stiffness ($E_x \cdot J_y(x)$) of the composite material.

The other method uses ABD matrices. The ABD matrices are assembled according to the classical laminate theory. The main problem is the determination of the bending stiffness of the whole shell and the related equivalent modulus of elasticity. In this case the equivalent modulus of elasticity of the whole material is obtained from the elements of the tensile stiffness matrix **A** from the equation [3]

$$\begin{bmatrix} \mathbf{N} \\ \cdots \\ \mathbf{M} \end{bmatrix} = \begin{bmatrix} \mathbf{A} & \vdots & \mathbf{B} \\ \cdots & \vdots & \cdots \\ \mathbf{B} & \vdots & \mathbf{D} \end{bmatrix} \begin{bmatrix} \boldsymbol{\varepsilon}^{\circ}_{\mathbf{m}} \\ \cdots \\ \mathbf{k} \end{bmatrix} \quad (3)$$

where **A** is the extensional stiffness matrix, **B** is the bending-extension coupling stiffness matrix and **D** is the bending stiffness matrix. The equivalent Young's modulus E_{eq} is determined from the matrix **A**. Than the equation (2) is used to obtain the deflection as in the previous case.

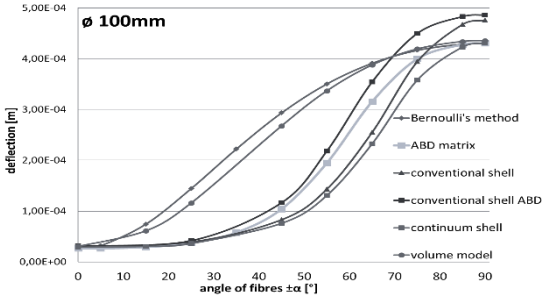

Fig. 2. The comparison of the deflection calculated on the same model by different ways [3].

3. Experiment

The experiment is described in detail in [4]. Two different beams (thick and thin walled) are used. The geometry of the tubes and the material constants are specified. The following experiment contain four types of layup on two diameters of the tubes and the three different materials are used for specimens.

4. Conclusions

The experimental analysis of the three-point bending of the composite tubes was performed. The same problem was modelled by the three different FEM models and two analytical methods for computation of the beam bending stiffness and the deflection. The results of the comparison of all computational methods with the experimental data will be presented. The results are satisfactory in the case of the thin-walled tubes. For the thick-walled case all methods give different values and great deviance compared with the experimental data. This is caused by the composite layup and it is apparent that the used computational methods are not good in predicting the stiffness of thick-walled beams from orthotropic material.

Acknowledgements

This work has been supported by project No. **SGS18/175/OHK2/3T/12** (FIS:16 - 1611816B001) of the Grant Agency of the Czech Technical University in Prague.

References

[1] Barbero, Ever J. Finite element analysis of composite materials using Abaqus. Boca Raton: CRC Press/Taylor & Francis Group; 2013. 413s. ISBN 978-14-6651-661-8

[2] Laš, Vladislav. *Mechanika kompozitních materiálů*. 2. přeprac. vyd. Plzeň: Západočeská univerzita, 2008. 200s. ISBN 978-80-7043-689-9.

[3] Zavřelová, Tereza. Analysis of composite beam bending. Diplomová práce (Ing.), České vysoké učení technické v Praze. Fakulta strojní, ústav mechaniky, biomechaniky a mechatroniky. Praha, ČR, 2015.

[4] Malá, Anna. Výpočtové metody pro analýzu tenkostěnných i silnostěnných kompozitních nosníků. Diplomová práce (Ing.), České vysoké učení technické v Praze. Fakulta strojní, ústav mechaniky, biomechaniky a mechatroniky. Praha, ČR, 2017.

STRUCTURE AND FATIGUE PROPERTIES OF SiMo AND SiCu TYPES OF NODULAR CAST IRON

Alan VAŠKO [1]

[1] University of Žilina, Faculty of Mechanical Engineering, Department of Material Engineering, Univerzitná 8215/1, 010 26 Žilina, Slovakia. e-mail: alan.vasko@fstroj.uniza.sk

1. Introduction

Nodular cast irons alloyed by Si and Mo are often used for high temperature applications, for example castings of the exhaust pipes of the combustion engine or turbo charger housings. SiMo-nodular cast iron usually has a ferritic matrix, but may also contain pearlite and carbides. Increasing content of silicon increases yield strength, but lowers toughness and elongation. Therefore, the material can be very brittle at room temperature. Molybdenum partially segregates during solidification and forms a carbidic phase on grain boundaries. This carbidic network improves dimensional stability, increases tensile strength, creep resistance and corrosion resistance but reduces plastic properties [1,2].

Nodular cast irons alloyed by Si and Cu are used in various components of tribotechnical units. SiCu-nodular cast iron is characterized by a high content of pearlite in a matrix and the presence of inclusions of a structurally free copper-bearing phase. Copper is a graphitizing element and it increases the degree of pearlitization of the structure. By hardening ferrite and pearlite, copper increases strength and hardness of nodular cast iron. It also raises corrosion resistance, improves wear resistance and decreases friction coefficient of nodular cast irons [3,4].

2. Experimental methods

For experiments, two types of nodular cast irons were used:

- SiMo-nodular cast iron with content of silicon 4 % and content of molybdenum 1 %, which corresponds to EN-GJS-X300SiMo4-1;
- SiCu-nodular cast iron with content of silicon 4 % and content of copper 1.5 %, which corresponds to EN-GJS-X300SiCu4-1.5.

Microstructure of the specimens was evaluated according to STN EN ISO 945 (STN 42 0461) and by automatical image analysis.

Fatigue tests were carried out according to STN 42 0362 at low frequency sinusoidal cyclic push-pull loading (stress ratio R = –1) at ambient temperature (T = 20 ± 5 °C). They were realised in the high cycle fatigue region (from 10^5 to 10^7 cycles) at frequency f ≈ 75 Hz using the fatigue experimental machine Zwick/Roell Amsler 150HFP 5100. For fatigue tests, specimens of circular cross-section with a diameter d_0 = 8 mm were used. For fatigue tests, 15 specimens from both melts were used to determine the fatigue characteristics [5,6].

3. Experimental results

From a microstructural point of view, the specimen of GJS-SiMo is ferrite-pearlitic nodular cast iron (Fig. 1a) and the specimen of GJS-SiCu is pearlite-ferritic nodular cast iron (Fig. 1b).

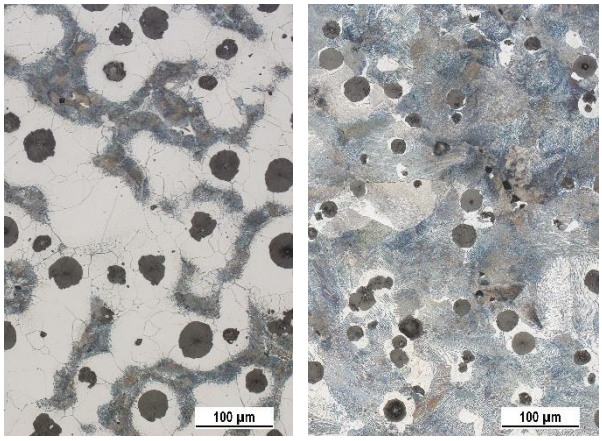

a) GJS-SiMo b) GJS-SiCu

Fig. 1. Microstructure of the specimens, etched by 1% Nital.

Evaluation of the microstructure of the specimens by STN EN ISO 945 (STN 42 0461) and by image analysis (shape factor, equivalent diameter of graphite, count of graphitic nodules per unit of area and content of ferrite) are presented in Tables 1 and 2.

Table 1. Microstructure according to STN EN ISO 945.

Melt	Microstructure
GJS-SiMo	90%VI6 + 10%V6 – Fe80
GJS-SiCu	90%VI6/7 + 10%V6 – Fe15

Table 2. Microstructure evaluation by image analysis.

Melt	Shape factor	Equivalent diameter of graphite [µm]	Count of graphitic nodules [mm^{-2}]	Content of ferrite [%]
GJS-SiMo	0.88	31.2	122.8	59.4
GJS-SiCu	0.84	24.3	172.4	19.7

Results of mechanical tests (tensile test, impact bending test and Brinell hardness test) are given in Table 3. The specimen of GJS-SiCu has higher yield strength $R_{p0,2}$, tensile strength R_m and Brinell hardness HBW, but lower elongation A and absorbed energy K0 than the specimen of GJS-SiMo. It has connection with the microstructure of the specimens, especially with the character of matrix (content of ferrite and pearlite) and also with size of graphite and count of graphitic nodules.

Table 3. Mechanical properties .

Melt	$R_{p0,2}$ [MPa]	R_m [MPa]	A [%]	K0 [J]	HBW 10/3000/10
GJS-SiMo	515.3	573.9	1.4	11.3	213.7
GJS-SiCu	631.1	652.7	0.7	8.0	247.3

Results of fatigue tests (relationship between stress amplitude σ_a and number of cycles to failure N_f) obtained at low frequency cyclic loading (f ≈ 75 Hz) are shown in Fig. 2.

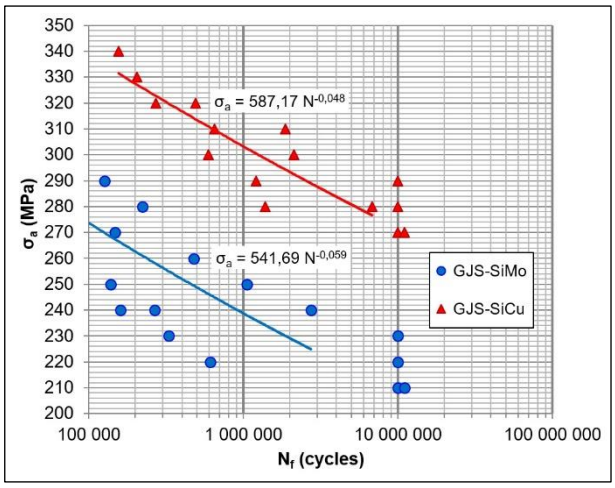

Fig. 2. Wöhler curves $\sigma_a = f(N)$.

The specimen of GJS-SiCu has higher tensile strength R_m as well as fatigue strength σ_c than the specimen of GJS-SiMo.

Results of experiments have shown that the fatigue strength of nodular cast irons increases with an increasing tensile strength.

4. Conclusions

- Copper has a pearlitizing and graphitizing effect, therefore the specimen of GJS-SiCu has lower content of ferrite, smaller size of graphite and higher count of graphitic nodules per unit of area than the specimen of GJS-SiMo.
- These structural changes have brought about a change of mechanical properties, which depend especially on the character of matrix (content of ferrite) as well as on size of graphite and count of graphitic nodules. Therefore, the specimen of GJS-SiCu has higher yield strength, tensile strength and hardness, but lower elongation and absorbed energy than the specimen of GJS-SiMo.
- Fatigue strength of nodular cast irons has connection with tensile strength. The specimen of GJS-SiCu has higher tensile strength, therefore it also has higher fatigue strength than the specimen of GJS-SiMo.

Acknowledgements

This work has been supported by the grant projects VEGA No. 1/0398/19 and KEGA No. 049ŽU-4/2017 and 012ŽU-4/2019.

References

[1] Matteis, P., Scavino, G., Castello, A., Firrao, D. High temperature fatigue properties of a Si-Mo ductile cast iron. *Procedia Materials Science*, 2014, 3, 2154-2159.
[2] Roučka, J., Abramová, E., Kaňa, V. Properties of type SiMo ductile irons at high temperatures. *Archives of Metallurgy and Materials*, 2018, 2, 601-607.
[3] Gumienny, G., Kacprzyk, B., Gawroński, J. Effect of copper on the crystallization process, microstructure and selected properties of CGI. *Archives of Foundry Engineering*, 2017, 1, 51-56.
[4] Siľman, G. I., Kamynin, V. V., Tarasov, A. A. Effect of copper on structure formation in cast iron. *Metal Science and Heat Treatment*, 2003, 45, 7-8.
[5] Vaško, A. Fatigue properties of nodular cast iron at low frequency cyclic loading. *Archives of Metallurgy and Materials*, 2017, 4, 2205-2210.
[6] Kuchariková, L., Tillová, E., Uhríčik, M., Belan, J. High-cycles fatigue of different casted secondary aluminium alloy. *Manufacturing Technology*, 2017, 5, 756-761.

ANALYSIS OF THE CAUSE OF FAILURE OF TITANIUM ENDOPROSTHESIS

Patrícia HANUSOVÁ[1], Peter PALČEK[1], Milan UHRÍČIK[1], Mária CHALUPOVÁ[1]

[1] University of Žilina, Faculty of Mechanical Engineering, Department of Materials Enginering, Univerzitná 8215/1, Žilina, Slovakia, E-mail: patricia.hanusova@fstroj.uniza.sk

1. Introduction

The performance of any material on the human body is controlled by two sets of characteristics: biofunctionality and biocompatibility. [1] The selection of materials for medical applications is usually based on a consideration of biocompatibility and suitable mechanical properties.

For the reliable applications of the titanium alloy endoprosthesis in functional medical components, the manufactured parts should be durable not only under static loading but also under cyclic loading. Therefore, the Ti64 alloys, which properties are relatively low modulus, good fatigue strength, formability, machinability, corrosion resistance biocompatibility [2], are most widely used in biomedical replacements, implants, and prosthesis.

Titanium and titanium alloys are widely used in biomedical devices and components, especially as hard tissue replacements as well as in cardiac and cardiovascular applications, because of their desirable properties, such as relatively low modulus, good fatigue strength, formability, machinability, corrosion resistance, and biocompatibility [2]. To judge the significance of a hip joint replacement, the clinical results over 10-20 years must be evaluated. Today, still over half of all hip endoprostheses involves cement fixation. The rest is uncemented, in direct contact with bone [3]. The endoprosthetic of hip joint replacements is currently the most common and successful method in advanced surgery to treat degenerative joint disease, for relieving pain and for correcting deformities [4].

Hip prostheses with a modular neck adapter have been used in orthopedic surgery. Neck modularity of the femoral component of total hip implants is attractive since neck length, anteversion and femur (Fig. 1) offset can be adjusted intraoperatively after implantation of the prosthesis stem. This allows fitting of the prosthesis to the individual anatomical and implantation condition, reducing wear rate, enhancing hip stability, increasing the range of motion and minimizing the risk of dislocation. The disadvantage of this flexibility of such system is an additional interface between the stem and the neck, which bears the risk of micromotions at the interface, resulting in a constant abrasion of the passivation layer and corrosion, especially for titanium alloys [5].

Fig. 1. The X-ray view of the cracked endoprosthesis.

Corrosion prevention in biomaterials has become crucial particularly to overcome inflammation and allergic reactions caused by the biomaterials implants towards the human body. When these metal implants contacted with fluidic environments such as bloodstream and tissue of the body, most of them became mutually highly antagonistic and subsequently promotes corrosion. Biocompatible implants are typically made up of metallic, ceramic, composite and polymers [6].

2. Materials and methodology

Titanium alloys are known for their high sensitivity to fatigue induced by notches.

Accordingly, prosthesis components must be designed in such a way that excessive stress due to construction notches is minimized. For this reason and other design factors, structural testing continues to be mandatory before a product is placed on the market [7].

This contribution deals with the microstructure, microhardness and fatigue behavior of experimental specimens of Ti64 alloy cut from real endoprosthesis. The fatigue test was performed on Vibrophores Amsler 150 HFP Zwick/Roell under three-point bending load at room temperature with a frequency of 65 Hz.

The microhardness was measured using a ZHVμ Vickers hardness tester with a load of 0.5 HV. The spectral analysis was determined by spectrum analyser Bruker.

3. Results

The mechanical properties and microstructure of titanium alloys are strongly dependent on their processing history and heat treatment. The microstructure of sample (Fig.2) was monitored on an optical and electron microscope. The endoprosthesis is composed of two parts- stem and neck, which are placed together. Both are made of titanium alloy but in different ways. The analyze of the cracked endoprosthesis by the light microscope is examining a dendrite structure.

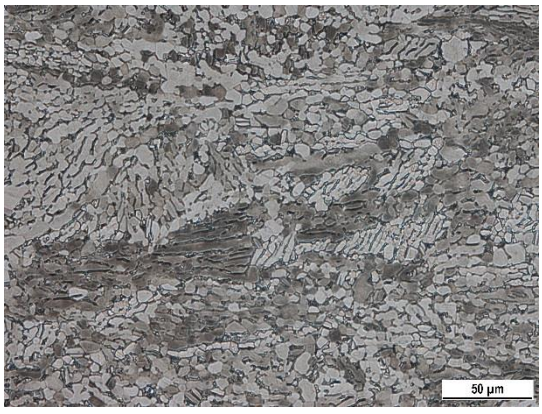

Fig. 2. The microstructure of endoprosthesis with 500x magnification.

4. Conclusions

The microstructure is an essential factor in implant design. It is very important in the role of prematurely failed implants to understand the physical and chemical phenomena at the surface and to minimize corrosion the femoral stem and neck. It is obvious that we need to keep an optimal microstructure regarding corrosion and mechanical properties, which can be controlled through processing parameters and be standardized in the near future. The present study established the surface of microstructures of biomaterials for hip endoprostheses.

Titanium alloys were subjected to thermomechanical and physicochemical processes during their production to obtain additional data for designers and implant producers.

5. Acknowledgements

This research was supported by Project KEGA n° 013ŽU-4/2019.

References

[1] Gotman, I. Characteristics of metals used in implants. *Journal of endourology*, 1997, 11(6), 383-389.

[2] Liu, X., Chu, P. K., & Ding, C. Surface modification of titanium, titanium alloys, and related materials for biomedical applications. *Materials Science and Engineering: R: Reports*, 2004, 47(3-4), 49-121.

[3] Semlitsch, M., Willert, H. G. Implant materials for hip endoprostheses: old proofs and new trends. *Archives of orthopaedic and trauma surgery*, 1995, 114(2), 61-67.

[4] Jenko, M., Gorenšek, M., Godec, M., Hodnik, M., Batič, B. Š., Donik, Č., Dolinar, D. Surface chemistry and microstructure of metallic biomaterials for hip and knee endoprostheses. *Applied Surface Science*, 2018, 427, 584-593.

[5] Jauch, S. Y., Huber, G., Hoenig, E., Baxmann, M., Grupp, T. M., Morlock, M. M. Influence of material coupling and assembly condition on the magnitude of micromotion at the stem–neck interface of a modular hip endoprosthesis. *Journal of biomechanics*, 2011, 44(9), 1747-1751.

[6] Asri, R. I. M., Harun, W. S. W., Samykano, M., Lah, N. A. C., Ghani, S. A. C., Tarlochan, F., Raza, M. R. Corrosion and surface modification on biocompatible metals: A review. *Materials Science and Engineering: C*, 2017, 77, 1261-1274.

[7] Windler, M., & Klabunde, R. Titanium for hip and knee prostheses. In *Titanium in medicine*, Springer Berlin; 2001; pp. 703-746.

THE USAGE OF RANDOM DECREMENT METHOD FOR LINEAR DAMPING ESTIMATION

Stipe PERIŠIĆ[1], Jani BARLE[2]

[1] FESB, Faculty of Electrical Engineering, Mechanical Engineering and Naval Architecture, University of Split, R. Boskovica 32, 21000 Split, Croatia, E-mail: sperisic@fesb.hr;

[2] FESB, Faculty of Electrical Engineering, Mechanical Engineering and Naval Architecture, University of Split, R. Boskovica 32, 21000 Split, Croatia, E-mail: barle@fesb.hr

1. Introduction

This paper presents a random decrement method (RDT) [1] in damping estimation while system is in operation conditions. For that purpose, it was developed mechanical, single degree of freedom (SDoF) experimental testbed, i.e air bearing [3], which can be seen in the Fig. 1. It is specifically designed to easily set and change system parameters, especially damping.

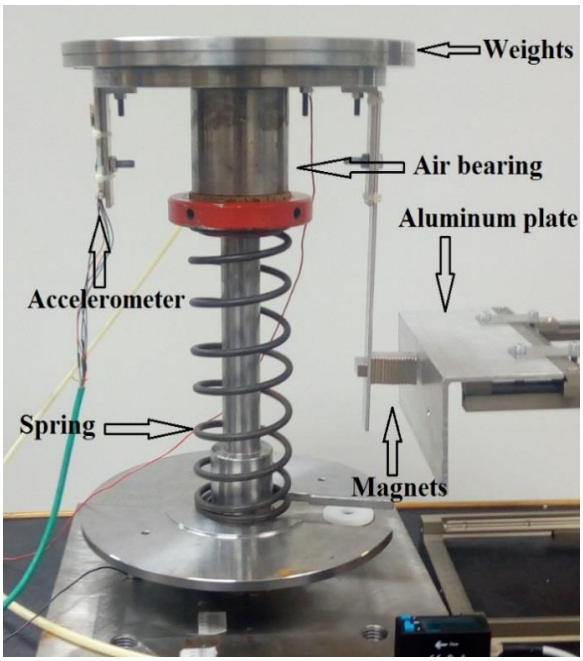

Fig. 1. Experimental test bed.

It is relatively easy to detect damping for simple SDoF system subjected to impulse or step input [4]. Dumping detection for the system while it is in operating condition is much more challenging, but regarding the technical diagnostic more realistic task. RDT method provides an easy way to estimate system parameters, while in operating condition, i.e. does not require knowledge of the input forces. The analysis demonstrated in the paper is directly applicable in technical diagnostics [2].

2. Testbed setup and data acquisition

Through the whole process of the data recording, mass and stiffness were kept constant and only damping was changed. It should be noted that mass and stiffness are also easy to change, by adding weight or use different spring respectively. The mass of the system is 10.9 Kg and the stiffness 3649 N/m. Regarding damping, several magnets and an aluminium plate (Fig. 1) were used. By movement of the magnet relative to the aluminium plate, Lorentz force is produced, which provides linear damping. Depending on the distance between plate and magnets the damping force is managed. Data collected from air bearing can be seen in Fig. 2. It represents acceleration, from a two-axes capacitive accelerator (only vertical axis), recorded with the NI-USB-6251 National Instrument module. Sampling rate was 1000 Hz, which is more than enough considering that the natural damped frequency of the system is just around 3 Hz.

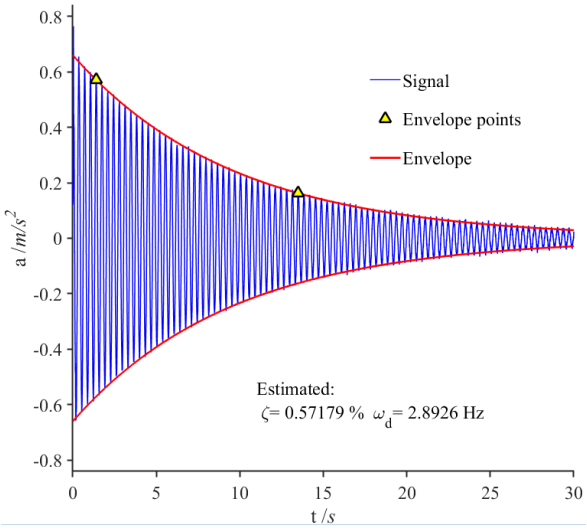

Fig. 2. System free decay and estimated values.

The depicted free decay was generated by a 2 mm initial displacement, and to estimate damping a simple logarithmic decrement technique was used [4]. As it can be seen in Fig. 2 the damping value is 0.57% (relative damping coefficient) and it is linear. Recorded data were compared with a dynamic model and shows very good match.

3. Discussion and analysis

The aim is to detect the same damping value as in the previous section (0.57%), while system is in operational condition. By applying RDT to the system response, it is possible to reconstruct a free decay response (impulse response function). The key is to have a long enough signal, so it can be divided into a sufficient number of segments. Averaging those segments, it filters out the noise, and leaves just free decay. In this paper segment length was 2 seconds. This is long enough to estimate the damping by the logarithmic decrement technique, while it enables a large number of segments. The analyzed case is depicted in Fig. 3. Top panel represents a detailed system response and middle panel is the full system response. Bottom panel is frequency analysis.

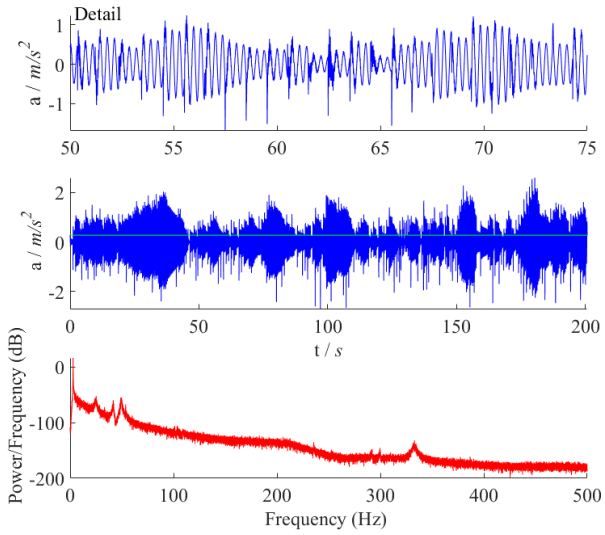

Fig. 3. System response subjected to random excitation.

Fig. 4 shows a comparison of model and RDT response. Although there is certain deviation present, deviation in damping is negligible because the envelopes slope between model and RDT is practically the same. The estimated value of the damping is 0.53%, which is more than satisfactory.

Change of damping could indicate a fault or a failure, so for the same system the greater value of damping is used. Graphical view of results is omitted due to the brevity. The result of analyses shows an estimate damping value was 0.7%. This is also satisfactory because the true damping was 0.8%, although comparing with previous case the estimated value shows the greater deviation.

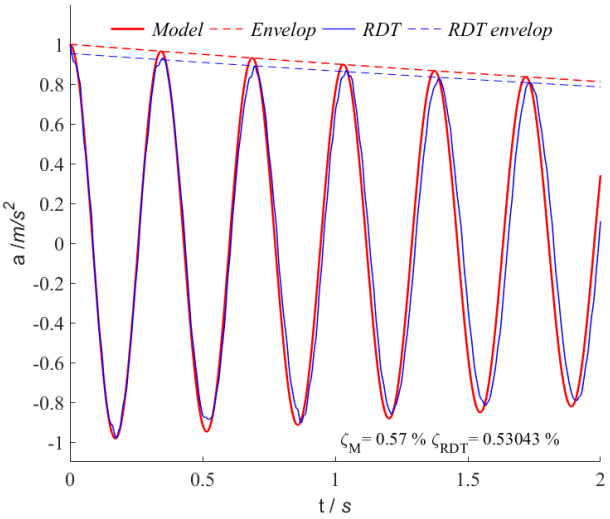

Fig. 4. RTD response and estimated damping.

4. Conclusion

The estimation of system parameters can be obtained using the RDT method. Since the method does not require knowledge of input forces, it is suitable for detecting a parameter while the system is still in operation. However, if the analysis is reduced to the evaluation of only one parameter, it is possible to make a much more efficient estimation, and such parameter could be used as a technical indicator. In this paper the highly sensitive testbed with the ability to change the system parameter was used. It has been shown that the damping can be estimated via RDT method reasonably well.

References

[1] Ibrahim, S.R. Random decrement technique for modal identification of structures. *Journal of Spacecraft and Rockets*, 1977, 14 (11), pp. 696-700.
[2] H. Czichos; *Handbook of Technical Diagnostics*, Berlin: Springer-Verlag , 2013..
[3] Chundong X., Shuyun J., Dynamic Analysis of a Motorized Spindle With Externally Pressurized Air Bearings, *Journal of Vibration and Acoustics*, 2015, 137, 041001
[4] Schmitzl T.L. Smith K.S. *Mechanical Vibrations-Modeling and Measurement*; Springer-Verlag New York; 2012

ON THE POSTERIOR PREDICTIVE IN BAYESIAN FAILURE ANALYSIS

Jani BARLE[1], Stipe PERIŠIĆ[2], Đorđe DOBROTA[3]

[1] FESB, Faculty of Electrical Engineering, Mechanical Engineering and Naval Architecture, University of Split, R. Boskovica 32, 21000 Split, Croatia, E - mail: barle@fesb.hr;

[2] FESB, Faculty of Electrical Engineering, Mechanical Engineering and Naval Architecture, University of Split, R. Boskovica 32, 21000 Split, Croatia, E - mail: sperisic@fesb.hr;

[3] PFST, Faculty of Maritime Studies, University of Split, R. Boskovica 37, 21000 Split, Croatia, E - mail: ddobrota@pfst.hr

1. Introduction

This paper presents one way of data processing for estimating the remaining life of a component or system. To achieve this failure distribution is needed. Every distribution is a function of parameter(s). Methods such as probability paper or Maximum Likelihood Estimator (MLE) are used to determine distribution parameters. For both of these methods, it is desirable to have a large number of data, which is not always the case. The data for parameter estimation can be obtained from the generic databases. The most famous example of such a base is OREDA Reliability Data Handbook [1]. The data in every used generic database may deviate from the actual values. The reason is the difference between data gathering conditions and exploration conditions. Bayesian analysis offer unique framework, which can take into account the manufacturer's or database data, combines them with an expert opinion and update data based on evidence. The final result of Bayesian analysis is distribution, i.e. posterior. If the whole posterior distribution is included in prediction instead of posterior expected value, then it gets posterior predictive distribution. The latter is the main scope of this paper.

2. Theoretical background of the Bayesian analysis

Bayesian analysis is based on a combination of prior distribution and the likelihood function as it is represented by Eq. (1)

$$\pi_1(\varphi|x) = \frac{f(x|\varphi)\pi_0(\varphi)}{\int_\Omega f(x|\varphi)\pi_0(\varphi)d\varphi} \qquad (1)$$

where $\pi_1(\varphi|x)$ is posterior distribution, $f(x|\varphi)$ likelihood function, and $\pi_0(\varphi)$ is prior distribution. For certain choices of the prior, the posterior has the same algebraic form, and such a choice is called a conjugate prior [2]. In this paper Gamma exponential conjugate prior were used. Future failures can be predicted by posterior predictive distribution by using Eq. (2).

$$f(x|T) = \int_\Omega f(x|\varphi)\pi_1(\varphi|T)d\varphi \qquad (2)$$

where $\pi_1(\varphi|T)$ is posterior distribution and $f(x|\varphi)$ is model, i.e. some distribution of interest. The posterior distribution of the Gamma exponential model [3] is :

$$f(\lambda|T) = \frac{{\kappa_n}^{\alpha_n}}{\Gamma(\alpha_n)}\lambda^{\alpha_n-1}e^{(-\kappa_n\lambda)} \qquad (3)$$

with hyperparameters $\alpha_n = \alpha_0 + n$ and $\kappa_n = \kappa_0 + \sum_{i=1}^{n} T_i$. The exponential distribution is represented by the Eq. (4).

$$f(t|\lambda) = \lambda e^{(-\lambda t)} \qquad (4)$$

Combining Eq. (3) and Eq. (4) with Eq. (2) it can be shown that the posterior predictive distribution takes form:

$$f(t|T) = \frac{\alpha_n {\kappa_n}^{\alpha_n}}{(t+\kappa_n)^{\alpha_n+1}} \qquad (5)$$

3. Discussion and analysis

Due to the complexity of Bayesian analysis, only one component was analyzed. It is a safety valve block noted as VB1 in functional scheme in Fig. 1. The failure rate of the safety valve block VB1 is estimated from the data in NPRD (Nonelectronic Parts Reliability Data) database [4]. The value is 0.22 failures per year. It is important to note that in all databases of this kind, the failure rate is given as a constant value, in other words, the model of failure is an exponential distribution. In the absence of actual data, five random failures were generated with mean value 0.22. The samples will be implemented in gamma-exponential model.

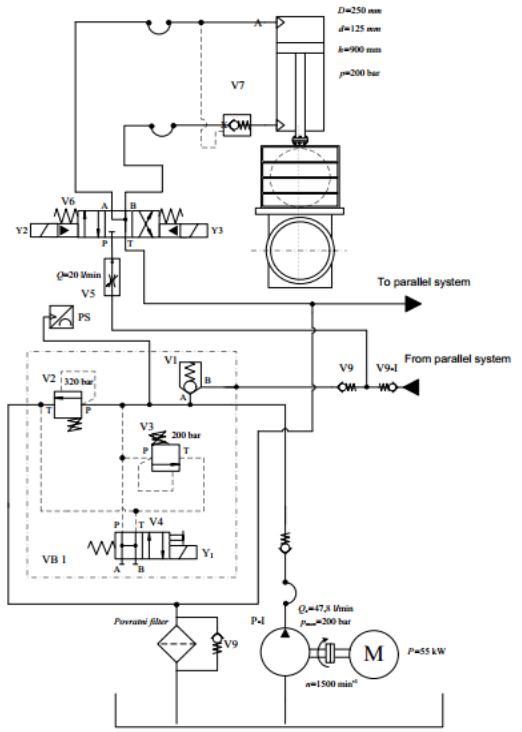

Fig. 1. Functional scheme [5].

Generated random failures are presented in Table 1. The prior parameters are $\kappa_0 = 15$ and $\alpha_0 = 2$.

Table 1. Generated random failures.

	T1	T2	T3	T3	T5
Time	6.2	2.2	3.4	4.7	0.8

Results of Bayesian analysis are presented in Fig. 2. The top plot is prior, middle plot is posterior after just 1 failure, and bottom plot is posterior distribution after all 5 failures. It is worth to note that target value is $\lambda = 0.22$ year^{-1}.

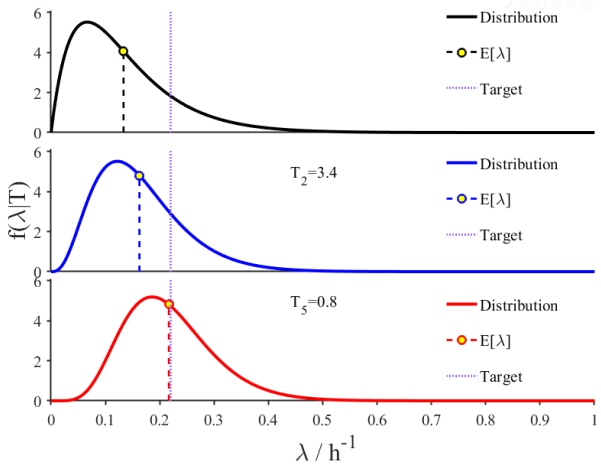

Fig. 2. Convergence of posterior distributions.

Instead of using one point estimation like previously in a Bayesian framework it is possible to use the whole posterior distribution, i.e. posterior predictive. The Fig. 3 shows the posterior predictive distribution (Eq. (5)). By calculating the mean time to failure for every single distribution mean residual life can be estimated.

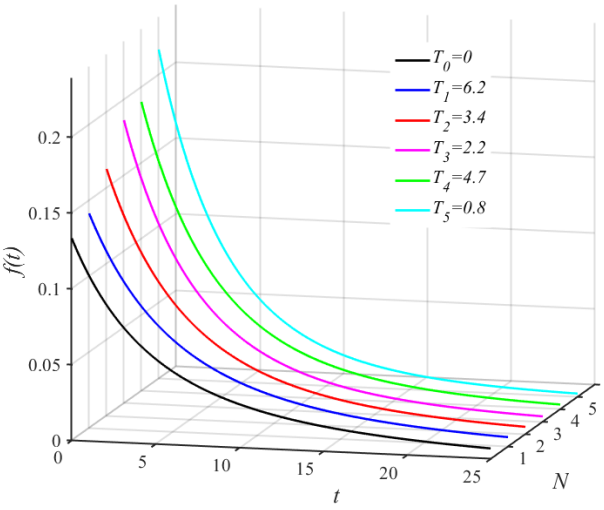

Fig. 3. Posterior predictive distribution of the Gamma-exponential model.

4. Conclusion

Since there is no large amount of data (failures) when reliability is analyzed, Bayesian analysis represents a good choice. It can combine several different sources and update belief when data occur. Generally, databases represent the most common form of data source. Since the failure rate occurs as constant value it is reasonable to use a Gamma-exponential model. It has been shown how to include whole posterior distribution in failure analysis via posterior predictive. Also, it has been shown that it is possible to avoid numerical integration, especially time consuming MCMC method via using conjugate priors

References

[1] Det Norske Veritas; Offshore Reliability Data Handbook (OREDA); Norway, 2002
[2] Rausand M. *System reliability theory*; John Wiley & Sons, New Jersey, 2004
[3] Barle J. Ban D. Ladan M. *Maritime component reliability assessment and maintenance using bayesian framework and generic data*; Advanced ship design for pollution prevention, pp 181-188; *Taylor & Francis Group*; London; 2010
[4] Nonelectronic Parts Reliability Data 2011; Quanterion Solutions Incorporated 2011
[5] Dobrota Đ. *Kvalitativna analiza u procjeni pouzdanosti pomoćnih brodskih sustava*; Qualification paper, FESB, 2014

STRAIN ANALYSIS OF CORD-RUBBER COMPOSITES USING DIC

Thomas LEHMANN[1], Jörn IHLEMANN[1]

[1] Chemnitz University of Technology, Professorship of Solid Mechanics, Reichenhainer Straße 70, 09126 Chemnitz, Germany, E-mail: thomas.lehmann@mb.tu-chemnitz.de

1. Introduction

Cord-rubber composites are applied in various technical applications, e.g. tires, sleeves, air springs and belts. The development of such components include numerical simulations, which require the knowledge of the material's characteristic described by suitable material models with respective material parameters [1]. Therefore, experimental tests for material characterization, parameter identification as well as validation of numerical models are necessary. Stressing of cord reinforced elastomers can result in strong inhomogeneous stress and strain fields. The experimental detection of the resulting large strain gradients requires high-performance measuring methods. In this contribution, 3D Digital Image Correlation (DIC) is used to determine the 3D coordinates, followed by the evaluation of strain fields on the surface of cord reinforced rubber specimens by means of a postprocessing procedure.

2. Experimental setup, procedure

Experiments were carried out using specimens with rubber matrix material (special composition of Vibracoustic AG & Co. KG) variable reinforced by polyamide cords, aramid cords or hybrid cords (consisting of polyamide and aramid yarns) with the cord angles φ of 10° and 35°. The geometry of the specimen was designed as a sleeve with the nominal dimensions: inner diameter 95 mm, sleeve thickness 1.5 mm, initial free length 75 mm. The specimen is clamped at the top and bottom sides, see Fig. 1. In order to visualize maximum strain differences on the surface of the specimens, a configuration without elastomer top layer was used. The experiments were performed in a servohydraulic test rig, which can be used for tension, compression and torsion tests, at Helmut-Schmidt-Universität / Universität der Bundeswehr Hamburg, see Fig. 1. The first step of the test procedure was the application of an initial inner pressure of 1 bar. Subsequent, axial compression in steps of 10 mm until $s = 50$ mm (nominal values) with following torsion by $\alpha = \pm 1°$ in every compression step was performed. The inner pressure was kept constant during the whole tests. An example of a loaded specimen is given in Fig. 2.

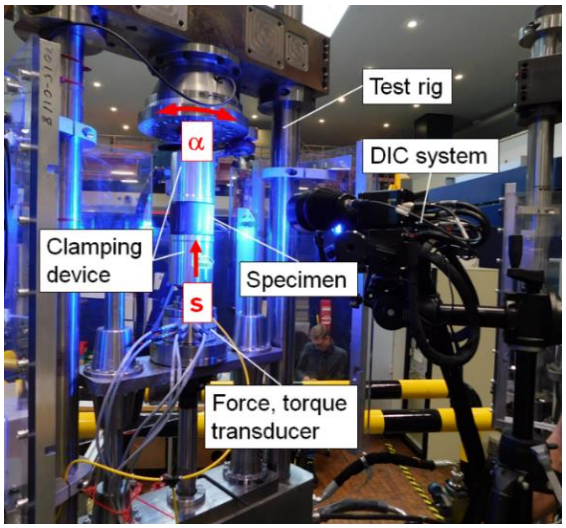

Fig. 1. Experimental setup of the tests.

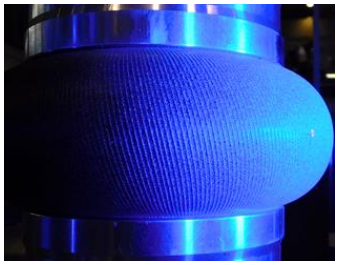

Fig. 2. Loaded specimen (cord angle 10°).

In the presented investigations, the 3D DIC system Gom Aramis 4M was applied using a small measuring volume with horizontal and vertical dimensions of 25x18 mm (nominal values). The specimens were coated with the required fine speckle patterns by means of white paint (achieving enough contrast to the dark surface of the specimens). Considering the limited depth of field using the small measuring volume, an out-of-plane-tracking of the cameras was performed since significant displacements of the analyzed section in this direction occured. This adaption was carried out in the respective loading steps to get well-focused images for the DIC. For strain evaluation, the 3D coordinates determined by DIC were used.

3. Evaluation method

Strains regarding tangential directions of the surface based on the 3D coordinates were calculated by means of a developed evaluation procedure using Matlab. Hereinafter, $\tilde{\mathbf{u}}$ and $\tilde{\mathbf{v}}$ (see Fig. 3) represent the local directions of curvilinear coordinate lines on the curved surface in the reference state. The DIC data was approximated by B-spline surfaces [2],[3]. The two-dimensional deformation gradient **F** regarding the tangential directions, which is calculated considering the curved geometry in the reference and the deformed state, was determined using the approximated spline functions of the 3D coordinates. As a strain measure, the Langrangian Hencky strain tensor was determined, which is given by:

$$\mathbf{H} = 0.5 \ln \left(\mathbf{F}^{\mathrm{T}} \mathbf{F} \right). \tag{1}$$

Furthermore, the Green-Langrange strain tensor (based on the deformation gradient **F** and the identity tensor **I)** is calculated by:

$$\boldsymbol{\gamma} = 0.5 \left(\mathbf{F}^{\mathrm{T}} \mathbf{F} - \mathbf{I} \right). \tag{2}$$

Calculating $\boldsymbol{\gamma}$ for transformed (rotated) evaluation directions ($\tilde{\boldsymbol{\xi}}$, $\tilde{\boldsymbol{\eta}}$, see Fig. 3) following the orientation of cord reinforcement (by angle φ, reference state), the shear angle $\theta_{\xi\eta}$ regarding these transformed directions is determined using:

$$\theta_{\xi\eta} = \arcsin \left(\frac{2\gamma_{\xi\eta}}{\sqrt{1+2\gamma_{\xi\xi}}\sqrt{1+2\gamma_{\eta\eta}}} \right). \tag{3}$$

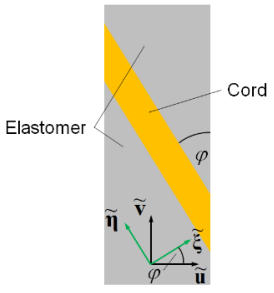

Fig. 3. Evaluation directions.

4. Results

In Fig. 4, an example of the evaluation for the maximum load step (without torsion) for polyamide reinforced rubber, cord angle 35° is given. At the left side the Hencky strain H_{uu} is shown. Large strain differences between cord and elastomer sections are well detected, where the strain in the cords is approximately zero. In addition, the distribution of the shear angle $\theta_{\xi\eta}$ is demonstrated (Fig. 4, right). The evaluation shows that the shear deformation is concentrated in the elastomer sections.

Furthermore, the actual direction of the elastomer and the cord sections can be reconstructed by means of the distribution of the deformations.

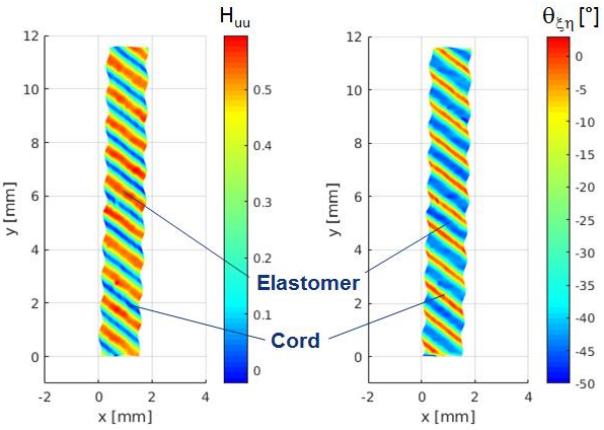

Fig. 4. H_{uu} (left) and $\theta_{\xi\eta}$ (right) (strip at the specimen's middle), axial compression of s = 47.7 mm.

5. Conclusions

Special sleeve specimens of cord-rubber composites were loaded by inner pressure, compression and torsion. In order to achieve a data base for validation of numerical simulations, experimental deformation analyses of the specimen surfaces were carried out. By means of 3D DIC and a special evaluation procedure, the challenging detection of the resulting large strain differences was successfully performed. As expected, the deformations are concentrated in the elastomer sections.

Acknowledgements

The authors gratefully acknowledge the financial support from ContiTech AG, Mehler Engineered Products GmbH, Goodyear S.A. and Vibracoustic AG & Co. KG.

References

[1] Donner, H. *FEM-basierte Modellierung stark anisotroper Hybridcord-Elastomer-Verbunde*, PhD Thesis, 2017.
[2] Hoschek, J., Lasser, D. *Grundlagen der geometrischen Datenverarbeitung*, second ed., Teubner, Stuttgart, 1992.
[3] Lehmann, T., Müller, J., Ihlemann, J. DIC deformation analyses of Mg specimens at elevated temperatures, *Mater. Today-Proc.*, 2018, 5, 26778–26783.

INFLUENCE OF IRON CONTENT ON MECHANICAL PROPERTIES OF SECONDARY AlZn$_{10}$Si$_8$Mg CAST ALLOY

Denisa MEDVECKÁ[1], Eva TILLOVÁ[1], Lenka KUCHARIKOVÁ[1], Mária CHALUPOVÁ[1], Denisa ZAVODSKÁ[1], Alan VAŠKO[1]

[1] University of Žilina, Faculty of Mechanical Engineering, Univerzitná 8215/1, 010 26 Žilina, Slovakia, E-mail: denisa.medvecka@fstroj.uniza.sk

1. Introduction

Commercial secondary (recycled) Al-alloys always contain Fe, often as undesirable impurity and occasionally as a useful minor alloying element. Depending on the quality of the incoming ore and the control of the various processing parameters and other raw materials, molten primary Al-metal typically contains between 0.02 - 0.15 wt. % iron, with ~ 0.07 - 0.10 % being average. Secondary Al-alloys (produced from Al-scrap) contains higher background iron levels than the primary metal. In an amount 0.3 - 0.5 wt. % of Fe, it prevents sticking casting on the metal mould (for casting under pressure), increases the strength and in larger quantities also the heat resistant. At higher contents, as 0.3 - 0.5 wt. % of Fe, it causes first of all formation of Fe-intermetallic phases [1].

The more important are α- $Al_{15}FeMn_3Si_2$ (with skeleton-like or Chinese script morphology) and β-Al_5FeSi phases (with needle/plate like morphology). The Al_5FeSi phase is mostly associated with greater iron levels, roughly the location of the eutectic trough on the Al-Si-Fe phase diagram. The β-Al_5FeSi phase is considered the most critical among the Fe-intermetallic, as it significantly reduces the alloy ductility and fracture toughness. Existing in the form of thin and brittle platelets that appear as needles in the microstructure, the size of these β-platelets or needles is controlled by the Fe-content and the solidification conditions of the alloy. In comparison, the α-iron phase, due to its compact morphology, is less harmful to the mechanical properties. Metallographic studies have shown that pores are nucleated along the long sides of the β-platelets. However, in spite of the harmful effect of these Al_5FeSi-platelets as pore nucleation sites, their presence also appears to limit pore growth. The size and density of Fe-based intermetallic phases are increased with increasing % of Fe, also the dimensions of the defects and porosity of casting. The higher content of Fe causes a negative influence to the strength and the plastic properties, and the corrosion resistant [2-3]. Control of the iron level is thus technically important, especially where the production of critical components is concerned.

Cast Al-Zn-Si-Mg has been developed in the recent years as a new generation of Al-alloy for automobile industry. The present study is a part of larger research project, which was conducted to investigate and to provide better understanding properties of secondary (recycled) Al-Si cast alloys. The main objective of this work was to study the effect of Fe-content on mechanical properties and fracture surface in self-hardening AlZn10Si8MgMn alloy.

2. Materials and methodology

The materials used in experiment were secondary (scrap-based, recycled) AlZn10Si8Mg cast alloys with different percentage of Fe (alloy A - 0.150 and alloy B - 0.559 wt. %). From AlZn10Si8Mg ingots were produced test bars (ø 20 mm with length 300 mm), by process of sand casting. Chemical composition of the alloys is given in Tab. 1.

Table 1. The chemical composition of AlZn10Si8Mg cast alloys in wt. %

Alloy	Si	Zn	Fe	Mg	Ti	Al
A	8.64	9.60	0.15	0.45	0.062	rest
B	8.83	9.30	0.56	0.32	0.050	rest
In alloys A, B: Cu (0.005); Ni (0.0022); Bi (0.0003); Sb(0.0007)						

The measurement of mechanical properties (YTS, UTS, ductility) was obtained after tensile tests at room temperature. The Brinell hardness test (HBS 5/250) was performed using a 5 mm diameter hard-metal ball pressed with a force of 250 kp for 10 seconds. Samples for metallographic analysis were chosen from cast specimen after tensile tests. The samples were etched by 0.5 %

HF. The fracture surface was observed and documentted on SEM.

The microstructures of alloys A and B are the same and consist of α-phase, eutectic and variously type's intermetallic phases (Mg_2Si, Al_5FeSi and Al-$MgZn_2$-Cu). In alloy A (0.15 % of Fe) compared to the alloy B (0.56 % of Fe) it is visible that eutectic silicon has a slightly coarser structure on the edge in α-phase and the Al_5FeSi needles are shorter and thinner (Fig. 1).

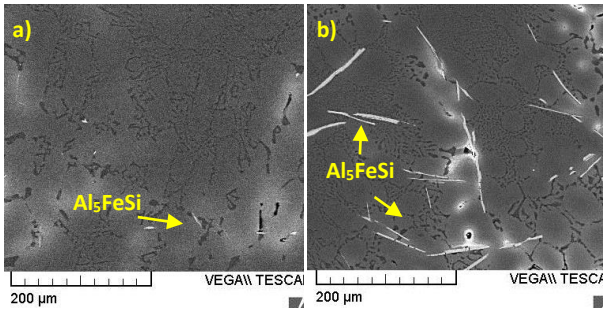

Fig. 1. Microstructure of AlZn10Si8Mg cast alloys: a) 0.15 % Fe; b) 0.56 % Fe.

3. Results

The cooling rate represents an important parameter which affects SDAS factor (secondary dendrite arm spacing), eutectic Si morphology and dimensions. For alloy A was measured SDAS = 59 µm and 51 µm for alloy B. As cooling rate increased SDAS values decreases, because of the higher undercooling and for faster movement of solid-liqiud interface. As cooling rate increases, the size of the Si particles became smaller and an important variation of the Si morphology has been observed - fine Si-bars.

Results from tensile tests are summarized in Fig. 2. The mechanical properties of alloy A and alloy B are not very different, but there is a decrease in alloy B in yield tensile strength (YTS) by 9 MPa and in ultimate tensile strength (UTS) by 10 MPa, it is 5.23 % decrease. Ductility has not changed. The results of Brinell hardness shown that with increasing iron content increase the hardness from 83 HB to 89 HB (+3.60 %). Needle-shaped edges and formation of sharp corners of Al_5FeSi phase reduced maximum yield tensile strength and UTS, but no markedly. Brittle phase cut the matrix and produced stress concentration and thus degrades the mechanical properties. Even though the values of YTS and UTS in alloys A and B are not different significantly, it can be seen, that character of the fracture surface after tensile tests is different.

The fracture surface was influenced very significantly by structural components and their distribution in the crosssection. The fracture surface of exp. samples in alloy A consists of transcrystalline ductile fracture. Cleavage fracture (related to the presence of hard and brittle Al_5FeSi phases) was observed not much. The ductile fracture on the eutectic and on the Al-matrix region is dominant; because Si-particles have fine bars morphology and Fe-rich phases are little and short. In alloy B transcrystalline cleavage fracture is dominant. Cleavage fracture is related to the presence of larger number of hard and brittle Fe-phases in the structure. The transcrystalline ductile fracture of Al-matrix (α-phase) is observed in the smaller surface, despite the fact that the Al-Si alloys are breaking exclusively by transcrystalline ductile fracture.

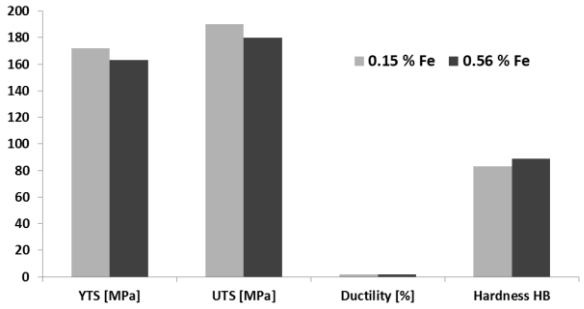

Fig. 2. Effect of Fe-content on mechanical properties.

4. Conclusions

All new contributions of the authors of the paper should be summarized briefly in the concluding remarks.

Acknowledgements

This study has been supported by projects VEGA 1/0398/19 and KEGA 049ŽU-4/2017.

References

[1] Schlesinger, M. E. *Aluminum Recycling*. 2nd ed. CRC Press: Boca Raton, 2013.
[2] Samuel, E. et all. Intermetallic phases in Al-Si based cast alloys: new perspective. *International Journal of Cast Metals Research*, 2014, 27(2), 107-114.
[3] Tillová, E., Chalupová, M., Kuchariková, L., Belan, J. Impact properties of self-hardening aluminium alloy (AlZn10Si8Mg) at elevated temperatures. *Manufacturing technology*, 2015, 15(4), 720-727.
[4] Kuchariková, L., Tillová, E. Elimination of the negative effect of Fe-rich intermetallic phases in secondary (recycled) aluminium cast alloy. *Manufacturing technology*, 2013, 13(1), 44-50.

SIMPLE CALIBRATION METHOD OF MIXED, STRAIN-STRESS FAILURE CRITERION FOR DUCTILE MATERIALS

Grzegorz SOCHA[1]

[1] Institute of Aviation, Al. Krakowska 110/114, Warsaw, Poland, E-mail: grzegorz.socha@ilot.edu.pl

1. Introduction

Many failure criteria for ductile materials were proposed by researchers. A good review of the most frequently used criteria was given in [1]. Seven criteria mentioned in this paper were formulated in the space of stress, strain or mixed strain-stress. The most popular one for ductile materials (i.e. most of metal alloys) is constant equivalent stress criterion and its popularity can be attributed to simplicity of calibration and availability of the material data. On the other side this criterion is in conflict with well-known phenomenon described in the beginning of 20th century [2] that can be expressed in the following way: the ability of achieving permanent deformation is influenced by stress state. This experimental observation can be taken into account only in the case of mixed strain-stress criterions like, for example, widely used Johnson criterion [3]. The problem with this and other mixed criteria is that its calibration for particular material requires complicated testing associated by sophisticated computer simulations (see paper [1]). Moreover, as it was reported in this paper, result of the proposed procedure is questionable due to fact that during reported experiments stress state (or stress triaxiality) changes with progressing deformation due to evolution of the specimen gage part geometry and localization of strain. In spite of this it seems obvious that the use of particular form of failure criterion is limited by ease and credibility of calibration method.

2. Criterion and the calibration method

Thera are many definitions of mixed strain - stress criteria for ductile materials. Already mentioned Johnson – Cook criterion can be written in following form:

$$\bar{\varepsilon}_f = C_1 + C_2 \exp\left(C_3 \eta\right) \tag{1}$$

, where ε_f is the failure strain intensity and η is the stress triaxiality factor (ratio of first and second stress tensor invariants). This criterion was proved to fit well experimental data, but its calibration requires determination of three coefficients (at least three points on the ε_f- η plane have to be determined under three different stress states).

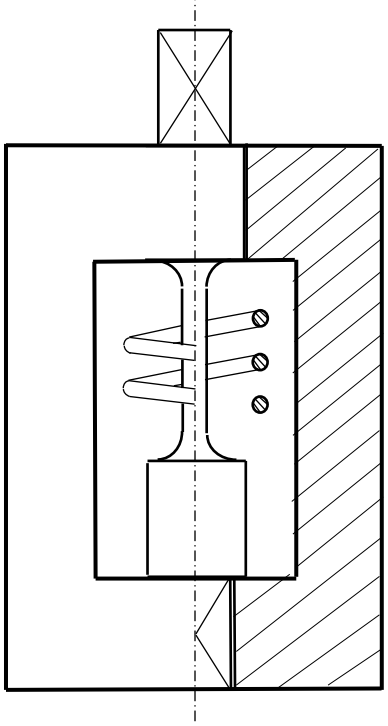

Fig. 1. Fixture for determination of failure strain intensity.

Simplified version of this criterion was given in earlier paper [4] in the following form:

$$\bar{\varepsilon}_f = \alpha e^{-\frac{3}{2}\eta} \tag{2}$$

Calibration of this criterion requires determination of only one coefficient α. This form of the criterion may not fit experimental data as well as Johnson – Cook criterion (1), but is far easier to calibrate and still stress-state sensitive. The easiest stress state to

be produced to determine failure strain intensity is pure shear. For this stress state $\eta = 0$ and failure strain intensity value is equal to value of coefficient α.

In patent description [5] a method and accessory for calibration of the failure criterion in the form of equation (2) was given. Fixture shown in figure 1 is proposed to be used for calibration of that criterion at room and elevated temperatures. Test setup consist of constrained yoke with inductive coil for material heating inside. Specimen inserted in that yoke is heated to achieve required temperature and then twisted to rupture using some kind of hand tool (testing machine is not required to perform this test). The only result of the procedure is angle of twist, that can be easily re-calculated into failure shear strain and finally into failure strain intensity.

Fig. 2. Specimen after test.

The specimen after test is shown in figure 2. It can be seen that no strain localization changing stress state at the surface of the specimen occurs during test. It means that the stress state at the surface of the gage part of the specimen was kept constant and uniform during all the deformation process from beginning to failure and it can be described as the pure shear in the plane stress state. So, for all the deformation process stress triaxiality factor $\eta=0$ and the value of coefficient α equal to strain intensity at failure was determined credibly.

For the material of specimen shown in figure 2 (alloy steel), angle of twist of the gage part measured using microscope was found to be φ = 8,792 rad. For the geometry of the specimen used, shear strain angle is:

$$\gamma = \varphi \frac{r}{l} = 1{,}08\, rad \qquad (3)$$

, and the failure strain intensity

$$\bar{\varepsilon}^f = \frac{\sqrt{2}}{3}\sqrt{\frac{3}{2}\gamma^2} = 0{,}622\, mm/mm. \qquad (4)$$

So, finally failure condition for the alloy in question takes form:

$$\bar{\varepsilon}^f = 0{,}622^{-\frac{3}{2}\eta}. \qquad (5)$$

Conclusions

Simple method and accessory for the calibration of mixed strain-stress failure criterion (2) was presented in this paper. Patented fixture [5] allows determination of failure strain intensity for all the stress states and wide range of temperatures without the use of sophisticated testing equipment (testing machine, specialized transducers). One of the most important advantages of proposed method is fact that the applied loading scheme allows to keep the same stress state at the surface of the gage part – experiment is performed for constant value of stress triaxiality factor η from the beginning of deformation to material failure.

References

[1] Wierzbicki T. et al., Calibration and evaluation of seven fracture models, *International Journal of Mechanical Sciences, Vol.47, pp. 719-743, 2005*
[2] Odqvist F. K. G., Die Verfestigung von flusseisenaehlichen Koerpern, *ZAMM 13, 1933*
[3] Johnson G. R., Materials Characterization for computations involving severe dynamic loading, *Proc. Army Symp. Of Solid Mechanics, pp. 62-67, Cape Cod, Mass., 1980*
[4] Hancock J.W., Mackenzie A.C. On the mechanisms of ductile failure in high-strength steels subjected to multi-axial stress-states, *J. Mech. Phys. Solids, Vol.24, pp.147-169, 1976*
[5] Socha G., A method and accessory for determination of failure strain for ductile materials subject to arbitrary stress state in the wide range of temperatures, *Polish Patent Office, patent pending 77P43754 PL00*

THE DAMAGE DEPTH EVALUATION BASED ON THE ACTIVE IR THERMOGRAPHY

Petra BAGAVAC[1], Lovre KRSTULOVIĆ-OPARA[1], Željko DOMAZET[1]

[1] Faculty of Electrical Engineering, Mechanical Engineering and Naval Architecture, R. Boškovića 32 21 000 Split, Croatia, E-mail: petra.bagavac@fesb.hr , opara@fesb.hr , domazet@fesb.hr

1. Introduction

Active infrared thermography is a NDT method capable of locating indications and damage in composites and metals. There are numerous approaches how to locate damage, but precise detection of depth was always an issue. A damage is fully described by its geometry and depth. Determination of damage geometry, based on thermal contrast between cooling curves of observed surface, is described in earlier work. Thermal contrast is the difference between the thermal properties of the observed material and the damage. Method of depth evaluation is demonstrated on an aluminum plate, where damage is simulated as Flat Bottom Holes (FBH) of different diameters, fig. 1.

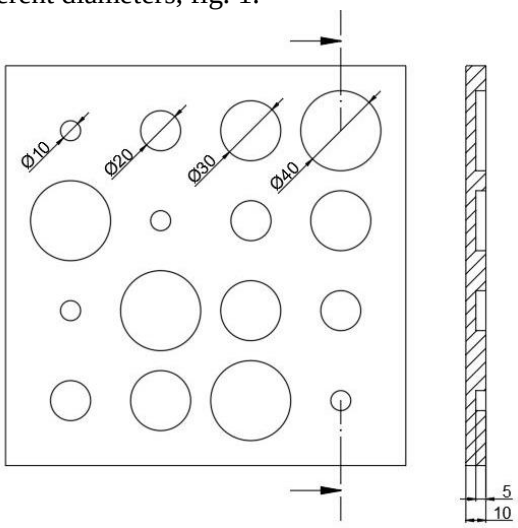

Fig. 1. Aluminum sample geometry

Aluminum, like all metals, is excellent heat conductor. IRNDT (InfraRed Nondestructive Testing) is possible on metal materials only with fast frame rate cameras and heat source with short and intensive heating period. Experimental setup included cooled middle wave InSb thermal camera and strong Xenon flesh lamp (releasing 6000J in 1/440 seconds), followed by signal postprocessing techniques.

2. Signal Reconstruction

To avoid reflections of surrounding objects and to reduce the signal to noise ratio of the camera FPA (Focal Plane Array) detector, postprocessing of the received signal (cooling curves) is needed [1, 2]. Fig. 2. shows the raw data of a single pixel cooling curve (blue line) and corresponding fitted curve (red line). Temperature cooling profiles for each pixel are fitted with the following logarithmic function:

$$\ln[T(t)] = \sum_{n=0}^{N} a_n [\ln(t)]^n \qquad (1)$$

$$T(t) = \exp\left(\sum_{n=0}^{N} a_n [\ln(t)]^n\right) \qquad (2)$$

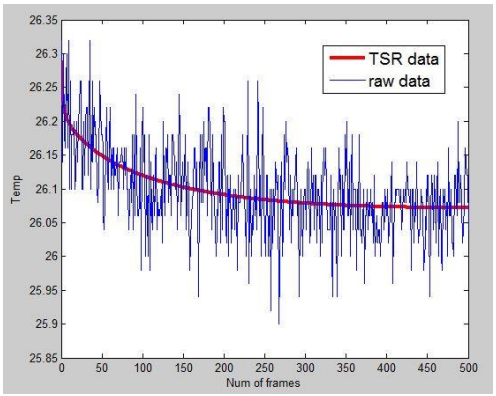

Fig. 2. Raw data and fitted data curve

Fitted data is processed by the Fast Fourier Transform (FFT) [3, 4], whereby the time domain is transferred to the frequency domain.

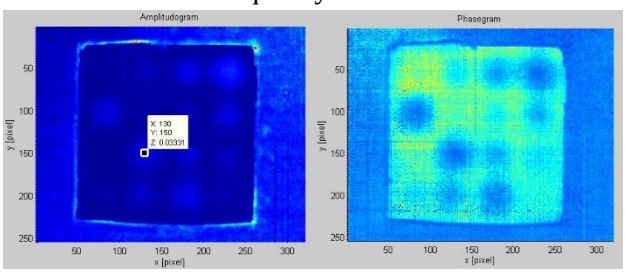

Fig. 3 a) Amplitude image and b) phase image

Damage geometry is visible in the amplitude image (fig. 3.a) and the phase image (fig. 3.b) of the aluminum sample.

3. Depth Estimation

In the frequency domain, blind frequency is the frequency at which there is no phase contrast between the the damaged zone and surrounding sane material.

$$\Delta f = \frac{1}{N_{tot} * \frac{1}{f_s}} \tag{3}$$

$$f_b = N * \Delta f \tag{4}$$

where N_{tot} is total number of thermal images in sequence, f_s is acquisition frequency, f_b is blind frequency and N is the number of thermogram on the frequency axis at which there is no phase contrast.

The damage depth can be estimated from the blind frequency as [5]:

$$z_{estimated} = 1.81 \sqrt{\frac{\alpha_{diff}}{\pi * f_b}} \tag{5}$$

where α_{diff} is thermal diffusivity. This value describes how quickly a material reacts to the change in temperature. The thermal diffusivity was determined by the infrared thermography based on the Flash diffusivity method [6]. Experimentally obtained value was is in good correspondence to the tabular values, so this method is proposed for determination the heat diffusion coefficient for composites and other anisotropic materials.

4. Results and Conclusions

Blind frequency is determined as the intersection of the phase curve for damaged zone pixel (drilled hole) and neighboring sane zone pixel (wall), Fig. 4.

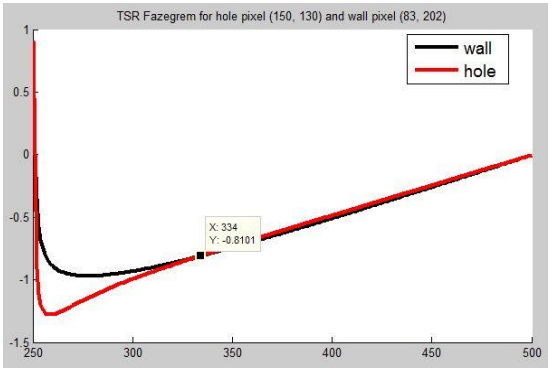

Fig. 4. FFT phase values for different frequencies

From such estimated blind frequencies and relations (3-5), depths of evaluated flat bottom holes are summarized in Table 1.

Table 1. Estimated depths of FBH defects

Pixel (x, y)	z_{true_value} [mm]	$N_{\Delta f}$	f_b [Hz]	$z_{estimated}$ [mm]
1 (150, 130)	5	84	4.2	4.8516
2 (230, 50)	5	82	4.1	4.9104
3 (80, 100)	5	85	4.25	4.8230

This method slightly underestimates the depth at which defects are found. The authors agree that this underestimation is result of the extremely rapid heat dissipation in the aluminum. We expect that the method will give more accurate results for defects in materials with lower thermal diffusion, such as composites.

References

[1] Ibarra-Castanedo C., Tarpani J. R., Maldague X. P. V. *Nondestructive testing with thermography.* Eur. J. Phys, 2013, 34, 91-109.

[2] J.M. Roche, D. Balageas. *Common tools for quantitative pulse and step-heating thermography-Part II: experimental validation.* The 12th International Conference on Quantitative InfraRed Thermography (QIRT 2014), Jul 2014, BORDEAUX, France.

[3] Umar M. Z., Ahmad I., Vavilov V., Swiderski W., Hamzah A. R. Abdullah W. S. *Developing Methodology of Pulsed Thermal NDT of Materials: Step-by-step Analysis of Reference Samples.* Journal of Nondestructive Testing, 2008.

[4] Ibarra-Castanedo C., Gonzales D., Galmiche F., Maldaque X. P., Bendada A. *Discrete signal transforms as a tool for processing and analyzing pulsed thermographic data*. In *Thermosense XXVIII vol. 6205, Defense and Security Symposium*, Florida, United States, 2006; Miles J. J., Peacock G. R., Knettel K. M., Eds: Procedures of SPIE, 2006.

[5] Ibarra-Castanedo C., Maldaque X. P. *Defect Depth Retrieval from Pulsed Phase Thermographic Data on Plexiglas and Aluminum Samples.* In *Thermosense XXVI vol. 5405, Defense and Security Symposium*, Florida, United States, 2006; Burleigh D. D., Cramer K. E., Peacock G. R., Eds: Procedures of SPIE, 2004.

[6] Meola C., Carlomagno G. M., Squillace A., Prisco U., Morace R. E. *Analysis of Composites with Infrared Themography*. Macromol. Symp. 2005, 228, 273-286.

VALIDATION METHOD FOR THICKNESS VARIATION OF THERMOPLASTIC MICROCELLULAR FOAMS USING PUNCH TESTS

Szabolcs BEREZVAI[1], Attila KOSSA[2], Adam K. KISS[3]

[1] Budapest University of Technology and Economics, Department of Applied Mechanics, H-1111 Műegyetem rkp. 3, Budapest, Hungary, E-mail: berezvai@mm.bme.hu

[2] Budapest University of Technology and Economics, Department of Applied Mechanics, H-1111 Műegyetem rkp. 3, Budapest, Hungary, E-mail: kossa@mm.bme.hu

[3] Budapest University of Technology and Economics, Department of Applied Mechanics, H-1111 Műegyetem rkp. 3, Budapest, Hungary, E-mail: kiss_a@mm.bme.hu

1. Introduction

Thermoforming is a commonly applied industrial process, in which the thermoplastic polymer sheet is heated above its glass transition temperature and gets stretched [1]. In the industry, there is significant need for the proper characterization of thermoplastic materials for developing accurate finite element (FE) simulations in order to predict and accelerate the whole production process [1]. During the forming procedure the material undergoes large and nonlinear deformations which have temperature dependent viscous-elastic-plastic properties [1,3]. In the literature the available constitutive models usually consist of parallel viscoelastic and viscoplastic branches like the two-layer viscoplastic model or the models in the PolyUMod library [2,3].

One of the key factors that characterize final shape of the part is thickness variation. However, the material characterization process is usually based on uniaxial measurements including creep, relaxation and cyclic tests performed at several temperatures. Therefore, the applicability of the fitted model is required to be validated with measurements by means of compare the thickness variation under biaxial load case.

In this contribution, we present a punch-test based on validation procedure via the case study of a thermoplastic microcellular polyethylene-terephthalate (MC-PET) foam material. In the proposed method the thickness variation is investigated both experimentally and numerically, by means of laser scanning method and FE simulations, respectively.

2. Punch tests

The schematics of the axisymmetric punch-test measurement is presented in Fig. 1. A piece of a raw MC-PET material sheet with dimensions of 75×75 mm and thickness of 0.94 mm was placed in a special fixture mounted in Zwick Z010 Testing System equipped with temperature chamber. The displacement-based loading consists of three parts: uploading with crosshead speed of 500 mm/min, relaxation for 30 s and unloading with 100 mm/min. Figure 2 illustrates the experimental punch test data at 10 different temperatures between 21°C and 210°C.

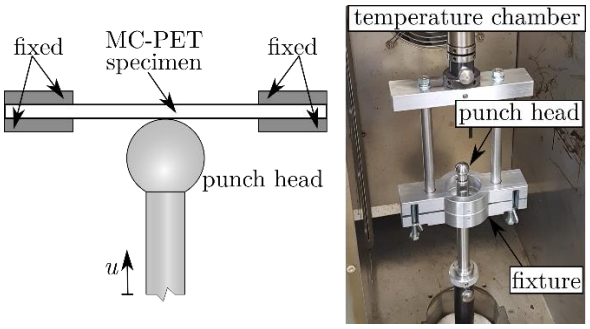

Fig. 1. Measurement layout of the punch test.

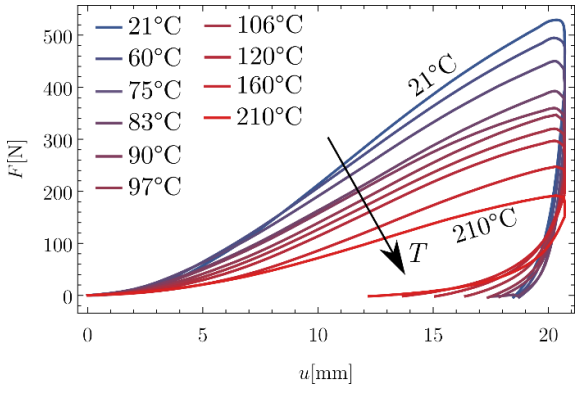

Fig. 2. The measured force-displacement characteristics in case of punch tests with spherical head.

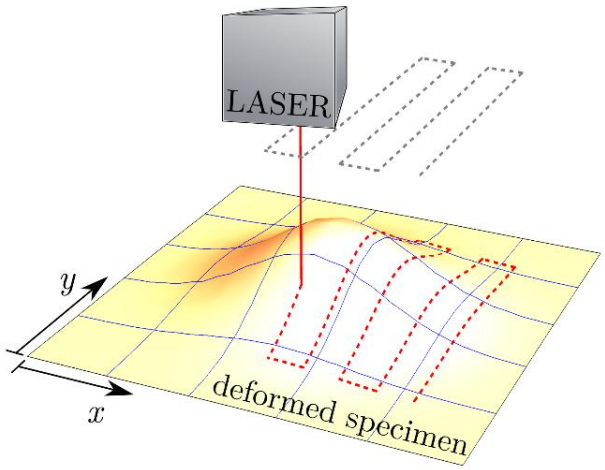

Fig. 3. Schematics of the deformed surface detection using laser scanner.

3. Surface detection

As the punch-tests were performed, the deformed specimens were placed in an NCT EmR-610Ms CNC milling machine, where the top and the bottom surfaces were scanned using a KEYENCE IL-030 Laser Differentiation Displacement Sensor using a predefined zig-zag path as shown in Fig. 3 (for further details of the laser system see [4]). After the synchronization of the time signal of the distance variation recorded by the Laser sensor and the position data provided by the CNC machine, the point clouds corresponding to both top and bottom surfaces of the deformed shape were obtained. Based on the scanned surfaces the sheet thickness variation could be determined along the surface and evaluated along the symmetry axes.

4. Model prediction using FE simulation

As a next step, in order to validate the accuracy of the applied material model, the previously determined thickness variation data were compared to the FE simulation of the punch-test in the commercial software ABAQUS [5].

In this case study, the MC-PET material was characterized by the two-layer viscoplastic (TLVP) model assuming nonlinear strain-hardening creep law and linear isotropic hardening yield stress. The parameters were obtained using inverse FE-based parameter fitting procedure (see [2]) by linking ABAQUS [5] with the optimization software Isight [6]. The comparison of the measured thickness variation and the FE simulation results is presented in Fig. 4.

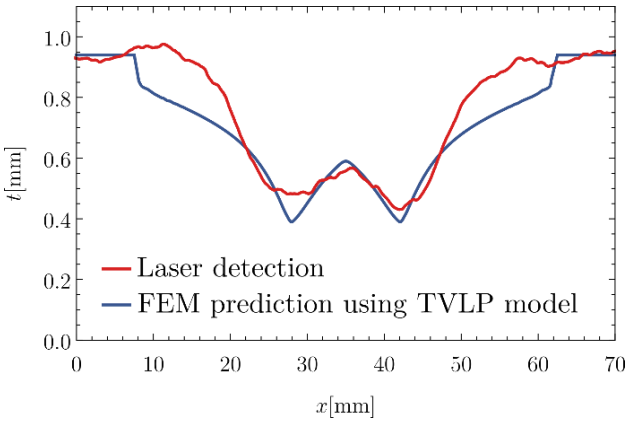

Fig. 4. Variation of the thickness obtained by FE prediction and laser measurement a T=60°C.

5. Conclusions

In this contribution an experimental validation method is proposed for thickness variation of thermoplastic materials using punch-tests and laser scanning technique. In case of the investigated MC-PET material, the comparison of the thickness variation obtained by FE prediction and the laser scanning method are in good agreement close to the punch head. A bit further, however, the discrepancy becomes more significant. Additionally, the results also revealed that the applied TLVP model is able to model the material behaviour in biaxial stress-state with adequate accuracy.

Acknowledgements

This research was supported by the János Bolyai Research Scholarship of the Hungarian Academy of Sciences. The MC-PET foam specimens were provided by Furukawa Electric Institute of Technology Ltd., Hungary. These supports are gratefully acknowledged.

References

[1] Klein, P. W. *Fundamentals of Plastics Thermoforming*; Morgan & Claypool: Boca Raton, 2009.
[2] Berezvai, S., Kossa, A. Characterization of a thermoplastic foam material with the two-layer viscoplastic model. *Mater Today-Proc*, 2017, 4(5), 5749-5754.
[3] Bergström, J. *Mechanics of Solid Polymers*, William Andrew, 2015
[4] Kiss, K. A, Bachrathy, D., Stepan, G. Laser scanned patterns of machined surfaces. *Proc CIRP*, 2018, 77, 355-358.
[5] ABAQUS 2019, Dassault Systèmes, Simulia Corporation, Providence, Rhode Island, USA
[6] ISIGHT 2019, Dassault Systèmes, Simulia Corporation, Providence, Rhode Island, USA

EXPERIMENTAL INVESTIGATION OF THE DEPENDENCE OF THE VISCOELASTIC PROPERTIES OF POLYAMIDE 6 ON TEMPERATURE AND HUMIDITY

Robert KIEßLING[1], Jörn IHLEMANN[1]

[1] Chair of Solid Mechanics, Chemnitz University of Technology, Reichenhainer Straße 70, 09126 Chemnitz, Germany, E-mail: robert.kiessling@mb.tu-chemnitz.de

1. Introduction

Environmental influences, like humidity and temperature, strongly affect the mechanical behaviour of polymers (see, for example, [1]). Consequently, this dependence has to be considered within the dimensioning of structural parts made of such materials. This contribution addresses the experimental investigation of the viscoelastic properties of Polyamide 6 under the influence of humidity and temperature. Besides that, first aspects of the development of an appropriate material model are presented.

2. Experimental setup

Aiming for the characterization of the viscoelastic behavior of Polyamide 6, uniaxial relaxation tests are carried out. To investigate the influence of the temperature, the applied 20kN testing machine by Zwick/Roell is extended by a temperature chamber. This temperature chamber enables the heating of the specimen due to the integrated heating elements as well as the cooling of the specimen by fluid nitrogen. Here, specimens with dimensions of 80mm x 10mm x 4mm, made from BASF Ultramid B40 (Polyamide 6) by injections molding, are utilized. To fulfill the requirements from the automotive industry, the tests are conducted in a temperature range from -20°C to 60°C. Within these relaxation tests, the temperature is measured by a thermocouple, which is mounted at the specimen. Additional to the temperature, the influence of the humidity on the mechanical behavior is analyzed. To this end, the specimens are conditioned in a water bath of 80°C. Depending on the duration of the conditioning, different moisture contents are adjusted. To measure the resulting moisture content, Karl Fischer titration is applied. Consequently, specimens with different moisture contents can be tested in the defined temperature range and the dependence of the viscoelastic behavior on temperature as well as on humidity can be investigated experimentally.

3. Experimental results

Applying the described experimental setup, the relaxation tests are conducted for four different moisture contents at seven different temperatures. Each relaxation test is repeated at least three times. Within these relaxation tests, the traverse is initially proceed about 0.75 mm with a speed of 200 mm/min. After a specific strain value has been reached, the strain ε, measured by an extensometer, is kept constant for 550s. During the whole testing, the required force F is detected by the load cell of the testing machine. Fig. 1 shows the averaged results of the relaxation tests performed with the specimens having the cross section area A. Here, the modulus

$$E(t) = \frac{T(t)}{\varepsilon(t)} = \frac{F(t)}{A\,\varepsilon(t)} \qquad (1)$$

is plotted over the time t. With respect to the shown experimental results, the influence of temperature and humidity on the viscoelastic behaviour of the investigated polymer can be identified. Generally, the polymer will be more compliant if the temperature is increased. Furthermore, the relaxation time will reduce. A similar effect can be observed for the moisture content. The lower the moisture content is, the stiffer the polymer is. Furthermore, the relaxation time will increase, if the polymer is drier.

4. Aspects of the development of an appropriate material model

To consider the characterised behaviour, for example, within a finite element simulation, an appropriate material model has to be developed. For this purpose, a concept by [2], which enables material modelling at large strains based on directly connected rheological elements, can be applied. According to this concept, a material model is derived from a rheological model. Here, a generalized Maxwell model can be utilized to

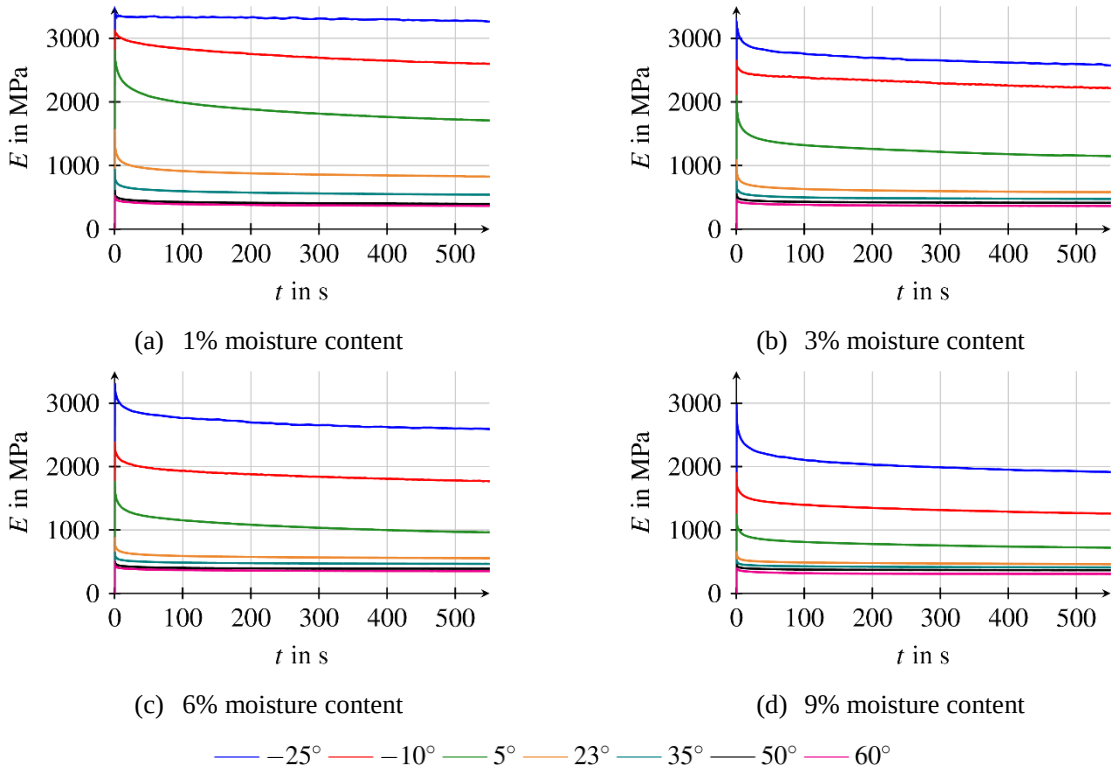

Fig. 1. Results of the performed relaxation tests.

formulate an appropriate material model. As shown in Fig. 2, a generalized Maxwell model consists of a parallel connection of an elastic element with an appropriate number of Maxwell models, i.e. series connections of an elastic element and a viscous element. With respect to this rheological model, a material model at large strains is formulated and implemented. Afterwards, a set of material parameters is identified from each relaxation test, which was carried out for a certain moisture content at a specific temperature. Based on these data, a set of material parameters for a combination of moisture content and temperature, which has not been characterized experimentally, can be determined by interpolation.

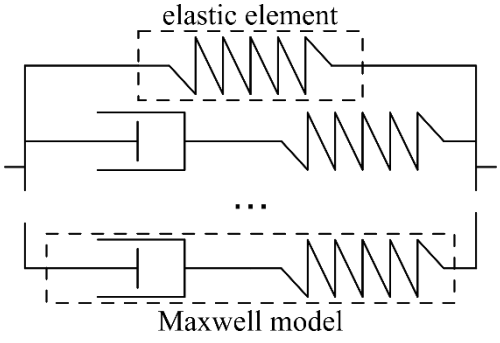

Fig. 2. Generalized Maxwell model.

5. Conclusion and prospect

Within this contribution, the influence of humidity and temperature on the viscoelasticity of Polyamide 6 was investigated experimentally. To this end, relaxation tests at specific temperatures were carried out. Thereby, specimens with different moisture contents were examined. Finally, aspects dealing with the formulation of an appropriate material model were presented.

Acknowledgements

This research was supported by the German National Science Foundation (DFG) within the Priority Program 1712.

References

[1] Rösler, J., Bäker, M., Harders, H. *Mechanical Behaviour of Engineering Materials*; Springer-Verlag: Berlin Heidelberg, 2007.

[2] Kießling, R., Landgraf, R., Scherzer, R., Ihlemann, J. Introducing the concept of directly connected rheological elements by reviewing rheological models at large strains. *Int J Solids Struct*, 2016, 97-97, 650-667.

BONE FRACTURE RISK: DENSITY AND MICROARCHITECTURE

F. COSMI[1,2], A. NICOLOSI[2], S. SACCO[3], L. SAIBENE[3], L. ABDI-ALI[3], G. SAVIOLA[3]

[1] Università di Trieste, DIA, via A. Valerio 10, 34127 Trieste, Italy, E-mail: cosmi@units.it;

[2] M2TEST srl, Padriciano 99, Trieste, Italy, E-mail: alessandra@bestest.it;

[3] IRCCS Maugeri Clinical Scientific Institutes, Pavia, Italy, E-mail: gianantonio.saviola@icsmaugeri.it

1. Introduction

Osteoporosis (OP) is a systemic skeletal disease where an increase in bone fragility is due to low bone mass and micro-architectural deterioration of bone tissue [1], which occur over a long period of time without clinical significance.

Currently, OP diagnosis is mainly based on bone densitometric measurements (BMD in DXA scans) at various sites, but over half of the fragility fractures in the population arise in women that would not be considered at risk based on BMD alone [2]. Therefore, other tools like FRAX [3], which may or may not include BMD, where mainly developed to validate treatment prescriptions. Bone turnover markers are indices of bone remodeling, useful for monitoring the patient assessing the response to therapy and treatment adherence [4].

The cortical BMD accounts for 80% of our skeleton, but bone mechanical resistance strongly depends also on the internal spatial arrangement of bone structure, that has long been considered the second key factor of bone load-bearing capacity, in addition to bone density, Fig.1.

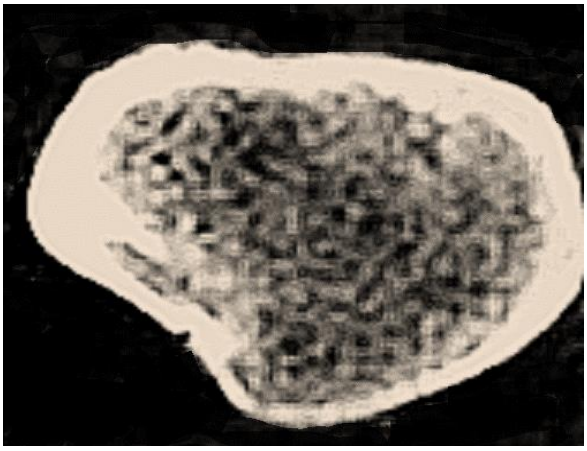

Fig. 1. TC scan femoral neck section from: outer compact part and internal spongeous structure.

In effects, most fractures occur in patients whose T-score is outside the osteoporosis range. DXA might not represent the elective exam, or be completely reliable [5], leading to the hypothesis that fracture risk depends not only on mass loss, but also on bone architecture, whose alterations are an independent factor of increased fragility.

1.1 Bone Elastic Structure Test

The Bone Elastic Structure Test, BESTEST®, is a recently introduced analysis that can be used to quantify the quality of bone micro-architecture and its pathological alterations induced by age, pathological conditions or lack of exposure to physiological mechanical stimuli. The test is based on an application of the Cell Method, a recent discrete method which is particularly effective from the point of view of computation time, memory requirements and accuracy of the results [6,7]. A radiographic virtual biopsy of the patient, acquired in the proximal phalanges of the non-dominant hand, is converted into a structural model and the response to compressive loads along the orthogonal axes is computed, Fig.2.

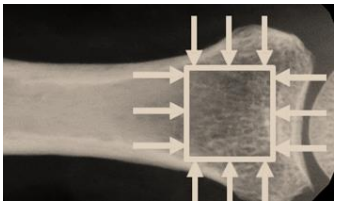

Fig. 2. Virtual biopsy of the patient and simulations.

The results are then combined in an index that gives an indication of the quality of the bone structure, the BSI (Bone Structure Index) [8,9]. Similarly to DXA, the BESTEST results are expressed in terms of BSI_T-score, which compares the patient's BSI with the mean BSI value for young Caucasian women (age 20-45) and measures this difference in number of standard deviations (SD).

Interpretation of BSI results match those typically used in bone density, as shown in Tab.1.

Table 1. Clinical reading of BSI

BSI T-score	Bone Structure Quality
≥ - 1	Normal
< -1 and > 2.5	First level deficiency
< 2.5	Significant worsening

The aim of this study is the comparison of DXA and BESTEST results in a clinical application.

2. Study population.

The examined population consists of 12 Caucasian women, age 39 - 74, Mean (SD) value 62.4 (10.8) years, with a normal or osteopoenic DXA femoral neck and lumbar T-score and a recent osteoporotic fracture. The control population consists of 15 Caucasian women, age 47 - 74, Mean (SD) value 64.7 (8.4) years, who had not suffered from osteoporotic fractures before the bone evaluation in 2015 described in [8], nor in the following three years (as confirmed by interview). The BSI T-score and the DXA femoral neck T-score were available for all the examined subjects.

3. Results

Results are summarized in Figures 2 to 5. As in in previous works [8, 9], there is no correlation between BSI and DEXA- T score. The DEXA T-score (neck) of the two groups was not significantly different (p=0.05). The BSI T-score of the two groups was significantly different (p= 0.0001).

4. Conclusions

Despite the small number of subjects, these data seem to confirm that the BSI could be helpful for predicting fragility fractures and patient monitoring.

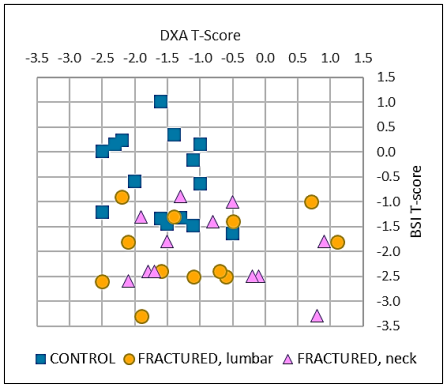

Fig. 2. DXA vs. BSI results are independent.

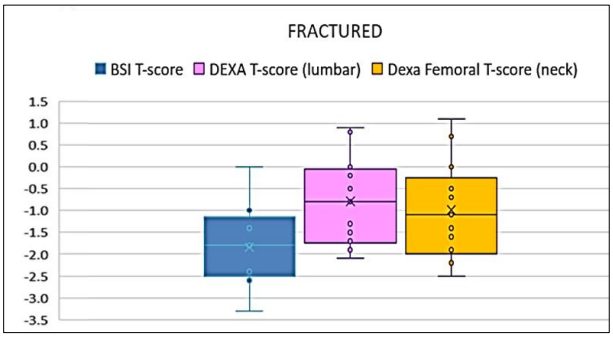

Fig. 3. Fractured group: min, max, mean, SD.

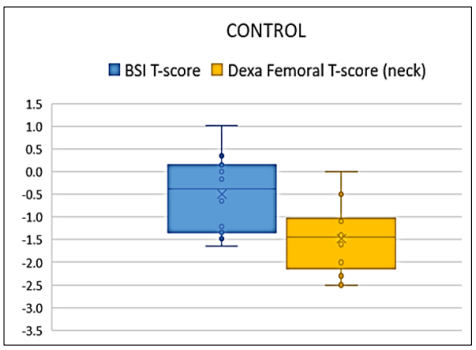

Fig. 4. Control group: min, max, mean, SD.

Conflicts of interest

This work would not have been possible without the cooperation of the patients.

Disclosure: FC is co-founder of M2TEST srl.

References

[1] Lane JM et al. Osteoporosis. *Clin Orthop Relat Res*, 2000, 372, 139-150.
[2] Pasco JA et al. The population burden of fractures originates in women with osteopenia, not osteoporosis. *Osteoporos Int*, 2006, 17(9), 1404-9.
[3] Kanis JA et al. Interpretation and use of FRAX in clinical practice. *Osteoporos Int*, 2011, 22, 2395-411.
[4] Rossini M et al. Dose-dependent short-term effects of single high doses of oral vitamin D(3) on bone turnover markers. *Calcif Tissue Int*, 2012; 91: 365-9
[5] Schuit SCE et al. Fracture incidence and association with bone mineral density in elderly men and women. *Bone*, 2004; 34: 195–202.
[6] Tonti E: A Direct Discrete Formulation of Field Laws: The Cell Method. *CMES* 1, 11-26.
[7] Cosmi F. Numerical Evaluation of Trabecular Bone Alterations, *MCB*, 201, 12, 87-105.
[8] Cosmi F et al. Osteoporosis risk factors and bone microstructure evaluation: a population breakdown. *Materials Today: Proceedings*, 2018, 5, 26772–77.
[9] Cosmi F, Saracchini S. Bone Structure Evaluation: Perspectives In Oncology. *Materials Today: Proceedings*, 2019, 7, 455–462.

USING POINT SYMMETRY IN FINITE ELEMENT ANALYSES

Ştefan SOROHAN[1], Dan Mihai CONSTANTINESCU[1], Marin SANDU[1], Adriana SANDU[1]

[1] University POLITEHNICA of Bucharest, Department of Strength of Materials, Splaiul Independeţei nr. 313, 060042 Bucharest, Romania. E-mail: stefan.sorohan@upb.ro

1. Introduction

Point symmetry is a rotational symmetry. A half of a part (see Fig. 1), which is rotated by 180º around an axis (Oz in this paper), generates the complete part. Sometimes it is called origin symmetry. It falls into the large category of cyclic symmetry where the numbers of sectors are only two. When the point symmetry is present, almost all papers in the literature neglect its effect; part of them consider only the reflective symmetry (*Z*–plane Sym) in analyzing some problems which fall into the category of the ones presented in Fig. 2. Only few papers, as [1] consider this type of symmetry but in an approximate manner. A recent work [2] briefly presented the advantages of using point symmetry for 2D analysis of a single lap joint under tensile load and pointed the basic conditions of constraint equations (CEs) which must be considered.

Commercial finite element codes, as ANSYS, may be used to efficiently solve the cyclic symmetry, but for this particular case, due to the methodology of implementation – as the basic sector is duplicated, considering the cyclic symmetry does not assure a beneficial computational effort.

This paper presents the conditions in which this type of symmetry may be used in finite element modeling to solve a large class of usual problems especially for linear and nonlinear static analysis.

2. Methodology

Let us consider a part as in Fig. 1a, which is also point symmetric in material properties and loads. An arbitrarily point symmetric C^0 surface, or a simple plane Σ cuts the part into two parts A and B (Fig. 1b–f). A point A in Part A has an associated point symmetric – point B in Part B (Fig. 1c). If the surface Σ is a plane, we can define an angle α (Fig. 1d) between this plane and the reference plane Oxz.

Due to the point symmetry conditions, the applied external forces $\boldsymbol{F}$ and moments $\boldsymbol{M}$, in the global system of reference Oxyz, must obey the conditions

$$\begin{aligned} &F_x^B = -F_x^A; \quad F_y^B = -F_y^A; \quad F_z^B = F_z^A; \\ &M_x^B = -M_x^A; \quad M_y^B = -M_y^A; \quad M_z^B = M_z^A. \end{aligned} \tag{1}$$

The degrees of freedom – displacements u and rotations φ in the parts A and B (or points A and B) will result in the form

$$\begin{aligned} &u_x^B = -u_x^A; \quad u_y^B = -u_y^A; \quad u_z^B = u_z^A; \\ &\varphi_x^B = -\varphi_x^A; \quad \varphi_y^B = -\varphi_y^A; \quad \varphi_z^B = \varphi_z^A. \end{aligned} \tag{2}$$

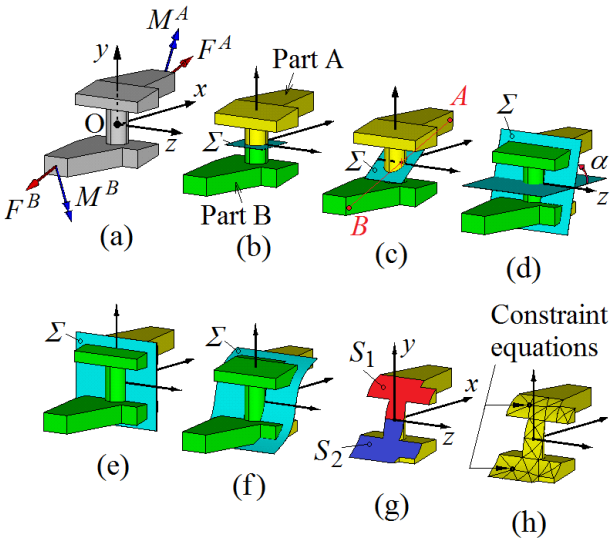

Fig. 1. Definition of a point symmetry part and some of its possible finite element models.

Also, the stresses will satisfy the conditions:

$$\begin{aligned} &\sigma_x^B = \sigma_x^A; \quad \sigma_y^B = \sigma_y^A; \quad \sigma_z^B = \sigma_z^A; \\ &\tau_{xy}^B = \tau_{xy}^A; \quad \tau_{yz}^B = -\tau_{yz}^A; \quad \tau_{xz}^B = -\tau_{xz}^A. \end{aligned} \tag{3}$$

If we keep in an analysis only Part A, the conditions (2) are valid on the points of the surfaces S_1 and S_2 in Fig. 1g. This implies that in the finite element model the mesh on these two surfaces must be also point symmetric and Eqs. (2) define the

constrained matrix between two-point symmetric nodes in the next equation

$$\begin{Bmatrix} u_x \\ u_y \\ u_z \\ \varphi_x \\ \varphi_y \\ \varphi_z \end{Bmatrix}_{S1} = \begin{bmatrix} -1 & 0 & 0 & 0 & 0 & 0 \\ 0 & -1 & 0 & 0 & 0 & 0 \\ 0 & 0 & 1 & 0 & 0 & 0 \\ 0 & 0 & 0 & -1 & 0 & 0 \\ 0 & 0 & 0 & 0 & -1 & 0 \\ 0 & 0 & 0 & 0 & 0 & 1 \end{bmatrix} \begin{Bmatrix} u_x \\ u_y \\ u_z \\ \varphi_x \\ \varphi_y \\ \varphi_z \end{Bmatrix}_{S2} . \quad (4)$$

For the common points of the surfaces S_1 and S_2, i.e. Oz axis, using Eq. (4) at limits, it yields:

$$u_x = 0; \quad \varphi_x = 0; \quad u_y = 0; \quad \varphi_y = 0, \quad \text{for nodes on Oz axis.} \quad (5)$$

In Fig. 2, some examples of possible application of point symmetry are presented: tapered single lap joint (a); wavy lap joint (b); reinforced scarf joint (c); rivet-bonded joint (d); reverse bent and bolted-bonded joints (e); symmetric lap test specimen (f); sandwich core specimen tested in compression (g). The red and blue surfaces correspond to the surfaces S_1 and S_2 where the conditions (4) and (5) must be applied. Using these conditions four rigid body motions are removed.

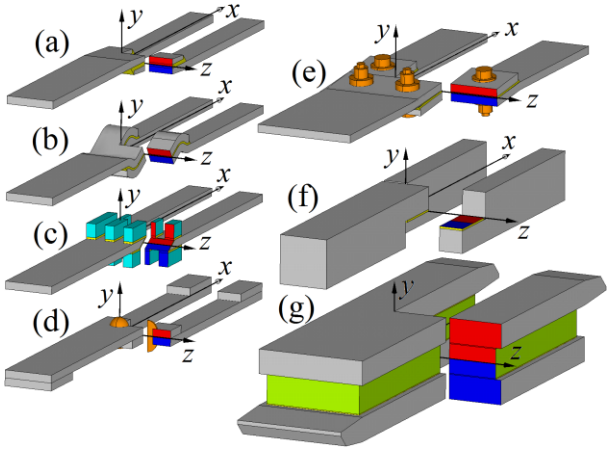

Fig. 2. Examples of point symmetric problems, where the Z-plane Sym exists and the quarter models that may be considered in the analyses.

It must be mentioned that CEs (4) are valid also for nonlinear analyses for large deflections.

3. An application and results

A plane shear specimen of a honeycomb core 1/4–5056–0.0025 (5.2 pcf) [3] in a tension test was analyzed using two different models – Model 1 and Model 2. Model 1, neglecting the adhesive between the cell walls, was meshed using only quadrilateral shell elements SHELL181 (6 DOFs/node) which include also in an approximate way the facesheet adhesive. Model 2 was meshed only with solid tetrahedral elements SOLID187 (3 DOFs/node) and replicates all the geometry details including the adhesive between all cell walls and facesheet adhesive with fillets. For both models full, half and quarter models, taking into consideration the reflective and point symmetry, were considered for static linear and large displacement nonlinear analyses. The main results: total number of active DOFs; memory RAM allocated by the code; elapsed time spent for computing the solution only for linear static analyses CP are presented in Table 1 and Table 2. The conditions (4) and (5) were imposed by an APDL file, developed by the authors of this paper.

Table 1. Results for Model 1 in ANSYS Classic.

Model	DOFs [-]	RAM [GB]	CP [sec]
Full	866,232	4.233	52.4
Half Z–Sym	433,116	1.694	20.6
Quarter $\alpha = 0^o$	216,554	0.791	9.8
Quarter $\alpha = 90^o$	216,554	0.761	10.3

Table 2. Results for Model 2 in ANSYS Workbench.

Model	DOFs [-]	RAM [GB]	CP [sec]
Full	4,101,997	8.065	1177.7
Half Z–Sym	2,066,299	4.122	1032.4
Quarter $\alpha = 0^o$	1,038,792	7.598	54.7
Quarter $\alpha = 90^o$	1,042,431	7.734	67.3

4. Conclusions

If we consider as reference the well known half reflective Z–Sym model, the additional consideration of the point symmetric model, i.e. quarter model in this paper, may reduce the computational effort with minimum 50%, or even more, depending on the size of the models and the used computer, or the finite element code. For example, considering the presented application and Model 2, the CP reduces almost 20 times (1032.4/54.7=18.87).

References

[1] Tsai, M.Y., Morton, J. Three-dimensional deformations in a single-lap joint. *J Strain Anal Eng*, 1994, 29(1), 137-145.

[2] da Silva, L.F.M., Öchsner, A. (Eds.). *Modeling of Adhesively Bonded Joints*; Springer-Verlag: Berlin Heidelberg, 2008.

[3] HexWeb™, Hexcel Corporation, 1999. https://www.hexcel.com. Accessed February 07, 2018.

INVESTIGATION OF MECHANICAL AND THERMOMECHANICAL EFFECTS IN SHAPE MEMORY ALLOY DURING TRANSFORMATION-INDUCED CREEP PHENOMENA

Elżbieta PIECZYSKA[1], Zbigniew KOWALEWSKI[1], Vladimir DUNIĆ[2], Radovan SLAVKOVIĆ[2] and Ryosuke MATSUI[3]

[1] Institute of Fundamental Technological Research, Polish Academy of Sciences, Pawińskiego 5b, 02-106 Warsaw, Poland; epiecz@ippt.pan.pl; zkowalew@ippt.pan.pl

[2] University of Kragujevac, Faculty of Engineering, Sestre Janjić 6, Kragujevac, Serbia; dunic@kg.ac.rs; radovan@kg.ac.rs

[3] Department of Mechanical Engineering, Aichi Institute of Technology, 1247 Yachigusa, Yakusa-cho, Toyota 470-0392, Japan; r_matsui@aitech.ac.jp

1. Introduction

An interruption of the loading, due to the accidents or a shortage of energy supply, is a situation that needs to be studied to anticipate the behavior of devices made of Shape Memory Alloys (SMA) such as sensors or actuators.

Recent research on this topic, e.g. Matsui et al. [1], Pieczyska et al. [2], considered that the strain-controlled loading interruption during the SMA tension, when the strain was kept constant, leads to the stress relaxation in the loading branch of the curve, and the stress increase in the unloading one.

According to the force-controlled tensile loading Pieczyska [3] presented procedure of experimental investigation of the force-controlled tensile loading of the TiNi SMA and studied the state and progress of the stress-induced transformation based on the temperature variation, captured by infrared camera. It was demonstrated that the nature of the SMA temperature change can manifest the current stage of the phase transformation.

Takeda et al. [4] investigated transformation-induced stress relaxation and recovery in TiNi SMA They concluded that for the higher loading rates, a loading break gave higher stress variation resulting in high thermo-sensitivity of the SMA.

The general assumption is that deformations in any material occur immediately after the application of the loading. The creep behavior in steel has been described as a time-dependent inelastic deformation which induces development of the permanent strains with time [5]. In the case of SMA, the inelastic deformations results mainly from martensitic transformation. So, the occurrence of deformation in SMA while keeping the loading constant can be classified as creep-like deformation.

A goal of the research is to investigate a creep-like deformation in TiNi SMA. To this end, the modified tensile loading program was conducted under the loading force kept constant at various stages of the stress-induced transformation (SIMT). The thermo-mechanical coupled numerical analysis using the finite element method (FEM) was engaged and the creep-like phenomena were analyzed.

2. Experimental procedure and results

The TiNi SMA belt specimens of the sizes 160 × 10 × 0.40 mm and constitution Ti-55.3 wt% Ni produced by the Furukawa Electric Co. in Japan were subjected to force-controlled tensile loading at room temperature on Instron 5867 testing machine. Its austenite finish temperature A_f was ≈283 K. The stress rate of the loading and unloading process was 12.5 MPa s^{-1}. The fast and sensitive infrared camera (IR) Therma CAM^{tm} FLIR Co. was used to record the infrared radiation from the specimen surface during the loading and estimate mean temperature of the SMA specimen for each instant of the straining with high sensitivity (0.02 K). The scheme of the experimental setup is presented in Fig. 1.

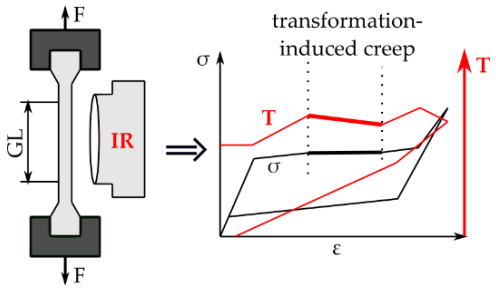

Fig. 1. Scheme of the experimental set-up for creep-like phenomena in SMA.

A difference between the mean value of temperature $T_{mean}(t)$ calculated for the gauge part of

the specimen and the mean temperature of the same area before the deformation $T_{mean}(t_0)$ was obtained.

The modified process of the TiNi SMA loading proposed in the experiment was conducted according to three different programs (1)–(3) (Fig. 2), i.e., the loading force was kept constant around 3 minutes at various stages of the localized martensitic transformation stage (LMT), monitored by infrared camera by thermograms (Th.):
- Program 1 - at the beginning of the LMT (Th. 1)
- Program 2 - in the middle of the LMT (Th. 2)
- Program 3 - at the end of the LMT (Th. 3).

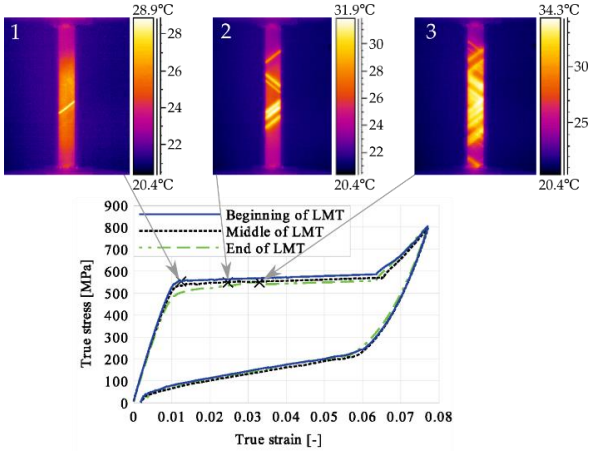

Fig. 2. Stress–strain curves of TiNi SMA; the marked points correspond to the thermograms 1, 2 and 3.

The obtained experimental (I) and numerical (II) results for TiNi SMA tension with 3-min loading interruption are compared in Fig. 3.

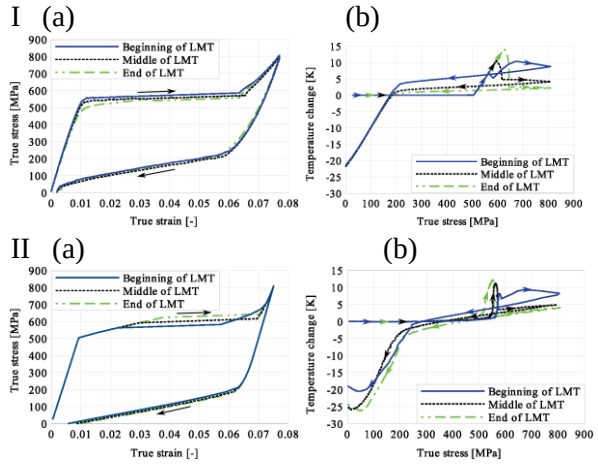

Fig. 3. Comparison of the experimental (I) and numerical (II) data for TiNi SMA tension with 3-min loading interruption induced at the beginning (1), middle (2) and end (3) of LMT: (a) stress vs. strain; (b) temperature change vs. stress.

It was confirmed by both experiment and model that thermo-mechanical coupling introduces significant influence on the transformation-induced creep phenomena in the TiNi SMA. Measuring temperature variations, accompanying the process, led to much better recognition of the phase transformation in the SMA than the mechanical characteristics. The lower temperature increase, observed during the reloading after the loading pause, pointed on the higher saturation of the martensitic transformation process during the pause.

3. Conclusions

The stress and related temperature changes demonstrated how the transformation-induced creep process started and evolved at various stages of the TiNi SMA tension loading.

The proposed model reproduced the stress, strain and temperature changes obtained during the experiment well; the latent heat production was in correlation with the amount of the martensitic volume fraction. It was demonstrated how the transformation-induced creep process occurring in the SMA under such conditions was involved in thermo-mechanical couplings and the related temperature changes.

Acknowledgements

This research was funded by the Polish National Centre of Science-Grants 2014/13/B/ST8/04280 and 2014/15/B/ST8/04368; and the Ministry of Education, Science and Technological Development Serbia Grant TR32036 and III41007.

References

[1] Matsui, R., Tobushi, H., Ikawa, T. Transformation-induced creep and stress relaxation of TiNi shape memory alloy. *Proc. Inst. Mech. Eng. Part L J. Mater. Des. Appl.* 2004, 218, pp. 343–353.
[2] Pieczyska, E., Kowalewski, Z., Dunić, V. Stress Relaxation Effects in TiNi SMA During Superelastic Deformation: Experiment and Constitutive Model. *Shape Mem. Superelasticity* 2017, 3, pp. 392–402.
[3] Pieczyska, E. Activity of stress - induced martensite transformation in TiNi shape memory alloy studied by infrared technique. *J. Mod. Opt.* 2010, 57, pp. 1700-07.
[4] Takeda, K., Matsui, R., Tobushi, H., Pieczyska, E.A. Transformation-Induced Relaxation and Stress Recovery of TiNi Shape Memory Alloy. *Materials* 2014, 7, pp. 1912–1926.
[5] Kojić, M., Bathe, K.J. *Inelastic Analysis of Solid and Structures*; Springer: Berlin, Germany, 2005.

ANALYSIS AND SIMULATION FILTRATION ORE DURING THE PROCESS OF ORE ENRICHMENT

Paweł MAŚLAK [1], Tomasz DOBOSZ[2]

[1] University of Science and Technology, Faculty of Mechanical Engineering, Department of Machine Design and Research, 5 Łukasiewicza st., 50-370 Wroclaw, Poland, e-mail: pawel.maslak@pwr.edu.pl

[2] University of Science and Technology, Faculty of Mechanical Engineering, Department of Machine Design and Research, 5 Łukasiewicza st., 50-370 Wroclaw, Poland, e-mail: tomasz.dobosz@pwr.edu.pl

1. Introduction

Nowadays during the process of underground mining there is a lot of explosive materials used. After that a lot of waste from explosive materials get to the ore. Valuable ore materials are mined with its unavoidable mix of unwanted solids. After getting the ore from underground it needs to be prepared for the melting process. That process is called ore enrichment. After that the ore from 2-3% of valuable metal can reach about 30 % of metal.

2. Analysis of the ore

During the transport of the ore the sampling and the analysis are being processed. Sampling is the removal from a given lot of material a portion that is representative of the whole yet of convenient size for analysis. After one or more samples are taken from an amount of ore passing through a material stream such as a conveyor belt, the samples are reduced to quantities suitable for further analysis. However sometimes it is impossible to take the best number of samples.

At the beginning a morphological analysis of the ore should be carried out. The view from the morphological analysis are shown in the figure 1. The morphological analysis shows that there is a lot of gravels.

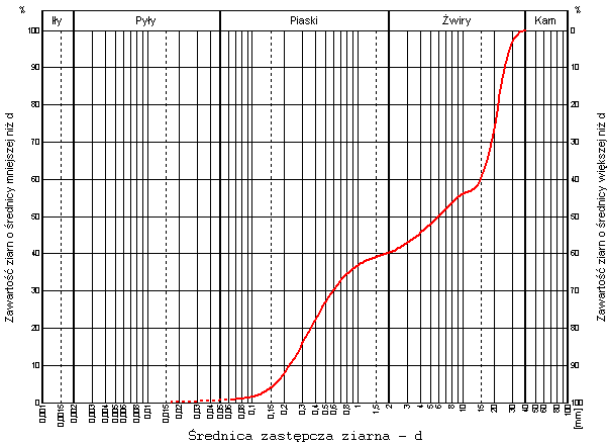

Fig. 1. Morphological analysis of the ore.

The next step while improving the enrichment process is to check what type of contaminants are found in the spoil. During the research it was found that the materials waste can be grouped into 6 groups:

- Wooden wastes
- Explosive wires
- Metals
- Rubbers and plastics
- Textiles
- Foils

The materials are found at the different place during the process of enrichment. All of them need to be separated as soon as possible to avoid them in the further steps of enrichment process. In the figure 2 there are shown the found unwanted materials in the ore.

Fig. 2. Unwanted materials found in the ore.

Table 1. Unwanted materials in one sample.

Case no.	Group of material	Mass [g]
1	Wooden waste	965
2	Explosive wires	700
3	Metals	33
4	Rubbers and plastics	915
5	Textiles	565
6	Foils	105

After the morphological analysis of the waste found in the ore the biggest amount are wooden waste and the rubber and plastics. Wooden waste are the most problematic during the next enrichment processes.

3. Filtration simulation

The filtration is designed to detect as much as possible impurities in the ore. Nowadays the filtration process is unsatisfactory. That process need to be autonomous, self-cleaning and not affecting the enrichment process, so the research were carried out. Present filtering process is shown in the figure 3.

Fig. 3. Filtration process.

4. Filtration simulation

The Filtration simulation was prepared to achieve the best size of holes in filtration shells.

Analysis with different type of falling elements were carried out – different size and different mechanical properties were simulated. In the full article there are shown the results from much more simulations. The view from the simulation is shown in figure 4.

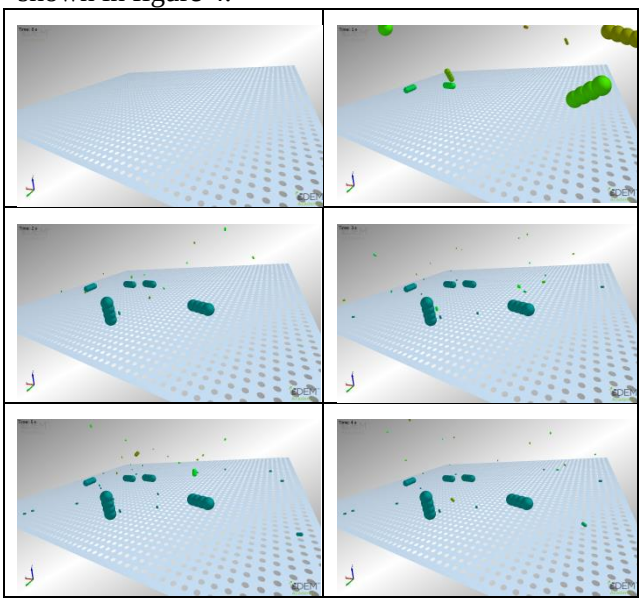

Fig. 4. View from the filtration simulation.

5. Conclusions

Analyzing the entire ore enrichment process is very necessary, as it allows the determination of process points that are key to improving the efficiency of the entire process. numerical modeling of the filtration process allows to accelerate the implementation phase of the filtering system change. The filtration simulation shows what kind of filter will be the best solution for the ore enrichment process.

References

[1] Rusiński E., Czmochowski J., Smolnicki T.: *Zaawansowana metoda elementów skończonych w konstrukcjach nośnych*, Oficyna Wydaw. PWroc., 2000

[2] Maślak P., Smolnicki T. *Strength and Fatigue Analysis of the Welding Connection on the Compressed Air Tank*, Proceedings of the 14th International Scientific Conference: Computer Aided Engineering, Springer 2018

[3] Mike D. Adams, Gold Ore Processing: Project Development and Operations, Elsevier, 2016

[4] *SHARMA B.K., Industrial Chemistry* Krishna Prakashan Media, 1991

MINIMALLY INVASIVE INTERNAL FIXATION TECHNIQUES FOR MANAGEMENT OF SACRAL BONE INJURIES

Libor LOBOVSKÝ[1], Martin SALÁŠEK[1,2], Milada KREJČOVÁ[1], Michaela MAREŠOVÁ[3], Jana HARTLOVÁ[1], Radek TUPÝ[4], Tomáš PAVELKA[2], Jiří KŘEN[1]

[1] NTIS - New Technologies for the Information Society, Faculty of Applied Sciences, University of West Bohemia, Univerzitní 8, 30100 Plzeň, Czech Republic, E-mail: lobo@kme.zcu.cz

[2] Clinic for Orthopaedics and Traumatology of Locomotive Organs, University Hospital Plzeň, alej Svobody 80, 304 60 Plzeň, Czech Republic

[3] Department of Mechanics, Faculty of Applied Sciences, University of West Bohemia, Univerzitní 8, 30100 Plzeň, Czech Republic

[4] Clinic for Radiology, University Hospital Plzeň, alej Svobody 80, 304 60 Plzeň, Czech Republic

1. Introduction

The presented research focuses on bone injuries in the region of human pelvic ring. A special attention is paid to fractures that usually occur during high-energy impact events such as car accidents or sports injuries.

Herein, minimally invasive internal fixation techniques that support the fractured bone structures are investigated. A unilateral transforaminal sacral bone fracture (Denis type II) [1] is selected as the reference case for this study. The mechanical response of the pelvic ring treated using a number of sacral bone fixation techniques is quantified.

Both experimental and computational analysis are conducted.

2. Studied fixation techniques

The studied sacral bone fixation techniques are based on application and/or a combination of the following orthopaedic fixators: transiliac internal fixator (TIFI) [2], iliosacral screw (ISS) [3], sacral bar (SB) [4] or transiliac plate (TP) [5]. Overall 9 fixation techniques were examined.

3. Methods

The experimental analysis is performed using orthopaedic models of male pelvis made of solid foam [6]. This enables to maintain consistency of the measured data, which would be hard to achieve if cadaveric pelves were applied.

The models are positioned in the rigid stand and the intact and treated pelvic structures are subjected to external quasi-static loading up to 300 N, 500 N respectivelly. The load is applied in a perpendicular direction to the base of the sacral bone. In general, the stability of each fixation technique is assessed according to the measured displacement of the sacral base, the ratio between the stiffness of the treated and intact pelvic structure respectively. This is supported by quantification of relative displacements of the fractured bone parts.

In order to quantify the motion of the bone structures, both an extensometer and a multi-camera digital image correlation (DIC) system are applied. The relative motion of the fractured sacral bone parts is captured from the dorsal view. In order to analyse the stability of each technique, dislocations of selected points at sacrum's dorsal surface are quantified.

The computational part of the study is based on the finite element (FE) analysis. The model geometry, the computational mesh of the FE model respectively, is based on CT scans of the experimentally studied pelves with fixators. Thus an exact orientation of the applied fixators within the bone structures is provided. The input data for validation of the numerical simulations are based on the results of the above described experimental campaing. An extra set of tensile and compression tests are performed in order to determine the material properties of the orthopaedic plastic models.

Within the FE analysis of elastostatics of the loaded pelvis, the interaction of the fractured bone parts is modelled by a standard surface-to-surface contact algorithm with a finite sliding formulation and a non-zero friction.

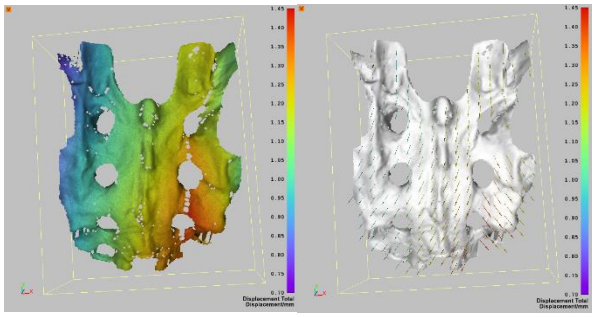

Fig. 1. Experimental analysis of pelvic ring ISS fixation: contour plot of displacement magnitudes (left) and displacement vectors (right) at dorsal surface of the sacral bone under load of 500 N.

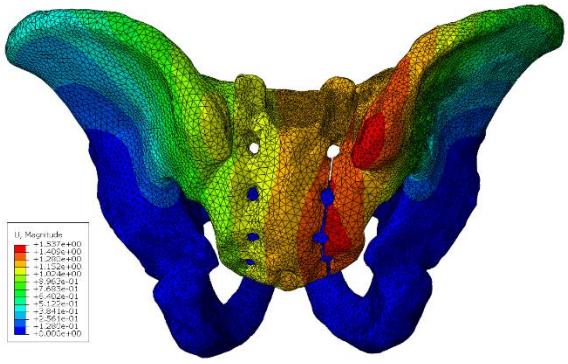

Fig. 2. Finite element analysis of pelvic ring ISS fixation: contour plot of displacement magnitudes under load of 500 N.

4. Results and discussion

The presented figures show results for pelvic ring ISS fixation technique. In Fig. 1, results of the DIC analysis of bone deformations during the experiments at maximal load of 500 N are displayed. Both contour plot of displacement magnitudes along the dorsal surface of the sacral bone and displacement vectors at selected locations are presented. The magnitude of displacements is symmetric along the fracture line which goes through foramina on the right side of sacrum. Similar results are also obtained from the computational analysis, as shown in Fig. 2.

5. Conclusion

The computational model is developed and validated based on the in-house experimental data. Both experimental and computational studies provide a direct comparison of the stability of selected pelvic ring fixation techniques, while the computational model is designed so that it enables an analysis of more complex pelvic ring injuries (which would be hard to assess experimentally) and an assessment of their optimal treatment in future.

Acknowledgements

This work is supported by the European Regional Development Fund-Project "Application of Modern Technologies in Medicine and Industry" (No. CZ.02.1.01/0.0/0.0/17_048/0007280) and by the project LO1506 of the Czech Ministry of Education, Youth and Sports under the program NPU I.

References

[1] Fakler, J.K.M., Stahel, P.F., Lundy, D.W., Classification of Pelvic Ring Injuries. In: Fractures of the pelvis and acetabulum, W.R. Smith, B.H. Ziran, S.J. Morgan (eds.), CRC Press, Boca Raton, 2007, pp.~11-26.

[2] Dienstknecht, T., Berner, A., Lenich, A., Zellner, J., Mueller, M., Nerlich, M., Fuechtmeier, B., Biomechanical analysis of a transiliac internal fixator, International Orthopaedics 35 (12) (2011) 1863-1868.

[3] Giráldez-Sánchez M.A., Lázaro-Gonzálvez, Á., Martínez-Reina, J., Serrano-Toledano, D., Navarro-Robles, A., Cano-Luis, P., Fragkakis, E.M., Giannoudis, P.V., Percutaneous iliosacral fixation in external rotational pelvic fractures. A biomechanical analysis, Injury 46 (2) (2015) 327-332.

[4] Gorczyca, J.T., Varga, E., Woodside, T., Hearn, T., Powell, J., Tile, M., The strength of iliosacral lag screws and transiliac bars in the fixation of vertically unstable pelvic injuries with sacral fractures, Injury 27 (8) (1996) 561-564.

[5] Suzuki, T., Hak, D.J., Ziran, B.H., Adams, S.A., Stahel, P.F., Morgan, S.J., Smith, W.R., Outcome and complications of posterior transiliac plating for vertically unstable sacral fractures, Injury 40 (4) (2009) 405-409.

[6] http://www.sawbones.com/products/product.aspx?231

EFFECT OF SHALLOW AND DEEP CRYOGENIC TREATMENT ON TRIBOLOGICAL PROPERTIES OF MONEL K-500

K. N. PANDEY[1], Ketan GUPTA[2]

[1] Motilal Nehru National Institute of Technology Allahabad, Prayagraj, India;
Email: knpandey@mnnit.ac.in; ketangupta19@gmail.com

1. Introduction

Cryogenic treatment is the process of treating work pieces to cryogenic temperatures in order to remove residual stresses and improve wear resistance on steels. It is considered as a process to reduce the retained austenite content and improve the performance of materials. Monel K-500 [1] is a nickel-copper alloy, precipitation hardenable through additions of aluminum and titanium. These alloys are well known for their corrosion resistance in a wide range of Environments such as sea water, acids, alkalis and sour oil. They are extensively used for components such as condenser tubing, marine fittings, pump shafts and impeller, and oil well drill collars [2-4]. The SCT and DCT are extensively studied for number of material and found as a novel technique for materials property improvement [5-9]. In the present work, the effect of shallow and deep cryogenic treatment (SCT and DCT) on the mechanical and tribological properties of Monel K-500 is studied. For comparison, conventionally heat treated samples were also tested.

2. Experimentation

2.1 Material:

The nominal composition of the alloy is given Table 1.

Table 1. Composition of Monel K-500 (wt %).

Ni	Cu	C	Mn	Fe	S	Si	Al	Ti
63	27-33	0.25	1.5	2	0.01	0.5	2.30-3.15	0.35-0.85

2.2 Heat treatments:

The austenizing temperature of Monel K500 is 875ºC [15]. Therefore for annealing, the samples were heated from 30ºC to 875ºC in 3 hours and maintained at 875ºC for 1 hour. After that the furnace was switched-off and samples were allowed to cool within the furnace itself.

While performing the quenching operation, the samples of Monel K 500 were heated at a rate of 5°C /min from 30°C (room temperature) to 875°C, at this temperature it is kept for an hour and then quenched in water to 30°C. During shallow cryogenic heat treatment (SCT) the samples were cooled from 30°C to -80°C by putting in the contact of vapour of liquid nitrogen. They were kept at -80°C for 5 hours and brought back to the room temperature of 30°C.

During deep cryogenic heat treatment the samples were dipped in liquid nitrogen to bring temperature from 30°C to -196°C. They were kept at -196°C temperature for 24 hour and then placed outside to regain temperature room temperature of 30°C. The Time Temperature plot for the Deep Cryogenic Treatment (DCT) of Monel K-500 is shown in Fig 2.

2.3 Tests

Vicker micro hardness measurement was performed using Radical Micro Tester-201 by means of Vickers indenter with of 1N dwelled for 15s. The indenter used in Vicker hardness test is a diamond type with square based pyramid base which has sides inclined to each other at 136º.

Wear Tests were performed on DUCOM Wear and Friction co-efficient Monitor, TR-20-M100 (Pin-On-Disc wear testing machine) as per the ASTM wear testing standard G99. For this 90 cylindrical specimens of 10mm diameter and 40mm length were prepared. The ends of specimen were made flat for proper contact during pin-on-disc wear test. The test is done by rotating a computer- face test disk against a stationary test specimen pin.

Tensile Test specimens of different heat treated including SCT and DCT material were prepared as per ASTM E8M-16a standard. A 25kN servo hydraulic test machine of BISS was used to conduct tension tests.

Fig. 1. Tension test specimen.

XRD Analysis

X- ray diffraction was performed in order to identify different phases in the material. XRD was carried out on a Rigaku 2500VB2þ/PC diffractometer with Cu K_α radiation. 5 samples were prepared of size 10mm in diameter and 2mm in length.

3. Results and Conclusions

It was observed that the application of a deep cryogenic treatment to Monel K-500 steel increases hardness and decreases structural defects, providing a dispersed network of fine carbides after the subsequent tempering stages. Tempering improved the strength of the material significantly.

In hardness test, it was found that deep cryogenic treated samples increased significantly (up to 10.51%) whereas in quenching and shallow cryogenic treated samples it increased nominally (2.77% and 3.88% respectively).

Ultimate tensile strength of DCT sample was obtained as 744.047 MPa whereas for SCT sample it was 671.897 MPa. Stress Strain curve for Untreated, Annealed, CHT and SCT samples is more or less similar. Maximum tensile strength was observed maximum for DCT samples. Strain before fracture is least in case of DCT Samples as compared to other Heat treatments (Table 2). Maximum tensile strength of DCT samples is attributed to the formation of higher volume fraction of martensite and due to precipitation of carbides due to cryogenic treatment.

Wear tests were conducted on pin-on-disc friction and wear test set-up as per L_9 orthogonal array of Taguchi design with load, wear track diameter and disc rotation as control factors. Three levels of these control factors were applied. For SCT, disc rotation was most significant parameter followed by wear track diameter and load. For DCT samples, disc rotation was most significant parameter followed by load and wear track diameter. In the initial stage of sliding weight loss was rapid and continuous with increase in sliding time. This indicated a completely steady-state behaviour. Sliding for long time and sliding over long distances causes hardening of the surface layer compounds of the waste debris and decreases the wear rate. Wear rate was minimum for DCT and maximum for annealed samples.

Table 2. Comparison of Ultimate Tensile Strength and strain at fracture point

S.No.	Sample Name	Ultimate Tensile Strength (MPa)	Fracture Strain (mm/mm)
1	Untreated	631.478	0.2622
2	Annealed	604.391	0.2769
3	CHT/Quenched	617.909	0.2747
4	SCT	671.897	0.27477
5	DCT	744.047	0.0779

The X-ray diffraction patterns characterized martensitic peaks, but there was no evidence of peaks corresponding to austenite. Therefore, it can be inferred that the volume fraction of austenite is below the detection threshold of the equipment. The microstrain in annelaled, SCT and DCT samples were 0.201831, 0.187860 and 0.260543 respectively. Increase in microstrain increased the strength.

Acknowledgements

Authors acknowledge CIR, MNNIT for extending facility for characterization. Financial assistance provided by TEQIP-III of MHRD, GoI is highly acknowledged.

References

[1] Handbook of Wiggin and Huntington Alloys, Henry Wiggin and Co., Hereford, 1973, p. 14.
[2] A. V. Dean and R. C. Owen, J. *Inst. Met., 100* (1972) 181.
[3] J. A. Harris, R. C. Scarberry and C. D. Stephens, *Corrosion, 28* (2) (1972) 57.P.Baldissera,C.Delprete,OpenMech.Eng.J.2(2008)1–11.
[4] P.Baldissera,C.Delprete,Mater.Des.31(2010)4731–4737.
[5] P.Baldissera,Mater.Des.30(2009)3636–3642.
[6] K.M.Asl,A.Tari,F.Khomamizadeh,Mater.Sci.Eng.A 523(2009)27–31.
[7] J.Liu,G.Li,D.Chen,Z.Chen,Chin.J.Aeronaut.25 (2012) 931–936.
[8] D.Das,A.K.Dutta,K.K.Ray,Mater.Sci.Eng.A527 (2010) 2194–2206.
[9] M. Araghchiz, H. Mansouri and R. Vafaei, YinaGuo, A novel cryogenic treatment for reduction of residual stresses in 2024 aluminum alloy, Materials Science & Engineering A 689 (2017) 48–52

TOWARDS ALTERNATIVE CONFIGURATIONS TO DETERMINE THE TENSILE STRENGTH OF BRITTLE MATERIALS

Christos F. MARKIDES[1], Stavros K. KOURKOULIS[1]

[1] National Technical University of Athens, Department of Mechanics, Laboratory for Testing and Materials, 5 Heroes of Polytechnion Avenue, Theocaris Building., Zografou Campus, 157 73, Athens, Greece, E-mail: markidih@mail.ntua.gr; stakkour@central.ntua.gr

1. Introduction

An alternative configuration of the ring test [1], which was introduced as a convenient substitute of the familiar Brazilian-disc test [2] for the determination of the tensile strength of brittle materials, is described here. The configuration proposed is complementary to the one discussed in a recent paper [3], dealing with the flexure of curved beams and the uniaxial stress state developed at critical points of its circumference, leading to tensile fracture.

The main features of the configuration are shown in Fig. 1. It consists of circular ring with a diametral cut, loaded by forces, P, acting normally to the cut and directed outwards with respect to the cut. Based on the well-known solutions for the curved beam, provided by Muskhelishvili [4], the maximum tensile stress, developed at the inner circumference of the ring at point B, σ_θ^B, (Fig. 1) is calculated in terms of geometry and P. The main idea is that σ_θ^B represents the tensile strength of the material, assuming that P attains the critical value that causes fracture.

According to Saint-Venant's principle, the stress field developed along the critical locus AB is due to two factors: (i) couples of magnitude Pc, where c is the eccentricity (Fig. 1), and (ii) a pair of collinear point forces, P, acting on the edges of the Circular Semi Ring (CSR) (Fig. 2). Both cause "opening" of the curved beam. Due to the high eccentricity, the couples induced are of high magnitude, resulting to fracture at point B under relatively low P-values.

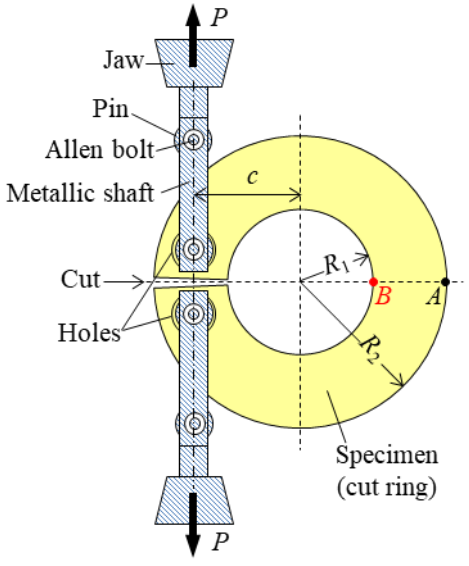

Fig. 1. The configuration of the problem.

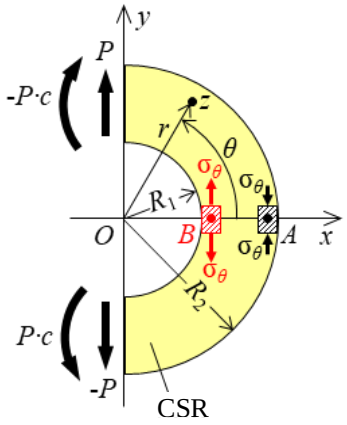

Fig. 2. The mathematical problem for the CSR.

2. Theoretical considerations

The stress field (and thus the tensile strength of the material) is here obtained in closed form using Muskhelishvili's formulae for the curved beam [4], assuming that the configurations of Figs. 1 and 2 are equivalent (at least for points relatively far from the load application area, as it is the neighborhood of line AB, where the maximum and minimum principal stresses are developed). In turn, assuming linear elasticity, the solution for the CSR is obtained by superposing the solutions of two problems, which are provided by Muskhelishvili, in terms of the dislocations concept [4]: Problem I, which deals with the CSR under couples $M=Pc$ (acting on its straight edges) and Problem II, dealing with the CSR under shear forces, P (both acting on its straight edges).

In this context, assuming that the CSR is lying in the complex plane $z=re^{i\theta}$ ($-\pi/2\le\theta\le\pi/2$, $R_1\le r\le R_2$), Fig. 2, with $\rho=R_2/R_1$, the relevant stress fields due to these two problems (I, II), read separately as:

$$\sigma_r^{(I)} = \frac{-2Pc}{hR_1^2}\cdot\frac{\left(\rho^2-1\right)\log\frac{r}{R_1}+\rho^2\left(\frac{R_1^2}{r^2}-1\right)\log\rho}{\left(\rho^2-1\right)^2-4\rho^2\left(\log\rho\right)^2} \quad (1)$$

$$\sigma_\theta^{(I)} = \frac{-2Pc}{hR_1^2}\cdot\frac{\left(\rho^2-1\right)\left(\log\frac{r}{R_1}+1\right)-\rho^2\left(\frac{R_1^2}{r^2}+1\right)\log\rho}{\left(\rho^2-1\right)^2-4\rho^2\left(\log\rho\right)^2} \quad (2)$$

$$\tau_{r\theta}^{(I)} = 0 \quad (3)$$

$$\sigma_r^{(II)} = \frac{P}{2h}\cdot\frac{\frac{\rho^2+1}{r}-\frac{r}{R_1^2}-\frac{\rho^2R_1^2}{r^3}}{\left(\rho^2+1\right)\log\rho-\rho^2+1}\cdot\cos\theta \quad (4)$$

$$\sigma_\theta^{(II)} = \frac{P}{2h}\cdot\frac{\frac{\rho^2+1}{r}-\frac{3r}{R_1^2}+\frac{\rho^2R_1^2}{r^3}}{\left(\rho^2+1\right)\log\rho-\rho^2+1}\cdot\cos\theta \quad (5)$$

$$\tau_{r\theta}^{(II)} = \frac{P}{2h}\cdot\frac{\frac{\rho^2+1}{r}-\frac{r}{R_1^2}-\frac{\rho^2R_1^2}{r^3}}{\left(\rho^2+1\right)\log\rho-\rho^2+1}\cdot\sin\theta \quad (6)$$

Summing up Eqs. (2) and (5), σ_θ is obtained for the problem shown in Fig. 2. Clearly, at point $B(R_1,0)$, the only non-zero stress component is the maximum principal stress $\sigma_\theta^B>0$, while at point $A(R_2,0)$ the only non-zero stress component is the minimum principal stress $\sigma_\theta^A<0$. It is seen that the ratio $k=\sigma_\theta^B/|\sigma_\theta^A|$

$$k = \left\{2c\rho\left[\rho^2-1-\left(3\rho^2+1\right)\log\rho+2\rho^2\frac{\rho^2+1}{\rho^2-1}\left(\log\rho\right)^2\right]\right.$$
$$\left.+R_2\left[\left(\rho^2-1\right)^2-4\rho^2\left(\log\rho\right)^2\right]\right\}\Big/\left\{2c\rho\left[1-\rho^2+\left(3+\rho^2\right)\log\rho\right.\right.$$
$$\left.\left.-2\frac{\rho^2+1}{\rho^2-1}\left(\log\rho\right)^2\right]+R_1\left[\left(\rho^2-1\right)^2-4\rho^2\left(\log\rho\right)^2\right]\right\} \quad (7)$$

always exceeds unity. It is therefore concluded that brittle materials of compressive strength significantly exceeding the tensile one, will likelihood fail, due to the configuration of Figs. 1 and 2, at point B, under a uniaxial tensile stress field. The ratio k is independent of the magnitude of the external load P, depending exclusively on the dimensions of the cut ring and the eccentricity c. Assuming R_2=5 cm, and $c=(R_1+R_2)/2$, the variation of k against the radius R_1 of the inner hole is plotted in Fig. 3.

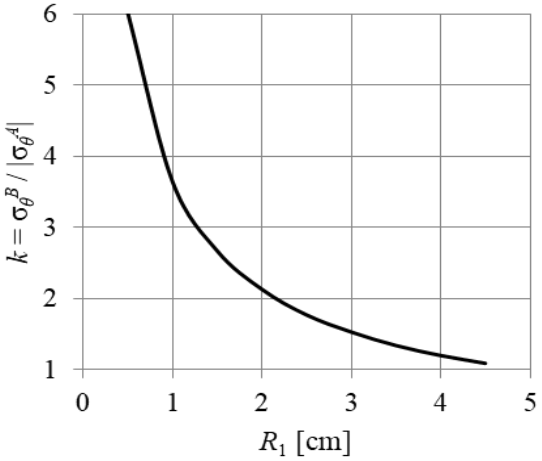

Fig. 3. Ratio k versus inner hole's radius R_1.

3. Discussion and Conclusions

An alternative procedure for the determination of the tensile strength of brittle materials by means of the cut-ring specimen, in conjunction with proper closed-form analytic formulae based on Muskhelishvili's solutions for the respective CSR configuration, was proposed. It was concluded that the tensile strength may be effectively determined in the case of a moderate inner hole of the ring.

It must be noticed however, that the proposed configuration should be handled with caution. For high R_1-values secondary effects due to buckling could influence the experimental procedure. On the other hand, for small R_1-values, Saint-Venant's principle should also be checked regarding the transition from the configuration of Fig. 1 to that of Fig. 2.

The procedure proposed is also to be tested for possible description of the stress concentration in the case of a small inner hole, somehow resembling relevant methods of ASTM standards [5].

References

[1] Ripperger, E., Davis, N. Critical stresses in a circular ring. *Trans. Am. Soc. Civil Engrs*, 1947, 619–627.
[2] Akazawa, T. New test method for evaluating internal stress due to compression of concrete. *J. Jpn Soc. Civil Engineers*, 1943, 29, 777-787.
[3] Kourkoulis, S.K., Pasiou, E.D., Markides, C.F. Analytical and numerical study of the stress field in a circular semi-ring under combined diametral compression and bending. *Frattura ed Integrità Strutturale*, 2019, 47, 247–265.
[4] Muskhelishvili, N.I. *Some basic problems of the mathematical theory of elasticity*, Noordhoff, Groningen, 1963.
[5] ASTM E399 - 90. *Standard Test Method for Plane-Strain Fracture Toughness of Metallic Materials*, 1997.

BIOMECHANICAL ANALYSIS OF THE EFFECT OF COMPRESSION SPORTSWEAR ON RUNNING

Zsófia PÁLYA[1], Rita M. KISS[1]

[1] Budapest University of Technology and Economics, Department of Mechatronics, Optics and Mechanical Engineering Informatics, Muegyetem rkp. 3., Budapest, 1111 Hungary.
E-mail: palyazsofia@gmail.com, : rita.kiss@mogi.bme.hu

1. Introduction

One of the most crucial factors in the design process is the comfort of clothing which is resulted of many interactions between physical and physiological factors. Our body maintain its comfort state by evaporating moisture to cause cooling, while the clothing could form a heat and vapor transmission barrier. Therefore, the ideal sportswear should be able to transport sweated water without feeling ourselves wet [1].

The aim of this present research was to compare a commercial compression sportwear with two different custom-made garments by applying biomechanical measurements. For this purpose, a complex measurement system was constructed, moreover, a pilot study was executed involving 4 female participants. According to MacRae et al. in terms of compression garments' efficiency in exercises, they can reduce oscillation and increase strength enhancing the performance [2]. Therefore, the different sportswear had the same cut and similar material composition but had different compression.

2. Materials and methodology

2.1 Investigated sportswear

Firstly, a purchased sportswear (P1) was tested which has been bought ready-made for all participants in the pilot-study. Secondary, the custom-made garments were prepared based on 53 different previously measured sizes. The first garment (CM-1) was made with body size below of 1% however, the second (CM-2) with body size below of 5 %. Body size below means that in the pattern circumferences were reduced by the given percentage to achieve different compression. Based on MacRae et al. the level of pressurization is a significant variable in compression garments [2]. Therefore, the compression of the different clothing was measured with a Picopress compression probe. These values are summarized in Tab 1. for the most relevant body segments.

Table 1. Measured compression values.

Name	Calves [Hgmm]	Knee [Hgmm]	Thigh [Hgmm]	Waist [Hgmm]	Crop [Hgmm]
P1	15	7.5	9	17.5	3.5
CM-1	7	5	7.5	9	2
CM-2	10.5	6.5	6	10.5	3.5

2.2 Measurement setup

The first goal of this present research was to construct a complex biomechanical measurement system through which the sportswears are comparable. The final setup is depicted in Fig. 1. As we can see on the figure three different measurement were carried out simultaneously. The motion was recorded with an Optitrack (*NaturalPoint, Inc*., Oregon, USA) based motion capture system with 120 Hz sampling frequency. In parallel with the motion analysis body temperature was captured with 8 FPS with the help of a Flir type (*Flir System*, Oregon, USA) thermometry. Moreover, the heart rate (HR) was monitored with the help of a Garmin Forerunner 310XT (*Garmin Ltd*., Kansas, USA) sport watch and its heart rate monitor strap.

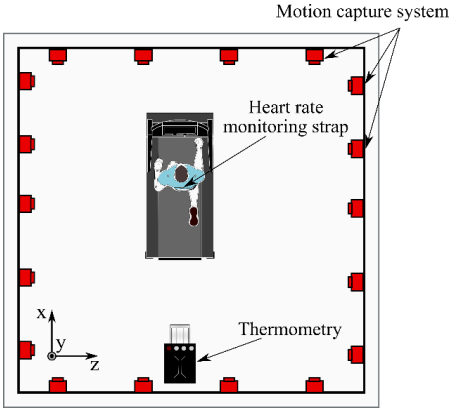

Fig. 1. Measurement setup.

2.3 Pilot-study

During the investigation a pilot-study was executed involving four healthy, well-trained female free-time runners (age: 21.0 ± 2.2 yrs, body mass: 63.3 ± 2.1 kg, height: 170.5 ± 2.5 cm). None of the participants had suffered from any injury

which affects to the locomotion system. The experimentation was performed on a treadmill applying gradually increasing velocity intervals. After 3 minutes of walking the following velocities were considered: 7 km/h, 8 km/h, 10 km/h, 11 km/h. The participants ran 3 minutes in each period without any break.

2.4 Data analysis

Applying the 3D position data of the 39 anatomical landmarks the angular and geometrical parameters could be calculated using an open-source software OpenSim (*NIH Center for Biomedical Computation*, Stanford, USA). Afterwards, a self-developed Matlab (R2017a, *The MathWorks*, Massachusetts, USA) script was utilized to split the motion into gait cycles and determine the relevant gait parameters. In this study the range of motion of knee extension (ROM_{knee}), the range of motion of hip extension (ROM_{hip}), the vertical displacement of center of mass (COM_y) and the step length were considered. The gait parameters were evaluated for the last 60 seconds of the velocity intervals. In case of hart rate measurements at least a 120 seconds interval is necessary to obtain a motion specific HR value [3]. Therefore, the measured HR values were averaged on the whole period (Table 2). Finally, 5 selected body segments' temperature were determined with the help of the data from the thermometry. The specific temperature (ΔT) of the different region were calculated from the measured values by normalizing the with a measured free surface's temperature (for the tight and waist region see on Fig. 3).

3. Results

The secondary aim of the research was to compare the different sportswear based on the pilot-study. Therefore, one-sample t-test was performed pairwise with significance level of 0.05. The result of the statistic probe is summarized in Fig. 2.

	Step lenght [m]				COM_y [m]		ROM_{knee} [°]				ROM_{hip} [°]			
	right		left				right		left		right		left	
	avg	CV	avg	CV	avg	CV	avg	CV	avg	CV	avg	CV	avg	CV
P1 vs CM-1														
7 [km/h]														
8 [km/h]														
10 [km/h]														
11 [km/h]														
P1 vs CM-2														
7 [km/h]														
8 [km/h]														
10 [km/h]														
11 [km/h]														
CM-1 vs CM-2														
7 [km/h]														
8 [km/h]														
10 [km/h]														
11 [km/h]														

Fig. 2. Significant differences (marked with red cells) in between the gait parameters.

Table 2. Measured heart rate values.

	heart rate [BMP]			
	7 [kmh^{-1}]	**8 [kmh^{-1}]**	**10[kmh^{-1}]**	**11[kmh^{-1}]**
P1	143 ±8	164 ±12	176 ±10	185 ±9
CM-1	140 ±12	160 ±14	173 ±12	182 ±11
CM-2	134 ±10	155 ±10	168 ±11	176 ±10

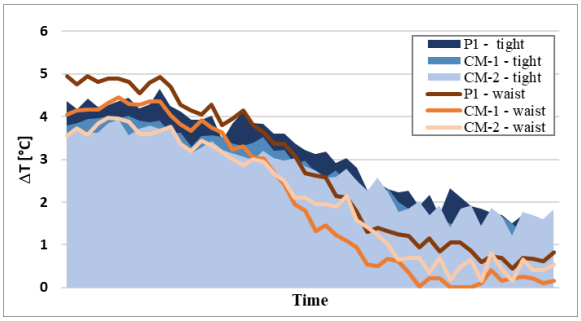

Fig. 3. Change of specific temperatures.

As a result of the pilot-study some remarks can be concluded. Firstly, in case of CM-2 garment the HR values are significantly smaller than the other two sportswear (see on Table 2). On the other hand, despite of different compression values e.g. in the tight and waist regions, the change of specific temperature data shows similar tendency (see on Fig. 3). Moreover, many of the significant differences were obtained in between the purchased (P1) and CM-2 garment in term of the gait parameters (see on Fig. 2) which pressure values are close to each other in the lower regions (Table 1).

4. Conclusions

To sum up, the compression of different running suit didn't necessarily influence the biomechanical parameters. Whereas, based on the HR results the custom-made design and the grater pressurization might improve the blood circulation and lead to smaller HR values.

Acknowledgements

This research has been supported by the ÚNKP-18-2 New National Excellence Program of the Ministry of Human Capacities Hungary.

References

[1] DeMartino, R. N., et al. Improved Comfort Polyester: Part III: Wearer Trials. *Textile Research Journal*, 1984, 54(7), 447-458.

[2] MacRae, B. A., et al. Compression garments and exercise. *Sports medicine*, 2011, 41(10), 815-843.

[3] Machado, F. A., et al. Effect of stage duration on maximal heart rate and post-exercise blood lactate concentration during incremental treadmill tests. *Journal of science and medicine in sport*, 2013, 16(3), 276-280.

IN-SITU CYCLIC EXPERIMENT ON GLASS FIBER REINFORCED COMPOSITES MONITORED VIA μ-TOMOGRAPHY

Zvonimir TOMIČEVIĆ[1], Benjamin SMANIOTTO[2], Amine BOUTERF[2], Clément JAILIN[2], Arturo MENDOZA-QUISPE[2], François HILD[2]

[1] University of Zagreb, Faculty of Mechanical Engineering and Naval Architecture, Ivana Lučića 5, 10000 Zagreb, Croatia, E-mail: zvonimir.tomicevic@fsb.hr
[2] Laboratoire de Mécanique et Technologie (LMT), ENS Paris-Saclay /CNRS/ University Paris-Saclay 61 avenue du Président Wilson 94235 Cachan Cedex, France

1. Introduction

The increasing demand for lightweight structures urges the development and utilization of innovative materials optimized for weight and mechanical performance. Among all material types, fiber reinforced polymer composites (FRPs) show one the greatest flexibility to adapt the material architecture to the applied loads. Although FRPs are employed in various industrial branches, there is an absence of the full understanding of their behavior in the whole service cycle.

Damage mechanisms occurring in FRPs are heterogeneous and initiate mostly in-depth and then propagate at different length scales. Hence, X-Ray computed tomography (XCT) is an appropriate inspection tool to monitor the material response in the bulk of the investigated specimen. The possibility for obtaining information on the full 3D material microstructure of the loaded specimen results in a new glimpse into the science of materials. This is especially favorable for FRPs since different damage mechanisms occur while prescribing load to the sample.

The aim of this in situ experimental study was to measure the 3D kinematics of a cyclically loaded dog-bone sample from the reconstructed scans obtained via μ-tomography. For that purpose, global Digital Volume Correlation (DVC) was used to evaluate displacement and strain fields within the glass fibre/polyester resin composite.

2. Experimental procedure

2.1 Material and Methods

The experimental investigation was performed on glass fibre reinforced polyester resin composites. The R-glass fibre mat yarns with an areal density of 300 g/m^2 and 50 mm long fibres were used as the reinforcement.

The dog-bone specimen was machined from a 5.6-mm thick GFRP plate. To ensure that the specimen would break in the ligament area and not in the grips, the central part was thinned with a radius of 39 mm. The ligament was 61-mm high, while the smallest cross-section of the sample was 5×5.6 mm^2.

The access to the true deformed GFRP composite microstructure acquired during in situ experiment via XCT were analysed with a volumetric correlation algorithm. The global (*i.e.* FE-based) DVC approach [1], in which the kinematic degrees of freedom are spatially coupled, was considered to determine the kinematics in the bulk of the dog bone specimen under uniaxial loading.T4 elements [2] with 32 voxel edges were used to faithfully mesh the curved geometry of the specimen.

2.2 Experimental setup

The X-ray μ-tomographic experiment was performed in the X50+ scanner (North Star Imaging) of LMT. A uniaxial specimen of the investigated GFRP was loaded in situ with a Deben testing machine (Fig. 1). The proposed loading device with nominal load of 20 kN is supported with four pillars that allow for the transfer of the applied load. However, the robustness of the loading platform and vertical supports exclude the possibility to use the tomograph turntable. Thus, two rotational actuators are mounted in the frame of the loading device. Consequently, they enable the loaded sample to be fully rotated (*i.e.* 360° or more) under load in addition to applying torsion.

2.3 Cyclic in-situ tomography experiment

From the results obtained in a previous study [3], it was decided to cycle the sample with maximum loads corresponding to 35%, 70% of the ultimate level (Fig. 2a). During the in situ test, six

scans in loaded and unloaded stages were acquired. To perform the mechanical test in a reasonable time period, two acquisition parameters (*i.e.* HQ and LQ) were employed.

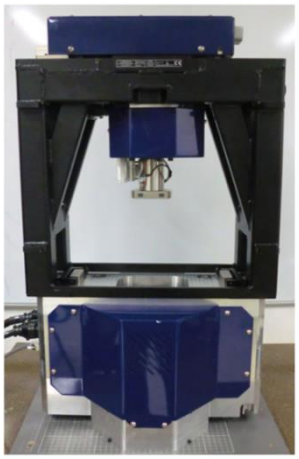

Fig. 1. Deben tension/torsion/compression testing machine

With the HQ settings (Fig. 2b), *i.e.* 800 projections, 50 ms delay, 20-frame average, 3 fps, the scanning procedure lasted approx. 2 h. Changing the number of averaging frames to 1 for the LQ settings (Fig. 2c) led to15 min acquisitions. Since two different 3D image qualities were selected, the first two scans of the mounted sample were acquired with no mechanical load.

Each tomographic scan was initially acquired with a definition of 1507 × 1507 × 1849 voxels, whose physical size was 14.6 µm, encoded as 8-bit deep gray levels. For those 3D images, the size of the ROI was adjusted to the sample geometry focusing on the thinned part of the dog-bone sample corresponding to a size of 610 × 410 × 1180 voxels.

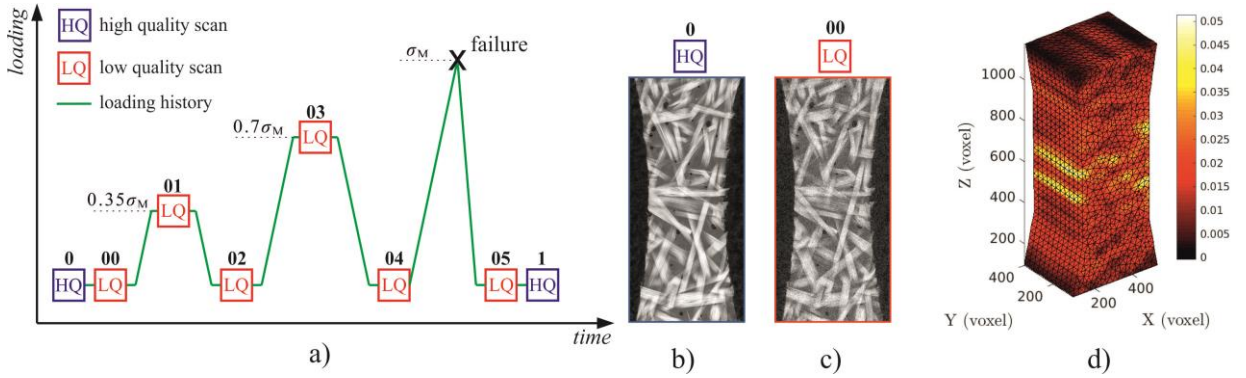

Fig. 2. (a) Schematic of the loading history and corresponding acquisitions. (b) Slice of the HQ scan 0. (c) Slice of the LQ scan 00. (d) Measured maximum principal strain via DVC.

3. Results and Conclusions

The correlation was performed between the undeformed volume (scan 0) and 'deformed' ones (scans 00-1). The HQ scan was taken as the reference due to the lowest noise level. Moreover, the most detailed information regarding the GFRP microstructure is registered with respect to the latter. Even though scans with different noise level were considered, global DVC successfully measured the kinematics over the entire 3D volume.

The maximum principal strain field evaluated for scan 3 is shown in Fig. 2d. From the measured map, several highly strained regions can be observed. The highest levels of strain are established in two horizontal bands on the left side of the notch. Furthermore, on the face normal to Y direction, several strain localizations are identified and quantified.

References

[1] Roux, S., Hild, F., Viot, P.,Bernard, D. Three-dimensional image correlation from X-ray computed tomography of solid foam.*Compos Part A*, 2008, 39(8), 1253-1265.

[2] Hild, F., Bouterf, A., Chamoin, L., Mathieu, F., Neggers, J., Pled F., Tomičević, Z., Roux S. Toward 4D mechanical correlation. *Adv Model Simul Eng Sci*, 2016, 3(17), 1-26.

[3] Tomičević, Z., Bouterf, A., Surma, R., Hild, F.Damage observation in glass fiber reinforced composites via µ-tomography. *In 35th Danubia Adria Symposium on Advances in Experimental Mechanics Extended abstracts*, Sinaia 25-28 Sep, 2018; Pastrama, S.D., Constantinescu, D.M., Eds.; Editura PRINTECH, Bucuresti,2018,pp. 53-54.

INFLUENCE OF SURFACE ROUGHNESS ON ADDITIVELY MANUFACTURED ALUMINUM COMPONENTS

Sebastian SPRINGER[1], Wolfgang SCHNELLER[1], Martin LEITNER[1], Florian GRÜN[1]

[1] Montanuniversität Leoben, Department Product Engineering, Chair of Mechanical Engineering, Franz-Josef-Straße 18, 8700 Leoben, Austria, E-mail: sebastian.springer@unileoben.ac.at

1. Introduction

Additive manufacturing (AM), in particular selective laser melting, is increasingly gaining importance in fabrication of complex components. A benefit of AM is the possibility to manufacture topologically optimized, lightweight parts [1]. However, a mechanical surface treatment of these complex structures is only possible to a limit extent or even not at all. A rough, non-machined surface acts like micro notches and influences the fatigue strength of AM components [2].

To assess the fatigue strength of parts with rough surfaces, standardized methods applying reduction factors, for example in the FKM guideline [3], exist. Mostly, these reduction factors are only applicable for directed and machined structures and within these concepts, only line-based surface parameters, according DIN EN ISO 4287, are included.

The aim of this research work is the assessment of as-built surfaces on the fatigue strength of AM aluminum components. In addition, area-based roughness parameters, according to DIN EN ISO 25178, are determined and applied for an advanced assessment of surface roughness effects on the fatigue strength.

2. Surface characterization

For the characterization of the unprocessed (as-built) surface and the determination of characteristic roughness parameters, the surface topography of each specimen was scanned with a digital light microscope. The scanned surface topography was subsequently processed by a user defined evaluation routine. Furthermore, the captured surface profile was filtered into a roughness and a waviness profile using a second-order robust Gaussian regression filter. The obtained areal roughness map was utilized to determine characteristic roughness parameters, which describes the as-built surface, see Fig. 1. The area-based arithmetic mean roughness S_a for the unprocessed surface is evaluated to 11.5 µm and the line-based arithmetic mean roughness R_a to 10.9 µm.

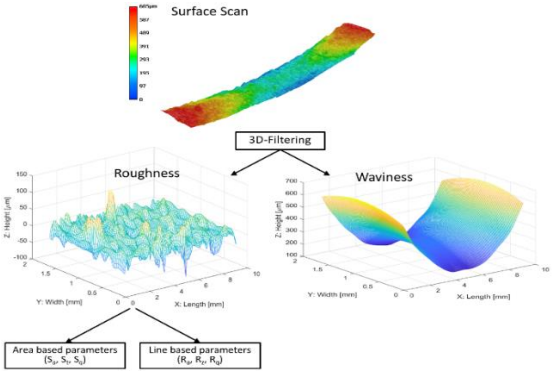

Fig. 1. Evaluation of surface parameters.

3. Experimental Results

The fatigue tests were performed under tension/compression at a load stress ratio of R= -1. One test series exhibits a machined, polished surface condition (P-AB) and a second batch features the unprocessed surface condition (UP-AB). The specimens were not heat treated. In Fig. 2. the results of the fatigue tests are shown. The results revealed a reduction in fatigue strength by 65%, comparing the rough specimen (b) to the machined test series (a).

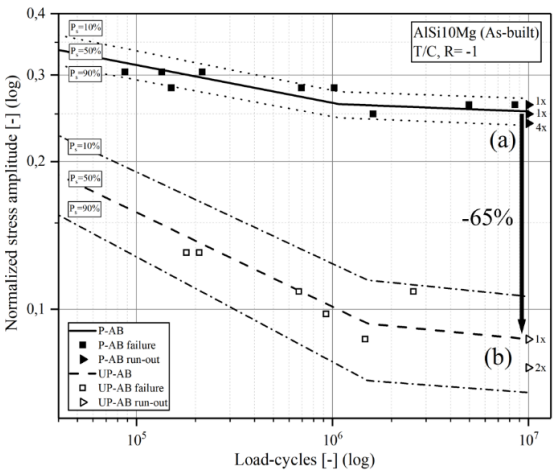

Fig. 2. Normalized S/N curves.

In Table 1. the fatigue strength (normalized to the nominal ultimate tensile strength of the base material) for a survival probability of 50% and the slope in the finite region is tabulated.

Table 1. High cycle fatigue test results.

Test-series	Surface condition	Normalized fatigue strength	Finite slope k_1
P-AB	Machined	0.253	13.0
UP-AB	As-built	0.087	5.2

To characterize the failure origin, an extensive fracture surface analysis was carried out for every tested specimen using a digital light microscope. In Fig. 3. the fractured surfaces of two specimens are illustrated. Within the fracture surface analysis, two different failure mechanism were observed. In case of the specimens with polished surfaces, the crack initiated from surface near pores (a). For the unprocessed surface condition, the failure originated from roughness valleys (b).

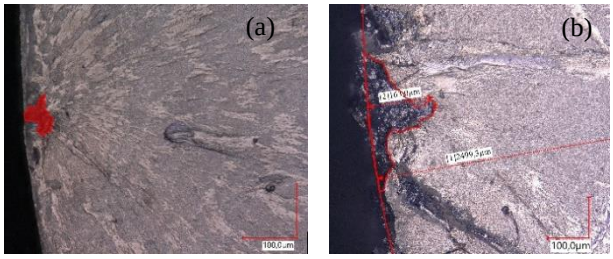

Fig. 3. Microscopic images of two characteristic defects

4. Assessment of surface effect on fatigue

For the assessment of the surface roughness effect on the fatigue strength, a model based on a stress concentration factor, according to a concept of Peterson, see Eq. (1), was applied [4]. Whereby, t stands for the notch depth and r is the notch root radius.

$$K_t = 1 + 2\sqrt{\frac{t}{r}} \qquad (1)$$

To estimate the reduction of the fatigue strength in case of a rough surface, the notch depth t was calculated as the mean value of the area-based maximum surface deviation S_t. The average notch ground radius r was measured in longitudinal direction of the scanned surfaces. In Table 2. the evaluated values for the analytical approach and the resulting stress concentration factor K_t are given. To facilitate a conservative approach, the support effect was not accounted for and the stress concentration factor K_t was equated to the notch factor K_f.

Table 2. Values for analytical estimation of K_t.

Test-series	Mean notch radius r	Notch depth t	K_t
UP-AB	197.6 µm	167.1 µm	2.86

The reduced fatigue strength $\sigma_{D,rough}$ of the unprocessed surface condition was estimated by dividing the experimental fatigue strength $\sigma_{D,polished}$ of the polished specimen, by the stress concentration factor K_t due to of the rough surface. A comparison of the estimated reduced fatigue strength $\sigma_{D,rough}$ with the experimentally determined fatigue strength $\sigma_{D,rough,exp}$ shows a sound correlation, see Table 3.

Table 3. Comparison of fatigue strength values.

$\sigma_{D,polished}$	K_t	$\sigma_{D,rough}$	$\sigma_{D,rough,exp}$	Deviation
0.253	2.86	0.089	0.087	+2.3%

Conclusions

Due to the micro notch effect of rough surfaces, the fatigue strength is significantly reduced. The presented evaluation concept, applying a stress concentration factor according to Peterson, allows a good estimation of the fatigue strength of AM structures including the surface roughness effect. Future research activities will focus on the impact of residual stresses and the support effect in order to holistically characterize influencing factors on the fatigue strength of AM components.

Acknowledgements

Special thanks are given to the Austrian Research Promotion Agency (FFG) that funded the research project by funds of the Federal Ministry for Transport, Innovation and Technology (bmvit) and the Federal Ministry for Digital and Economic Affairs (bmdw).

References

[1] Buchmayr, B., Panzl, G. Eine SWOT-Analyse zum Einsatz der Additiven Fertigung für metallische Bauteile. *BHM Berg- und Hüttenmännische Monatshefte*, 2015, 160(1), 15-20.

[2] Aboulkhair, N. T., Maskery, I., Tuck, C., Ashcroft, I., Everitt, N. M. Improving the fatigue behaviour of a selectively laser melted aluminium alloy. *Materials & Design*, 2016, 104, 174-182.

[3] Forschungskuratorium Maschinenbau. *Rechnerischer Festigkeitsnachweis für Maschinenbauteile aus Stahl, Eisenguss- und Aluminiumwerkstoffen*; VDMA Verlag: Frankfurt/Main, 2012.

[4] Pilkey, W. D. *Peterson's Stress Concentration Factors*; John Wiley & Sons Inc.: Chichester, 2008.

STRESS AND STRAIN DISTRIBUTION IN PERFORATED PLATE LOADED IN MEDIAN PLANE

Adrian PASCU[1], Valentin OLEKSIK[1], Eugen AVRIGEAN[1]

[1] Lucian Blaga University of Sibiu, 10, Victoriei Boulevard, Sibiu, Romania, E-mail: adrian.pascu@ulbsibiu.ro; valentin.oleksik@ulbsibiu.ro; eugen.avrigean@ulbsibiu.ro

1. Introduction

As is well known, the distribution of stresses in thin planar plates with circular holes and loaded by forces situated in the median plane of the plate can be determined using by analytical, numerical and experimental methods. Analytical solutions [1], [2] are typically obtained for simple cases by using complex variable functions and conforming transformations. In the case of complex structures, their analytical solution is rather difficult, the solutions being somewhat complicated.

As for the numerical methods, they allow for an approximation of any problem of static analysis, but in some cases the results obtained are not covert, the values obtained are often undervalued and sometimes these results are affected by very high errors (bigger then 15-20%).

From the experimental methods that can be used to determine the stress distribution pattern in a thin planar plate with circular holes, is the photoelasticity method. In the present paper is presented a comparative study between the experimental study, using the photoelasticity method, on plates with 7 circular holes having the same diameter, holes arranged in zig-zag, thus determining the state of tension on the perimeter of the holes and the values of the stress concentration coefficient, respectively the results obtained by numerical analysis, by the finite element method, for the same types of structures.

2. Experimental study

The perforated plates studied in this paper had 7 zig-zag holes in two configurations, as shown in figure 1.

For the experimental study, the plates were made from polycarbonate with a thickness of 4 mm. For a first plate, the diameters of the circular holes have 14 mm, and the distance between centers of two neighboring holes is 20 mm in the horizontal direction and in the vertical direction. For the second plate we increase the diameter of holes at 18 mm, keeping the same distance between centers of two neighboring holes in vertical direction and horizontal direction.

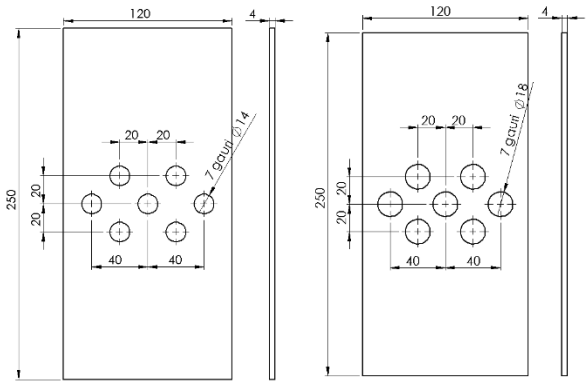

Fig. 1. Dimensions of perforated plates.

The plates thus obtained were solicited at uniaxial traction (in the direction of the Oy axis, with a uniformly distributed load (p = 5 N/mm^2) over the entire width of 120 mm of the plate and analyzed in monochromatic light, observing and photographing the distribution of isochromatic lines The applied load was chosen so as to obtain an isochromatic line field suitable for stress state analysis [3].

On the perimeter of the holes, where the stress has the maximum value, the stress is determined using next relation:

$$\sigma_{max} = N \cdot f_\sigma \qquad (1)$$

where: N is the value of the order of isochromated line (fringe) line, and f_σ is the photoelastic constant of the photoelastic material used (polycarbonate) determined using calibration method with compressed disk ($f_\sigma = 0.766$ MPa/fr).

The stress concentration factor in one point from perimeter of holes can be calculated with next relation [4]:

$$\alpha_k = \frac{\sigma_{max}}{\sigma} \qquad (2)$$

where: σ is stress in one point from unperforated plate.

Figure 2 shows the mode of distribution of the isochromate lines for the plate with seven circular holes of 18 mm diameter.

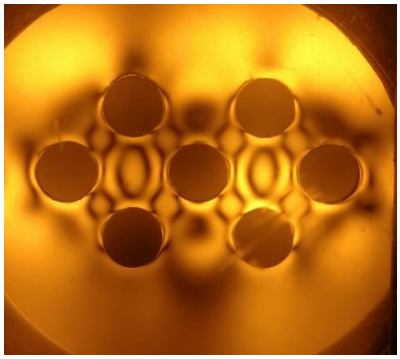

Fig. 2. Distribution of the isochromate lines.

3. Numerical simulation

Considering the geometric symmetry and loading of such a perforated plate, to shorten the time for the finite element analysis it was modeled, using the Abaqus 6.14 software package, only a quarter of the plate applying symmetry conditions to the left side respectively to the bottom side of the plate, and we apply a distributed load by the top of the plate ($p = 5$ N/mm^2).

For meshing the plates, we use shell element type (S4R - a 4-node doubly curved thin or thick shell, reduced integration, hourglass control, finite membrane strains). In figure 3 are presented a model of quarter of the plate meshed, with applied symmetry conditions and loads.

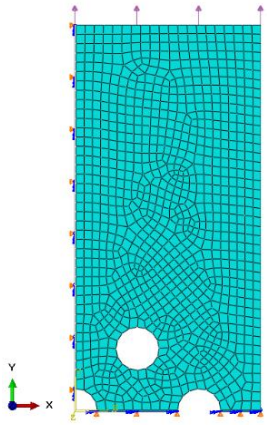

Fig. 3. Model of perforated plate meshed and loaded.

After or meshing the plates, we use shell element type (S4R - a 4-node doubly curved thin or thick shell, reduced integration, hourglass control, finite membrane strains) with approximate global size 3 mm. In figure 3 are presented a model of quarter of the plate meshed, with applied symmetry conditions and loads.

In the next figures are shows the results obtained after we are running the numerical simulation. Thus, in figure 4 are shows the Von Mises stress distribution for both case (14 mm and 18 mm diameter of holes).

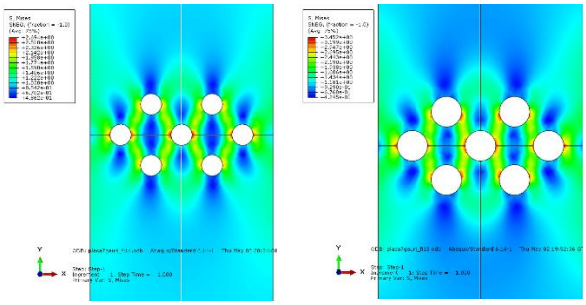

Fig. 4. Von Mises stress distribution.

Figure 5 shows distribution of first 5 isosurface obtained after we are running the numerical simulation for plate with seven circular holes of 18 mm diameter.

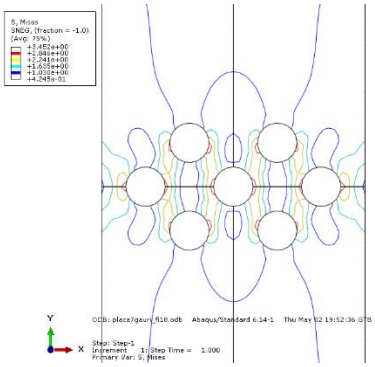

Fig. 5. Distribution of the isochromate lines.

4. Conclusions

By comparing the results obtained experimentally with those by the finite element method one can observe a good similarity between the distribution of stress in perforated plate.

References

[1] Atanasiu, C., Iliescu, N., et.al., *Modelarea stării de tensiune în jurul găurilor, nervurilor şi locurilor de aplicare a sarcinilor în plăcile plane şi curbe*. Contract de cercetare UPB-MCT, 1993-1995.

[2] Sandu, M., *Analiza stărilor de tensiuni în jurul orificiilor nervurilor şi zonelor de rezemare ale învelişurilor de rotaţie*, Teză de doctorat, UPB, 1992.

[3] Mocanu, D.R., *Analiza experimentală a tensiunilor, vol I*, Editura Tehnică, Bucureşti,1976.

[4] Pilkey, W. D., *Peterson's Stress Concentration Factors*, Wiley, New York, 1997.

ADAPTATION OF A CRUCIFORM TESTING MACHINE ZWICK/ROELL Z050 FOR BIAXIAL COMPRESSION CREEP EXPERIMENTS

Eva BINDER[1], Roland REIHSNER[1], Olaf LAHAYNE[1], Josef EBERHARDSTEINER[1], Bernhard L.A. PICHLER[1]

[1] Institute for Mechanics of Materials and Structures
Vienna University of Technology, Karlsplatz 13/E202, 1040 Vienna, Austria
E-mail: Eva.Binder@tuwien.ac.at, Roland.Reihsner@tuwien.ac.at, Olaf.Lahayne@tuwien.ac.at, Josef.Eberhardsteiner@tuwien.ac.at, Bernhard.Pichler@tuwien.ac.at

1. Introduction

The cruciform testing machine Zwick/Roell Z050 (Fig. 1) is designed for uniaxial or biaxial experiments on sheet metals, elastomers, plastics, etc. Four electromechanical testing actuators provide maximum forces up to 50 kN. They are installed in a vertically oriented support frame. Two actuators are positioned vertically, the other two horizontally.

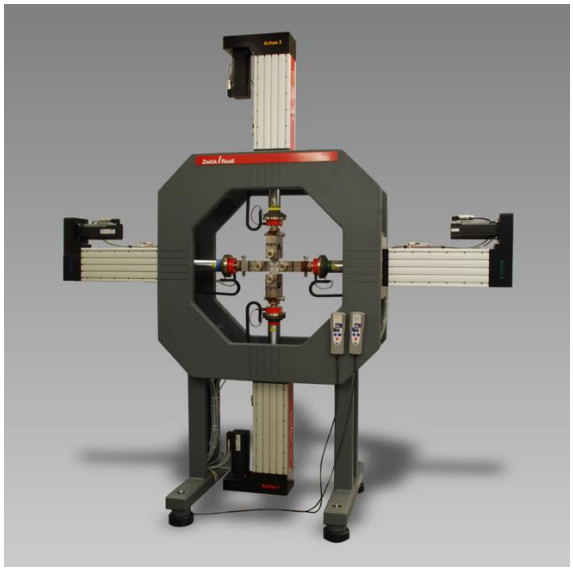

Fig. 1. Cruciform testing machine Zwick/Roell Z050 [1]

2. Adaptation for biaxial creep testing in compression

The test machine shown in Fig. 1 shall be used for biaxial creep tests of building materials in compression. Thus, the target is to achieve spatially *uniform* stress and strain states inside the test specimens. This is a challenging task, because it requires highest precision standards regarding the test samples, the load application system, and the measurement equipment used to quantify the deformation of the specimens.

2.1 Test samples

The test samples are rectangular platy prisms (Fig. 2). It is of great importance that opposite faces of the specimens are coplanar and that the differently oriented faces are mutually orthogonal. This represents a challenge for the manufacturing of the specimens.

2.2 Load application system

The application of the loading shall be uniform. In order to avoid significant in-plane bending of the specimens, it is important that the load platens are coplanar to the loaded faces of the specimens. This calls for a very accurate positioning of the specimens relative to the load platens.

Friction in the interfaces between the load platens and the loaded faces of the specimens must be reduced to the possible minimum. The principle of Saint Venant [2] implies that the self-equilibrated shear stresses decrease with increasing distance from the interfaces between the load platens and the specimen. They reach insignificant magnitudes in a distance amounting to one-times the side-length of the specimens. This implies that the *entire* volume of the specimen is affected from the influence of undesired friction-induced shear stresses activated at the surface of the specimen. In this context, brush platens enjoy great popularity (Fig. 2). Their design will be explained in more detail in the poster.

In order to avoid significant out-of-plane bending of the specimens, the out-of-plane motion of the actuators, the brush platens, and the specimen must be reduced to the possible minimum. To this end, it is important to support all four of the brush platens such that they are initially positioned inside *one* plane, and that they stay inside this plane also during testing. In this context, it must be accounted

for that the actuators (and, hence, also the brush platens) will move during testing in their axial direction. The out-of-plane support must allow this axial motion and, at the same time, it must not introduce significant axial forces into the actuators, because this would render the measurement of the forces based on the in-built load cells inaccurate. The proposed solution to this problem is a support system based on columns hinged at both ends. One end is supporting the brush platens, the other is fixed to a stiff frame construction (Fig. 2). The design of this add-on equipment will be explained in more detail in the poster.

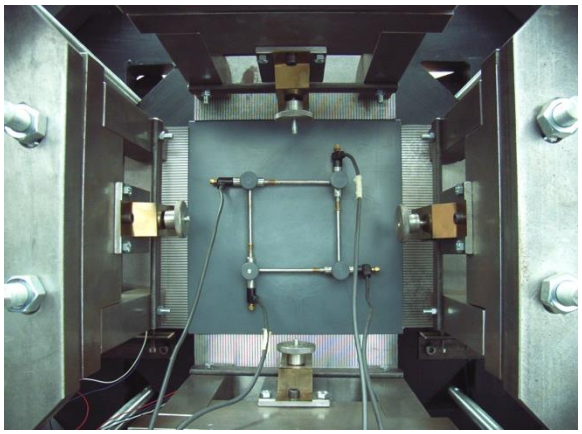

Fig. 2. Test setup showing the specimen, four Linear Variable Displacement Transducers, four brush platens, and eight columns hinged at both ends; the latter prevent out-of-plane motions of the test setup.

2.3 Measurement equipment

The testing machine provides averaged signals of the forces of two opposite actuators. In this context, it must be taken into account that undesired friction forces could be activated in the interfaces between the brush platens and the specimens. Provided that this happens, the forces of two opposite actuators could be different. This would remain unnoticed, because the testing machine does not provide the force readings of each actuator separately. This issue calls, once more, for a very careful positioning of the specimen inside the testing machine. A more detailed discussion will be provided in the poster.

A Linear Variable Displacement Transducer (LVDT) is used in order to monitor the out-of-plane motion of the center of the specimen (not shown in Fig. 2). This is part of the implemented quality management approach. The corresponding readings allow for a quantitative assessment of the functionality of the out-of-plane supports described above.

Eight LVDTs are used to measure the deformations of the test specimens. They are directly attached to the surface of the specimens. Four at the front-side (Fig. 2) and the other four at the backside of the specimen. Two out of the four LVTDs, which are positioned on the same side of the specimen, are aligned with the vertical loading axis, the remaining two with the horizontal loading axis. The chosen setup allows, again in the sense of a quality management approach, for quantifying both in-plane bending and out-of-plane bending of the specimens. In addition, it allows for compensating of the bending, as long as it appears to be acceptably small.

2.4 Reference samples

In order to be able to perform highest-quality experiments, standard test with a reference sample will be carried out always before and after actual testing. Given the interest in carrying out biaxial creep tests in compression, the reference sample shall also be creep active when subjected to biaxial compression. Therefore, polyvinylchloride was used as the material for the reference specimen (Fig. 2).

3. Conclusions

Biaxial creep testing is a rather challenging task, provided that highest precision standards are required. This calls for a very careful design of the test samples, the load application system, the measurement equipment, and, last but not least, for interdisciplinary cooperation with desirably strong contributions from experienced physicists, mechanical engineers, and civil engineers.

Acknowledgements

Interesting discussions and support regarding the design and realization of the out-of-plane support system as well as the brush platens provided by Ing. Christian Schmid and by Wolfgang Dörner are gratefully acknowledged.

References

[1] Specifications of the Zwick/Roell cruciform biaxial testing machine Z050. Available online at: https://www.zwickroell.com/en/biaxial-testing-machines/cruciform-testing-machine. Last access: April 15, 2019.

[2] Barré de Saint Venant. Mémoire sur la torsion des prismes, [Memory on twisting prisms], Mémoires des Savants étrangers [Memoires of foreign scholars]. Comptes rendues de l'Académie des Sciences, 14:233-560, 1855.

STRAIN ANALYSIS IN NARROW BOREHOLES BY MEANS OF MICROSCOPIC DIGITAL IMAGE CORRELATION

Edgar PERETZKI[1], Thomas LEHMANN[1], Martin STOCKMANN[1], Jörn IHLEMANN[1]

[1] Chemnitz University of Technology, Chair of Solid Mechanics, Reichenhainer Str. 70, 09126 Chemnitz, Germany, E-mail: edgar.peretzki@mb.tu-chemnitz.de

1. Introduction

The Digital Image Correlation (DIC) is a frequently used method for the analysis of displacement and strain fields in experimental mechanics. It is widely used due to its versatility. Thus, analyses can be performed on very large down to microscopically small objects [1,2]. This abstract describes, how the displacement field at the bottom of a narrow borehole can be investigated using DIC. In the following section, the investigated specimen is described, as well as the application of the speckle pattern required for the DIC.

2. Specimen and speckle pattern application

For the investigations a test specimen was designed and manufactured from polycarbonate, see Fig. 1. The borehole has a diameter of 6 mm and a depth of 8 mm with a plain bottom.

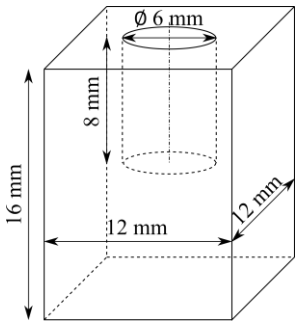

Fig. 1. Test specimen with borehole.

The DIC requires a randomly distributed speckle pattern. Its manufacture and application are described below. The structure of the speckle pattern is directly related to the size of the object field. The smaller the field, the finer the speckle pattern has to be, so that a high resolution can be achieved. The production of such a pattern was already described in [3], but slightly modified. Instead of a direct application on the measuring object, a thin foil was first produced, which was then applied to the test specimen using adhesive, see Fig. 2.

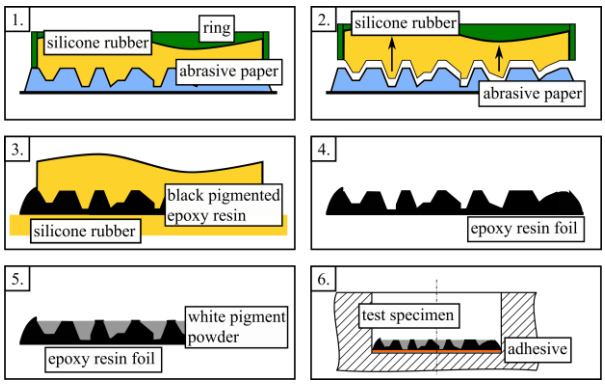

Fig. 2. Manufacturing of the speckle pattern.

The first step of the preparation was to cast liquid silicone rubber on the surface of an abrasive paper with the grain size 1000. After curing, the rubber could be separated with the negative of the abrasive paper. In the third step a drop of black pigmented epoxy resin was applied to a plane silicone rubber surface and covered with the abrasive paper negative. A thin epoxy foil was separated after curing that contains a rough surface. The hollows were coloured with white pigments. In the last step, a suitably cut foil was adhered to the hole bottom of the specimen using epoxy resin or cyanoacrylate.

3. Experimental setup

In the previous section, the preparation of the specimen was described. For future investigations, it is necessary to have a 2 mm diameter hole in the bottom of the 6 mm diameter borehole, see Fig. 3.

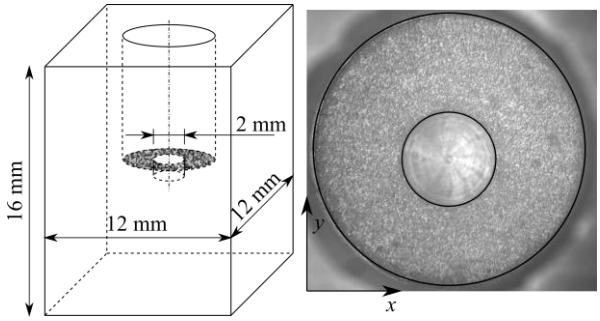

Fig. 3. Test specimen and speckle pattern at the bottom.

In Fig. 3 the test specimen and the view into the borehole containing the speckle pattern is shown. The test specimen was integrated into the experimental setup, as depicted schematically in Fig. 4.

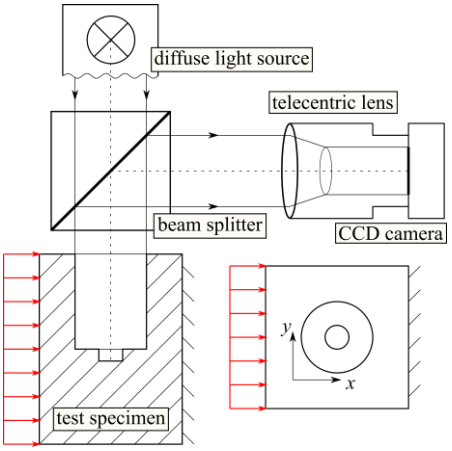

Fig. 4. Experimental Setup.

Illuminating of the borehole bottom is essential to achieve the image quality, which is required for the DIC. A beam splitter enables the illumination with simultaneous image acquisition. The images were taken by a CCD camera with a telecentric lens. Fixed in a loading device, the specimen was set under compressive forces that were monitored with a load cell (10 kN) in several load steps. With each load step, the compressive force was increased by 200 N and an image was captured. These images are the basis of the evaluation, which is described in the next section.

4. Analysis and Results

The used CCD camera has a resolution of 1280 × 980 pixel. The selection of the telecentric lens results in an object field of 8.8 mm × 6.6 mm, that allows optimal observation of the prepared annulus at the bottom of the hole.

For the evaluation, the program GOM Correlate Professional 2018 was used first. The captured images were imported into this program. The software creates facets and tracks them during the load steps. For further processing of the data in Matlab, the coordinates of the facets were exported. The displacement and strain fields were calculated from the exported data. A parametrisation was used which is based on calculations in [4] that was adapted to the annulus around the small borehole. Fig. 5 shows the measured displacement field and the calculated strain field of the annulus at a load of 1000 N. A superposition of rigid body displacement and deformation occurs. The further away the coordinates are from the clamping, the greater the displacement.

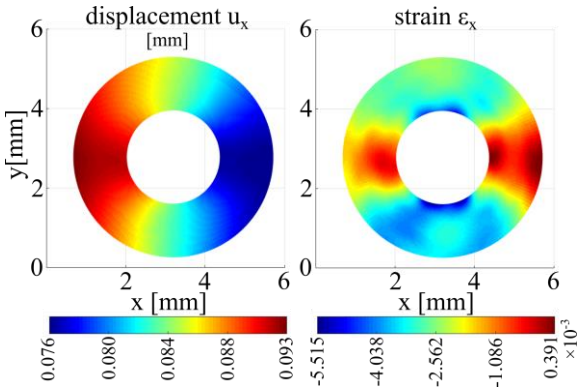

Fig. 5. Displacement and strain field of the annulus at a force of 1000 N.

The resulted strain is almost symmetrical to the horizontal in the middle of the borehole, which corresponds to the expectations.

5. Conclusions

The speckle patterns based on abrasive paper could be applied in a narrow borehole. By the described measuring strategy, it was possible to take pictures of the borehole bottom, from which displacement and strain fields could be determined by DIC and a parameterised evaluation.

Acknowledgements

This work is part of a measure which is co-financed by means of taxation on the basis of that of the deputies of the Saxon Parliament (Landtag) decided budget. The financial support is gratefully acknowledged.

References

[1] Rastogi P. K., Photomechanics. Springer Berlin Heidelberg, 2000.

[2] Sutton, M. A., Orteu, J., Schreier, H., Image correlation for shape, motion and deformation measurements. Springer Science+Business Media, 2009.

[3] Peretzki, E., Stockmann, M., Lehmann, T., Ihlemann, J. A new surface preparation method for microscopic digital image correlation applications. In *Extended abstracts of the 35th Danubia Adria Symposium*, Sinaia, 25-28 Sep, 2018, 81-82

[4] Lehmann, T., Stockmann, M., Ihlemann, J. A method for strain analyses of surfaces with curved boundaries based on measured displacement fields. In *Extended abstracts of the 35th Danubia Adria Symposium*, Sinaia, 25-28 Sep, 2018, 13-14

SIMULATION AND THERMAL ANALYSIS OF GLASS BLOWING

Paweł MAŚLAK [1], Tadeusz SMOLNICKI[2]

[1] University of Science and Technology, Faculty of Mechanical Engineering, Department of Machine Design and Research, 5 Łukasiewicza st., 50-370 Wroclaw, Poland,
e-mail: pawel.maslak@pwr.edu.pl

[2] University of Science and Technology, Faculty of Mechanical Engineering, Department of Machine Design and Research, 5 Łukasiewicza st., 50-370 Wroclaw, Poland,
e-mail: tadeusz.smolnicki@pwr.edu.pl

1. Introduction

The process of making Christmas balls is still largely a human-dependent process. The process of blowing Christmas baubles manufacturers try to automate, but only on the basis of experimental settings. In connection with this, the topic of scientific considerations emerged: how to choose the parameters of glass blowing, in order to obtain the best final results.

2. Glass properties

The thermal properties of glass refers to those properties, which depends with high range from temperature. The first is the heat capacity C or specific heat c – defined by heat needed to change the body temperature in a unit mass by one unit.

The specific heat c_p depends from the temperature, what is shown in the fig. 1. The research done by the Ulrich Fotheringham[1] shows, that is very important to do the variety of research before simulating the process.

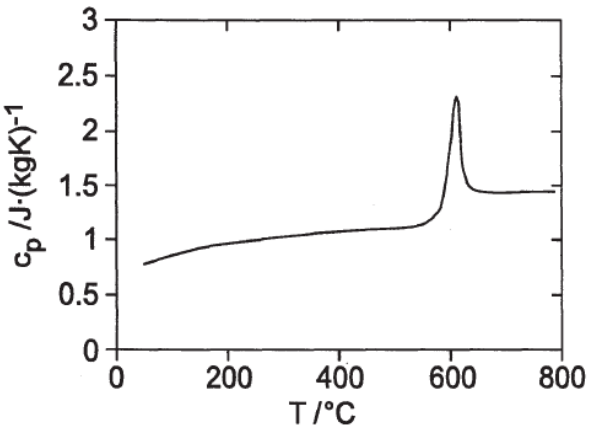

Fig. 1. Measured Cp of optically cooled Schott BK 7® glass [1].

The thermal properties that need to be defined for the analysis are:

- specific heat,
- heat capacity,
- thermal conductivity,
- thermal expansion,
- viscosity,
- emissivity.

To prepare the simulation also the mechanical properties need to be defined.

3. Thermovision measurements

Thermovision measurements were done in the factory, that produces Christmas balls. The measurement were done on each step of the process: from heating the glass tubes, thought blowing balls to melting the tube to cut out the balls. The process of blowing glass balls consist of 5 stages:

- heating tube,
- stretching to make narrowing,
- heating end of tube,
- blowing the ball,
- cut out the ball by heating and melting the tube.

View of the process is shown in the fig. 2

Fig. 2. Semi-automated process of blowing glass balls.

Thermal measurement are shown in the fig. 3-4. The temperature of annealing point is 570 °C, softening point is 820°C and the melting point is 1250°C.

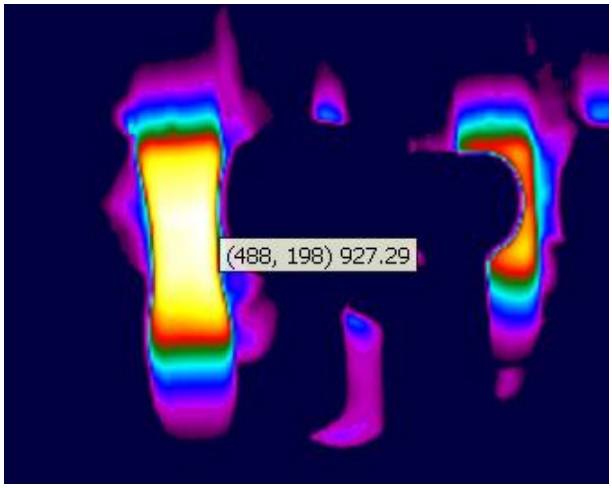

Fig. 3. Temperature during heating tube.

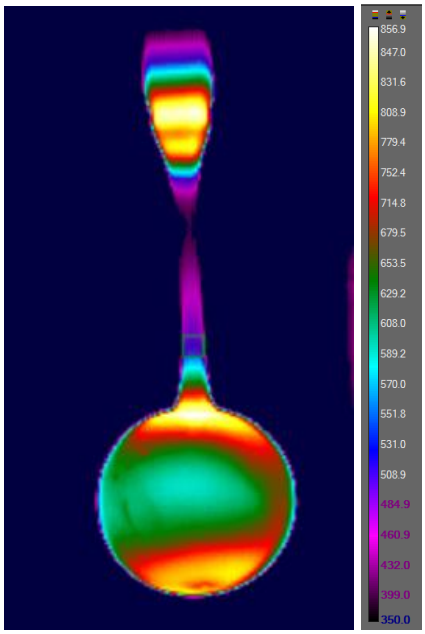

Fig. 4. Temperature after blowing ball

The measurements were done for three different size of glass balls.

4. Simulation of glass blowing

Simulation of the glass balls blowing process has been carried out in several stages. The calculations were done in Abaqus and in NX Siemens. The static, thermal and dynamic analysis were conducted[2,3]. Some of the results from the analysis are shown in the fig. 5.

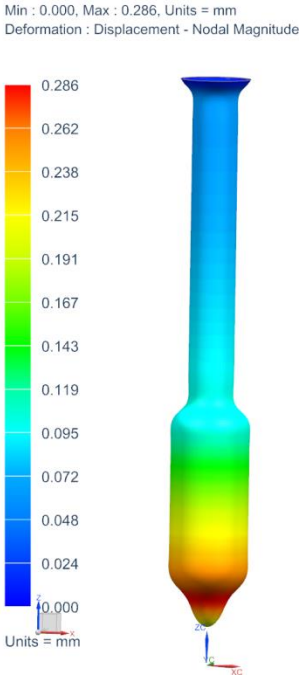

Fig. 5. Analysis of stretching to make narrowing – displacement [mm].

In the full article more results will be shown.

5. Conclusions

To prepare the good quality simulation of the glass blowing it need to get many data of glass temperature-dependent properties.

The simulation was correlated with the experiment.

After correlation it was possible to prepare new simulation for other thickness of glass tube and variety of temperature in process to predict how the glass will behave.

References

[1] Bach H.,Neuroth N. The *Properties of Optical Glass*, Springer 1998.
[2] Maślak P., Smolnicki T. *Strength and Fatigue Analysis of the Welding Connection on the Compressed Air Tank*, Proceedings of the 14th International Scientific Conference: Computer Aided Engineering, Springer 2018
[3] Rusiński E., Czmochowski J., Smolnicki T.: *Zaawansowana metoda elementów skończonych w konstrukcjach nośnych*, Oficyna Wydaw. PWroc., 2000

ELECTRIC AND ACOUSTIC ACTIVITY IN NOTCHED FIBER-REINFORCED CONCRETE BEAMS UNDER THREE-POINT BENDING

Dimos TRIANTIS[1], Dimitri K. TSAOUSI[1], Ermioni D. PASIOU[2], Stavros K. KOURKOULIS[2]

[1] Electronic Devices and Materials Laboratory, University of West Attica, Greece
E-mail: triantis@uniwa.gr; jimcaushi@gmail.com
[2] Laboratory for Testing and Materials, Dept of Mechanics, National Technical University of Athens, Greece
E-mail: epasiou@teemail.gr; stakkour@central.ntua.gr

1. Introduction

An experimental study is presented, aiming to comparatively consider the electric and acoustic activity in fiber reinforced concrete beams subjected to three-point bending (3PB). The study is part of an ongoing project attempting to detect phenomena considered as warning signals of upcoming catastrophic fracture, in case brittle materials are loaded mechanically at levels approaching the critical ones.

In this direction, a mature and well established monitoring tool (i.e., Acoustic Emissions - AE) is used, in conjunction with a relatively new sensing technique, based on the detection of very weak electric currents (known as Pressure Stimulated Currents - PSC [1]), produced during the various damage processes preceding and leading up to final macroscopic fracture of brittle materials.

It is concluded that, independently of the nature of the reinforcing fibers, both techniques (i.e., AE and PSC) follow pretty faithfully the time evolution of the respective mechanical quantities and, what is more important, they provide well distinguishable features considered as pre-failure indicators.

2. The experimental protocol

Prismatic concrete beams (length L=700 mm) of square cross section (150x150 mm^2) were subjected to 3PB with the aid of a stiff servo-hydraulic loading frame. The beams were mechanically notched at their central section. The depth and the width of the notches were equal to w=25 mm and s=5 mm, respectively. Three types of specimens were tested: (i) without reinforcement, (ii) with short steel fibers, at a portion of 25 kg/m^3 and (iii) with short plastic fibers, at a portion of 4 kg/m^3 (denoted from here on as "R"-, "M"- and "P"- type, respectively.

The beams were supported with the aid of two rollers (diameter d=30 mm) at a distance of 300 mm from either side of the notch. The load was imposed at the central section with the aid of a third roller of the same diameter. Eight acoustic and two electric sensors, attached at strategic points of the specimens, recorded the acoustic and electric activity. In addition, a clip-gauge was used to record the Notch Mouth Opening Displacement - NMOD.

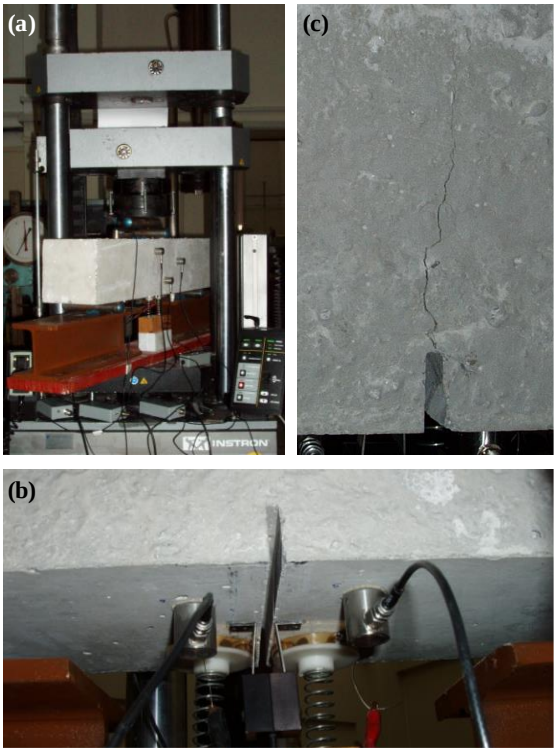

Fig. 1. (a) The experimental set-up; (b) View of the sensors at the lower side of the specimens; (c) Typical slow crack propagation pattern for reinforced beams.

The load was applied monotonically until fracture, under displacement control mode, at a rate of 0.08 mm/min (for NMOD values lower than 1 mm) and 0.20 mm/min from this NMOD level on.

3. Experimental results

The NMOD is plotted as a function of the stress imposed for all three types of specimens in Fig.2. It is seen that while the gain in strength is rather small

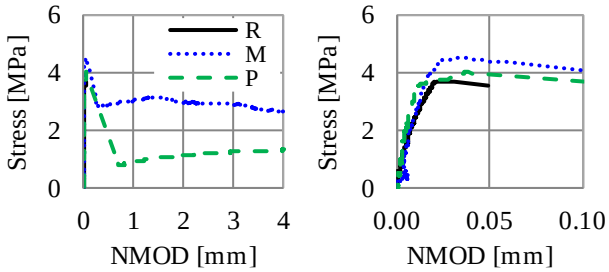

Fig. 2. Effective stress versus NMOD (left plot) and a detailed view for very small NMOD values (right plot).

(especially for the specimens reinforced with plastic fibers) the gain in ductility is huge for both the M- and P-type of specimens.

The PSC recorded is plotted as a function of the normalized (over the duration of the tests) time in Fig.3a. The electric activity for the P-specimens is almost identical to that of the unreinforced ones. On the contrary, the electric activity for the M-type is quite different: the PSC is of much higher intensity and the plot is characterized by a dense network of successive peaks. The acoustic activity, represented by the cumulative number of acoustic hits, is plotted in a semi logarithmic scale in Fig.3b. Again the R- and P-specimens exhibit almost identical behaviour while that of the M-specimens is clearly different.

4. Discussion and conclusions

According to the familiar approach for classifying cracking modes, based on the relation between

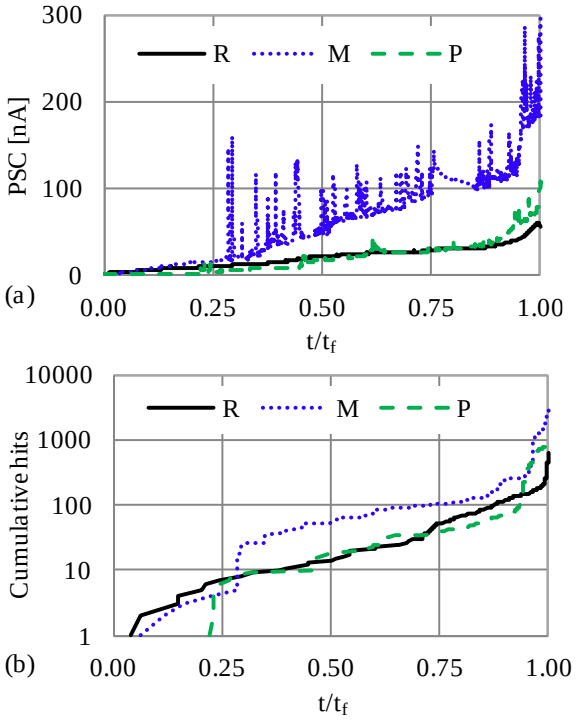

Fig. 3. (a) Electric and (b) acoustic activity vs. time.

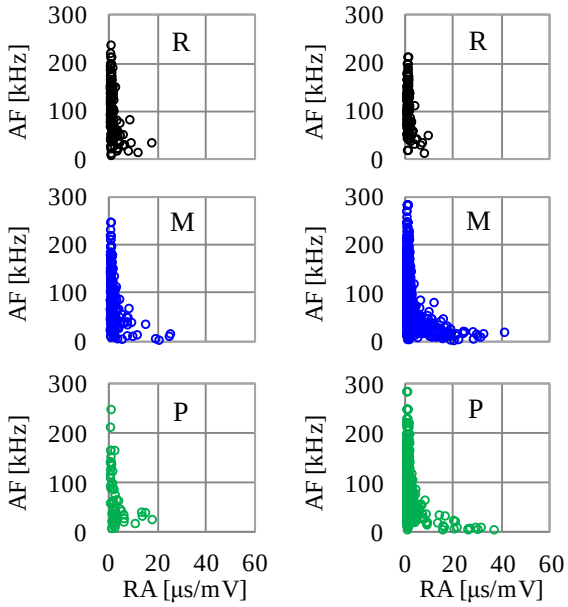

Fig. 4. AF vs. RA (left: early-, right: ultimate-load steps).

the Rise time per Amplitude (RA) and the respective Average Frequency (AF) of the AE signals [2], it can be concluded that: During the first loading steps (up to about 90% of the fracture load) the cracking mode is almost exclusively tensile (Fig.4, left column). For loads exceeding 90% of the fracture load events of shear nature (almost 5% of the total events detected) appear (Fig.4, right column).

The time evolution of the cumulative AE energy and the PSC is shown in Fig.5 for a P-specimen. The similarity of the plots is obvious. Moreover, abrupt increases of the AE energy are accompanied by peaks of the PSC, while both quantities exhibit characteristic changes well in advance of fracture.

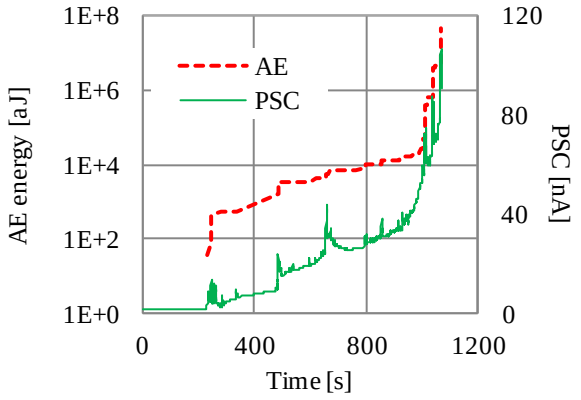

Fig. 5. The cumulative AE energy and the PSC vs. time.

References

[1] Triantis, D. et al. An analysis of pressure stimulated currents (PSC), in marble samples under mechanical stress. *Phys Chem Earth*, 2006, 31, 234-239.
[2] Grosse, C.U., Ohtsu, M. *Acoustic Emission testing*; Springer-Verlag, Heidelberg, Berlin 2008.

ELECTRICAL RESISTANCE TOMOGRAPHY IN A SMALL THIN SQUARE-SHAPED AREA

Marek STEPNOWSKI[1], Iga KOWALIK[1], Paweł PYRZANOWSKI[1]

[1] Warsaw University of Technology, Institute of Aeronautics and Applied Mechanics, Nowowiejska str. 24, 00-665, Warsaw, Poland, e-mail: mstepnowski@meil.pw.edu.pl, pyrzan@meil.pw.edu.pl

1. Introduction

For conductive materials, such as carbon-epoxy composites, Electrical Resistivity Tomography (ERT) can be used to detect and localize damages of the structures [1, 2, 3]. Unfortunately, their relatively high conductivity makes it necessary to measure very small electrical currents, which is associated with large problems, especially the low signal-to-noise ratio. It may be a good solution to apply a graphite layer with a relatively high specific resistance to the non-conductive surface of the investigated element [4].

In the present study a resistance tomography method was used at square specimen. The influence of the damage in the conductive layer on resistance changes between electrodes in a square plate was investigated.

2. Materials and methodology

Used specimens had a form of a thin graphite layer applied at non-conductive base. Conductive area has shape of 50 mm x 50 mm square with 18 equal spaced silver electrodes on each edge (layer thickness about 10 μm). Electrical resistivity of electrodes was much lower than the graphite layer. Damage of surface was created by 4 mm diameter hole. Electrical resistance between pairs of opposites electrodes was measured at 4 directions: *x*,*y* prescribed by the edges of specimen and *u*,*v* parallel to diagonals. Measurements were taken for specimen without and with damage performed with a high accuracy digital multimeter Agilent 34401A.

Numerical analysis was performed in ANSYS code using electric analysis module. Constant current flow was simulated and the voltage change was measured.

3. Results

Figure 1 shows specimen and measurement results expressed by relative change in normalized resistance obtained by experiment and FEM analysis.

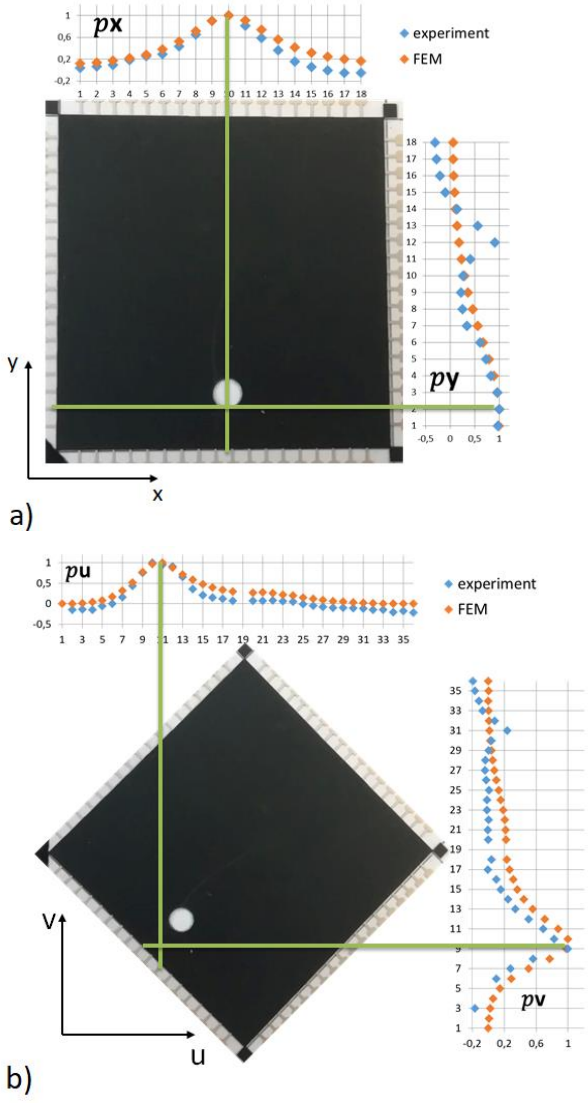

Fig. 1. Experimental and FEM results. Distribution of resistance between pairs of electrodes: a) direction x,y; b) direction u,v.

The resistance was measured at directions x,y (18 electrodes couples each) and u,v (36 electrodes couples each). There is visible increase in resistance caused by layer damage. The change in resistance

was observed entire width of the specimen and is clearly greater on the pairs between which the damage exist. Thick green lines indicate the location of the center of the damage measured on the sample in perpendicular directions. Measurements were made for different damage locations. The largest increase in the resistance is visible on the electrodes that are closer to the edge of specimen than the damage. If damage is closer to the edge the effect is more visible. Basing on the FEM analyzes the correction functions were determined. Example of correction function shows at figure 2.

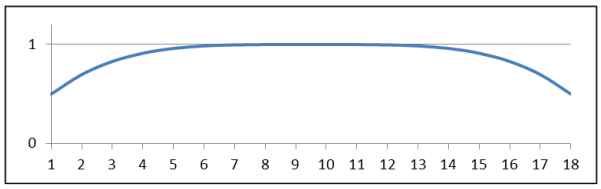

Fig. 2. Correction function – direction x.

The location of the damage can be determined by function *Z* in a similar way to that described in the work [4] (figure 3).

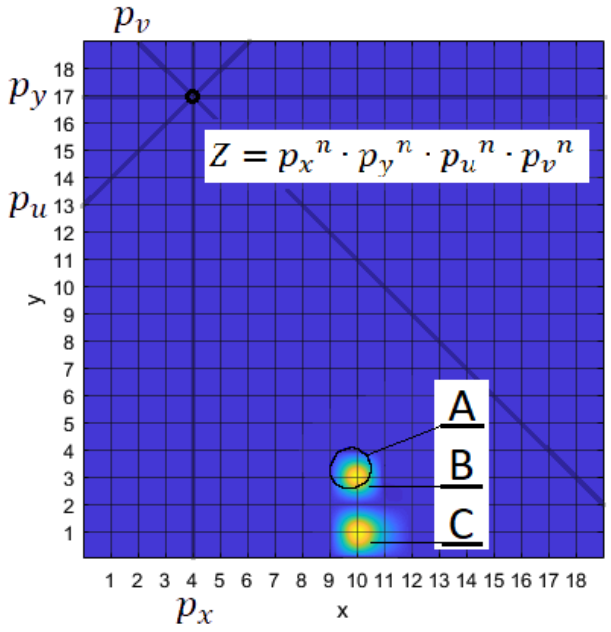

Fig. 3. Z-formula and Z-maps for experiment. A: Real hole shape; B: hole detected by Z-formula which correcting function; C: hole detected by simple Z-formula.

Figure 3 shows the real damage location (fig. 3, contour A), distribution of *Z* in the case with the use of corrective functions (fig. 3, shape B) and without the use of corrective functions (fig. 3, shape C)

4. Conclusions

In both the FEM analysis and experiment, a relationship between distribution of the resistance change and the location of the damage was observed. The influence of the edge is visible and can be corrected by the experimentally determined correction function.

The proposed method can be used for detection of damages on the surface of elements and for estimation of their location.

References

[1] Angelidis N., Khemiri N., Irving P. E.: Experimental and finite element study of the electrical potential technique for damage detection in CFRP laminates, *Smart Mat. and Struct*., 2005, 14, 147–154

[2] Schueler R., Joshi S.P., Schulte K.: Damage detection in CFRP by electrical conductivity mapping, *Composites Science and Technology*, 2001, 61(6), 921-930

[3] Gadomski J., Pyrzanowski P.: Experimental investigation of fatigue destruction of CFRP using the electrical resistance change method, *Measurement*, 2016, 87, 236-245

[4] Stepnowski M., Janczak D., Jakubowska M., Pyrzanowski P.: Detection of surface damage using resistance tomography in thin graphite layer, *Materials Today: Proceedings, (in Press)*

EFFECT OF THE SEMI-ELLIPTIC SPRING MOUNTING ON ITS STIFFNESS

Mariusz STAŃCO[1], Paulina DZIAŁAK[2]

[1] University of Science and Technology, Faculty of Mechanical Engineering, Department of Machine Design and Research, Łukasiewicza 5, 50-371 Wroclaw, Poland, e-mail: mariusz.stanco@pwr.edu.pl

[2] University of Science and Technology, Faculty of Mechanical Engineering, Department of Machine Design and Research, Łukasiewicza 5, 50-371 Wroclaw, Poland, e-mail: paulina.dzialak@pwr.edu.pl

1. Introduction

Properly selected stiffness of heavy duty vehicles suspension affects the driver and passenger comfort by reducing or increasing the level of vibrations caused by the unevenness of the road. The stiffness of the suspension should be adjusted in such a way that the frame of the vehicle overcoming the given obstacle does not move with the suspension in vertical direction. The energy generated as a result of driving through the road unevenness should mostly be absorbed by the suspension. The stiffness of the suspension in turn depends on the spring stiffness and torsional stiffness of the stabilizer. Therefore, the correct selection of the spring stiffness is extremely important.

In trucks where the traditional suspension based on leaf springs is applied, semi-elliptical springs are rarely used due to their high weight. In military vehicles semi-elliptical springs is a basic component of the front axle suspension (Fig. 1), and in many vehicles of the tandem type suspension (Fig. 2). Both types of springs are connected in their middle part with the vehicle axle by screw or with the tandem axle cradle by U-bolts [1,4] interconnected by a clip (Fig. 3).

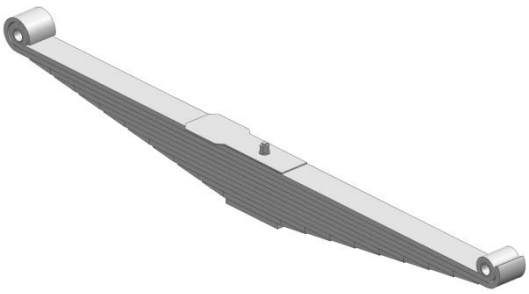

Fig. 1. Semi-elliptical spring of the front axle.

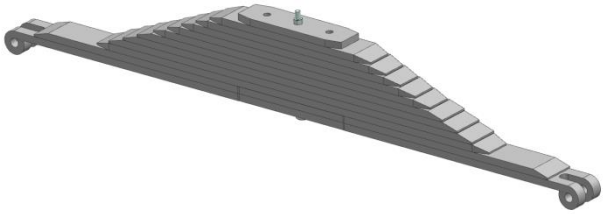

Fig. 2. Tandem type semi-elliptical spring.

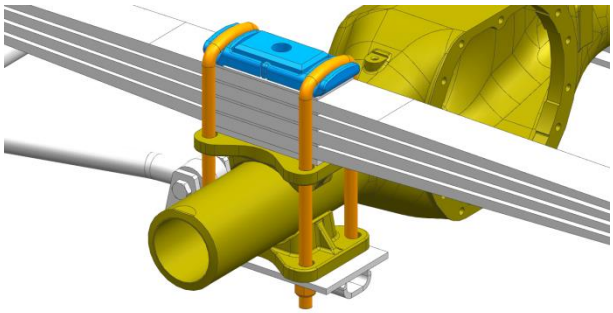

Fig. 3. Mounting of the spring on the vehicle axle.

2. Experimental studies

The measurements of spring deflection and the deflection force were performed. On their basis spring stiffness characteristics were determined. The measurements were made for a semi-elliptic spring with a length of 1600mm consisting of nine leaves [2]. Measurements were made on one spring in two different variants:

- spring fastened by a central screw (Fig. 4a),

- spring clamped with the U-bolts tightened with the required torque (Fig. 4b).

The second variant of the spring represents the actual spring mounting on the truck during its operation.

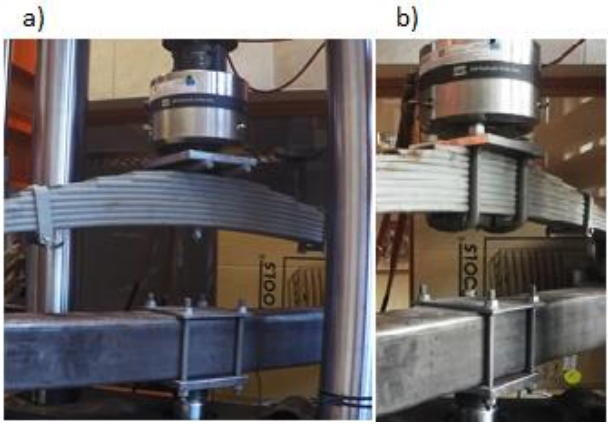

Fig. 4. Semi-elliptical spring; a – fastened with central screw, b – connected with U-bolts.

Hysteresis loops for both versions of the spring were determined based on the conducted tests (Figures 5, 6). The stiffness of both springs was also obtained in compliance with current standards [3].

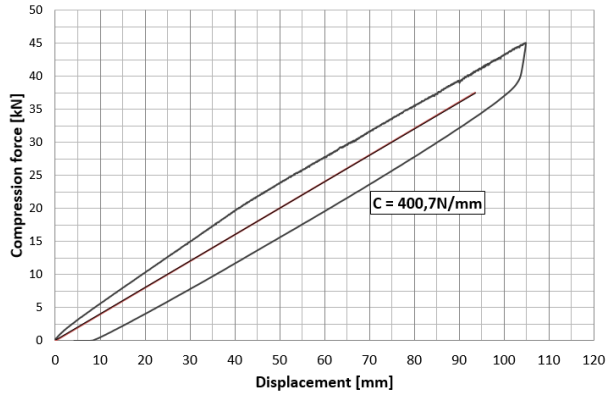

Fig. 5. Hysteresis loop obtained during the compression of the spring fastened with the clamp.

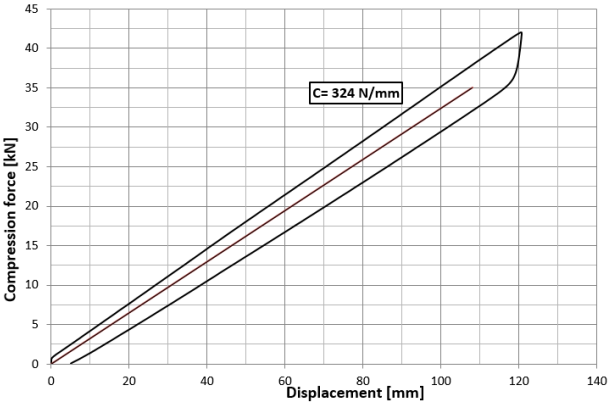

Fig. 6. Hysteresis loop obtained during the compression of the spring fastened with the central screw.

The studies of the spring stiffness with mounting similar to the one on the actual vehicle frame is 23% higher than the stiffness of the spring tested according to the guidelines recommended by the standard. This results from the fact that the leaf springs fastened with the clip in the central part are stiffened and are not allowed to work freely. The distance between the U-bolts is about 160mm. This reduce the active length of the spring by 10%.

The hysteresis loops of both springs also differ from each other (Fig. 7). In the spring connected with U-bolts, significant influence of the friction may be noticed. It generates strain, contributing to increased wear of the leaves.

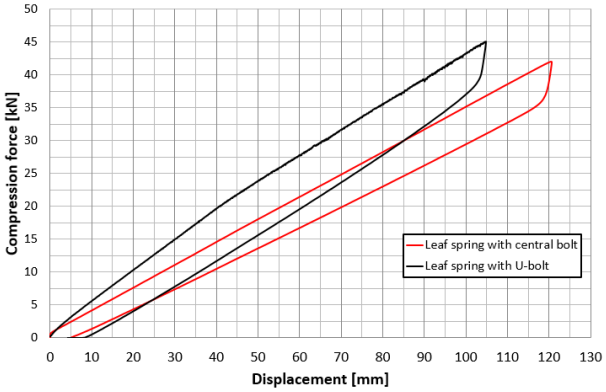

Fig. 7. Hysteresis loops of both springs.

3. Conclusions

Presented results of the experimental studies conducted on the semi-elliptical spring indicated that in the process of a new leaf spring selection it is necessary to take into consideration the mounting on the axle. In the analysed case, the actual stiffness of the spring was 23% higher than the stiffness determined on the basis of the recognised standard.

References

[1] Stańco M., Działak P., Hejduk M.: Failure analysis of a damaged U-bolt top plate in a leaf spring. *Proceedings of the 14th International Scientific Conference: Computer Aided Engineering*, 2019, 736-743

[2] Stańco M., Iluk A., Działak P., Numerical and experimental analysis of stress of a semi-elliptical spring. *Materials Today: Proceedings*, 5 (13), Part 2, 2018, 26760-26765

[3] PN-S-47250:1990: Pojazdy samochodowe i przyczepy - Resory piórowe - Wymagania i badania

[4] SAE, Spring Design Manual – Design and Application of Leaf Springs, HS-744, AE-11,90, *SAE International*, 1990.

THE INFLUENCE OF THE CALLUS SHAPE AND LEVEL OF CONSOLIDATION ON STRESS AND STRAIN IN FEMUR WITH DISTRACTION INTRAMEDULLARY NAIL–FE STUDY

Jan KONVALINKA[1], Zdeněk FLORIAN[2], Petr MARCIÁN[3]

[1] Dept. of Solid Mechanics, Mechatronics and Biomechanics, Brno University of Technology, Technická 2896/2, 616 69 Brno, Czech Republic, E-mail: Jan.Konvalinka@vutbr.cz

[2] Dept. of Solid Mechanics, Mechatronics and Biomechanics, Brno University of Technology, Technická 2896/2, 616 69 Brno, Czech Republic, E-mail: marcian@fme.vutbr.cz

[3] Dept. of Solid Mechanics, Mechatronics and Biomechanics, Brno University of Technology, Technická 2896/2, 616 69 Brno, Czech Republic, E-mail: florian@fme.vutbr.cz

1. Introduction

Leg length discrepancy (LLD) is a common condition that affects up to 70 percent of the population [1]. In most cases, however, the LLD does not require surgical treatment and is treated by shoe lifts or not treated at all [1]. Surgical treatment is usually applied when the LLD is bigger than 40 mm [2].

The most common surgical technique for treating LLD is currently the distraction osteogenesis [2, 3]. The study of the distractor-bone system may provide new information about nail loading during the healing process and consequently improve the treatment strategy.

The aim of this study is to assess biomechanical performance of the distraction intramedullary nail.

2. Materials and Methods

CT images of the human femur in physiological state were obtained from the Visible Human Project datasets [4]. The model of geometry is composed of two solid parts representing the cortical and trabecular bone structure. To model the state after lengthening, i.e. femur with callus, the solid model was cut in accordance to the surgical guides for osteotomy. Different callus shapes were obtained on the basis of case studies which contained the information about the shape of callus or the x-ray images. Shapes were divided into four groups partially reflecting the classification proposed by Li et al.: fusiform, medially fusiform, cylindrical and asymmetric (see Fig. 2).

The geometrical model of distraction intramedullary nail was created based on PRECICE intramedullary nail [5]. The geometrical model of the nail is the antegrade variant with trochanteric entry.

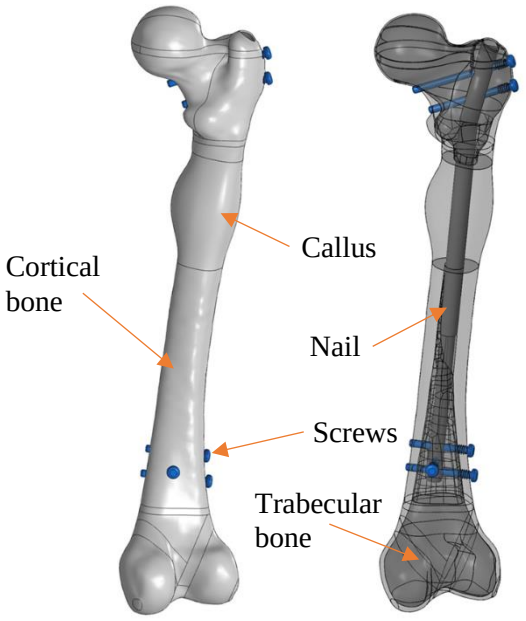

Fig. 1. Geometrical model of femur with intramedullary distraction nail and callus.

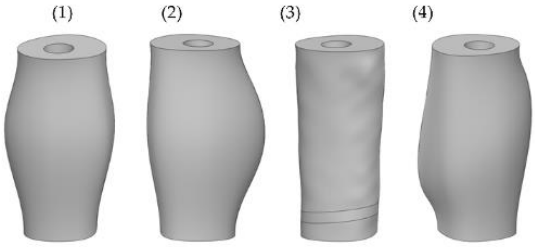

Fig. 2. Four different callus shapes used in this study: (1) Fusiform, (2) Medially fusiform, (3) Cylindrical and (4) Asymmetric.

The isotropic homogenous linear material model was used in this study; material properties of tissues

were taken from literature. Material properties of bone tissues were prescribed as follows: cortical bone E = 17 000 MPa and μ = 0.3, trabecular bone E = 800 MPa, μ = 0.3. Material properties of the callus tissues were prescribed as follows: soft tissues E = 10 MPa and μ = 0.167, bone in different stages of consolidation E = 1000, 3000 and 6000 MPa and μ = 0.3. Distraction intramedullary nail and fixation screws are made from titanium alloy Ti6Al4V with material properties E = 113 800 MPa and μ = 0.342.

All DOF on both condyles and intercondylar fossa were set to zero. The model was loaded with two static forces applied on femoral head F_H and trochanter major F_T. Three sets of force values were used to simulate different loading of the limb during the healing process corresponding to 20, 60 and 100 % of body weight (BW).

For the simulations, the ANSYS 18.1 software was used. Model of geometry was discretized using SOLID186 and SOLID187 elements, contact surfaces were created using CONTA174 and TARGE170 elements. Contact behavior between the nail parts and the bone and the nail parts and the screws was prescribed frictional with frictional coefficient 0.01. Connections between the screws and the bone and between the bone parts were defined as bonded.

3. Results and discussion

Von Mises stresses in the nail components were compared. In the nail itself there were significantly higher stresses in model with cylindrical and asymmetric callus shape in comparison to fusiform and medially fusiform callus shape. Also stresses in proximal screws were higher for cylindrical callus shape. Von Mises stresses in distal screws were significantly lower than stresses in other parts and there were small differences between callus shapes.

The influence of the level of the consolidation of the callus was investigated through the von Mises stresses in the nail under loads of partial and full weight-bearing. Maximum von Mises stresses in variant with material properties of callus for soft tissues were 533 MPa for 60 % of BW and 896 MPa for 100 % of BW which exceeds the yield strength of Ti6Al4V (890 MPa [6]). Von Mises stress in nail in variants with bony callus material properties were approximately six times lower both for partial and full weight-bearing.

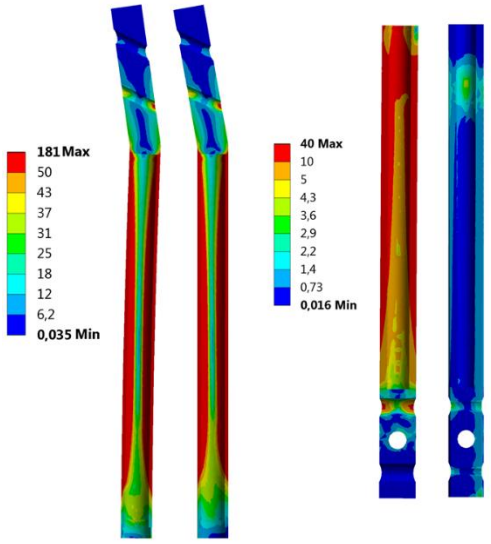

Fig. 3. Results: von Mises stress [MPa] in nail parts.

4. Conclusions

Results show significant influence of callus shape on stresses in the nail components. The variant with cylindrical callus shape shows highest stresses in nail and the variant with fusiform shape shows lowest stresses in nail.

Full weight-bearing in the early stages of consolidation results in high stress in the nail body.

References

[1] Gurney, B. Leg Length Discrepancy. *Gait Posture.* 2002 Apr;15(2):195-206.
[2] Sailhan, F. Bone lengthening (distraction osteogenesis): a literature review. *Osteoporos Int*. 2011 Jun;22(6):2011-5.
[3] Schuelke J, Meyers N, Reitmaier S, Klose S, Ignatius A, Claes L (2018) Intramembranous bone formation after callus distraction is augmented by increasing axial compressive strain. *PLoS ONE* 13(4): e0195466.
[4] University of Iowa. *Visible Human Project Datasets*. (2012).
[5] NuVasive, Inc. *PRECICE system*. [online]. 2019 [Accessed 5 May 2019]. Available from: https://www.nuvasive.com/procedures/limb-lengthening/precice-system/
[6] M. Wirwicki et al. Fatigue Testing of Titanium Alloy Ti6Al4V Used in Medical Devices, *Solid State Phenomena*, Vol. 250, pp. 250-254, 2016

IMPROVEMENT OF IMPACT PROTECTION BY KORDCARBON-CPREG-200-T-3K-EP1-42-A COMPOSITE

Radek KOTTNER[1], Sandra KAŇÁKOVÁ[1], Tomasz BOŃKOWSKI[1], Ronaldo YEUNG[2], André PUKARO[2]

[1] University of West Bohemia, Univerzitní 8, Plzeň, 301 00, Czech Republic, E-mail: kottner@kme.zcu.cz, kanaksan@students.zcu.cz, tomasz@ntc.zcu.cz;

[2] University of Campinas, Cidade Universitária Zeferino Vaz - Barão Geraldo, Campinas - SP, 13083-970, Brazil, E-mail: [rndyeung, apukaro]@gmail.com;

1. Introduction

Impact protection is an important task in many modes of transport. Composites are good energy absorbers, whether used as a part of a vehicle [1, 2] or part of a human body protector [3].

Viscoelastic foams are often used to protect motorcyclists' shoulders, elbows, and knees, There are two European standards covering motorcyclists' protective clothing against mechanical impact: EN1621-1 and EN1621-2. Since testing at temperature of 40 °C is not obligatory according these standards, the producers usually test their foam protectors only at 23 ± 2 °C. However, it was found out that the foam significantly lowers its stiffness in dependency on the rising temperature, which has distinctive influence on its maximum compression and transmitted force during an impact [4].

This work is focused on the improvement of the impact protection of a foam absorber when temperature is higher than 23 °C. The improvement using a composite shell consisting of carbon fibres and epoxy resin was investigated.

2. Materials and methodology

The foam protector SAS-TEC SCL-2 [5], which meets protection level 2 of EN1621-1, was investigated. Protection level 2 means that the maximum transmitted force *F* in the impact test must be less than 20 kN when the central area of the protector is tested. The thickness of the central area was 11 mm.

The composite shell was attached to the outside of the foam protector. The composite shell was made of 4 layers of KORDCARBON-CPREG-200-T-3K-EP1-42-A prepreg [6]. The fabric weave of the prepreg is twill 2/2. The first, third and fourth layers (counted from the interface between the foam and the shell) had the fibres oriented identical, the second layer being rotated by 45° (Fig. 1). The proper shape was ensured by the 3D printed negative mould. The ASC autoclave was used in the curing process. The thickness of the cured shell was 1.2 mm.

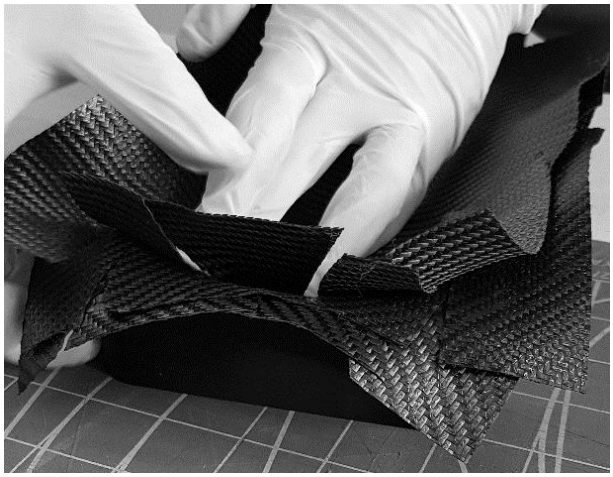

Fig. 1. Placing composite layers in mold.

Both the foam protector without the composite shell and the foam protector including the composite shell were subjected to an impact test (Fig. 2) after the protectors were one hour heated at temperature of 22, 40, and 50 °C. The impactor and the anvil corresponded to EN1621-1. The weight of the impactor with a flat steel head was 5 kg and was dropped from the height of 1 m. The diameter of the spherical anvil was 100 mm. The transmitted force *F* was measured by the force cell KISTLER 9351B. The impactor displacement was measured using Micro-Epsilon optoNCDT 2300-50 lasers. The impactor deceleration was measured by the accelerometer KISTLER 8742A5. The sampling frequency was 26 kHz.

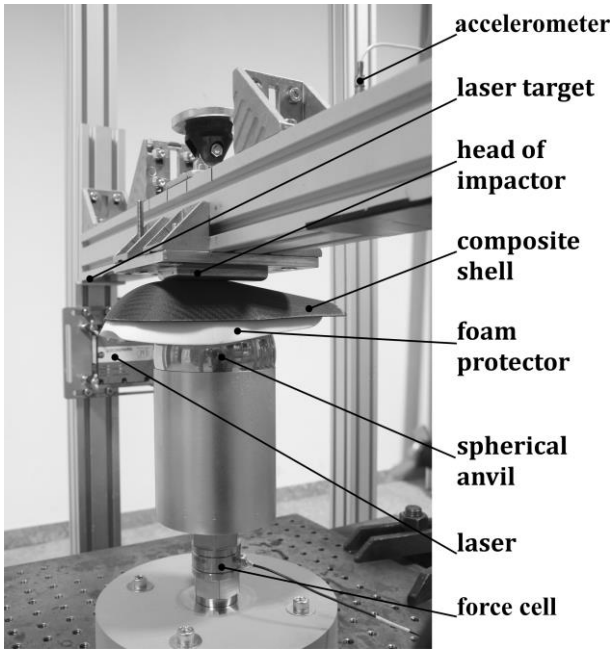

Fig. 2. Impact test.

3. Results

Fig. 3 shows the comparison of the maximum transmitted forces in the impact test. It is obvious that the values are smaller when the foam protector including the composite shell was tested. Moreover, when the protector was tested without the shell, the increase in temperature-induced force was more significant.

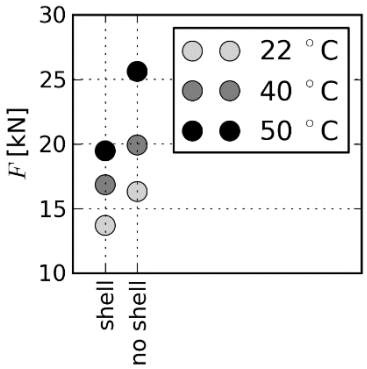

Fig. 3. Maximum transmitted forces in impact test.

The positive effect of the composite shell (reducing the maximum transmitted force) was caused by more uniform distribution of the impact force into the foam protector. When the protector was tested without the shell at a higher temperature, a foam failure occurred (a visible hole at the point of contact with the top of the spherical anvil, see Fig. 4).

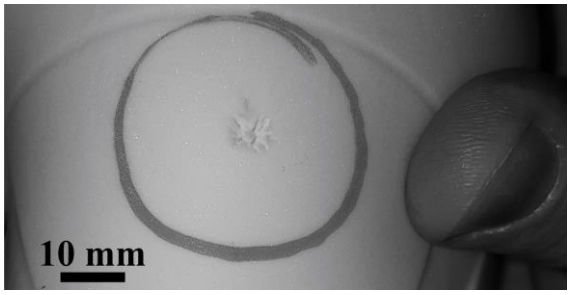

Fig. 4. Failure of foam.

4. Conclusions

The positive effect of the composite shell attached to the foam energy absorber was demonstrated. In future, obtained experimental data will be used for the validation of numerical models of the investigated foam and composite.

Acknowledgements

This publication was supported from the European Regional Development Fund-Project ,,Research and Development of Intelligent Components of Advanced Technologies for the Pilsen Metropolitan Area (InteCom)" (No. CZ.02.1.01/0.0/0.0/17_048/0007267) and by the internal grant project SGS-2019-002 “Biomechanical models of human body, biological tissues and biomechanical processes with application in industry and medicine”. The authors would like to thank PSí Hubík for providing foam samples.

References

[1] Muhammad Nasiruddin, S., Hambali, A., Rosidah, J., Widodo, W.S., Ahmad, M.N. A Review of Energy Absorption of Automotive Bumper Beam . *Int J Appl Eng Res*, 2017, 12(2), 238-245.
[2] Wang, T., Li, Y. Design and analysis of automotive carbon fiber composite bumper beam based on finite element analysis. *Adv Mech Eng*, 2015, 7(6), 1-12.
[3] Khosroshahi, S.F., Ghajari, M, Galvanetto, U. Assessment of the protective performance of neck braces for motorcycle riders: a finite-element study. *Int J Crashworthiness*, 2018, in press.
[4] Kaňáková, S., Kottner, R., Bońkowski, T. Influence of temperature on foam used in motorcycle protective equipment. In *Proceedings of the 57th Conference on Experimental Stress Analysis*, Luhačovice, 3-4 June, 2019; in press.
[5] *SAS-TEC body protection systems*. https://www.sas-tec.de/en/protectors/shoulder-protectors/scl-2/. Accessed May 05, 2019.
[6] *KORDCARBON*. http://www.kordcarbon.cz/produkty. Accessed May 05, 2019.

FRACTURE SURFACE OF NORMAL STRENGTH CONCRETE UNDER VARIOUS LOADING RATES

Michal MÁRA[1], Petr MÁCA[2], Radoslav SOVJÁK[3], Manfred CURBACH[4]

[1] Czech Technical University in Prague, Faculty of Civil Engineering, Experimental Centre, Prague, Czech Republic, E-mail: michal.mara@fsv.cvut.cz

[2] Technische Universität Dresden, Faculty of Civil Engineering, Institute of Concrete Structures, Dresden, Germany, E-mail: petr.maca@tu-dresden.de

[3] Czech Technical University in Prague, Faculty of Civil Engineering, Experimental Centre, Prague, Czech Republic, E-mail: sovjak@fsv.cvut.cz

[4] Technische Universität Dresden, Faculty of Civil Engineering, Institute of Concrete Structures, Dresden, Germany, E-mail: manfred.cubach@tu-dresden.de

1. Introduction

The aim of this paper is to compare the fracture areas of normal strength concrete that were subjected to various loading rates. The main objective of this paper is a presentation of measured data, which can be used to determine the speed of the applied loadings using reverse engineering. The main hypothesis is that under quasi-static loading the cracks have time to propagate along the path of least energy consumption i.e., around aggregate particles and through the weakest zones of the matrix (Figure 1a) while under impact loading the crack are forced to develop along straight paths throughout the stronger matrix zones and some aggregate particles (Fig. 1b) leading to the higher measured strengths and lower superficial area [1].

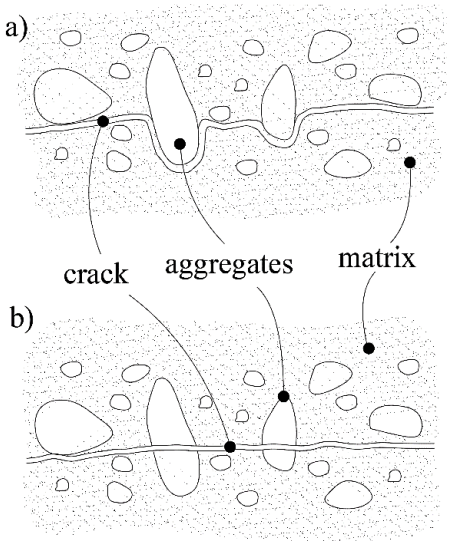

Fig. 1. Crack propagation through NSC.
a) quasi-static loading; b) increased rate loading.

2. Theoretical background

Strain rate $\dot{\varepsilon}$ can be defined as the strain that is applied to the structure over the time (Eq. 1). Unit of this value is second to the minus first (s^{-1}). The strain rate can be, therefore, defined as follows:

$$\dot{\varepsilon} = \frac{d\varepsilon}{dt} = \frac{d}{dt}\left(\frac{l-l_0}{l_0}\right) = \frac{1}{l_0}\frac{dl}{dt} = \frac{v}{l_0} \qquad (1)$$

where l is the length of the specimen after the loading was applied, l_0 is the initial length of the specimen and v is the speed of loading (mm/s). It is a well-established fact that both tensile and compressive strength increase with incrasing strain-rate [2]. This phenomenon is quantified via the dynamic increase factor (DIF), which expresses the ratio of strength measured under increased strain rate loading conditions to the strength measured under quasi-static loading conditions. It is also known that tensile mechanical properties are more sensitive to the strain rate in comparisson to the compressive mechanical properties [3].

3. Experimental part

Concrete prismatic specimens 100 mm × 100 mm × 400 mm in size were subjected to the three-point bending tests under various loading rates ranging from quasi-static to impact. Quasi-static loading rates were realized by hydraulic loading machine and impact loading was performed by using an impact pendulum device [4]. The impactor mass was 37 kg and its head was round with a diameter of 50 mm. Support rollers with a diameter of 50 mm were used, which are similar as for quasi-

static loading in order to eliminate differences arising from diffrerent support or loading geometry. From each test, both halves of the prisms were scanned by the 3D laser scanner (Fig. 2) and evaluated in the graphics programme. For every loading rate, at least 16 superficial areas were evaluated. Normal strength concrete with a target compressive strength of 37 MPa was used with a maximal aggregate size of 8 mm.

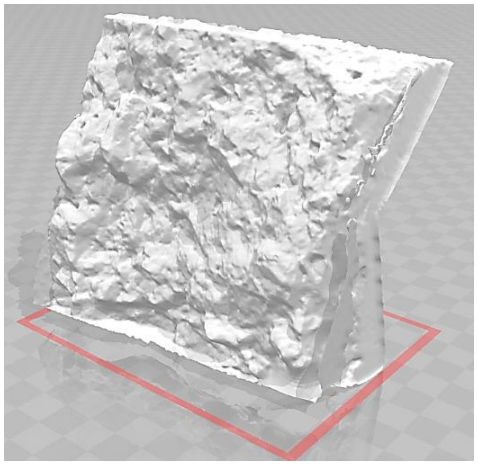

Fig. 2. Scanning of the superficial area of NSC.

4. Results and discussion

It was found out that an increase in the loading rate leads to a decrease in the fracture surface. The dependence of the superficial area on the loading rate is depicted in Fig. 3. It must be noted that a significantly large scatter of the measured data was obtained. This is caused by the natural non-homogeneity of the concrete which results from the non-uniform placement of the aggregate over the cross-section. However, it seems that with an increase in the loading rate the fracture surface area decreases. This may support the assumption that in case of impact loading, the crack does not have enough time to pass through the areas of least resistance as during the quasi-static loading. On the contrary, it follows the shortest possible path, possibly through zones with higher resistance, which yields a lower superficial area.

5. Conclusions

The major aim of this paper was to quantify the fracture surface in terms of superficial area under various loading rates. It was found, despite the significant scatter obtained, that higher loading rates yield lower superficial area in comparison to the quasi-static loading.

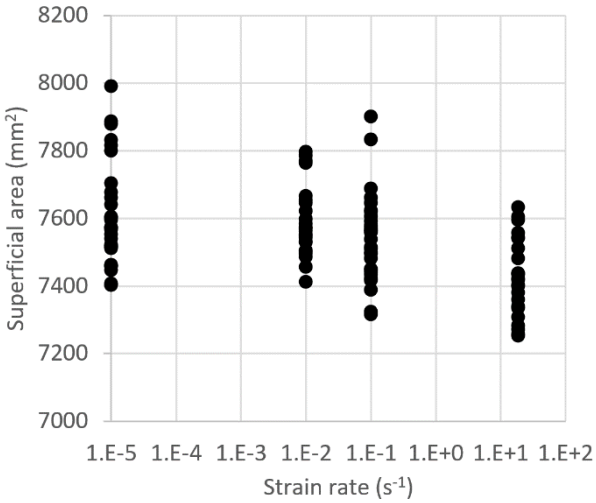

Fig. 3. Development of superficial area of NSC under various loading rates.

Acknowledgement

This work was supported by the Ministry of Interior of the Czech Republic [grant number VI20172020061]. The authors also acknowledge assistance from the technical staff at the Experimental Centre, Faculty of Civil Engineering, CTU in Prague; and the students who participated in the project.

References

[1] Tran, T.K. and Kim, D.J., 2014, "High strain rate effects on direct tensile behavior of high performance fiber reinforced cementitious composites", Cement and Concrete Composites, 45 (0), p. 186–200.

[2] Hao, Y. and Hao, H., 2014, "Influence of the concrete DIF model on the numerical predictions of RC wall responses to blast loadings", Engineering Structures, 73, p. 24–38.

[3] Hong, J., Fang, Q., Chen, L. and Kong, X., 2017, "Numerical predictions of concrete slabs under contact explosion by modified K& C material model", Construction and Building Materials, 155, p. 1013–1024.

[4] Konrád, P. and Sovják, R., 2019, "Experimental procedure for determination of the energy dissipation capacity of ultra-high-performance fibre-reinforced concrete under localized impact loading", International Journal of Protective Structures.

DEVELOPMENT OF MOBILE ROAD BARRIER MADE OF ULTRA-HIGH PERFORMANCE FIBRE-REINFORCED CONCRETE

Michal MÁRA[1], Petr KONRÁD[1], Jindřich FORNŮSEK[1], Jan ZATLOUKAL[1], Michal FRYDRÝN[2], Tomáš MIČUNEK[2], Radoslav SOVJÁK[1]

[1] Czech Technical University in Prague, Faculty of Civil Engineering, Experimental Centre
Thákurova 7, 166 29 Praha 6, Czech Republic, E-mail: sovjak@fsv.cvut.cz

[2] Czech Technical University in Prague, Faculty of Transportation Sciences, Department of Forensic Experts in Transportation, Horská 3, 128 03 Praha 2, Czech Republic, E-mail: micunek@fd.cvut.cz

1. Introduction

Mobile barriers can be used for more flexible protection against vehicle ramming attacks and can be easily removed when not needed. Since these barriers are usually not connected to the surface, their working principle usually uses just their mass and friction to stop the incoming vehicle. This means that they are very hard to set up, remove and transport. It is therefore desirable to have relatively light mobile barriers, that would interact with the impacting vehicle in such a way, that mass of the barrier is not the main stopping principle.

One such barrier is the Czech Hedgehog developed in the 1930s for military defence. The barrier consisted of three steel beams of the same length connected in their centres. The intended stopping principle was that the Hedgehog would roll underneath a moving vehicle, lifting its tracks off the ground, therefore completely immobilising it.

In this research, the Czech Hedgehog is revisited using ultra-high performance fibre-reinforced concrete with additional steel reinforcement. This barrier was tested in real life conditions using ordinary road vehicles.

2. Material

Ultra-high performance fibre-reinforced concrete (UHPFRC) that was used to create the barriers was applied in previous studies and is in detail described elsewhere [1,2]. Fibres added into the mix were straight steel smooth fibres with length and diameter of 14 mm and 0.13 mm, respectively.

3. First attempt

At first, the barrier was created to resemble the original Hedgehog in terms of size. 1500 mm was chosen for the barrier segments' length. Therefore, the assembled barrier was approximately 930 mm tall. The three segments, from which the barrier is assembled, are identical and are connected using a single steel bolt 20 mm in diameter. At the ends, there are steel plates which are welded to the reinforcement bars (two bars 6 mm in diameter). These plates are used to strengthen the segments' ends for better interaction with the surface. The assembled barrier is shown in Fig. 1. Weight of one segment is approximately 50 kg.

Fig. 1. The barrier for the first crash test.

The barrier was first tested with a full-scale crash test using an ordinary road vehicle weighing approximately 1300 kg. Speed of the vehicle before the impact was chosen to be 48 km/h (30 mph) according to the PAS 68 [3]. Three barriers were placed in a line perpendicular to the vehicle's path. Barriers were tied together using a steel rope. The barrier in the middle was placed directly against the incoming vehicle.

From the captured high-speed camera footage, it is clear, that the middle barrier failed very quickly after the impact. The steel rope connection between the barriers also failed, but was strong enough to propel the side barriers which caused damage to the sides of the vehicle, but didn't contribute to slowing the vehicle down. Failure of the barrier occurred, where the segments were bolted together. An

important observation for later studies was the interaction between the barriers' steel ends and the asphalt surface. In Fig. 2 the segment can be seen carving into the surface, leaving in it approximately 5 cm deep groove.

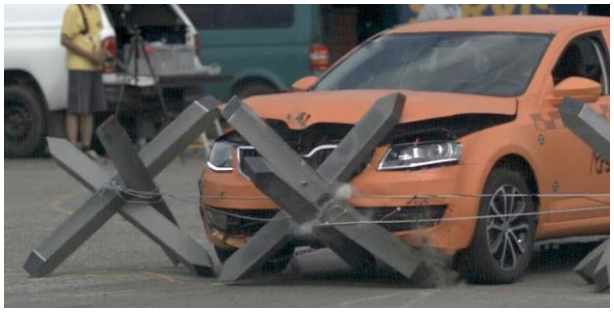

Fig. 2. The first crash test.

4. Numerical simulation

After the first experiment, numerical simulations were carried out to better understand the behaviour of the barrier. All simulations were made using LS-DYNA. Barrier outlined in the previous chapter was simulated together with different variants in terms of size. Additionally, an asymmetrical barrier (with one segment longer than others) was tested. Asphalt surface was simplified in these simulations due to insufficient data from the experiment. Several surface parameters were tested, which confirmed that surface quality (in terms of its softness) plays a crucial role in the barrier's behaviour. For the next experiment, an asymmetrical barrier (Fig. 3) was chosen, as it showed the best behaviour for softer and moderately harder surfaces. Additional steel reinforcement was used.

Fig. 3. The second crash test setup.

5. Second attempt

The second crash test experiment was carried out with similar road vehicle impacting again at 48 km/h (30 mph). Two rows of barriers were placed against the vehicle to ensure it would come to a full stop. The barriers were also placed much closer to each other in one row and were not tied together. The vehicle impacted approximately to the centre of the first row.

This time, the barriers managed to completely stop the vehicle by lifting its front of the ground. From high-speed camera footage, it was clear that the second row of barriers was needed. The barriers did perform as expected based on the numerical simulations

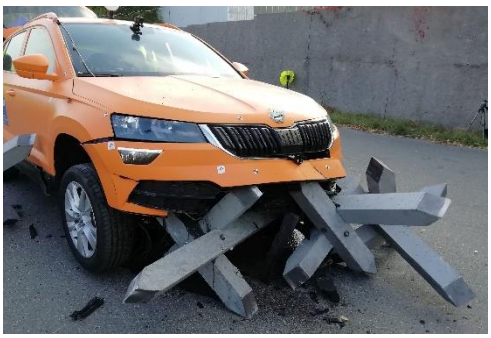

Fig. 4. The second crash test result.

6. Conclusions

In this research, UHPFRC was used to revisit the Czech Hedgehog design to create a modern mobile barrier intended to stop a relatively fast moving road vehicle. It is clear, that simply copying the historical design will result in a non-effective barrier for these kinds of situations.

After the first crash tests, numerical simulations proved that the barriers need to be smaller than the original design and that asymmetrical geometry could prove beneficial in terms of interaction with the vehicle. This was confirmed with the second crash test, where a full stop of the vehicle was achieved, but two rows of the barriers needed to be used. It is clear, that the barriers' effectiveness is strongly dependent on the surface properties.

Acknowledgements

This work was supported by the Technological agency of the Czech Republic [project number TG02010033].

References

[1] Bažantová Z., Kolář K., Konvalinka P., Litoš J., Petrtýl M. Controlled Hardening of Silicate Binders for the Optimization of High Performance Composites. *Key Engineering Materials*. 2016, **722**, 281-285.

[2] Kolář K., Bažantová Z., Konvalinka P. Suchá prefabrikovaná směs multifunkčního silikátového kompozitu. 2015. CZ 306663 B3. Czechia: Industrial Property Office

[3] BSI Group (2013) BS PAS 68 Impact test specifications for vehicle security barrier systems.

LEVERING IN THE TOOTHED CLAMP GEAR – INITIAL INVESTIGATIONS

Łukasz BEREŚ[1], Jerzy GRYGORCZUK[1], Marcin OBSZAŃSKI[2], Paweł PYRZANOWSKI[2]

[1] Astronika Sp. z o.o., Research and Developmnet Department, Bartycka str. 18, 00-716 Warsaw, Poland, E-mail: lberes@astronika.pl, jgrygorczuk@astronika.pl

[2] Warsaw University of Technology, Institute of Aeronautics and Applied Mechanics, Nowowiejska str. 24, 00-665 Warsaw, Poland, E-mail: mobszan@meil.pw.edu.pl, pyrzan@meil.pw.edu.pl

1. Introduction

The toothed clamp is a new generation of gear for reducing force acting in Hold Down and Release Mechanisms (HDRM-s). The toothed clamp gear is patented by Astronika company.

HDRM holds down a rod despite the large forces acting on the rod and releases the rod after the activation of the release module. Mechanisms of this type are widely used in space industry - HDRM protect moving parts and payloads of a spacecraft during launch of the rocket.

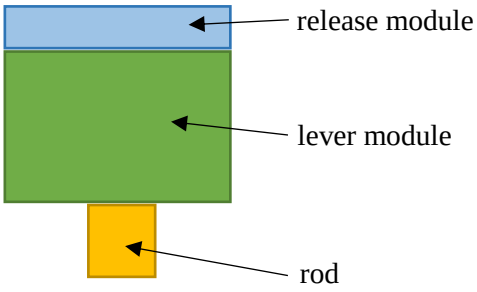

Fig. 1. General construction of the HDRM.

The lever module can be built based on various simple machines. The tooted clamp gear is a kind of inclined plane, which was repeated 8 times on Archimedes' spiral. The toothed clamp is characterized by a large gear ratio and the ability to easily deployment - in addition, it takes up little space and has a small mass compared to other existing solutions. The high gear ratio allows to build the small release module that consumes little energy during release.

In the present study a strain gages were used for to measure strains. Then, based on the strains, the gear ratio was determined. Comparison with the gear ratio theory for toothed clamp has been carried out.

2. Theoretical levering in the toothed clamp gear

Fig. 2. shows an example of HDRM based on the toothed clamp gear.

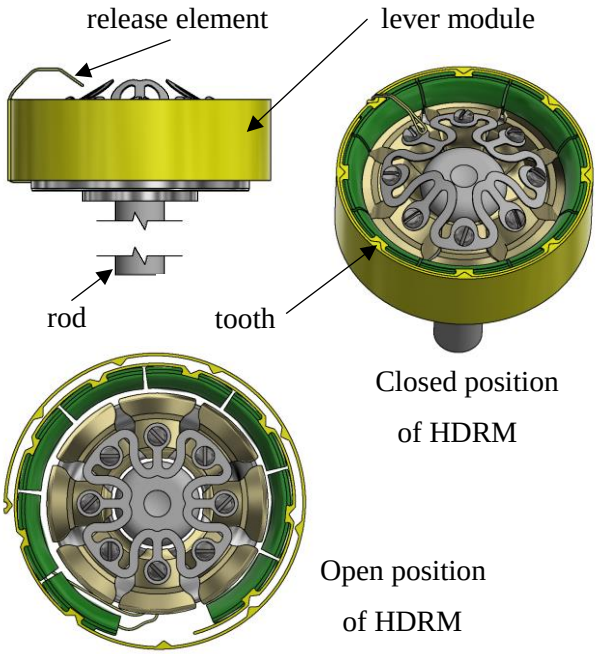

Fig. 2. General construction of the HDRM based on the toothed clamp gear.

The gear ratio has been introduced for one tooth based on general mechanics:

$$R2 = \frac{R1}{\cos\theta + \mu * \sin\theta + \frac{\sin\theta * \sin\gamma}{\cos\gamma} + \frac{\mu * \cos\theta * \sin\gamma}{\cos\gamma}} \quad (1)$$

$$R3 = \frac{R2 * \sin\theta - T2 * \cos\theta}{\cos\gamma} \quad (2)$$

$$\gamma = \frac{360}{n} \quad (3)$$

$$i4 = \left(\frac{R1}{R3}\right)^7 \quad (4)$$

where:

$R1$ $[N]$ – force before the tooth

$R2$ $[N]$ – reaction for the tooth

$R3$ $[N]$ – force after the tooth

$\theta = 30$ $[deg]$ – angle of tooth inclination

$n = 8$ [1] – number of all teeth

μ [1] – coefficient of friction (variable)

$i4$ [1] – gear ratio for 7 teeth

For last tooth gear ratio $i5$ have other value (calculation are not show).

$i5$ [1] – gear ratio for 8 tooth

Theoretical levering for different coefficient of friction in the toothed clamp gear is presented in Table 1.

Table 1. Theoretical levering in the toothed clamp gear.

	μ [1]		
	0.00	**0.053**	**0.16**
R1/R3 [1]	1.932	2.242	3.100
i4 [1]	100.4	284.7	2751.6
i5 [1]	1.732	1.965	2.617

3. Experiment description

During the test, the strain during closing of the toothed clamp and caused by applying force to the rod were measured. Strain gages were glued before each subsequent tooth. The strain gages from Hottering Baldwin Messtechnik GmbH were used (k-Faktor 2.08 ± 1.0%, resistance 120.0Ω ± 0.2%). During the test, the mechanism was loaded until it was destroyed. Data for calculations was taken for the moment just before plasticization.

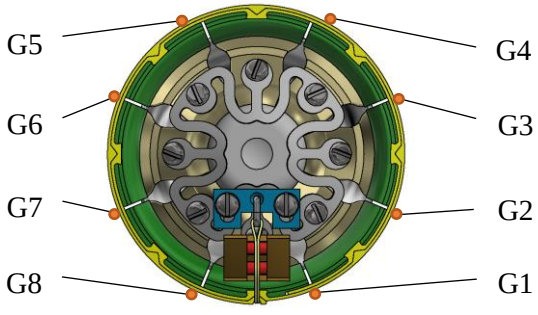

Fig. 3. Position of the strain gages.

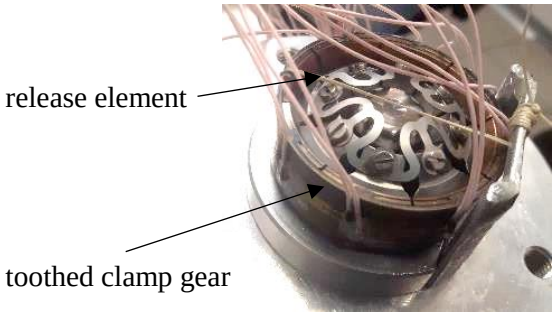

Fig. 4. HDRM before applying the force to the rod.

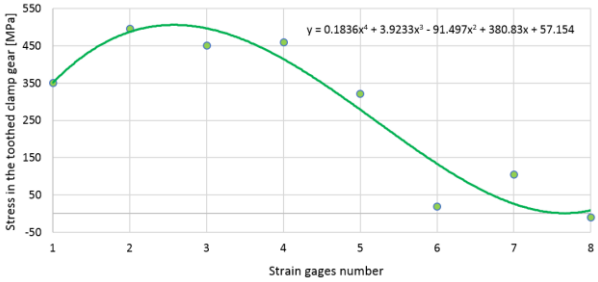

Fig. 5. Stress distribution in the toothed clamp gear.

The calculated levering in the toothed clamp gear based on test data is shown in Table 2.

Table 2. Stress and levering in the toothed clamp gear.

No. of strain gages	**Stress in the toothed clamp gear [MPa]***	**Levering for each tooth [1]**
G1	351	0.720
G2	487	0.980
G3	497	1.199
G4	415	1.486
G5	279	2.088
G6	134	5.114
G7	26	2.989
G8	9	n/a
	Average levering:	**2.082**
*Stress were calculated based on the curve from Fig. 5		

4. Conclusions

Measurements have shown that the teeth produce the levering. The levering is slightly different from the theoretical predictions – the levering is not constant for each tooth (Table 2). Stress distribution in the toothed clamp gear is very similar to the stress distribution for a typical thread connection (Fig. 5).

References

[1] Hendzel, Z., Żylski, W.: Determination of the theoretical levering in the toothed clamp, *Mechanika Ogólna, Statyka*, Rzeszów, 2000.

[2] Gasiak, G.: *Analysis of thread coil effort in the screw – nut joint*, http://sjsutst.polsl.pl/archives/2014/vol82/87_ZN82_2014_Gasiak.pdf, 2014.

NEW SCISSOR-GRASPING TOOL FOR PARALLEL GRIPPERS, ENSURING STROKE ENHANCEMENT

Dan DUMITRIU[1], Marius IONESCU[1], Daniel Octavian MELINTE[1]

[1] Institute of Solid Mechanics of the Romanian Academy, 15 Constantin Mille, 010141 Bucharest, Romania, E-mail: dumitriu.dan.n@gmail.com, dan.dumitriu@imsar.ro

1. Introduction

In the framework of national contract no. 22 PCCDI /2018, project entitled "Autonomous robot systems for waste management in the context of smart city" (acronym SIRAMAND), the idea is to build a mobile robotic system carrying a *x-y-z* robotic manipulator or a Delta parallel robot, equipped with an electric parallel gripper, as schematized in Fig.1. The gripper is the end-effector tool responsible for grasping various waste objects from the ground and to manipulate them to a box container placed on the mobile robot.

Fig. 1. Overall scheme of SIRAMAND mobile system.

The overall actuation of this mobile/autonomous robotic system must be performed using only 24 VDC, technological constraint which led us to the choice of a FESTO *x-y-z* robotic manipulator, composed of planar surface gantry EXCM-30-700-510 for $x+y$ actuation, plus an electrical slide EGSK-26-200-2P for actuation on *z*-axis. In fact, this is one of the few robotic systems capable of carrying 2-3 kg of load, considering the 24 VDC voltage limitation.

In order to collect waste objects, the mobile robotic system must be equipped with a rotary electric gripper, using 24 VDC actuation, not too heavy, but providing enough stroke and gripping force for grasping as much types of waste objects as possible.

2. Festo HGPLE electric parallel gripper

For full compatibility of the overall robotic system, a FESTO electric parallel gripper has been selected. More precisely, the solution of a *FESTO parallel gripper HGPLE-14-60 [1], plus a rotary drive ERMO-16, has been selected*. So, our HGPLE-14-60 gripper provides a total stroke of 120 mm and a gripping force varying between 104 N (for 5 mm/s closing speed), up to 173 N (for a closing speed of 10 mm/s) [1[.

Of course, numerous various electric in-house grippers has been proposed in the literature. For example, Barbieri et al. [2] proposed an underwater robotic arm with an adaptive rotary gripper, having two fingers with an anthropomorphic kinematic structure. Each finger is composed of two phalanges. Due to the special parallel structure of the first/proximal phalanx (incorporating a helical elastic spring), when it comes in contact with the grasped object, its rotation is blocked, but the actuation enables still the rotative closure of the second/intermediate phalanx (until it comes also in contact with the object). Moreover, the intermediate phalanx is naturally continued with a distal phalanx having the form of a FinRay pattern structure, patented by FESTO. The current FESTO product based on this FinRay pattern structure are the adaptive gripper fingers DHAS [3]. When such a gripper grasps an object by closing its two fingers, this flexible FinRay bionic structure of DHAS fingers [3] has the property of adapting to the shape of the object, thus significantly increasing the contact surface between the fingers and the object.

Another in-house gripper is proposed by Bonello et al. [4], mounting in parallel a 2-finger mechanical gripper and a vacuum cup, respectively. Combining classical grasping using friction with the supplementary vacuum aspiration, this versatile gripper is able to successfully grasp objects of different shapes, sizes and weights [4].

In order to be able to grasp larger objects and to improve the grasping, we propose to replace the classical or the adaptive fingers of HGPLE-14-60 gripper with the following innovative stroke enhancement adapter, inspired from the operating mechanism of scissors.

3. New scissor-grasping tool

This paper's contribution is to present a new scissor-grasping tool to be mounted on the FESTO HGPLE-14-60 gripper, equipping the x-y-z robotic system conceived for grasping waste objects. This innovative scissor-grasping tool represents an alternative to classical rigid BUB-HGPL fingers or to adaptive gripper fingers DHAS-GF [3], provided by FESTO as gripper grasping tools.

The idea is to study a different type of grasp, the proposed innovative scissor-grasping tool fulfilling also the role of stroke enhancement adapter. Fig. 2 shows a frontal view of the scissor-grasping tool, indicating all the geometrical design elements needed to express the scissor equations.

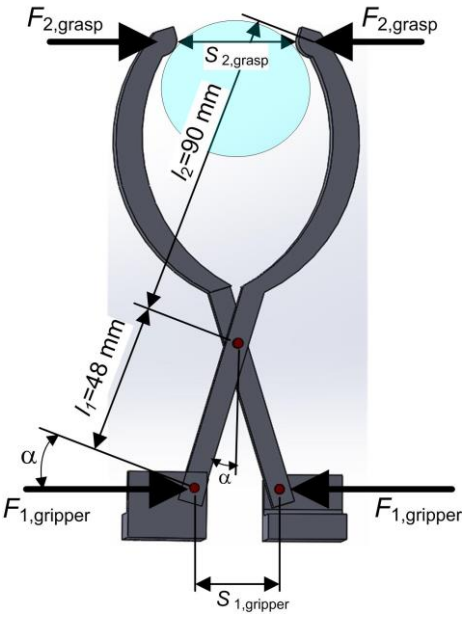

Fig. 2. Frontal view of scissor-grasping tool.

The scissor-grasping tool is characterized by the following torque transmission equation:

$$F_{1,\text{gripper}} l_1 \cos\alpha = F_{2,\text{grasp}} l_2 \cos\alpha \qquad (1)$$

to which must be added the geometrical condition:

$$\frac{s_{2,\text{grasp}}}{s_{1,\text{gripper}}} = \frac{l_2}{l_1} = \frac{90\ \text{mm}}{48\ \text{mm}} = 1.875 \qquad (2)$$

So, our scissor-grasping tool is a stroke enhanement adapter, able to almost double the stroke. For example, considering a gripper total stroke $s_{1,\text{gripper}}$ of 100 mm (for safety reasons, it is recommended to avoid working in the proximity of 120 mm maximum stroke), one obtains a grasping effective stroke $s_{2,\text{grasp}}$ = 187.5 mm. The only drawback, but acceptable, is that the grasping force will be 1.875 times smaller than the force provided by the gripper: $\frac{F_{2,\text{grasp}}}{F_{1,\text{gripper}}} = \frac{l_1}{l_2} = \frac{1}{1.875} = 0.53$.

4. Conclusion and further validation

A new scissor-grasping tool has been proposed, being also a stroke enhancement adapter. This innovative tool has been already manufactered by classical 3D printing, using PLA filament material. Grasping tests will be further performed on cylindrical glass bottles, cylindrical plastic bottles and cubic wood pieces. Another further issue is to cover the interior side of the scissor with anti-skidding material, in order to increase the frictional force and thus the graspable object weight.

Acknowledgements

This work was supported by a grant of the Romanian Ministry of Research and Innovation, CCCDI – UEFISCDI, project number PN-III-P1-1.2-PCCDI-2017-0086 / contract no. 22 PCCDI /2018, within PNCDI III.

References

[1] FESTO. *Parallel grippers HGPLE, sturdy with long stroke, electric*. https://www.festo.com/cat/en-us_us/data/doc_enus/PDF/US/HGPLE_ENUS.PDF. Accessed May 5, 2019.

[2] Barbieri, L., Bruno, F., Gallo, A., Muzzupappa, M., Russo, M.L. Design, prototyping and testing of a modular small-sized underwater robotic arm controlled through a Master-Slave approach. *Ocean Engineering*, 2018, 158, 253–262.

[3] FESTO. *Adaptive gripper fingers DHAS*. https://www.festo.com/cat/en-gb_gb/data/doc_ENGB/PDF/EN/DHAS_EN.PDF. Accessed May 5, 2019.

[4] Bonello D., Saliba M.A., Camilleri K.P. An exploratory study on the automated sorting of commingled recyclable domestic waste. *Procedia Manufacturing*, 2017, 11, 686–694.

[5] Dumitriu, D., Ionescu, M., Melinte, D.O., Mărgăritescu, M. Stroke enhancement adapter for electric parallel gripper equipping a mobile x-y-z robotic system. In *Proceedings of the 42th International Conference on "Mechanics of Solids, Acoustics and Vibrations" ICMSAV 2018*, Braşov, Romania, 25-26 Octobrie 2018; pp. 49–52.

EXPERIMENTAL IDENTIFICATION OF ELASTOPLASTIC PROPERTIES OF Al/Cu BIMETALLIC SHEET OBTAINED BY COLD ROLLING

Robert UŚCINOWICZ[1]

[1] Bialystok University of Technology, Faculty of Mechanical Engineering, Department of Mechanics and Applied Computer Science, 15-351 Bialystok, Wiejska 45C, Poland, E-mail: r.uscinowicz@pb.edu.pl

1. Introduction

The design process of plastic forming the machine parts requires the knowledge about elastoplastic properties of used material. The identification of the mechanical properties by experimental tests is relatively easy in the case of isotropic and homogeneous structures. In the case of modern constructional materials, which are characterised by the complex internal structure, determination of physical properties by tests is difficult operation and need special approach. An example of such material may be a bimetallic sheet manufactured by hot or cold rolling by joining of two or more metal sheets with different physical properties. Experimental tests of these materials for determination their mechanical properties were conducted by Lee and Kim [1], Semiatin and Piehler [2], Choi et al.[3] and Uścinowicz [4].

The aim of the study was determination the directional values of the mechanical parameters, which were described the elastic and plastic properties of the Al/Cu bimetal in the form of a metal sheet taking into account the varying thickness of the copper layer.

2. Materials, specimens and methods

In experimental tests three types of specimens were used, i.e.:1) flat specimens with a "dog-bone" shape and made from Al/Cu bimetal, 2) bimetallic Al/Cu specimens in the shape of rectangular prisms, 3) aluminium specimens obtained from bimetallic sheet, but completely devoid of the copper layer. Specimens were cut from Al/Cu sheet in two directions, i.e. in the rolling direction (RD) and the transversal direction (TD). The mean share of metal components in the as-delivered Al/Cu bimetal was: Cu - 49% and Al - 51%. The essential group of bimetallic Al/Cu specimens were machined by milling to reduce the thickness of the copper layer in comparison to the aluminium layer. This involved reducing the thickness of the Cu layer by approx. 0.6 mm. The share of copper in Al/Cu bimetallic specimens amounted, as a percentage, respectively was: 0%, 25%, 40%, 45%, 50%. For the as-rolled Al/Cu sheet, no cracks and no intermetallic layer on the interface was observed.

In order to obtain information about the mechanical properties of the tested Al/Cu bimetal two experimental methods were used: 1) uniaxial quasi-static monotonic tensile test realised on flat specimens, 2) dynamic method of determination of elastic properties using impulse excitation technique in which an acoustic resonance frequency analyser for rectangular prisms specimens was applied. Basic elastic and plastic properties of the tested materials were determined for the selected RD, TD directions and in the direction perpendicular to the plane of sheet - ND (normal direction), i.e.: elastic limit ($R_{p0.05}$), yield point ($R_{p0.2}$), tensile strength (R_m), Young's (E) and Kirchhoff's (G) moduli, internal friction parameters (Q^{-1}), maximum uniform plastic strain (ε_u) and hardening curve coefficients (n, K, ε_o), specific energy of uniform elastic and plastic strains (L_e, L_p) as well as Lankford's coefficient (r) describing the normal anisotropy.

3. Results

The hybrid approach to mechanical tests, with the use of two methods, gave the possibility to determine the elastic constants in the plane of Al/Cu sheet and in perpendicular direction to it taking into account varying thickness of the copper layer (parameter f_{Cu}).

Figure 1 presents changes the values of elasticity moduli E_{ND}, E_{RD}, E_{TD} in three orthotropic directions. The values of moduli E_{RD}, E_{TD} change non-linearly as the share of copper in the Al/Cu bimetal increased and charts have progressions of similar shape. They achieve an extreme value for the share of copper as 38-39% in the Al/Cu

bimetal. In the case of E_{ND} modulus a non-linear increase of the values of moduli E_{ND} is also observed.

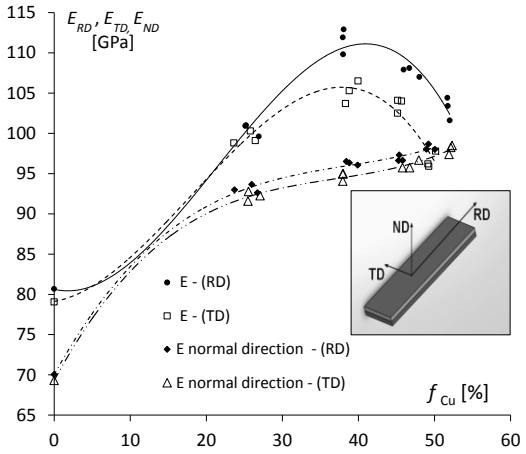

Fig. 1. The effect of increase the percentage fraction of copper in Al/Cu bimetal on values of E_{ND}, E_{RD}, E_{TD}.

Another interesting parameter obtained from measurements by using impulse excitation technique was internal friction (Q^{-1}). Non-linear changes of Q^{-1} accompanying the growth of f_{Cu} in two modes (flexural and torsional) are illustrated in fig. 2. It seems the rolling process caused greater hardening of Al/Cu specimens in TD direction, which had a more plasticized structure (texture). Charts of Q^{-1} in flexural and torsional modes have different progressions with increasing Cu content in the Al/Cu.

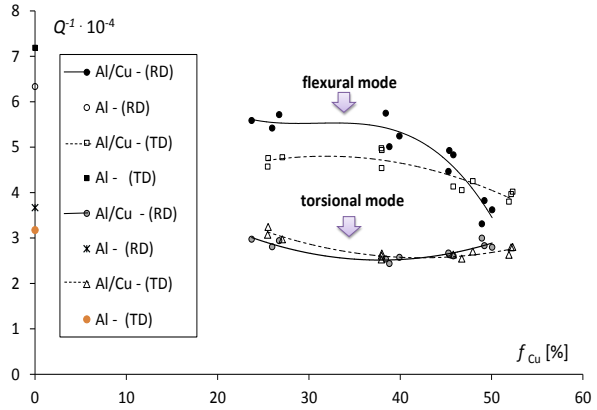

Fig. 2. Variability of internal friction Q^{-1} during the increase of Cu fraction in Al/Cu bimetal.

The changes of the normal anisotropy, which was connected with plastic deformation of the bimetallic sheet, was recorded by the Lankford's coefficient r. The variability of the value of coefficient r for aluminium and Al/Cu bimetal accompanying the growth of parameter f_{Cu} is shown in fig.2. It should be highlighted that values of Lankford's ratio for Al/Cu bimetal decrease more quickly in RD direction than TD accompanying growth of parameter f_{Cu}.

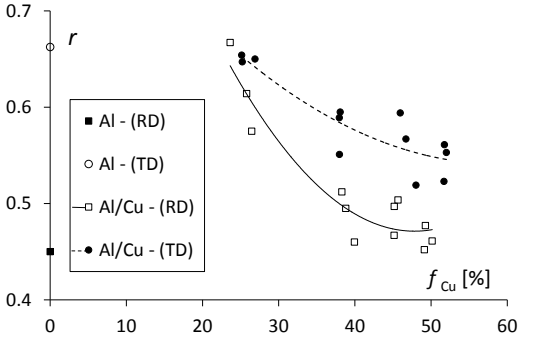

Fig. 3. Variation of values of Lankford's coefficients with increase of the copper content in Al/Cu bimetal.

4. Conclusions

- The quasi-static tensile tests and impulse excitation technique allowed to determine the values of the Young's modulus in the directions of orthotropy.
- The law of mixtures incorrectly describe the changes of elastic constants (E_{ND}, E_{RD}, E_{TD}) accompanying the growth of parameter f_{Cu}, i.e. percentage shares of Cu component in Al/Cu bimetal.

Acknowledgements

The paper was prepared as a part of the research project No. S/WM/4/2017 of Bialystok University of Technology financed by the Polish Ministry of Science and Higher Education.

References

[1] Lee D. N.and Kim Y. K., On the rule of mixtures for flow stresses in stainless-steel-clad aluminum sandwich sheet metals, 1988, *J. Mater. Sci.*, vol. 23, no. 2, pp. 558–564.

[2] Semiatin S. L., Piehler H. R., Deformation of sandwich sheet materials in uniaxial tension, *Metall. Trans. a-Physical Metall. Mater. Sci.*, 1979, vol. 10, no. 1, pp. 85–96.

[3] Choi S. H., Kim K. H., Oh K. H., Lee D. N., Tensile deformation behavior of stainless steel clad aluminum bilayer sheet, *Mater. Sci. Eng. a-Structural Mater. Prop. Microstruct. Process.*, 1997, vol. 222, no. 2, pp. 158–165.

[4] Uścinowicz R., *Procesy odkształcania metalowych kompozytów warstwowych*; (in Polish), Oficyna Wydawnicza Politechniki Białostockiej, Białystok, 2015.

EXPERIMENTAL VERIFICATION OF NUMERICAL SIMULATION OF THE FLOW INSIDE THE TIP-JET HELICOPTER PROPULSION SYSTEM

Stevan CRNOJEVIĆ[1], Nenad LATKOVIĆ[2], Nenad KOLAREVIĆ[1], Marko MILOŠ[1]

[1] University of Belgrade, Faculty of Mechanical Engineering, Kraljice Marije 16, Belgrade, Serbia,
E-mail: nkolarevic@mas.bg.ac.rs;

[2] EDePro d.o.o., Kralja Milutina 33, Belgrade, Serbia

1. Introduction

This paper presents the research that determines the total pressure loss of the high speed, high temperature compressible flow of turbine exhaust gas products through the tip-jet helicopter propulsion system [1, 2]. The combustion products are transmitted from the area after the gas generator nozzle [3] to the tips of the blades with a specially designed system of channels inside the specially developed laser welded Inconel blades [4] (Fig.1). Blade tips are equipped with the nozzles for creating the maximum thrust force in tangent direction, which created the torque that drives the entire helicopter rotor [5, 6]. This force is depended on the mass flow and pressure of the operating fluid, and it governs the performance of the whole tip-jet propulsion system and helicopter.

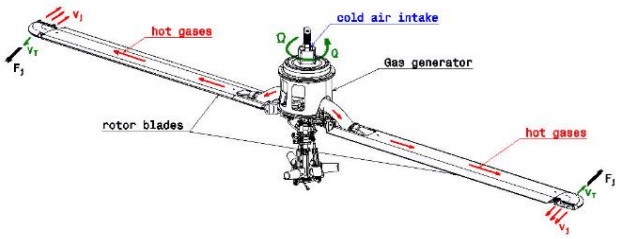

Fig. 1. Tip-jet helicopter propulsion system.

In order to increase the performance of the tip-jet propulsion system, this flow should be optimized in the sense of making the compromise that leads to a solution that minimizes the total pressure drop along the pipeline, and at the same time keeping the mass and dimensions within the acceptable limits. Therefore, a numerical mathematical 3D model has been made for this case. Results obtained from the numerical model are compared and verified with experimental results gained from a series of tests carried out in EDePro laboratory facilities.

2. Experimental measurement

The acquisition system consists of several sensors in order to determine the state and behavior of the gas generator and it is explained in detail in paper [7]. This way, the inlet parameters for the distribution channel system for the tip-jet helicopter can be concluded. Two pressure sensors are added in order to measure the pressure after the distributor, where the flow is divided into two branches for each blade (Fig. 2), and the pressure on the nozzle of one of the blades (Fig. 3). In this way, the first sensor measures the pressure drop through the distributor, and the second sensor measures the pressure drop through the blade channel and nozzle.

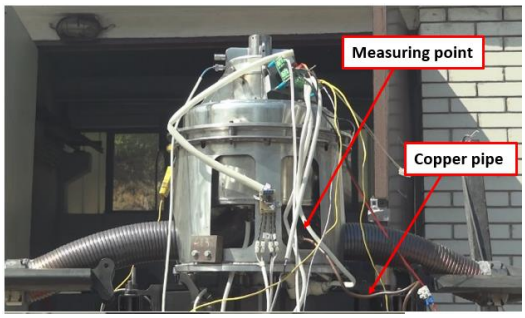

Fig. 2. Pressure sensor on the distributor.

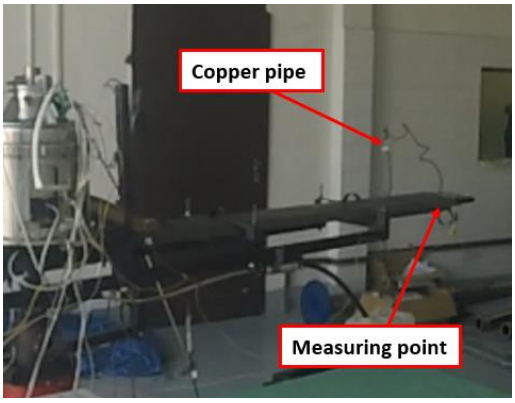

Fig. 3. Pressure probe on the nozzle.

OMEGA PX602-150GV pressure sensors are used for measuring and they have the following characteristics: accuracy 1%, span 150 psig, maximum pressure 300 psig, input voltage 5-10Vdc, etc. The temperature of the combustion products that are transmitted through the propulsion system is around 650°C. Therefore, a special pipe system from copper pipes is installed between the measuring point and the pressure sensor, in order to cool down the combustion products mixture to an appropriate level that will not damage the sensor. A similar solution used for measuring the total pressure on gas generator nozzle, is explained in paper [8]. The measured values during the static test for defining the thrust force on the blades nozzles are shown in the diagram in the following Fig. 4.

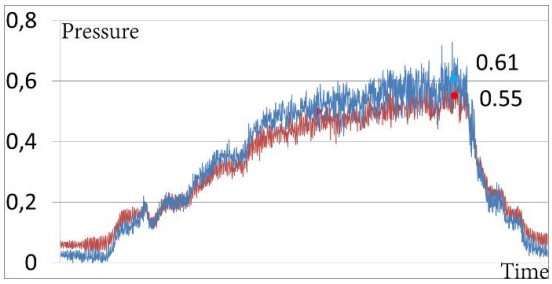

Fig. 4. Overpressure on the distributor (red) and on the blade nozzle (blue).

3. Numerical model

The Darsie equation was used for the calculations.

$$\Delta p = \rho Y_g = \lambda\left(\frac{\delta}{D}, Re\right)\frac{l}{D}\frac{\rho v^2}{2}$$

So were the equations for the hydraulic local resistance for every critical cross section.

$$\Delta p = \rho\zeta v^2/2$$

The coefficient ζ was taken from a specific table. The Mach number was calculated from the following equation.

$$\frac{p_0}{p} = \left(1 + \frac{\kappa - 1}{2}M^2\right)$$

Numerically calculated values for pressure and Mach number were taken and verified during the experiment.

4. Conclusions

The experiment and numerical simulations show that there is a significant pressure drop through the channel system inside the tip-jet propulsion system. This directly influences the losses in the entire system. But it can be concluded that the efficiency can be increased by elongation of the blades, i.e. with an increase in the rotor diameter, the pressure losses are greater but the force arm is bigger, so the torque is larger and it can overcome greater resistance. This is the reason why tip-jet helicopters have the larger rotor diameter compared to the conventional helicopters.

Acknowledgements

The authors wish to acknowledge and thank the company EDePro – Engine Design and Production in Belgrade for support and for encouragement in the project realization.

References

[1] N. Kolarević, N. Kosanović, M. Miloš: *Methodology for efficiency determination of tip-jet helicopter propulsion system*, Machine Design, Vol. 8, No.4, pp. 133-136, 2016. ISSN: 1821-1259

[2] 5. N. Kolarević, N. Kosanović, M. Miloš: *Tip-jet helicopter propulsion system testing*, KOD 2016 – The 9th International Symposium Machine and Industrial Design in Mechanical Engineering, Balatonfüred, Hungary, pp. 221-224, 2016. ISBN: 978-86-7892-821-5

[3] Claire Soares, "Gas Turbines," Elsevier, 2015.

[4] 17. Nebojša Kosanović, Nenad Kolarević, Marko Miloš: *Laser welded Inconel rotor blades for tip-jet helicopter*, 34th Danubia-Adria Symposium on Advances in Experimental Mechanics, Trieste, Italy, 2017. ISBN: 978-88-8303-863-1

[5] Watkinson, J.; (2004) *the Art of the Helicopter*, Elsevier Butterworth-Heinemann.

[6] Seddon, J.; (1990) *Basic Helicopter Aerodynamics*, BSP Professional Books.

[7] N. Kolarević, N. Kosanović, M.Miloš, "Measuring parameters of Phoenix-100 gas-generator", Proceedings of the 34th Danubia-Adria Symposium on advances in experimental mechanics, Trieste, 2016.

[8] N. Kolarević, N. Kosanović, M. Miloš: *Crucial parameters of gas generator on tip-jet helicopter*, Materials today: Proceedings, Elsevier, Vol. 5, Issue13, Part 2, pp. 26715-26720,2018.DOI: 10.1016/j.matpr.2018.08.141

HYBRID SLAM MODELLING OF AUTONOMOUS VEHICLE WITH AUGMENTED REALITY DEVICE

Reza MOEZZI[1], David KRCMARIK[2], Jaroslav HLAVA[3]

[1] Institute for Nanomaterials, Advanced Technologies and Innovation, Technical University of Liberec, Studentská 2, 461 17, Liberec, Czech Republic, E-mail:reza.moezzi@tul.cz;

[2] Institute for Nanomaterials, Advanced Technologies and Innovation, Technical University of Liberec, Studentská 2, 461 17, Liberec, Czech Republic, E-mail: david.krcmarik@tul.cz;

[3] Faculty of Mechatronics, Informatics and Interdisciplinary Studies, Technical University of Liberec, Studentská 2, 461 17, Liberec, Czech Republic, E-mail: jaroslav.hlava@tul.cz

1. Introduction

Nowadays we meet more and more autonomous vehicles. The concept of autonomous issue is closely related to enhancements in sensors and mathematical models. To design fully autonomous vehicle is unfortunately still a hard task. It is due to the fact that many situations during controlling the vehicle can be non-expectable and only undergone experiences and deduction from such knowledge can handle such situations. Human brain with its vast library of experiences accumulated during various situations is a perfect solution solver for such events. For such reasons the vehicles are often constraint to certain areas such as lanes, barriers, certain area, predefined expectable space.

In order to successfully perform during autonomous navigation we have to divide the whole process into two parts. The first one is the way how to obtain as much accurate map of surrounding environment as possible and the second one is how to autonomously control the vehicle according to certain expectations. The concern of this article is mainly the localization of the vehicle in real time and mapping its surroundings. Interesting approach is described in [1] as SLAM (Simultaneous Localization and Mapping) which is becoming an essential element for navigation [2].

The basis for SLAM procedures is an Extended Kalman Filter (EKF) described in [3]. For successful localization deep mapping has to be performed. During mapping many obstacles are found around the vehicle. Such obstacles have to be somehow categorized in order to decide to which superior landmark it belongs to. One of the key information about each obstacle is its position. Anyway there are new interesting SLAM techniques nowadays [4]. We will discuss mainly fastSLAM and L-slam approaches in this paper. FastSLAM was introduced firstly by Montemerlo & Thruns [5] as so called "stochastic SLAM". This algorithm uses division of stare variables into two different groups. The first group is evaluated with the help of particle filtering and for the second group the EKF is used. We can observe noticeable problem simplification [6]. The second approach (L-SLAM) is mainly focused on each distinct obstacle characterization - mainly its orientation to real-time vehicle position [7]. Unfortunately both methods experience a quadric computational complexity [8].

In the presented paper we would like to introduce new approach to perform mapping of the environment based on commercially available Microsoft HoloLens technology. Such a device is the first functional augmented reality gadget offered to a wide audience. Easily obtained example of mapping based on HoloLens is in Fig. 1. The environmental scanning is performed in real time. Such technology is meant for mostly static or slowly moving environments which will be enhanced in the already released version 2 of the equipment. The whole architecture is a hybrid one preserving locations of the landmarks. For certain landmarks EKF is applied. Hence the computational complexity is minimized remaining the information for absolute reliable and accurate locations of them.

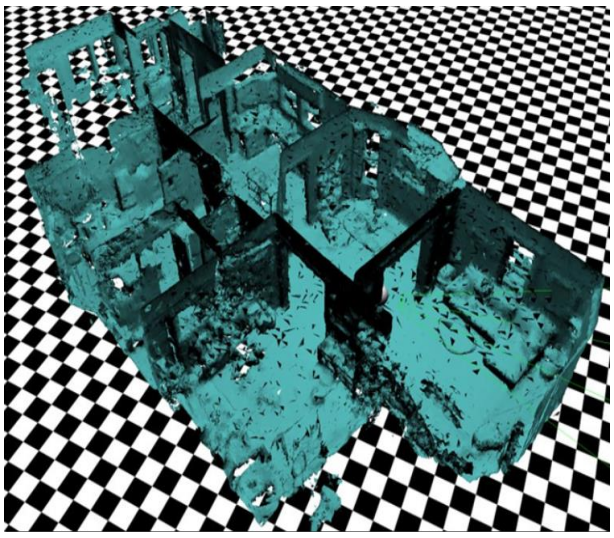

Fig. 1. Map of indoor environment with HoloLens.

Acknowledgements

The result is obtained through the financial support of the Ministry of Education, Youth and Sports of the Czech Republic and the European Union in the frames of the project "Modular platform for autonomous chassis of specialized electric vehicles for freight and equipment transportation", Reg. No. CZ.02.1.01/0.0/0.0/16_025/0007293

References

[1] R. Siegwart, I. Nourbakhsh and D. Scaramuzza, Introduction to Autonomous Mobile Robots, London, England: The MIT Press, 2011.

[2] J. Sasiadek, A. Monjazeb and D. Necsulescu, "Navigation of an autonomous mobile robot using ekf-slam and fastslam," 16th Mediterranean conference on Control and automation, p. 517–522, 2008.

[3] Sol`a, Simulataneous localization and mapping, Barcelona: Institut de Robòtica i Informàtica Industrial, CSIC-UPC, 2014.

[4] Röfer, F. Udo and W. T. René, "A SLAM Overview from a User's Perspective," Künstl Intell, vol. 24, p. 191–198, 2010.

[5] M. Montemerlo and S. Thrun, "Simultaneous localization and mapping with unknown data association using fastSLAM," Proceedings of IEEE International Conference on Robotics and Automation, ICRA, vol. 2, no. 3, p. 1985–1991, 2003.

[6] J. Sasiadek, A. Monjazeb and D. Necsulescu, "Navigation of an autonomous mobile robot using ekf-slam and fastslam," 16th Mediterranean conference on Control and automation, p. 517–522, 2008.

[7] V. Petridis and N. Zikos, "L-slam: reduced dimensionality fastslam algorithms," in WCCI, Barcelona, 2010.

[8] L. Wei, W. Tao and Z. Yachong, "A Relative Map Approach for Efficient EKF-SLAM," in Proceedings of 2014 IEEE Chinese Guidance, Navigation and Control Conference, Yantai, China, August 8-10, 2014.

DESIGN AND CONSTRUCTION OF A ROTOR TEST BENCH FOR TESTING SENSORS

Helmut J. HOLL[1], Martin PFAFFENBAUER[2]

[1] Johannes Kepler University of Linz, Institute of Technical Mechanics, Altenbergerstr. 69, A-4040 Linz, Austria. E-mail: helmut.holl@jku.at

[2] Sensideon GmbH, Ligusterstr. 4/2, A-4600 Wels, Austria, E-mail: martin.pfaffenbauer@gmail.com

1. Introduction

The actual temperatures for the bearing and the rotating parts of a motor are important for a proper monitoring. For a temperature measuring sensor system in a motor only a very limited space is available. The high requirements are provided by a telemetric system. For the temperature measurement sensors at characteristic positions of the rotor system have to be mounted and a transmitter and receiver module has to be added. A suitable rotation test bench has been developed to perform long time tests in a temperature range from -40°C to 220°C. High rotation speeds up to 18000 rpm have to be maintained so that very good balancing is required and the testing time of the sensor has to be between 8 and 250 hours.

For the temperature measurements on rotating objects a telemetric system is used which is combined with a wireless equipment. The passive sensor can be applied to high temperatures up to 400 °C, high rotation speeds and difficult accessibility. For the application of such a system e.g. in the automotive industry a detailed test schedule has to be performed and the present rotation test bench is developed.

2. Development procedure

The design of the test bench consists of a frame, a rotating shaft on two bearings, a driving motor and a housing for the high temperature chamber. The high temperature chamber is made of a material with good isolation property and the mechanical requirements are fulfilled by a composite of ceramic, steel and plastics. The surface of the temperature chamber is as small as possible to keep the necessary heating power small. Within this high temperature heating chamber a special designed rotor is placed on the shaft. On the rotor the electronic equipment of the sensor with the transmitter module has to be mounted. The frame is constructed of standardized parts so that it is cheap and modular, see [1] and [2].

As the performance of tests on the real motors is not possible, the properties of the rotating shaft of the test bench have to be similar to represent the actual motor. Specially the position and radius of the sensor has to be kept close to the original application. A high temperature load at the rotor position and the heat conduction of the steel shaft results in high temperatures at the bearings, which have been placed outside of the insulated heating chamber. Among different possible shaft designs like using ceramic parts a hollow shaft has been applied. Based on a Finite-element-calculation for various shaft geometries, materials and thermal boundary conditions the dimension of the shaft has been derived iteratively. On the left end a temperature of 250 °C is defined for the different shaft configurations. The result of the temperature distribution in the shaft and the hollow shaft with different surface heat conduction conditions is shown in Fig. 1. The shaft configuration with the lowest possible temperatures at the position of the bearings has been chosen.

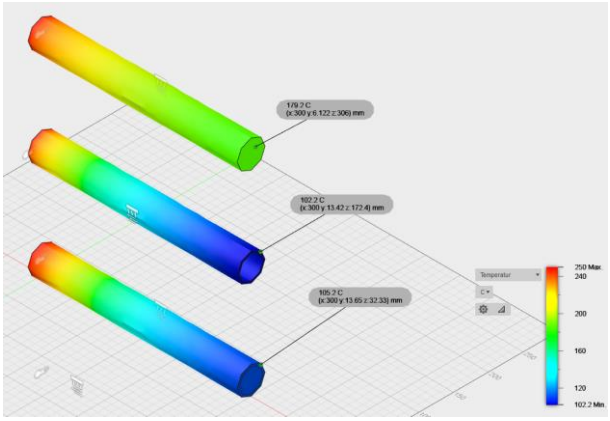

Fig. 1. Temperature distribution of three different configurations of the shaft.

3. Rotor test bench and measurements

The resulting rotor test bench is shown in Fig. 2 with the isolated heating chamber. At the position of the bearings an accelerometer can be seen, which is used for the balancing process. The rotor has been placed within the heating chamber and has been design in order to provide a proper mounting position for the sensor and the electronic equipment.

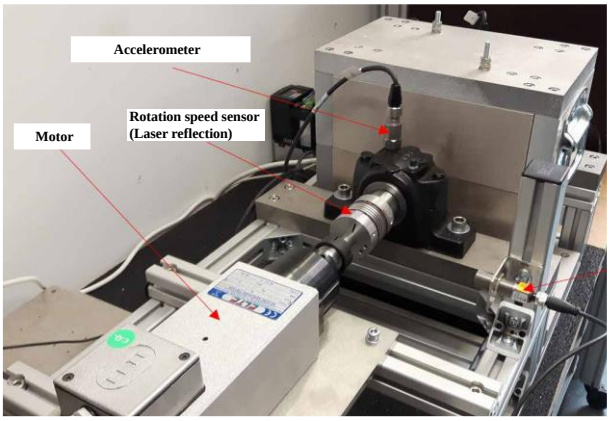

Fig. 2. Rotation test bench with the shaft, heating chamber, motor, bearings and sensors.

The dimensions of the elements and parts of the test bench have been calculated for the improved shaft with respect to the allowable stresses and temperatures, for the motor with respect to the moment of inertia, the power and the resonance case and for the bearings with respect to static and dynamic load, see [3], [4] and [5].

In the preparation step first the sensor equipment has been tested and then it was attached onto the rotor. The position of the equipment at the rotor as well as the bearings had to be mounted very carefully in order to prevent vibrations due to high eccentricity. The signals of the accelerometer and the laser sensor have been read by a NI-card to an industrial PC and the further processing was done using Matlab and toolboxes.

For the used high rotation speed a careful balancing is necessary, see [6]. The center of gravity is usually not at the axis of rotation as the tested sensor has been mounted. A static and dynamic balancing procedure has to be performed at different rotation speeds by balancing at operating conditions presented in [7]. In Fig. 3 reference measured signals are shown for the vertical acceleration of both bearings and the signal of the optic rotation sensor. Measurements have been performed with and without added mass. Based on the evaluation of the computed power cross spectra involving the phase shift of the different configurations the position of an additional mass for an improved balance state has been determined. The procedure of balancing has been carried out at different rotation speeds and it is similar to that described in [7].

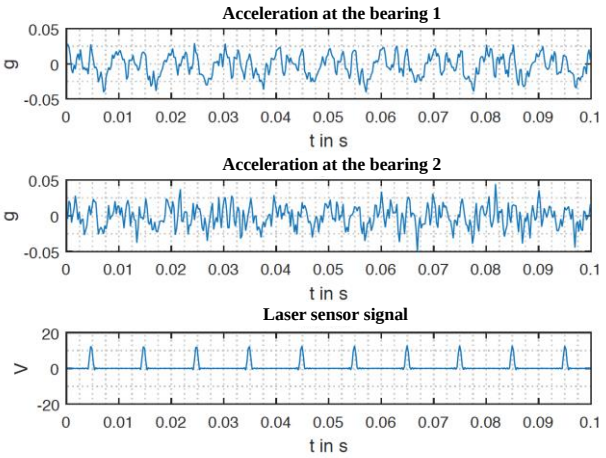

Fig. 3. Measured signals for the vertical acceleration at the bearings and the laser rotation sensor.

4. Conclusions

A rotor test bench has been designed and constructed for the testing of a sensor equipment at rotation speeds of 18000 rpm and at temperatures of -70 °C to 280 °C for up to 2,5 hours. With the improved balanced rotor also the vibrations and the emitted acoustic noise have been reduced. The measurement system detects the vibrations of the bearings so that also wear and faults can be monitored. The sensor tests have been performed successfully.

References

[1] Profos, P., Pfeifer, T.: *Handbuch der industriellen Messtechnik*. 6th edition, Oldenbuourg, 1994.
[2] Kobayashi, A.S.: Handbook on Experimental Mechanics. 2nd edition, VCH, 1993.
[3] Höhn, B.-R., Niemann, G., Hans Winter, H.: *Maschinenelemente: Konstruktion und Berechnung von Verbindungen, Lagern, Wellen.* Springer, 2005.
[4] Pahl, G., Beitz, W., Feldhusen, J., Grote, K.-H., *Konstruktionslehre.* 7th ed, Springer, 2007.
[5] Ehrenspiel, K., *Integrierte Produktentwicklung*. Carl Hanser Verlag, 2007.
[6] Gasch, R., Nordmann, R., Pfützner, H. : *Rotordynamik*, 2nd edition, Springer, 2005.
[7] MacCamhaoil, M.: *Application notes - static and dynamic balancing of rigid rotors* (bo0276). https://www.bksv.com/media/doc/bo0276.pdf. Accessed Feb. 25.2018.

DEVELOPMENT OF VIBRATION EQUIPMENT FOR THE PRODUCTION OF POLYCOMPONENT PHYTOMIXTURES

Vitalii YANOVYCH[1], Daniel DUDA[2], Olena RUBANENKO[2], and Václav URUBA[4]

[1] Faculty of Mechanical Engineering, University of West Bohemia in Pilsen, Univerzitní 22, 306 14 Pilsen, Czech Republic: yanovichvitaliy@i.ua

[2] Faculty of Mechanical Engineering, University of West Bohemia in Pilsen, Univerzitní 22, 306 14 Pilsen, Czech Republic: dudad@kke.zcu.cz

[3] The Regional Innovation Centre for Electrical Engineering, University of West Bohemia in Pilsen, Univerzitní 22, 306 14 Pilsen, Czech Republic: olenarubanenko@ukr.net

[4] Faculty of Mechanical Engineering, University of West Bohemia in Pilsen, Univerzitní 22, 306 14 Pilsen, Czech Republic. Institute of Thermomechanics, Czech Academy of Sciences, Dolejškova 5, 182 00, Prague, Czech Republic: uruba@kke.zcu.cz

1. Introduction

One of the most important stages of the technological process of manufacturing complex pharmaceutical mixtures is the grinding of pre-dried phytosteramines with a gradual sifting and giving it a homogeneous consistency of up to 97-98% with additional pharmaceutical ingredients due to mixing.

Thanks to the grinding, the specific surface of the treated material increases from 270-520 $cm^2 \cdot g^{-1}$ to 4100-4300 $cm^2 \cdot g^{-1}$, which makes it possible to significantly accelerate dissolution, chemical interaction and the separation of biologically active substances from the raw material [1].

Sifting is used as an auxiliary operation for preliminary preparation of the material for grinding, as well as an independent stage for obtaining the finished product with a particle size of 0.1-0.07 mm.

2. Disadvantages of existing technology for the production of phyto-mixtures

The technological scheme of production of pharmaceutical mixtures, which exists today, has a number of shortcomings, in particular energy-cost gradual implementation of technological operations of grinding, separation and alternate mixing phytocomponents with pharmaceutical ingredients in the form of certain powdery masses (talc, lactose).

Obviously, the solution of the problem of increasing the efficiency of the processes of preparation of pharmaceutical mixtures is possible by developing and creating equipment that combines the execution of the above technological operations into a single system [2].

3. Development and research of a vibrating equipment

On the basis of the analysis of the process of shredding of pharmacological materials the task was to develop a fundamentally new vibration equipment, which could realize the idea of integrated implementation of processes of crushing and mixing of bulk materials.

Constructive implementation of the equipment is presented in Fig. 1.

Fig. 1. Construction of a vibration equipment. Phytomixture material before a) and after b) processing.

The principle of this equipmentis to combine the vibration and rotation of the working container in relation to two mutually perpendicular planes. In turn, the working container consists of dividing

sections, for shredding and mixing of the processed material. In the section for crushing, there are crushing balls.

In the process of grinding, the size of the particles is reduced, they begin to be classified: particles that have fewer sieve openings – enter the mixing compartment, others – before regrinding.

Such a combination of technological and constructive factors can significantly increase the degree of destruction of particles and their simultaneous mixing with additional components, creating an effective comprehensive impact on the material being processed.

4. Results of experimental studies

Experimental studies were carried out using valerian roots, melissa leaves, peppermint and hawthorn fruit as a material for processing.

On the basis of the experiments, the dependence of the amplitude of the oscillations on the parameters of the labor force of the forced force F = 3.6 kN was obtained from which it is evident that with increasing angular velocity ω, the curve of the analytical amplitude of the fluctuations of the container A is divided into three zones. First – resonance, in which there is a gradual increase in the amplitude A = 3 mm in the range of values of the angular frequency ω = 0-36 rad·s^{-1}. The second – resonance, where the maximum value of the amplitude A = 7.8 mm is observed at ω = 36-60 rad·s^{-1}. Third zone – after resonance, the amplitudes of oscillations in the range A = 2.0-2.2 mm are stabilized. With the increase of the load of the total volume of the working chamber of the vibration equipment, the peak values of the amplitude of oscillations, namely during the period of resonance, decrease as a result of the growth of the dissipative forces of the technological environment. The analysis of the experimental dependence of the velocity of oscillation of the oscillation of the executive body on the vibration equipment from the angular velocity showed a peak value of 350 mm·s^{-1} as a result of the resonant phenomenon at 45 rad·s^{-1} . While the vibration acceleration of the executive body of the vibrating equipment acquires its maximum values a = 24-28 m·s^{-2} also at 45 rad·s^{-1}. We also conducted a series of experiments to determine the effect of the oscillation frequency of a vibration equipment on the qualitative characteristics of the investigated process.

Analyzing the relationship between the efficiency of material shredding and the frequency of oscillations of a equipment, one can conclude that the increase in the specific surface of the material increases with the frequency of oscillations due to the increase in the magnitude of the impact pulse crushing balls. At the same time there is a decrease in the area of the treated material, as well as processing time depending on the physical and mechanical parameters of raw materials.

On the basis of the obtained data on the kinetics of material shredding, it was concluded that the efficiency of the process to a large extent depends on the amplitude-frequency parameters of the equipment. However, it should be noted that the technological load in the form of balls with a diameter of 12-18 mm is better to use for rough grinding. Although for fine grinding it is better to use small diameters – 6-9 mm, which leads to an increase in the number of collisions with the material and reduce the probability of its aggregation. It can also be concluded that the greatest productivity of the grinding process is achieved when the balls are loaded at 75-80% of the total volume of the chamber. However, the results of experimental data show that when the filling of the technological environment reaches 50% of the total volume of the chamber, the energy consumption remains constant. However, when the amount of technological environment is 75-80%, energy costs are rising sharply.

The productivity of the developed equipment is 450 kg·h^{-1}. The specific surface of the crushed material is 4080-4190 cm^2·g^{-1}. Homogeneity of the resulting mixture is 98-99%.

Acknowledgements

We want to express our deep gratitude University of West Bohemia in Pilsen for all-round support in scientific activity.

References

[1] Cole G. *Pharmaceutical Production Facilities: Design and Applications.* Chichester, West Sussex: Ellis Horwood Ltd1. 1990.

[2] Dudnikov A.A., Belovod A.I., Pasyuta A.G. Relationship parameters of vibration processing quality of the surface layer. *Vibration in engineering and technology*, 2015, №2(78), pp. 70-74;

MECHANICAL TESTING OF KAPTON FILMS

Tomáš KROUPA[1], Hana ZEMČÍK[1], Robert ZEMČÍK[1], Petr KADLEC[2], Josef PIHERA[2]

[1] NTIS – New Technologies for the Information Society, Faculty of Applied Sciences, University of West Bohemia, Technická 8, 301 00 Plzeň, Czech Republic, Corr. author: kroupa@kme.zcu.cz

[2] University of West Bohemia, Faculty of Electrical Engineering, Regional Innovation Centre for Electrical Engineering (RICE), Univerzitní 8, 301 00 Plzeň, Czech Republic

1. Introduction

Kapton is a material developed by DuPont company that is commonly used for insulation of electric and electronic devices. It offers excellent physical, electrical, thermal and chemical resistant characteristics. It is a polyimide (PI) and it is usually available in a form of a homogeneous film wound onto a drum. There exist several types of Kapton [1]. Kapton CRC100 [2] has been developed for use as an electrically insulating material for high voltage environments where the potential for corona discharge is present (in motor and generator applications as magnet wire, turn to turn strand, coil, slot liner and ground insulation materials; it can be laminated too). Kapton HN [3] general-purpose film has been used successfully in applications at temperatures as low as –269°C and as high as +400°C. It can be laminated, metallized, punched, formed or adhesive-coated. Other manufacturers produce similar polyimide films, e.g. the Chinese Kingzom company. The manufacturers mostly provide measured values of mechanical quantities, such as the tensile strength and tensile modulus, obtained only either along one direction of testing, which can be sufficient only if the material could be regarded as isotropic, or along two directions (machine and transverse), which would suggest that the material is orthotropic.

The goal of this work is to compare stiffness and strength properties of three different films (only two known [2, 3]), analyze the dependence on strain-rate, and quantify the expected material anisotropy. The tensile tests were performed according to CSN EN ISO 527-3 and ASTM D-882-02.

2. Tensile modulus and strength

Five rectangular specimens having dimensions 100 mm × 10 mm and thickness 27 μm (datasheet value is 25 μm) were cut using scalpel from each tested material. The longer side was aligned with the longitudinal (machine) direction of the film. The specimens were loaded up to break using hydraulic jaws (see Fig. 1) and constant crosshead velocity 50 mm/min. The measured values are displayed in Tab. 1. The values of Young's modulus were obtained from the linear parts of the stress–strain diagrams for the range of stress between 5 MPa and 50 MPa (see Fig. 2).

The measuring of deformation proved to be complicated using standard extensometer with sensor arms as they can easily displace the thin specimens to the sides. Therefore, three methods for the measurement of elongation (or strain) of specimens were compared – extensometer (central part of specimen), crosshead (whole specimen), and DIC using digital camera (central part of specimen). An example of displacement field obtained using DIC is shown in Fig. 3.

Fig. 1. Specimen during (left) and after the test (right).

3. Strain rate effect

The dependency of stress–strain to strain-rate was analyzed on Kapton 100CRC (best candidate for our project). Three velocities of the crosshead were used, namely 50 mm/min, 100 mm/min, and 200 mm/min. Three samples for each velocity were tested. The strain-rate effect was found negligible especially in the linear part of the curves.

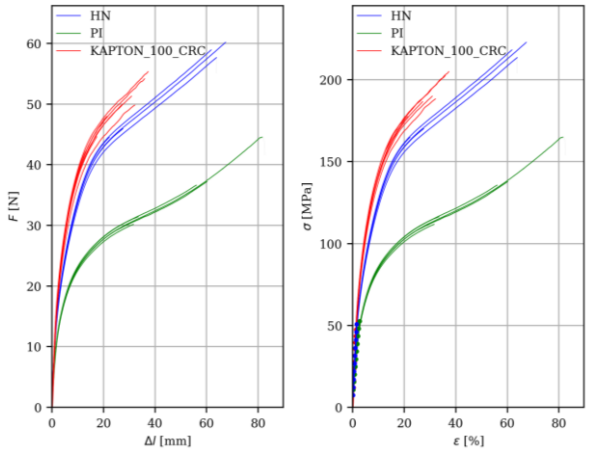

Fig. 2. Stiffness and strength comparison for the three tested materials.

Table 1. Comparison of tested materials' properties.

Material	Modulus [Pa]	Strength [Pa]
Kapton 100CRC	3.80×10^9	188.17×10^6
Kapton HN	2.86×10^9	197.91×10^6
Unknown PI	1.70×10^9	133.30×10^6

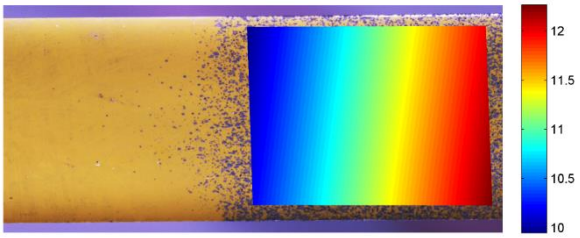

Fig. 3 DIC contours of longitudinal displacement [mm] on a specimen with a sprayed random pattern.

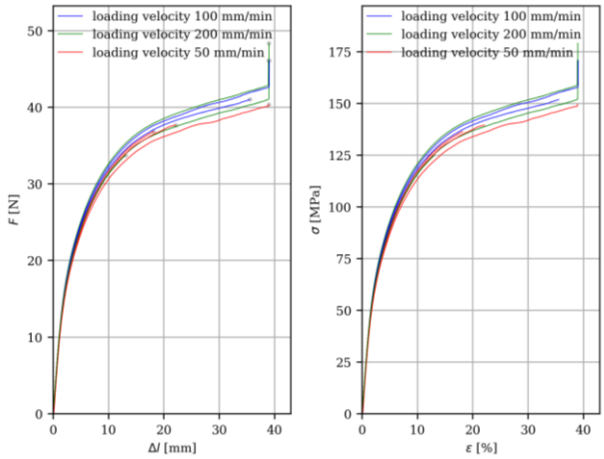

Fig. 4. Stiffness and strength for different strain-rates.

4. Anisotropy

The tests were performed on samples made of Kapton 100CRC with three different material orientation (1~0°, 2~90°, and 3~45°) with respect to the longitudinal axis of the film.

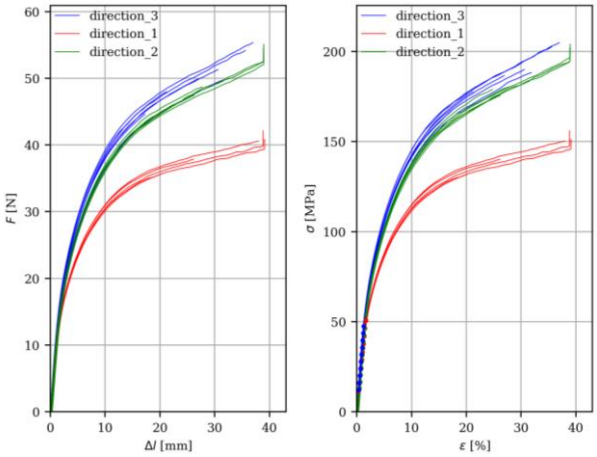

Fig. 4. Stiffness and strength comparison in three different directions of Kapton 100CRC.

Table 2. Directional dependency of stiffness and strength of Kapton 100CRC

Direction	Modulus [Pa]	Strength [Pa]
1	2.96×10^9	142.84×10^6
2	3.68×10^9	190.57×10^6
3	3.85×10^9	188.17×10^6
datasheet [2]	3.48×10^9	227.00×10^6

5. Conclusions

It was shown that the properties of various versions of polyimide films in general can be significantly different. Moreover, the material exhibits anisotropic properties, most likely orthotropic due to the manufacturing process. The strain-rate effect (at least for the tested machine direction and velocity range) was found negligible.

Acknowledgements

This publication was supported by the project TRIO FV30382 "Braided composite construction in electrical engineering – NAPREKON" of Czech Ministry of Industry and Trade, by the project LO1506 of the Czech Ministry of Education, Youth and Sports under the program NPU I. and by the project LO1607 of the Ministry of Education, Youth and Sports of the Czech Republic under the RICE – New Technologies and Concepts for Smart Industrial Systems.

References

[1] DuPont Kapton, General Specifications, 2018. www.kapton.com
[2] DuPont Kapton 100CRC, Technical Data Sheet, 2018. www.kapton.com
[3] DuPont Kapton HN, Polyimide film, 2018. www.kapton.com

TESTING OF SANDWICH SPECIMENS FOR SPACE APPLICATIONS

Robert ZEMČÍK[1], Jan KRYSTEK[1], Tomáš MANDYS[1], Vladislav LAŠ[1], Petr PRŮCHA[2]

[1] NTIS – New Technologies for the Information Society, Faculty of Applied Sciences, University of West Bohemia, Technická 8, Plzeň, Czech Republic, corr. author: zemcik@kme.zcu.cz

[2] LA COMPOSITE, s.r.o., Beranových 65, 199 02 Prague 9, Czech Republic, prucha@lacomposite.com

1. Introduction

This work focuses on the mechanical testing of sandwich structures for space application made mainly of composite skins, aluminum honeycomb core, and joints in the form of inserts. The tests are conducted mainly according to ESA (European Space Agency) specifications (ECSS Standards and Requirements) [1] with the aim to participate in its future projects jointly with LA COMPOSITE company [3].

Structures for space applications must undergo a specific set of mechanical tests that will guarantee that all components of the structure will survive the harsh conditions during launch, in orbit and during landing. During launch the structure is exposed to broad spectrum of strong vibrations caused by the rocket engines or pyrotechnic devices. During the mission, e.g. in orbit, the structure is exposed to vacuum (i.e. no atmospheric pressure), and heat flux and temperature gradients caused by the orientation of the surfaces to Sun or its shadow. The landing phase exposes the structure again to strong oscillations and extreme temperatures.

2. Materials and specimens

All specimens were manufactured in LA COMPOSITE [3] from materials complying with ECSS Structural Materials Handbook [2]. The skins were made of prepregs consisting of carbon fibers and cyanate ester resin. The core was made from perforated aluminum honeycomb. The core and skins were glued with epoxy film adhesive. The insert were made of blind threaded aluminum inserts with Helicoil (M5 and M8 size). Some skin lay-ups contained also a copper mesh within the epoxy film adhesive on the outer surface. The skins were also tested for connecting with flush head blind rivets. One sandwich specimen with insert is shown in Figure 2 before and after testing.

3. Apparatus and testing

The mechanical testing performed in the labs of University of West Bohemia can be separated into three phases (see Table 1 and Figure 1). The first one was used to verify the properties of the prepreg material in form of unidirectional specimens. The second one concerned the skin (quasisotropic layup) and sandwich specimens. The third phase concerned the same specimens as in the second phase but after their exposure to thermal–vacuum cyclic conditioning (5 cycles, ±100 °C, gradient 2-3 °C per minute).

Table 1. Summary of main tests performed.

Phase	Test description	Standard / Specs.
1, 2, 3	Interlaminar shear strength test (ILSS)	DIN EN 2563
1, 2, 3	Lap-shear strength test of adhesives	EN 2243-1, EN 1465
1, 2, 3	Tensile test (various material orientations of unidirectional and quasiisotropic lay-ups)	DIN EN 2561, EN 2597, CSN EN 14129
1, 2, 3	Compression test	EN ISO 14126-2
1, 2, 3	DSC and DMA tests to assess the glass transition temperature	EN ISO 11357:1, EN 6032/A
2, 3	Sandwich flatwise tension test	ASTM C297
2, 3	Sandwich edge compression test	ASTM C 364
2, 3	Sandwich 4-point bending test (4PB)	ASTM D7249
2, 3	Insert pull-out, shear and compression tests	ESA PSS-03-1202, ECSS-E-HB-32-22A
2, 3	Rivet joint bearing and pull-through tests	ASTM D5961, ASTM D7332

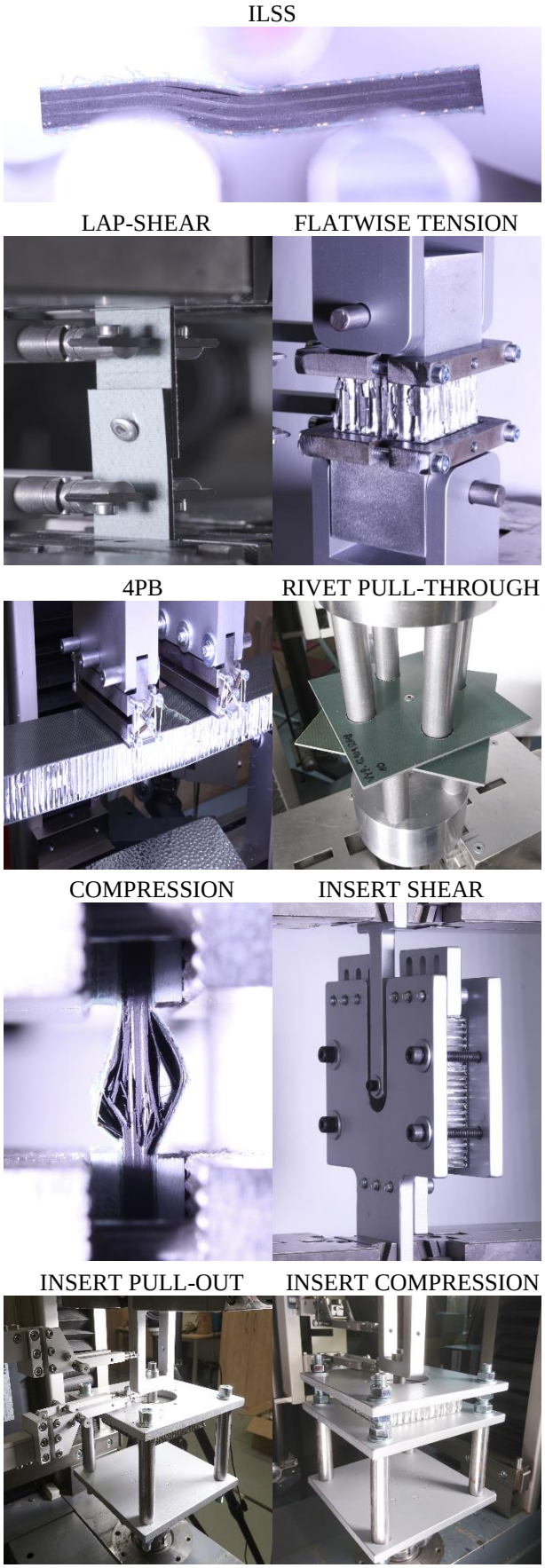

Fig. 1. Various specimens and apparatus used.

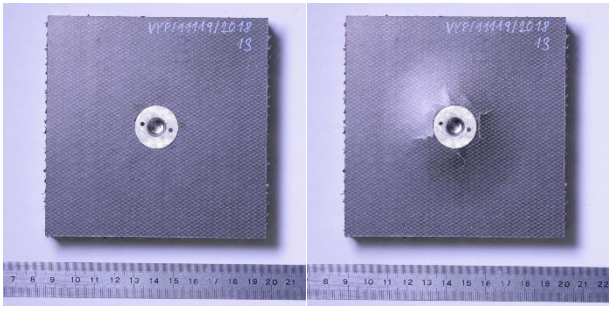

Fig. 2. Typical sandwich specimen (top view) with insert prior (left) and after (right) pull-out test.

Some testing fixtures needed to be designed and manufactured. The fixtures for flatwise tension, insert pull-out and compression were tweaked so that extensometer with arms could be used. This will help to obtain more data for future numerical models such as those in [4] compared to standard approaches where only the less accurate force–crossbar displacement dependency is normally available.

Further testing will concern the verification of sandwich panels with added mass at the inserts subjected to vibrations using a shaker device.

4. Conclusions

A successful cooperation between the manufacturer LA COMPOSITE and University of West Bohemia was established. The experience gained in this project will help both parties to participate in future space project of ESA and its subcontractors.

Acknowledgements

This work was supported by the project TRIO FV10400 “Development of processes applicable to development and production of components for the space industry” of Czech Ministry of Industry and Trade and by the project LO1506 of the Czech Ministry of Education, Youth and Sports under the program NPU I.

References

[1] ECSS-E-HB-32-22A, ESA Requirements and Standards Division, Netherlands, 2011.
[2] ECSS- E- HB- 32- 20 Part 1A, ESA Requirements and Standards Division, Netherlands, 2011.
[3] LA COMPOSITE, s.r.o., https://lacomposite.cz/.
[4] Mandys T., Laš V., Zemčík R., Krystek J. Testing of honeycomb sandwich panel with potted insert. In: Experimental Stress Analysis – Conference Proceedings, pp. 273-278, Luhačovice, 2019.

INFLUENCE OF VIBRATION OF CONTACTS ON FURTHER OPERATION OF HIGH-VOLTAGE SWITCHES

Olena RUBANENKO[1], Vitalii YANOVYCH[2], Olexander RUBANENKO[3,]

[1] The Regional Innovation Centre for Electrical Engineering, University of West Bohemia in Pilsen, Univerzitní 22, 306 14 Pilsen, Czech Republic: olenarubanenko@ukr.net

[2] Faculty of Mechanical Engineering, University of West Bohemia in Pilsen, Univerzitní 22, 306 14 Pilsen, Czech Republic: yanovichvitaliy@i.ua

[3] Department of Electric Stations and Systems, Vinnytsia National Technical University, Khmelnytske shose str., 95, Vinnytsia, Ukraine: rubanenkoae@ukr.net

1. Introduction

Nowadays, there is a big variety of different types of high-voltage switches operating in the power plants. For instance: oil, air, vacuum and insulated gas, that have to correspond to different requirements after taking into operation and after major and current repairs, maintenance and installation of new equipment. These requirements are presented and their technical characteristics are checked and saved in the test reports. These characteristics include the time difference between closing of the contacts (from the first vibration-closing to the termination of the vibration of the contacts) [1].

When the contacts clash to each other the kinetic energy is released and the contacts' springs begin to fluctuate. It is so called vibrations of the contacts phenomenon. During the vibrations, the contacts are dispersed at a slight distance, with electrical breakdowns occurring in the insulation gaps.

During the switching process, the possibility of the simultaneous closing / opening of contacts there is a short-term operation mode, during which the over-voltage can occur during multiple times. With the increase of the rate of non-simultaneous closing of the contacts, which depends partially on the vibration of the contacts, the over-voltages increase.

Contacts in the case of a collision can bounce in the absence of a sufficient damping effect. In this case, the breakage of arc current occurs with the occurrence of single and many high-frequency breakdowns. The characteristics of contact vibration have mechanical nature and can be evaluated with the help of oscillograms of high-speed characteristics. These oscillograms are the most informative for representing the test results.

Figure 1 shows a graph of the dependence of the oscillation from the time for the oil type circuit breaker MKP-110M-1000/630.

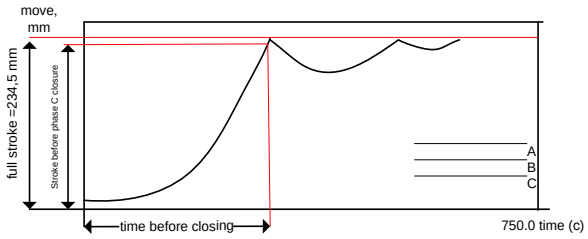

Fig. 1. Dependence of the oscillation from time.

The oscillation-like movements of the traverses at the end of the movement occur because of the failure of the oil buffer and the lack of pressure. Such a type of the failure of the switch is quite harmful because when the oil buffer stops to operate, the switch mechanism gets large dynamic loads that can lead to its breakage.

Figure 2 represents the oscillogram of the switching process in the air circuit breaker (type VVN-110-6-31,5 / 2000).

As shown in Figure 2, the vibration of the contacts occurs when the air circuit breaker was switched on. The reason of this vibration of contacts for these particular types of switches is the loss of mechanical characteristics of the springs belonging to moving and fixed contacts and the reduced use of mobile contacts.

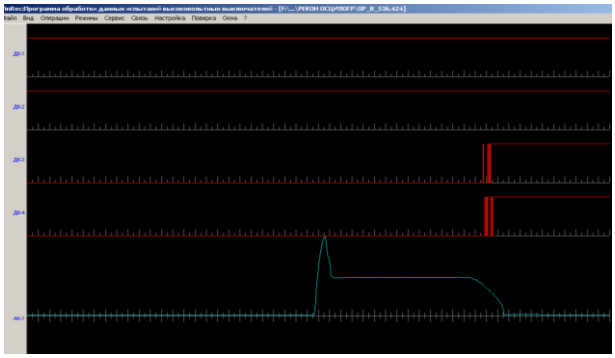

Fig. 2. Switching oscillogram for the air circuit breaker (type VVN-110-6-31,5 / 2000).

The switches mainly use a spring drive. During the switch-on operation and the switch-off at the end of the motion of the moving contact, the residual kinetic energy of the switching springs is spent on the shock absorber during on or off operation. Therefore, the level of vibration of the contacts of the circuit breakers is very small.

When the contacts vibrate, the electric arc re-lights up, inside the arc the temperature can vary from 6000 to 10,000 ° C inside the plasma. The high-voltage arc has a characteristic of a blue hue, which is represented by the light of copper ions, which evaporates from the contacts. The side effect of evaporation is the precipitation of metal vapor on the insulation elements, which reduces the electrical strength of the insulation gap.

Also, with the re-ignition of the electric arc, the surface and the roughness of the contact surface increases, which leads to an increase in the transient resistance of the direct current of the contacts and their heating. The maximum increase in temperature due to the presence of contact can be calculated from the equation:

$$\Delta \nu_k = \frac{\Phi_x}{\sqrt{kS\lambda F}} \qquad (1)$$

where, S is the perimeter of the section, F is the cross-sectional area of the current line, k is the heat transfer coefficient, λ is the specific heat conductivity of the medium, Φ_x is the value of the heat flux according to the formula:

$$\Phi_x = \frac{1}{2} I^2 R_k , \qquad (2)$$

where, I is the current flowing through the contact; R_k – transient resistance of contacts, which is determined by:

$$R_k = c_k \rho H_B^{0.5} p_k^m , \qquad (3)$$

where, ρ - specific resistance, Ohm·cm·10^{-8}; H_B - metal hardness by Brinel, kg/sm^2; $P_к$ - contact pressure, kgs.

Coefficient q - depends on the treatment of the contact surface. In calculating the contacts of the switch should come from a coarse and very rough sweep, with which respectively c_k = 2÷3. The power factor m depends on the contact pressure and the working surface of the contact. In the case of explicit plastic deformation, m=0,5 can be taken.

As can be seen from formula (1), the maximum increase in the heating temperature of the contact joints depends to a large extent on the heat flux, which in turn depends on the transient resistance of the contacts. The transient resistance depends on the roughness of the contacts, which appears during both the burning of the electric arc and the vibration of the contacts during the commutation of the nominal currents.

Conclusions

The reliability of the operation of high-voltage switches greatly depends on the level of vibration of moving contacts. The main causes of vibrations are the loss of initial technical characteristics of the springs of moving contacts and the lack of contact pressure, improper operation of the oil buffer, and others.

All these defects during the operational work can be determined from the speed characteristics. It is quite promising to improve the developed method of controlling the speed characteristics by checking the current of the test signal, which passes between the contacts of the switch when it is switched on or off.

Acknowledgements

We want to express our deep gratitude University of West Bohemia in Pilsen for all-round support in scientific activity.

References

[1] Norms of testing of electrical equipment. - K.: GRIFRE, ME of fuel and energy of Ukraine. Association of Energy Enterprises, MO MoU «Military Publishing Ukraine», 2007. (Normative document of the Ministry of Fuel and Energy of Ukraine).

LOADS ACTING ON THE SPARE WHEEL DURING OPERATING THE TRUCK

Mariusz STAŃCO [1], Jerzy CZMOCHOWSKI[2], Paweł MAŚLAK[3]

[1] University of Science and Technology, Faculty of Mechanical Engineering, Department of Machine Design and Research, 5 Łukasiewicza st., 50-370 Wroclaw, Poland, e-mail: mariusz.stanco@pwr.edu.pl

[2] University of Science and Technology, Faculty of Mechanical Engineering, Department of Machine Design and Research, 5 Łukasiewicza st., 50-370 Wroclaw, Poland, e-mail: jerzy.czmochowski@pwr.edu.pl

[3] University of Science and Technology, Faculty of Mechanical Engineering, Department of Machine Design and Research, 5 Łukasiewicza st., 50-370 Wroclaw, Poland, e-mail: pawel.maslak@pwr.edu.pl

1. Introduction

Loads caused by the use of vehicles, especially those that run on off-road are very often difficult to define, because each terrain is different. In many literature items are given general values of overload which should be taken while designing any vehicle. These values are average values measured for the whole vehicle [2,3]. In the literature, it is difficult to find information about the loads of a particular vehicle element. Usually, the general available values are adopted, for which the appropriate safety factor is then selected. Such a design method leads to overestimation or underestimation of the designed element. An example for which the literature does not provide any guidance is the spare wheel bracket, which in special-purpose trucks often has to be installed just behind the cabin. The center of gravity of the wheel is raised above the upper shelf of the longitudinal frame (Fig. 1). In addition to the forces resulting from the mass of the wheel itself, such an element has to transfer the loads resulting from its inertia when moving on paved roads and off-road roads.

Fig. 1. Spare wheel behind the cabin [1]

The installation of a spare wheel behind the cabin is caused by the lack of free space within the frame of the longitudinal frame or the need to provide adequate ground clearance, which ensures the vehicle moves along off-roads.

2. Experimental research

Experimental tests of loads acting on the spare wheel installed just behind the cab were carried out. The tests consisted of measurements of inertia forces during vehicle operation in the field as well as along paved roads. In the center of gravity of the wheel there is an acceleration sensor measuring the acceleration in three directions. A piezoresistive sensor measuring also the gravity constant was used for the measurements. The sensors were connected by means of cables with a recorder placed in the vehicle's cabin.

Fig. 2. Recorder inside the cabin.

3. Measurement results

Measurements of overloads were obtained from the measurements, which are presented in the form of diagrams shown in Fig. 3-5. The presented measurement results are shown for the maximum values for individual vehicle driving directions and the corresponding remaining directions in a given measurement time. The X direction is the measurement along the vehicle, the Y direction across the vehicle, while the Z direction is the vertical direction.

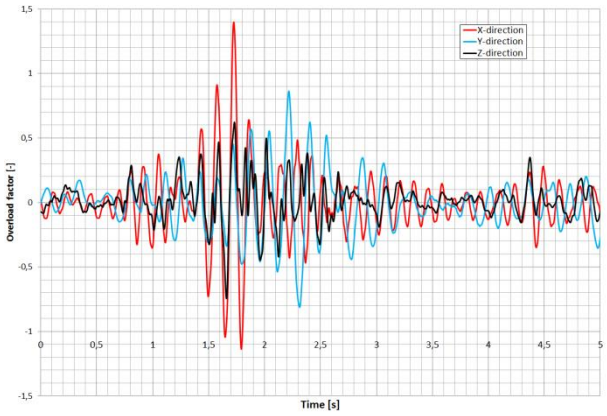

Fig. 3. Maximum longitudinal loads acting on the wheel

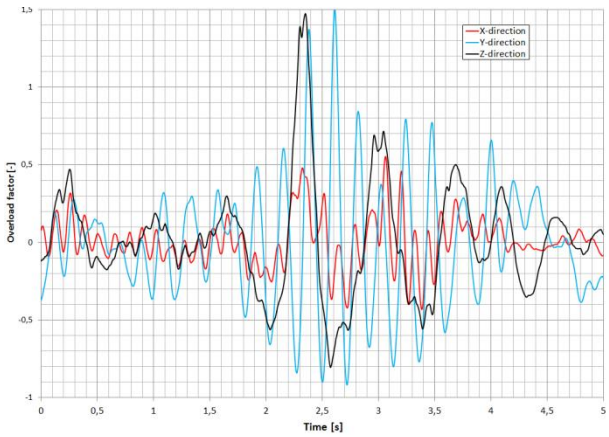

Fig. 4. Maximum transverse loads acting on the wheel

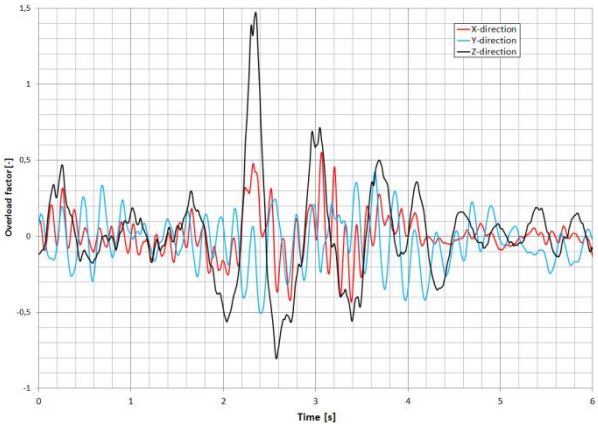

Fig. 5. Maximum vertical overloads acting on the wheel

4. Conclusions

The tests allowed determination of the loads acting on the spare wheel while driving in variable road conditions. Figure 6 shows the overload sequences for the maximum values in each direction. It can be seen that in each of the directions the maximum value of the overload is similar and amounts to about 1.5.

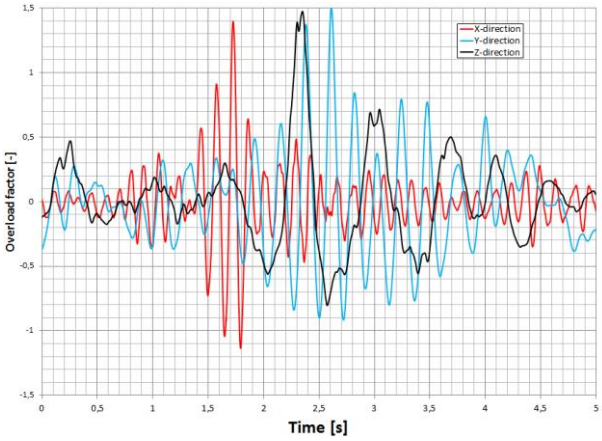

Fig. 5. Maximum longitudinal (X), transverse (Y) and vertical (Z) overloading forces acting on the spare wheel while driving.

References

[1] https://commons.wikimedia.org/wiki/File:Lippujuhlan_p%C3%A4iv%C3%A4n_paraati_2014_065_Karjalan_prikaati_Mercedes-Benz_Actros.JPG
[2] Stańco M., Kosobudzki M., Derlukiewicz D., The experimental identification of effort state oftruck load carrying frame. Croatian Society of Mechanics, 2013. s. 254-255
[3] Kosobudzki M., Stańco M., Kowalczyk M., Akwizycja obciążeń dynamicznych działających na pojazd generowanych przez układ jezdny. Transport Przemysłowy. 2007, nr 4, s. 82-85

MECHANICAL CHARACTERIZATION OF SLA 3D-PRINTED PARTS

Francesca COSMI[1], Alberto DAL MASO[2]

[1] University of Trieste, Via Valerio 1, Trieste, Italy, E-mail: cosmi@units.it;

[2] University of Trieste, Via Valerio 1, Trieste, Italy, E-mail: albertodalmaso92@gmail.com;

1. Introduction

Stereolithography is becoming a more and more popular 3D-printing technology, as it offers superior dimensional accuracy and overall part quality when compared to the cheaper and more widespread Fused Deposition Modeling. [1] The price of stereolithography (SLA) printers is nowadays affordable when compared to several other technologies on the market. Originally, SLA was used only for concept models or ornamental purposes, however, improvement in material properties encourages several makers and engineers to apply this technology also in load-bearing applications. For this purpose, it is vital to know the mechanical characteristics of the materials used. In this work, tensile tests on SLA 3D-printed clear resin samples are performed and results are compared with the manufacturer's datasheet.

2. Materials and methods

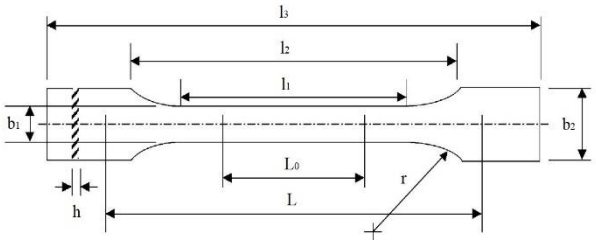

Fig. 1. Geometry of the 1BA specimens used.

Tensile tests were performed following ISO 527-1 norm [3]. The specimens adopted are of type 1BA: Figure 1 shows the geometry of the samples. Specimens were 3D-printed in a Formlabs™ Form 2™ SLA machine, using Clear V4™ resin. Layer height was set to 50 µm. Specimens were printed at different orientations, with θ varying from 0° to 90° at 15° intervals, where θ is defined as the angle between the specimen's axis and the vertical direction (z axis), as shown in Figure 2. Three samples were printed for each orientation.

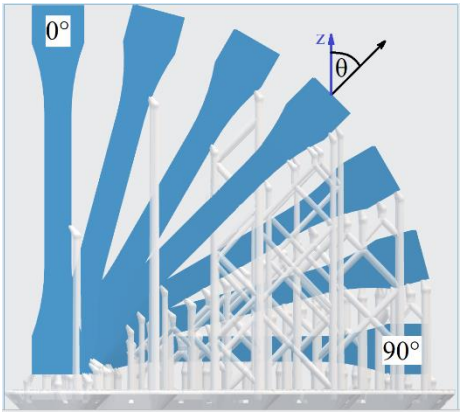

Fig. 2. Different printing angles.

The in-house-designed tensile machine adopted for these tests consists of two caps, which are mounted on the opposite ends of a stiff cylindrical frame. On the lower end, a grip is mounted on a platform. A load cell is positioned on the support connecting the platform to the frame. The upper cap hosts the hand-driven screw mechanism through which the displacement is applied. An extensometer measures the distance between the cap and the grip. **Chyba! Nenalezen zdroj odkazů.** shows a CAD drawing of the system.

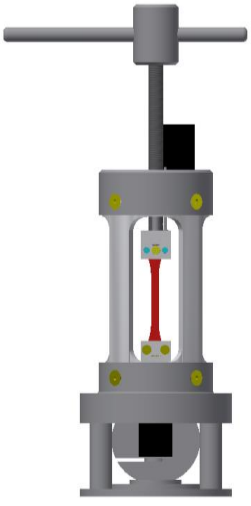

Fig. 3. CAD drawing of the tensile testing machine.

3. Results and discussion

Stress-Strain curves were obtained for each specimen and are reported in Figure 4.

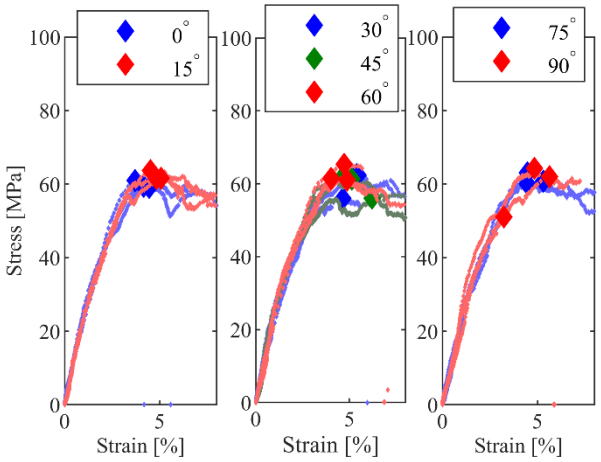

Fig. 4. Stress-Strain curves for the 21 tested specimens.

Maximum stress and Young's modulus were calculated for each sample. The mean value for each angle is plotted in Figure 5.

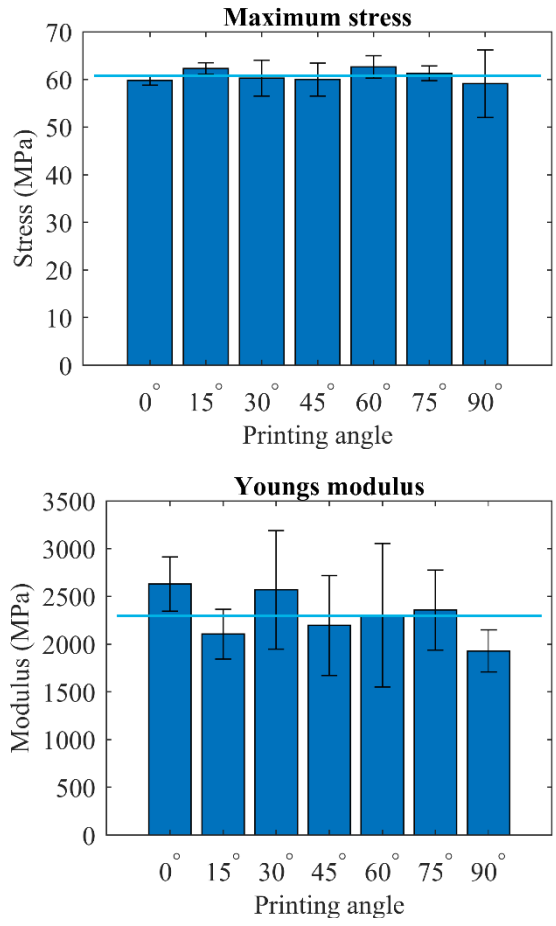

Fig. 5. Mean characteristics per printing angle θ.

Overall statistics for the material properties are summarized in Table 1. These are compared to the technical datasheet provided by the manufacturer [4].

The results obtained in-house show, on average, a slightly lower maximum stress than the manufacturer's datasheet, while the Young's modulus is very similar. This study confirms the Formlabs™ statement that SLA 3D-printed parts are isotropic: in fact, there is no evident relationship between printing orientation and mechanical characteristics, as shown in Fig. 4 and 5.

Table 1. Isotropic behavior material characteristics.

		Max stress [MPa]	Strain at max stress [%]	Young's modulus [MPa]
In-house test	**Mean** (Std.)	**60.8** (1.33)	**4.75** (0.42)	**2298** (249)
Formlabs™ datasheet	**Mean**	**67.1**	-	**2388**

4. Future developments

The final goal of this work is the experimental validations of numerical simulations, i.e. of the mechanical properties of bone structure and for the topological optimization of load-bearing parts, Fig. 6. To this aim, the mechanical characterization of Clear V4™ resin will be completed by compression tests.

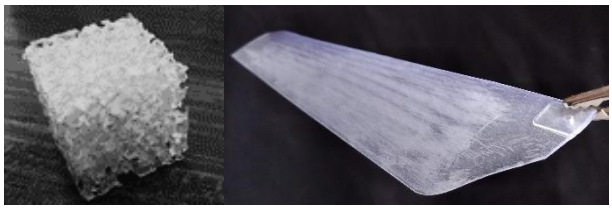

Fig. 6. Examples of SLA load-bearing applications:
internal bone structure (left);
model helicopter replacement blade (right).

References

[1] Redwood B., Schöffer F., Garret B The 3D Printing Handbook. *3D Hubs B.V.*, 2018.
[2] Dr. Ian Gibson et al. Additive Manufacturing Technologies - Rapid Prototyping to Direct Digital Manufacturing. *Springer*, 2010
[3] UNI EN ISO 527-1: Plastics - Determination of tensile properties. 2012.
[4] *Formlabs – Validating isotropy in SLA 3D printing*. https://formlabs.com/blog/isotropy-in-SLA-3D-printing/. Accessed February 03, 2019.

MONOTONIC TENSILE, CREEP AND FATIGUE TESTS OF ALUMINUM ALLOY ACCOUNTING FOR DYNAMIC RECRYSTALLIZATION

Adam TOMCZYK[1], Andrzej SEWERYN[1]

[1] Bialystok University of Technology, Faculty of Mechanical Engineering, 45C Wiejska St, 15-351 Białystok, Poland, a.tomczyk@pb.edu.pl, a.seweryn@pb.edu.pl

1. Introduction

In practice, it may occur that a structural element will be subjected to the action of short- or long-term, time-constant mechanical and thermal loading, followed by cyclically varying loadings at ambient temperature after the temperature drops. The paper presents an investigation of monotonic tensile and creep tests at the elevated temperatures of 100 °C, 200 °C, and 300 °C taking into account the effect of dynamic recrystallization (DRX) process. As-received material was subjected to creep process with constant force at elevated temperatures, until two varying degrees of deformation ε_s and ε_t were reached. After cooling at ambient temperature, the pre-deformed material was subjected to monotonic and fatigue tests as well as metallographic analysis.

2. Experiment details

EN AW-2024 T3511 aluminum alloy, in form T3511, was used in tests [1,2]. Bars with a length of 3 m and diameter of 16 mm were prefabricate for making axisymmetric specimens. According to the attestation, the material was hardened $AlCu_4Mg$, and the rod was manufactured by extrusion.

Specimens applied in monotonic tensile and creep tests were characterized by identical shape and dimensions. Gauge length and diameter dimensions were 13mm and 6.5mm respectively. The gripped part of specimens was threaded, as dictated by the design of the creep testing machine. Monotonic tensile tests and creep tests were conducted on a 4-column Kappa 100 SS creep testing machine from the Zwick/Roell, with an electro-mechanical drive. An electric Maytec furnace with three heating zones, with a temperature range up to 900°C, controlled by universal Zwick/Roell controller, was used for tests at elevated temperature. A device specially designed and made for measuring deformations was used [3]. Axial extensometer (Epsilon 3542050M-50-ST) with a variable measuring base of 25/50mm and a range of +25mm and -5mm was used in cooperation with the grip described above. The samples after the tensile and creep tests were subjected to metallographic analysis. The metallographic specimen were polished and etched with Keller's reagent (1.5%HCl+1%HF+2.5% HNO_3+95% H_2O).

All low-cycle fatigue tests were conducted on a servo-hydraulic MTS 322 unit with an actuator range of ±50 kN. An Instron 2620-601 dynamic axial extensometer with a gauge length of 12.5 mm and range of ±5 mm was used in tests. Tests were conducted at room temperature (20 °C) with a frequency of f=0.2 Hz and strain ratio $S=\varepsilon_{min}/\varepsilon_{max}=-1$. The control variable was the amplitude of total strain ε_a. In the first stage, as-received specimens were tested, followed by specimens made from material with creep pre-deformation at elevated temperature (100°C, 200°C, 300°C) at two different strain levels, ε_s and ε_t. The idea was that the smaller deformation ε_s corresponds to the beginning of the second creep stage. The choice of larger deformation (ε_t) was encouraged by the need to achieve a specific strain close to the end of the secondary creep and the beginning of the tertiary creep.

Low-cycle fatigue tests were conducted on as-received material and material with pre-deformation at 100°C, 200°C and 300°C. Undamaged (as-received) material was chosen for comparison purpose. The material with pre-deformation–due to the possibility of investigating the impact of the DRX process on the cyclic properties of the material. Five degrees of total strain amplitude were selected (i.e., 0.02, 0.01, 0.008, 0.005, 0.0035), and tests on each level were repeated three times.

3. Results and discussion

The description of the fatigue life was made using Manson–Coffin–Basquin model [1]. In

Fig. 1, typical curves of fatigue life obtained for as-received material are compared with those obtained for material with pre-deformation at 300°C.

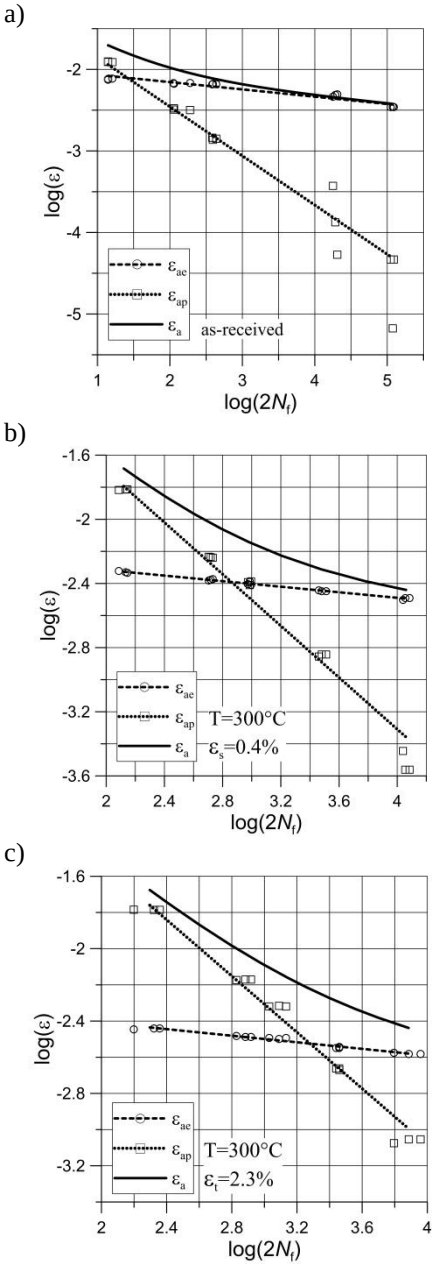

Fig. 1. Fatigue life curves at room temperature, obtained for as-received specimens (a) and for specimens with creep pre-deformation at 300°C: b) ε_s=0.4%, c) ε_t=2.3%.

A significant increase in the fatigue life was observed in the area dominated by plastic deformation in the samples with creep pre-deformation at 300°C, where clear dynamic recrystallization occurred. This applied to the samples pre-deformed to both values of strain (ε_s=0.4% and ε_t=2.3%), although the improvement was more significant for ε_t. The inverse situation could be observed in the area dominated by elastic strains. In this case, the fatigue life decreased in comparison with as-received material.

4. Conclusion

This paper presents results of the study on the influence of preliminary creep at elevated temperature on the monotonic and cyclic properties of 2024 aluminium alloy. In the case of low temperature (100°C) and high strain value, these properties were determined to be affected mostly by mechanical hardening of the material. In the case of higher temperatures (200°C, 300°C), the possibility of continuous dynamic recrystallization gained significance. This possibility occurred even at low loading speeds (i.e., 0.0015/s), although in the monotonic tension process only at the temperature of 300°C. In the case of creep at 200°C, the recrystallization process occurred only in cases of loading until a greater level of pre-strain ε_t=2.3% was achieved. In the case of creep at 300 °C, this process occurred for preliminary strain of both ε_s=0.4% and ε_t=2.3%. However, in the latter case, the process covered a noticeably greater number of grains.

The improvement of the fatigue life was determined to take place at the cost of the decline of its fatigue strength at constant value of the strain-control variable. Such regularity was most visible in the material pre-deformed at the temperature of 300°C, and was much less visible at 200°C.

Acknowledgements

The present paper is financially supported by the National Science Centre of Poland (research project No 2018/29/B/ST8/00697) and realized in Bialystok University of Technology.

References

[1] Tomczyk, A., Seweryn, A., Grądzka-Dahlke, M., The effect of dynamic recrystallization on monotonic and cyclic behaviour of Al-Cu-Mg alloy, *Materials*, 2018, 11, 874.
[2] Tomczyk, A., Seweryn, A., Doroszko, M., Monotonic behaviour of typical Al-Cu-Mg alloy pre-strained at elevated temperature, *J. Theoret. Appl. Mech.*, 56,1055-1068.
[3] Tomczyk, A., Koniuszewski, R., Construction of a System for Measuring Sample Elongations at Elevated Temperatures Using Devices Intended for Work at Room Temperature, *Patent No. PL 68955 Y1, 31 March 2017* (in Polish).

INVESTIGATION OF FIBRE BRAGG GRATING RESPONSE UNDER INHOMOGENEOUS DEFORMATIONS

Susann HANNUSCH[1], Katharina SCHICH[1], Edgar PERETZKI[1], Thomas LEHMANN[1], Jörn IHLEMANN[1]

[1] Chemnitz University of Technology, Chair of Solid Mechanics, Reichenhainer Str. 70, 09126 Chemnitz, Germany, E-mail: susann.hannusch@mb.tu-chemnitz.de

1. Introduction

By the usage of strain sensors, the assumption is often that the strain is measured at one point. In reality, the sensors are often exposed to variations of strain state along its dimensions. This fact is observed for electrical strain gauges e. g. in [1]. We know that the strain gauges display an integral value of the deformation over the strain gauge area.

For the analysis of fibre-Bragg-grating (FBG) sensors a narrowband reflected peak, which arises from homogeneous deformation, is assumed [2]. This requirement is rarely satisfied by grating length of 2 to 8 mm. Thereby, the questions raise: What happens with the reflected wavelength peak of the FBGs and how is the degenerated wavelength peak to be evaluated?

2. Layout of specimen

For the investigation of the FBG response of inhomogeneous deformations, a well-defined strain state is applied. Different opportunities exist to generate an inhomogeneous strain state in a component. In this abstract, the inhomogeneous strain is generated by a bending test with different notched aluminium beams.

In this paragraph, the shape development of the different notched beams are described. To display the influence of the inhomogeneous strains, different geometries of the notch causes a different strain gradient, whereby the notch geometries are selected in this way that the strain gradients are differed considerably. To evaluate the strain gradients, numerical simulations are performed with the tool Ansys®. The beam is a symmetric 2D half model and the strain gradient is determined by a path on the unnotched side of the beam. For the comparison, an unnotched beam is also investigated, which occurs homogeneous strain. In Fig. 1, the different notch geometries and the strain distributions in longitudinal direction of the beam are displayed.

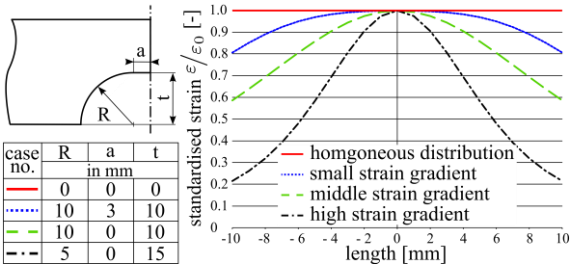

case no.	R	a	t
	in mm		
—	0	0	0
·····	10	3	10
– –	10	0	10
–·–	5	0	15

Fig. 1. Geometries of used notches and corresponding strain distributions.

Besides the FBG sensor, which are draw tower gratings with 8 mm length, an electrical strain gauge is applied on the surface of the bending beam. This strain gauge is installed in central position above the notch. On the right and left side, two FBG sensors are applied. One FBG sensor is positioned above the centre of the notch position (centric FBG) and one sensor aligns with the centre of the notch (eccentric FBG). The realised application of the different sensors is shown in Fig. 2.

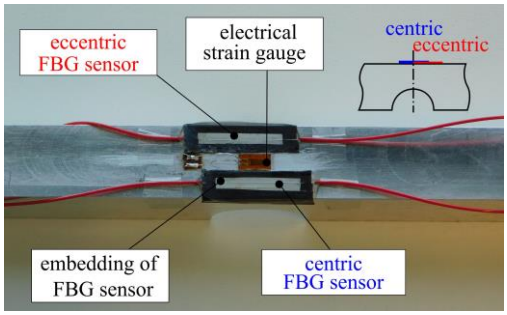

Fig. 2. Application of strain gauge and FBG sensors.

3. Experimental setup

In the following, the notched beams are investigated in a four point bending test, which is similar to the test setup explained in [3]. The experimental setup is depicted in Fig. 3. Therefore, the upper and lower bearings are pivot-mounted rolls to apply a defined load conditions.

The experimental sequence starts with a small preload. Afterwards, the system is reset and a given displacement of the upper bearings is reached. At the given displacement, the strain at the surface amounts approximately 2000 µm/m. This value is determined by a simulation of the specimen with the largest strain gradient and ensures that the beam is loaded only in the elastic range. Thus, the beams can be investigated several times as well as in different directions e. g. tension and compression.

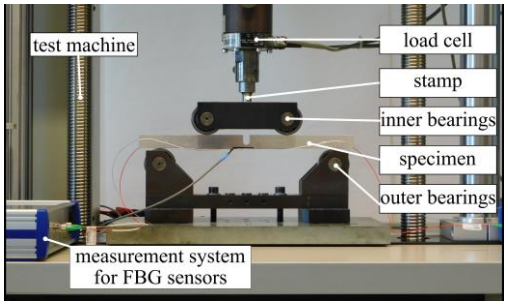

Fig. 3. Setup of four-point-bending test.

4. Analysis of experimental data

Expectedly, the FBG responses of the homogeneous beam show no significant changes during the loading. The peak stays narrowband and has a high reflectivity. The peak fulfils the Bragg conditions and a reflected wavelength can be detected. This reflected wavelength is required to calculate the strain in the fibre. In Tab. 1, the calculated strains of centric and eccentric FBGs are compared with the strain of the strain gauge for tension loading. A very good reproducibility is recognisable.

Table 1. Experimental results of homogeneous beam with tension load

case no.	force [N]	strain of strain gauge [µm/m]	strain of centric FBG [µm/m]	strain of ecc. FBG [µm/m]
1	5492	1929	1924	1938
2	5496	1931	1932	1946
3	5496	1931	1930	1946
AVG	5494	1931	1929	1943
STD	2	1	4	4

For the notched beams the peaks get an expanded shape, whereby a strain can be calculated by the peak shift. The strain analysis fails if the peak splits, which occur by the loaded beams with middle or high strain gradient. One example is shown in Fig. 4, where distribution of the FBG response of the beam with high strain gradient is shown. First, the enlarging of the peak and the decreasing of the reflectivity can be observed and up to 950 µm/m the central, centric peak splits and enlarges more and more. This peak splitting is reversible and vanishes if the beam is unloaded.

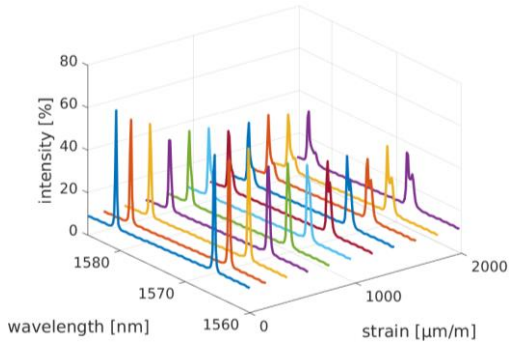

Fig. 4. Distribution of FBG spectra above the strain.

5. Challenges and conclusions

In this abstract, a four-point-bending test of notched aluminium beams is presented. This bending test is used to introduce inhomogeneous strain in FBG sensors. Thereby, the FBG response of an unnotched beam is as expected. For the notched beams, the reflected peak enlarges and decrease in the reflectivity. For a critical value of inhomogeneous strain, the reflected peak splits. At this point, the analysis of FBG signal collapses.

In literature, it is described to reconstruct a FBG spectra with e.g. the T-matrix method [4] which can be specified as a mathematical forward model. The challenge is to determine strain distributions from measured FBG spectra with splitted peaks by the solution of the inverse problem.

Acknowledgements

This work is part of a measure which is co-financed by means of taxation on the basis of that of the deputies of the Saxon Parliament decided budget. The financial support is gratefully acknowleged.

References

[1] Hofmann, K. An Introduction to Stress Analysis using Strain Gauges. *www.hbm.com*, 03.05.2019
[2] Kersey, A., Davis, M.A., Patrick, H., Leblanc, M., Koo, K., Askins, C.G., Putnam, M.A., Friebele, E. Fiber Grating Sensors. *J of Lightwave Technology*, 1997, Vol. 15, pp. 1442-1463.
[3] VDI/VDE/GESA 2660, Optical strain sensor based in fibre Bragg grating – Fundamentals, characteristics and sensor testing. 2010.
[4] Peters, K., Pattis, P., Botsis, J., Giaccari, P. Experimental verification of response of embedded optical fiber Bragg grating sensors in non-homogeneous strain fields. *J Optics and Lasers in Engineering*, 2000, pp. 107-119.

MICROMECHANICS OF NON-EMBEDDED SPRUCE WOOD: NOVEL POLISHING AND INDENTATION PROTOCOL

Luis ZELAYA-LAINEZ[1], Olaf LAHAYNE[1], Giuseppe BALDUZZI[1], Christian HELLMICH[1]

[1] Institute for Mechanics of Materials and Structures, Vienna University of Technology - TU WIEN, Karlsplatz 13/E202, Vienna, Austria

E-mail: Luis.Zelaya.Lainez@tuwien.ac.at, Olaf.Lahayne@tuwien.ac.at, Giuseppe.Balduzzi@tuwien.ac.at, Christian.Hellmich@tuwien.ac.at

1. Introduction

The material properties, such as the reduced elastic modulus, of wood can be determined by indentation protocols and resulting unloading displacement curves [1]. There are several indentation campaigns performed in wood [2,3]. Nevertheless, most of them use embedding substances, such as resin, to stabilize the material for surface polishing protocols [4]. Thus, we propose a novel polishing protocol without the need of an embedding medium. This will be complemented by an extensive number of indents and a statistical nanoindentation technique [5,6] to identify the phase with non-mechanical damage. Namely, we are focusing on indents different than air phase and mechanically damaged cell wall, as seen in Fig.2.

2. Materials and Methods

12 cubes of Norway spruce (*Picea abies*) with dimensions of approximately 2x2x2 cm^3 were harvested by means of different circular saws. Subsequently, each of the cubes was attached to a microscope glass slide using a 2 components glue. Later, the samples were stored in a climate chamber at 21 centigrade and 35% relative humidity until further steps.

2.1 Polishing

The surface perpendicular to the grain direction was polished by means of an ultra-miller (Leica Microsystems GmbH, Germany). The resulting finish of the surfaces were examined first by means of a light microscope, as seen in Figs. 1 and 2. Furthermore, the roughness of a region in each sample was examined by means of a Triboindenter (Hysitron Inc., USA), equipped with a three-sided pyramid-shaped tip (Berkovich type).

2.2 Indentation

The nano-indentation protocol was performed in displacement control mode by the beforementioned indenter. Conditions inside the indenter chamber were kept constant at 21 centigrade and 35 % RH. Two early and two late wood areas were selected at each of the 12 samples surfaces. Subsequently, 100 indents were performed on each of the areas, resulting in a total of 4800 indents. The indentation depth was 300 nm, and the separation in between indents was 30 micrometers. The probability distributions of the resulting elastic modulus were interpolated using a linear combination of three log-normal Probability Density Functions. The non-mechanically damaged phase will be represented by the distribution with the highest statistical mean.

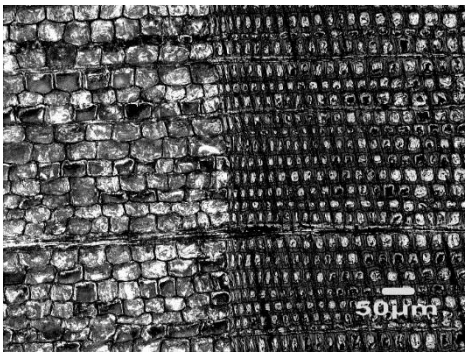

Fig. 1. Light microscopy image of spruce wood with 100x magnification of the transition area between early wood (left) and late wood (right). Sample number 2/12.

3. Results

Three probability distribution functions work adequately for our resulting reduced elastic modulus. Figs. 3, 4, 5, show the beforementioned statistical approach. The mechanical undamaged phase (cell wall) is the mean of the distribution with the highest mean elastic modulus and is represented in our figures as a red-colored PDF.

4. Discussions

The proposed polishing and indentation protocol allow a new methodology to study the microstructure of wood without the influence of external agents. The embedding with resin of wood, consist of an unknown saturation of porosity with resin. This has unknown effects on cell wall stiffness. [7] documented around 17 GPa for embedded samples. Meanwhile, we obtained around 15 GPa for the mean late wood undamaged phase. Our lower value may result from a higher hydration level of the cell wall, meditated through open pores in a climate chamber. Embedding of wood with resin typically does not lead to complete filling of lumen pores.

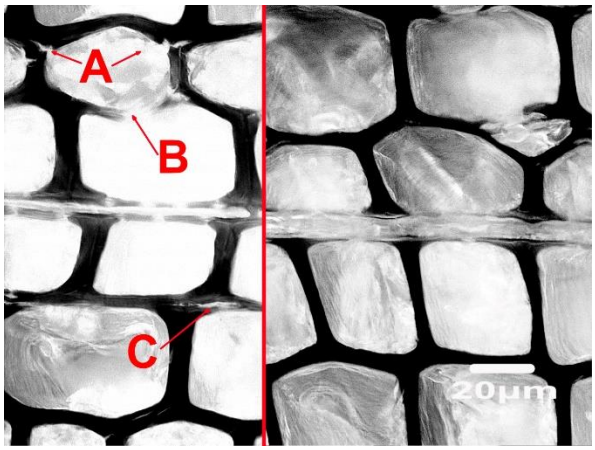

Fig. 2. Light microscopy image of spruce wood with 500x magnification of early wood. Sample number 4/12 (left) shows the mechanical damages: (A) cracks (B) wall failure (C) delamination. Sample number 1/12 (right) shows mostly desired undamaged cell walls.

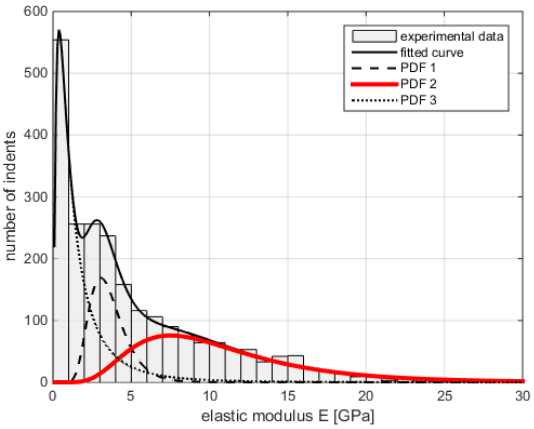

Fig. 3. Probability distribution functions and histogram of elastic modulus from 2400 indents on early spruce wood (fitted curve with Root Mean Squared Error of 0.00165 and R-Squared of 0.999). PDF 2 represents the undamaged cell wall.

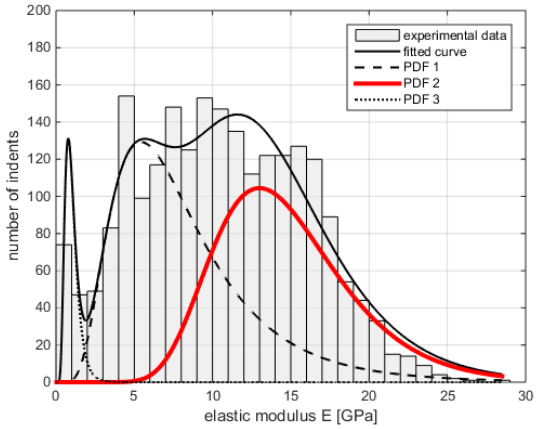

Fig. 4. Probability distribution functions and histogram of elastic modulus from 2400 indents on late spruce wood (fitted curve with Root Mean Squared Error of 0.00828 and R-Squared of 0.925). PDF 2 represents the undamaged cell wall.

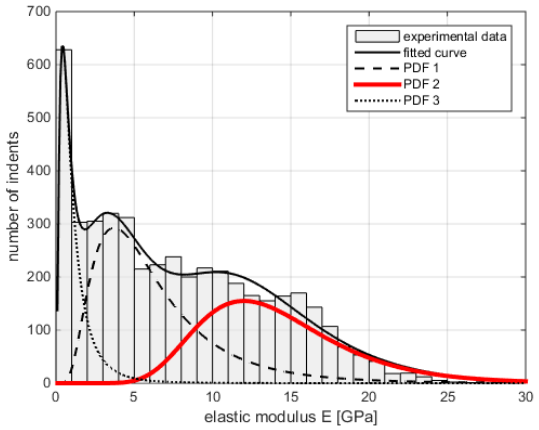

Fig. 5. Probability distribution functions and histogram of elastic modulus from 4800 indents on early and late spruce wood (fitted curve with Root Mean Squared Error of 0.00266 and R-Squared of 0.992). PDF 2 represents the undamaged cell wall.

References

[1] Oliver WC, Pharr GM (1992) J Mater Res 7:1564
[2] Gindl W, Gupta HS (2002) Compos Part A: Appl S 33:1141
[3] Konnerth J, Gierlinger N, Keckes J, Gindl W (2009) J Mater Sci 44:4399.
[4] Meng Y, Wang S, Cai Z, Young TM, Du G, Li Y (2013) Appl Phys A 110:361
[5] Kariem H, Pastrama M-I, Roohani-Esfahani SI, Pivonka P, Zreiqat H, Hellmich C (2015) Mat. Sci. Eng. C 46 553-564.
[6] Furin I, Pastrama M-I, Kariem H, Luczynski KW, Lahayne O, Hellmich C (2016) MRS A 1(11), 693–704.
[7] Wagner L, Bader TK, de Borst K (2014) J Mat Sci 49:94-102.

PLATYNEREIS DUMERILII CHAETAE: MECHANICAL LOADING ESTIMATION FROM KINEMATICS IN LARVA STAGE

Luis ZELAYA-LAINEZ[1], Giuseppe BALDUZZI[1], Kyojiro N. IKEDA[2], Florian RAIBLE[3], Christian HELLMICH[1]

[1] IMWS, TU Wien – Vienna University of Technology, Karlsplatz 13/202, 1040 Vienna, Austria, E-mail luis.zelaya.lainez@tuwien.ac.at, giuseppe.balduzzi@tuwien.ac.at, christian.hellmich@tuwien.ac.at;

[2] Department of Microbiology, Immunobiology and Genetics, University of Vienna, Dr.-Bohr-Gasse 9, 1030 Vienna, Austria, E-mail kyojiro.ikeda@univie.ac.at

[3] Max F. Perutz Laboratories, Vienna Biocenter (VBC), Dr. Bohr-Gasse 9, 1030 Vienna, Austria, E-mail florian.raible@mfpl.ac.at

1. Introduction

Bristle worms (Polychaeta) take their name from the bundles of bristles (chaetae) borne by the appendages (parapodia) of their segmented body. Chaetae are extremely well-tailored chitinous extracellular beam-like structures, often combining materials with different density and texture, and exhibiting medullary and cortical channels of different size, stiffening diaphragm, joints, and teeth [1, 2].

On the one hand, the outward appearance of chaetae were extensively investigated by biologists as a means for the species determination [3]. On the other hand, chaetae turn out being an interesting case study for engineers. Indeed, deciphering the engineering principles of nature can improve the design and manufacturing of artificial structures. However, the systematic analysis of chaetae functions is at its very infancy.

1.1 Chaetae function and worm behavior

Our research focuses on *Platynereis dumerilii*, a well-established laboratory reference species of bristle worms [4]. The mixed benthonic-pelagic lifestyle of *Platynereis dumerilii* suggests that chaetae have versatile functions during worm life. Furthermore, from the second to the seventh day of development, *Platynereis dumerilii* larvae have both chaetae bundles and ciliary bands (prototroch and metatroch) both used for swimming, rendering the perception of chaetae function a challenging task.

Qualitative analysis of swimming larvae have highlighted two different swimming strategies: (i) slow crawling-like movements, when larvae swim using chaetae and (ii) fast torpedo-like movements, when larvae swim using cilia. In particular, during torpedo-like swimming, chaetae are tightly attached to the animals bodies (Figure 1, left), while larvae stretch chaetae apart from the body for effective deceleration and swerve actions (Figure 1, right).

Fig. 1. P. Dumerilii larvae at the third day of development. Position of the chaetae during torpedo-like swimming (left) and decelerating (right) larvae.

1.2 Aims

According to the considerations introduced in Section 1.1, inertial forces acting on larva body during decelerations are identified as an interesting estimator for the mechanical loads acting on the chaetae, allowing for the definition of a well-set engineering problem. Aiming at estimating the inertial forces, the present contribution discusses the procedure used for the evaluation of the accelerations experienced by *Platynereis dumerilii* larvae in laboratory conditions.

2. Materials and methods

Swimming *Platynereis dumerilii* early nectochaete (i.e., the development stage of larvae at 72 hours post fertilization) were filmed. Images were recorded with a frequency of 5 frames per second with a 5x magnification and a resolution of 1920 x 1080 pixels. Frames were processed with the software ImageJ. The positions $\boldsymbol{p}_i = (x_i, y_i)$ of the

early nectochaete at time t_i (for $i = 1...N_f$, being N_f the total number of frames) have been recorded using a semi-automatic tracking procedure.

The instantaneous velocity $\boldsymbol{v}_i$ and acceleration $\boldsymbol{a}_i$ are estimated using finite difference formulas of second order of accuracy, reading

$$\boldsymbol{v}_i = \frac{\boldsymbol{p}_{i+1} - \boldsymbol{p}_{i-1}}{2\,\Delta t} \quad (1)$$

$$\boldsymbol{a}_i = \frac{\boldsymbol{p}_{i+1} - 2\,\boldsymbol{p}_1 + \boldsymbol{p}_{i-1}}{\Delta t^2} \quad (1)$$

The unit vector tangent to the trajectory is evaluated as $\boldsymbol{t}_i = \boldsymbol{v}_i / |\boldsymbol{v}_i|$ and the tangential component of the acceleration was computed as $a_{t\,i} = \boldsymbol{a}_i \cdot \boldsymbol{t}_i$.

Globally, 5220 velocities and accelerations were recorded and analyzed. Since we are interested in the deceleration mechanism, we limited the statistical analysis to negative tangential accelerations $a^-_{t\,i}$ and we interpolate their absolute value distribution using a lognormal curve.

3. Results

Fig. 2 summarize the results obtained from the procedure described in Section 2. The interpolations based on a lognormal curve seems appropriate. Indeed, the obtained results are associated with an extremely low Root Mean Squared Error (RMSE) and a high coefficient of determination.

Maximal deceleration was estimated as the 98th percentile of lognormal curve, resulting equal to 5930 micron/sec^2. Knowing the mass of the larva, we estimated the inertial forces acting on the larvae. Finally, we estimated the chaetae maximal stress assuming that all the chaetae contribute equally to the deceleration of the larvae and modeling the chaetae as a cantilever with uniformly distributed load. The resulting maximal stress ranges between 10 and 100 Pa.

The obtained the maximal stresses looks small in comparison with the strength of chitin (ranging from 0.4 to 400 MPa, according to data available in literature [5, 6]). Such a result suggests that the considered loading mechanism is not significant for chaetae in considered stage development and environment conditions.

4. Conclusions

The proposed methodology has allowed to analyze fundamental kinematic quantities associated to the swimming of *Platinereis dumerilii* early nechtochaetae. The adopted interpolation has the capability to provide accurate and quantitative information on empirically observed phenomena, allowing for a simple preliminary analysis of the magnitude of loads acting on chaetae.

Future research will include the extension of the proposed analysis to other development stages of *Platinereis dumerilii* and more realistic life conditions, aiming at identifying loads inducing highest stresses.

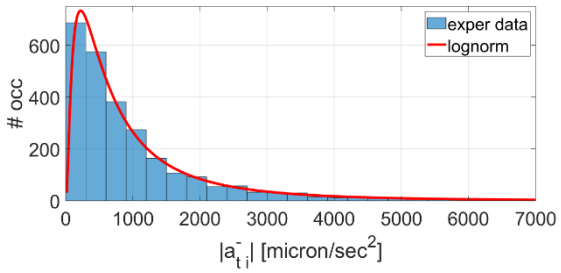

Fig. 2. Statistical distribution of recorded negative acceleration (fitting curve RMSE = 9.14E-6, coefficient of determination R2 = 0.998).

Acknowledgements

This work was supported by grant Bio3DPrint from the Austrian Academy of Sciences (OeAW).

References

[1] Hausen H. Chaetae and chaetogenesis in polychaetes (Annelida). *Morphology, Molecules, Evolution and Phylogeny in Polychaeta and Related Taxa*, 2005, 37-52.

[2] Westheide W., Russell C.W. Ultrastructure of chrysopetalid paleal chaetae (Annelida, Polychaeta). *Acta Zoologica*, 1992, 73(3), 197-202.

[3] Merz R.A., Woodin S.A. Polychaete chaetae: function, fossils, and phylogeny. *Integrative and comparative biology*, 2006, 46(4), 481-496.

[4] Fischer A.H., Henrich T., Arendt D. The normal development of Platynereis dumerilii (Nereididae, Annelida). *Frontiers in zoology*, 2010, 7(1):31.

[5] Lee Y.M., Kimt S.H., Kimt S.J. Preparation and characteristics of β-chitin and poly (vinyl alcohol) blend. *Polymer*, 1996, 37(26), 5897-5905.

[6] Vincent J.F., Wegst U.G. Design and mechanical properties of insect cuticle. *Arthropod structure & development*, 2004, 33(3), 187-199.

SIMULATION OF THE CORROSION-INDUCED CRACKS WITH EQUIVALENT ARTIFICIAL SURFACE NOTCHES

Nikolaos D. ALEXOPOULOS[1], Christina Margarita CHARALAMPIDOU[1], Paraskevas PAPANIKOS[2], Stavros K. KOURKOULIS[3]

[1] Department of Financial Engineering, School of Engineering, University of the Aegean, 41 Kountouriotou str., 82132 Chios, Greece, e-mail: nalexop@aegean.gr

[2] Department of Product and Systems Design Engineering, School of Engineering, University of the Aegean, 1 Konstantinoupoleos str, Ermoupoli, 84100 Syros, Greece

[3] Laboratory for Testing and Materials, Department of Mechanics, National Technical University of Athens, 5 Heroes Polytechnion Str., 15773 Athens, Greece

1. Introduction

Corrosion of aluminium alloys is among the greatest problems in maintenance and repair of aircraft structures. Interaction of corrosion with other forms of damage, e.g. fatigue cracks, can result in loss of the structural integrity of aircrafts components mainly due to accelerated crack propagation [1] The major damage mechanism on the corroded surface is the formation of pits that act as stress concentrators and assist cracking formation and therefore affects the integrity of aircraft structures [2-4]. Aluminium alloys such as 2024, which are widely used in the aircraft industry due to their improved mechanical properties, are susceptible to corrosion attack due to their microstructure [5-6]. To face the corrosion-induced structural degradation issue, available data usually refer to accelerated laboratory tests including weight loss measurements, metallographic analysis, measurements of the depth of corrosion attack etc. The most common accelerated corrosion laboratory test used for the aeronautical aluminium alloys 2xxx and 7xxx is the exfoliation corrosion (EXCO) test, according to ASTM G34 specification. Except from atmospheric corrosion, it is not foreseen in any specification/standard to perform mechanical tests on pre-corroded materials and the rate of the corrosion degradation rate is not correlated to the residual mechanical properties. However, for the AA2024-T3, various mechanical tests had been carried out to assess the influence of corrosion damage on the structural integrity of the material. Tensile and fatigue tests in pre-corroded material resulted to a moderate degradation of the material's mechanical strength properties, e.g. yield stress and ultimate tensile strength, along with a significant reduction of the tensile ductility [7-9]. According to Alexopoulos et al. [10] the cross-sectional area of AA2024 specimens that is unaffected by the corrosion-induced micro-cracks, also referred as 'effective thickness', decreases exponentially with increasing corrosion exposure time due to the crack propagation mechanism. The reduction of the specimens load carrying cross section as well as the notch effects caused by pitting formation are responsible for the moderate reduction of the tensile strength properties. In the present work, simulation of the real corrosion-induced degradation of the mechanical properties due to micro-cracks as well as hydrogen embrittlement and correlation with the equivalent degradation by artificially-induced surface notches was investigated. A finite element model was developed to calculate the residual mechanical properties of the simulated technological problem with artificial notches.

2. Materials and methodology

Material used was a wrought aluminium alloy 2024-T3 received in sheet form of 3.2 mm nominal thickness. The chemical composition of 2024 alloy is 4.35% Cu, 1.50% Mg, 0.64% Mn, 0.50% Fe, 0.50% Si, 0.10% Cr, 0.25% Zn, 0.15% Ti and Al rem. Tensile specimens were machined from the sheets longitudinal to the rolling direction and according to ASTM E8 specification. The geometrical dimensions were 12.5 mm x 3.2 mm at the reduced cross section with total length of 150 mm. Artificial surface notches of different depths, e.g. 0.15, 0.30 and 0.50 mm in each surface, were machined in the specimens large (top) surfaces in order to simulate the gradually increasing corrosion attack.

Specimens geometry was modeled with the aid of the ANSYS program. Modeling was conducted

along the thickness of the specimens (width in real specimens). Due to symmetry in both axes, only ¼ of the specimen's width was modeled. Hence, the geometrical dimensions of the modeled area were 1.60 mm width (half of the thickness) x 12.5 mm length, since the length of the extensometer in the tensile tests was 25 mm. Two dimensional elasto-plastic finite element analyses were conducted to calculate the behavior of the specimen with artificial notches. Since the width of the specimen is large compared to its thickness, plane strain conditions were assumed. The stress-strain curve of AA2024-T3 was used as input to the model.

3. Results

Fig.1 shows the calculated tensile curve for 0.15 mm notch depth and is directly compared against the experimental results of the tensile tests. A good correlation between the experimental results and the calculated from the FEM is evident. Additionally, typical sketches of the development of plastic zone at different loading levels are depicted. In the case (a) the specimen is loaded to the plastic region up to 2 % nominal strain while levels up to 5 % and 6 % are depicted in (b) and (c), respectively. The developed plastic zone tends to increase in size and morphology is changed such as in high plastic strain region. This is the typical geometry of the ductile fracture in 45° to the loading axis. Fracture is assumed to occur at the loading level at which the plastic zone is stretched to the whole width of the specimen of the modeled area, as can be seen in case (d).

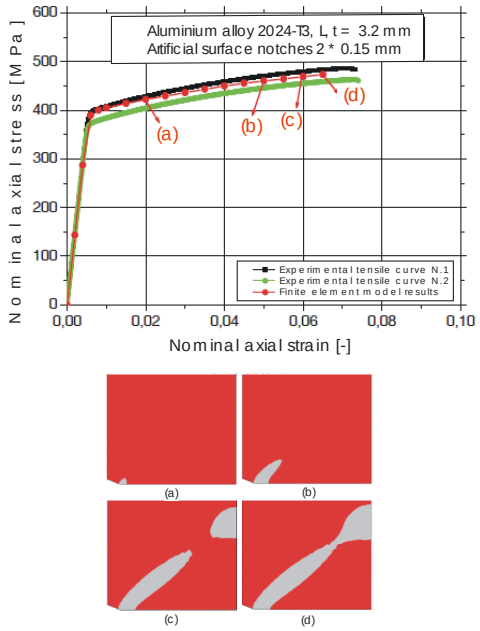

Fig. 1. Experimental tensile curves of AA2024-T3 pre-corroded specimens (upper) compared against the FEM calculated curve and plastic zone development at different tensile loading levels (lower).

4. Conclusions

Artificial surface notches of different depths were machined on the tensile specimens surfaces for the simulation of corrosion-induced mechanical properties degradation. The corrosion exposure time was empirically correlated to the total notch depths regarding the remaining tensile ductility. A finite element model was developed to simulate the real corrosion-induced mechanical properties degradation of the artificially notched specimens. A good correlation between the calculated results from the model and the experimental results was noticed.

References

[1] F. Menan, G. Henaff, Influence of frequency and exposure to a saline solution on the corrosion fatigue crack growth behavior of the aluminum alloy 2024, Int. J. Fatigue, 2009, 31, 1684–1695.

[2] G. S. Chen, M. Gao, R. P. Wei, Micro constituent-induced pitting corrosion in aluminum alloy 2024-T3, Corrosion, 1996, 52, 8–15.

[3] K.N. Lyon, T.J. Marrow, S.B. Lyon, Influence of milling on the development of stress corrosion cracks in austenitic stainless steel, J. Mat. Process. Tech., 2015, 218, 32–37.

[4] S. Ishihara, et al., Prediction of corrosion fatigue lives of aluminium alloy on the basis of corrosion pit growth law, Fatigue Fract. Eng. Mater. Struct., 2005, 29, 472–480.

[5] A. Boag, A.E. et al. Corrosion of AA2024-T3 part I: localised corrosion of isolated IM particles, Corros. Sci., 2011, 53, 17–26.

[6] J.A. DeRose, et al., Localised corrosion initiation and microstructural characterisation of an Al2024 alloy with a higher Cu to Mg ratio, Corros. Sci., 2012, 55, 313–325.

[7] K. Jones, D.W. Hoeppner, Prior corrosion and fatigue of 2024-T3 aluminum alloy, Corros. Sci., 2006, 48, 3109-3122.

[8] Al. Th. Kermanidis, P. V. Petroyiannis, Sp. G. Pantelakis, Fatigue and damage tolerance behaviour of corroded 2024 T351 aircraft aluminum alloy, Theor. Appl. Fract. Mech., 2005, 43, 121–132.

[9] Sp.G. Pantelakis, P.G. Daglaras, Ch.Alk. Apostolopoulos, Tensile and energy density properties of 2024, 6013, 8090 and 2091 aircraft aluminum alloy after corrosion exposure, Theor. Appl. Fract. Mech., 2000, 33, 117–134.

[10] N.D. Alexopoulos, P. Papanikos, Experimental and theoretical studies of corrosion-induced mechanical properties degradation of aircraft 2024 aluminum alloy, Mater. Sci. Eng. A, 2008, 498, 248–257.

NUMERICAL ANALYSIS OF DUCTILE FRACTURE

Jelena ŽIVKOVIĆ[1], Vladimir DUNIĆ[1], Miroslav ŽIVKOVIĆ[1], Nenad GRUJOVIĆ[1]

[1] University of Kragujevac, Faculty of Engineering, Sestre Janjić 6, 34000 Kragujevac, Serbia,
E-mail: jelena.zivkovic@kg.ac.rs; dunic@kg.ac.rs; miroslav.zivkovic@kg.ac.rs; gruja@kg.ac.rs

1. Introduction

The largest issue in fracture mechanics is the lack of possibility to detect damage nucleation and the way it will merge into a new initial crack. This paper presents a comparison of numerical results given in [1], obtained by using the phase-field model for ductile fracture of elasto-plastic solids, and numerical results obtained by using in-house software package PAK [2], for calculations of structures based on the Finite Element Method. The numerical analysis was done for the example of tension of Steel-1.0553 flat specimen.

2. Large strain analysis

The stress integration algorithm of large strain deformations in isotropic plasticity based on the multiplicative decomposition of the deformation gradient, using the logarithmic strains, is given:

1. Determination of the relative and normalized relative deformation gradient

$${}^{t+\Delta t}_{t}\mathbf{F} = \mathbf{1} + \frac{\partial^{\Delta t}\mathbf{u}}{\partial {}^{t}\mathbf{x}}, \qquad {}^{t+\Delta t}_{t}\overline{\mathbf{F}} = \left|{}^{t+\Delta t}_{t}\mathbf{F}\right|^{-\frac{1}{3}} {}^{t+\Delta t}_{t}\mathbf{F}$$

2. Elastic trial solution

$${}^{t+\Delta t}\overline{\mathbf{b}}^{E^*} = {}^{t+\Delta t}_{t}\overline{\mathbf{F}}\,{}^{t}\overline{\mathbf{b}}^{E}\,{}^{t+\Delta t}_{t}\overline{\mathbf{F}}^{T} = \sum_{A=1}^{3}\left(\bar{\lambda}_A^{E^*}\right)^2 \mathbf{q}_A \otimes \mathbf{q}_A$$

$${}^{t+\Delta t}\overline{\mathbf{e}}^{E^*} = \sum_{A=1}^{3}\ln\left(\bar{\lambda}_A^{E^*}\right)\mathbf{q}_A \otimes \mathbf{q}_A$$

3. Determination of the trial deviatoric elastic stress tensor and trial equivalent elastic stress:

$${}^{t+\Delta t}\mathbf{S}^{E^*} = G\,dev\,{}^{t+\Delta t}\overline{\mathbf{b}}^{E^*}, \quad {}^{t+\Delta t}\sigma^{E^*} = \sqrt{\frac{3}{2}}\left\|{}^{t+\Delta t}\mathbf{S}^{E^*}\right\|$$

4. Checking of yield condition

$${}^{t+\Delta t}f_y^{E} = {}^{t+\Delta t}\sigma^{E^*} - {}^{t}\sigma_y \le 0$$ - elastic sol., go to 6

5. Calling the program for the integration of constitutive relations [3, 4] to determine deviatoric stress tensor and determinant of plastic deformation gradient

$${}^{t+\Delta t}\sigma = \sqrt{\frac{3}{2}}\left\|{}^{t+\Delta t}\mathbf{S}\right\|$$

$$\left|{}^{t+\Delta t}f_y\right| = \left|{}^{t+\Delta t}\sigma - {}^{t}\sigma_y\right| > 0$$ - new iter., go to 5

6. Deformation gradient and determinant of elastic deformation gradient using multiplicative decomposition

$${}^{t+\Delta t}_{0}\mathbf{F} = {}^{t+\Delta t}\mathbf{J}^{T}\left({}^{0}\mathbf{J}^{-1}\right)^{T} \qquad \left|{}^{t+\Delta t}_{\tau}\mathbf{F}_E\right| = \frac{\left|{}^{t+\Delta t}_{0}\mathbf{F}\right|}{\left|{}^{\tau}_{0}\mathbf{F}_P\right|}$$

7. Final stress solution

$$\sigma_m = c_m e_m \qquad e_m = \frac{1}{3}\left(\left|{}^{t+\Delta t}_{\tau}\mathbf{F}_E\right| - 1\right)$$

$$c_m = \frac{E}{1-2\nu} \qquad {}^{t+\Delta t}\boldsymbol{\sigma} = {}^{t+\Delta t}\mathbf{S} + \sigma_m \mathbf{1}$$

8. Correction of elastic configuration at the end of the step

$${}^{t+\Delta t}\overline{\mathbf{b}}^{E} = \frac{1}{G}\,{}^{t+\Delta t}\mathbf{S} + \bar{b}_m^{E}\mathbf{1} \qquad \bar{b}_m^{E} = \frac{1}{3}\,{}^{t+\Delta t}\bar{b}_{ii}^{E^*}$$

3. Numerical results

In this section we investigate the ability of our in-house software PAK to capture representative aspects of the fracture process in ductile materials. The numerical analysis was done on flat tensile specimen made of Steel 1.0553 shown in Fig.1. The specimen is modeled using the 3D solid elements with 8 and 20 nodes per element. An elastic-plastic material model with isotropic hardening was used. Hardening zone is described by Ramberg-Osgood's curve ${}^{t}\sigma_y = \sigma_{yv} + C_y\left({}^{t}\bar{e}^{P}\right)^{n}$. Material parameters for hardening law proposed by Simo, [5], used in [1] were fitted for Ramberg-Osgood's law, Fig.2.

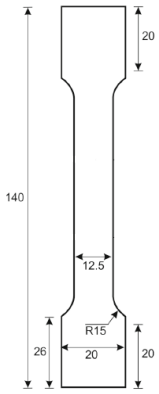

Fig. 1. Flat tensile specimen Steel-1.0553.

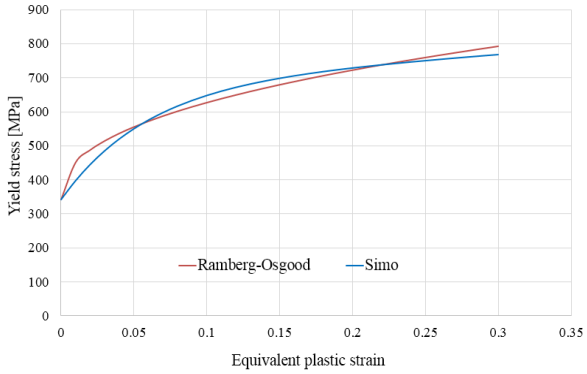

σ_y =343MPa,
σ_∞ =680MPa,
δ= 16.93
H =300MPa,
E =2.1×10^{5}MPa,
ν =0.3

σ_y =343MPa,
C_y =743.32MPa,
m=0.41705
E =2.1×10^{5}MPa,
ν =0.3

Fig. 2. Simo and Ramberg-Osgood hardening curves.

Fig. 3 shows a comparison of load-displacement curves for the results obtained by software PAK, for solid 8-node and 20-node elements (RO8 and RO20 in Figure 3, respectively), and the results given in [1] for phase-field model, elasto-plastic model without phase-field and the results obtained experimentally.

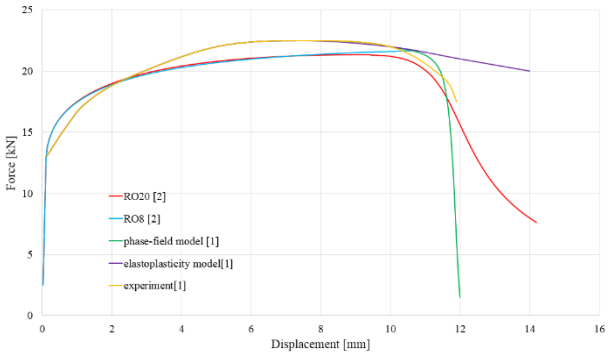

Fig. 3. Load-displacement curves for flat tensile specimen Steel-1.0553.

The results of elastoplastic model with phase-field predicts crack initiation and propagation, but so as the results of elastoplastic model in PAK in case of 20-node elements. During the numerical simulation it was observed that as the deformation progresses, equivalent plastic strain concentrates in the necking zone, taking the maximum value in the middle of the specimen and it is followed by propagation towards the edge of the specimen.

4. Conclusions

This paper shows comparison of results obtained by using the software package PAK with the results given in [1] obtained by experiment, and the elastoplastic model with and without phase-field. The comparison was done in order to investigate the ability of PAK to capture representative aspects of fracture in ductile materials.

It is shown that the elastoplastic model in PAK gives similar results as the model with the phase-field given in [1]. Model used for calculations in this paper showed that it can capture sequence of elastoplastic deformation and necking in flat specimens in case of solid 20-node elements. As the deformation progresses, the equivalent plastic strain concentrates in the necking zone, taking the maximum value in the middle of the specimen and it is followed by propagation towards the edge, which corresponds with experimental observations.

Acknowledgements

The part of this research is supported with the Project TR32036 financed by the Ministry of Education, Science and Technological Development, Republic of Serbia

References

[1] Ambati, M., et al., A phase-field model for ductile fracture at finite strains and its experimental verification. Computational Mechanics, 2016, 57, pp. 149-167
[2] Kojić, M., et al., PAK-S: Program for FE Structural Analysis, Faculty of Mechanical Engineering, University of Kragujevac, Kragujevac, Serbia, 1999
[3] Kojić, M., Bathe, K.J., Inelastic Analysis of Solids and Structures, Springer-Verlag Berlin Heidelberg, 2005, ISBN 3-540-22793-8
[4] Živković, M., Nelinearna analiza konstrukcija, Univerzitet u Kragujevcu, Mašinski fakultet, ISBN 86-80581-59-3, Kragujevac, 2006
[5] Simo, J.C., Hughes, T.J.R., Computational Inelasticity, Interdisciplinary applied mathematics, Springer-Verlag Berlin Heidelberg, 2000, ISBN 0-387-97520-9

EXPERIMENTAL AND NUMERICAL INVESTIGATION OF SLIDING BOLT CONNECTION ON THE TANK WAGON

Miroslav ŽIVKOVIĆ[1], Vladimir MILOVANOVIĆ[1], Nikola JOVANOVIĆ[1], Milan BOJOVIĆ[1]

[1] University of Kragujevac Faculty of Engineering, Sestre Janjić 6, Kragujevac, Serbia, E-mail: miroslav.zivkovic@kg.ac.rs; vladicka@kg.ac.rs; ing.jovanovic.nikola@gmail.com; mbojovic@outlook.com

1. Introduction

The problem considered in this paper relates to the correct modelling of the sliding bolt connection [1,2], in the strength analysis of the tank wagon in accordance to the standard [3]. Due to the complexity of the geometry and the FEA model with large number of contact pairs and bolt connections, it is necessary to find the easiest way for modelling bolt connections, which will fully correspond to the bolt connections on real model.

2. Problem description

During exploitation the wagon is exposed to thermal loads. In order to allow free expansion and to avoid the occurrence of significant deformations, one side of the wagon is designed to allow the relative sliding of the tank along the longitudinal direction in relation to the side wings. On the other side the tank is connected with fixed bolt connection for underframe side wings. The wagon structure is made so that there are three basic connection between its parts: connection between the tank and saddle (contact pair), middle connection (combination – contact pair and sliding bolt connection) and side connections between side wings and tank (combination – contact pair and sliding bolt connection; combination – contact pair and fixed bolt connection on the side of hand brake). The tank is leaning on the saddles, which are located above the main transverse girders.

The tank is connected to the side wings with 60 bolts, 15 per one connection, while the middle connection is achieved by the 8 bolts. It means that there are 30 fixed and 38 sliding bolt connections in the FEA model.

Bolt connections are modelled using the beam element. At the place of fixed bolt connection, all degrees of freedom are disabled, while sliding bolt connection using the "beam release" option allows sliding in the direction of the groove. The initial bolt preloads of all bolts in the bolt connections are in accordance with [4].

3. Functionality of modeled bolt connections

In order to verify the correct method of modelling and functionality of bolt connections, calculation results are shown to demonstrate the behavior of the FEA model for different types of loads. Due to the fact that the sliding, or relative displacement of the tank in relation to the wagon's chassis, is the most dominant for horizontal loads, in Figure 1, the longitudinal displacement field of the wagon is shown, for load case - compressive force at buffer level; F=1000kN at each buffer.

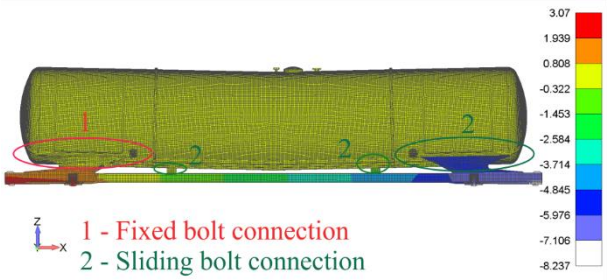

Fig. 2. Longitudinal displacement field – compressive force at buffer level; F=1000kN at each buffer.

Based on the displacement field shown in Figure 2, the character of the behavior of bolt connections is clearly seen. At the place of the sliding bolt connection, it can be seen that there is a difference in the values of the tank displacement and displacement of the wagon chassis at the place of the sliding bolt connection, Figure 3. At the place of the fixed bolt connection, it can be seen that there is no relative displacement of the tank in relation to the wagon chassis, Figure 4.

4. Comparative analysis of obtained results

Prototype of the tank wagon was made and measurements for all load cases defined in accordance with the relevant standards had done. Strain gauges were set up on prototype of the wagon and measurements were carried out in order to

compare the values of the stress obtained by the experimental and numerical FEA analysis [5].

In the Table 1 are shown comparative results obtained by rosettes and appropriate von Mises equivalent stress obtained by FEA. In the Table 2 are shown comparative results obtained by strain gauges and appropriate normal stress obtained by FEA. A special attention is placed on measuring points near the sliding bolt connection, which is also the primary goal of the research in this paper. The results are presented only for those load cases that showed higher stress values at control measuring points (stress values above 200 MPa).

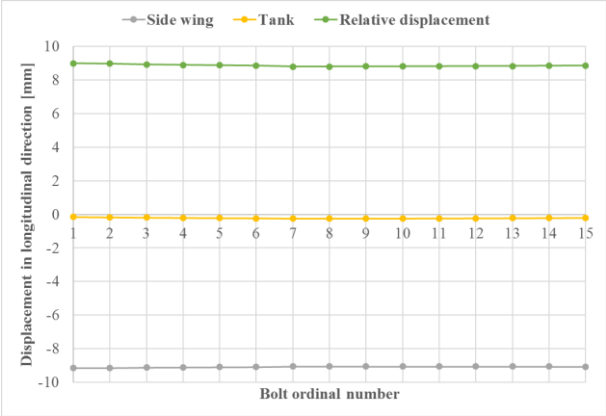

Fig. 3. Displacement in longitudinal direction – sliding bolt connection.

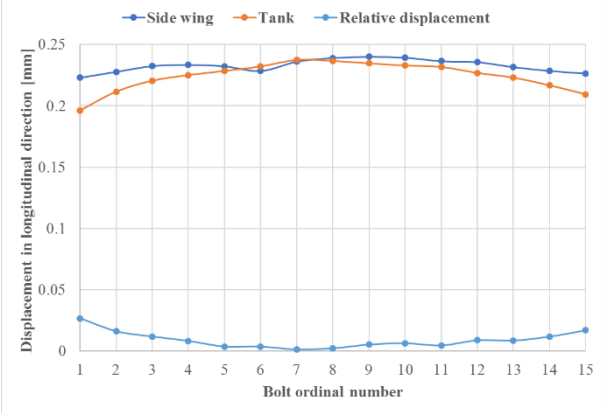

Fig. 4. Displacement in longitudinal direction – fixed bolt connection.

Table 1. Comparative results obtained by rosettes and FEA.

Rosette mark	Measured stress [MPa]	FEA [MPa]
R01	282.7	259.9
R02	221.3	218.1
R05	230.3	258.5

Table 2. Comparative results obtained by strain gauges and FEA.

Strain guages mark	Measured stress [MPa]	FEA [MPa]
T02	267.6	276.0
T05	-279.7	-274.6
T11	197.5	188.9
T23	-202.3	-222.4
T27	-229.1	-215.3

5. Conclusions

The aim of this paper was to take into account the effects of bolt connection on the complex model of tank wagon, which will completely correspond to the real connections. Using the "beam release" option for defining the beam elements for modelling the bolts, sliding was provided in the direction of the groove. Comparing the numerical results with the results of measuring, it is verified that FEA model gives good agreement with the experimental results. According to analysis of results, it has been concluded that modelled bolt connections in the manner shown in the paper really transfer loads to other parts of the wagon construction and can be used for analysis complex structures exposed to different types of loads.

Acknowledgements

The authors gratefully acknowledge partial support by Ministry of Education, Science and Technological Development, Republic of Serbia, Grant TR32036.

References

[1] Kim, J., Yoon, J. C, Kang, B. S., Finite element analysis and modeling of structure with bolted joints, Applied Mathematical Modelling, 2007, 31, 895-911.
[2] Díaz, C., Martí, P., Victoria, M,. Querin, O. M., Review on the modelling of joint behavior in steel frames, Journal of Constructional Steel Research, 2011, 67, 741–758.
[3] BS EN 12663-2:2010 - Railway applications – Structural requirements of railway vehicle bodies, Part 2: Freight wagons, European Standard.
[4] http://www.tribology-abc.com/calculators/default.htm
[5] RC-ENGINEERING - ZACENS TYPE FREIGHT WAGON EN12663-2 STATIC TEST REPORT, I.T.U Mechanical Engineering Strength of Materials Division, September 2016.

EXPERIMENTAL ANALYSIS OF COMPOSITE JET ENGINE AIR INLET

Karel DOUBRAVA[1], Milan DVOŘÁK[2], Nikola SCHMIDOVÁ[3], Tomáš KOSTROUN[4], Jan VÁCLAVÍK[5] and Milan RŮŽIČKA[6]

[1] Czech Technical University in Prague, Faculty of Mechanical Engineering, Technická 4, 166 07 Prague, Czech Republic, E-mail: Karel.Doubrava@fs.cvut.cz

[2] Czech Technical University in Prague, Faculty of Mechanical Engineering, Technická 4, 166 07 Prague, Czech Republic, E-mail: Milan.Dvorak@fs.cvut.cz

[3] Czech Technical University in Prague, Faculty of Mechanical Engineering, Technická 4, 166 07 Prague, Czech Republic, E-mail: Nikola.Schmidova@fs.cvut.cz

[4] Czech Technical University in Prague, Faculty of Mechanical Engineering, Technická 4, 166 07 Prague, Czech Republic, E-mail: Tomas.Kostroun@fs.cvut.cz

[5] AERO Vodochody AEROSPACE a.s., U Letiště 374, 250 70 Odolena Voda , Czech Republic, E- mail: jan.vaclavik@aero.cz

[6] Czech Technical University in Prague, Faculty of Mechanical Engineering, Technická 4, 166 07 Prague, Czech Republic, E-mail: Milan.Ruzicka@fs.cvut.cz

1. Introduction

Aero L-39 light jet trainer is widely used in many countries around the world. One important element of the structure is the air inlet. Fatigue life of the metal air inlet is one of the factors limiting service life of entire aircraft. The new generation L-39NG jet trainer (see Fig. 1) represents deep modernization of the L-39 combining latest engine and aircraft systems technology with traditional advantages of L-39s legacy.

Fig. 1. Light jet trainer Aero L-39NG [1].

The new air inlet design is based on a composite material, with a view to increasing service life and using a new jet engine. The determination of operational loading was necessary to verify numerical model where the aim was to examine the load during the ground engine test run.

2. Air inlet

The complete air inlet (see Fig. 2) is composed of three main composite parts.

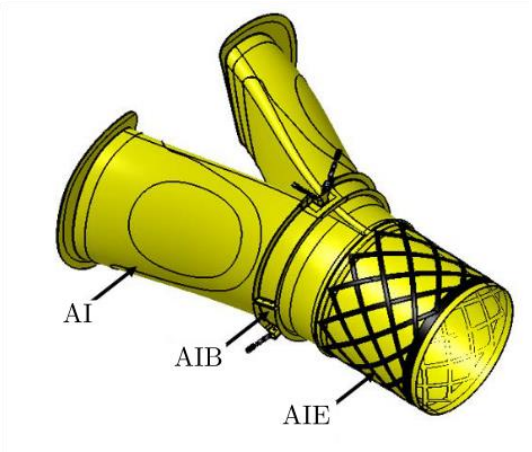

Fig. 2. Composite air inlet (AI – Air Inlet, AIB – Air Inlet Brace, AIE – Air Inlet Extension) [2].

The main material used for the air inlet is pre-impregnated carbon fiber reinforced plastic (CFRP). The minimum used number of CFRP layers is 12, while the maximum number of layers is 24 at the main reinforcement area. Left and right parts of the air inlet are connected by the air inlet brace. The brace is fitted to the fuselage by using four rods, which are main load connections between the fuselage and the air inlet.

3. Air inlet instrumentation

The places for strain measurements were selected on the basis of assumed load peaks obtained by numerical simulations. The 31 places were selected on each inlet arm, with a resistance strain gauge rosettes installed.

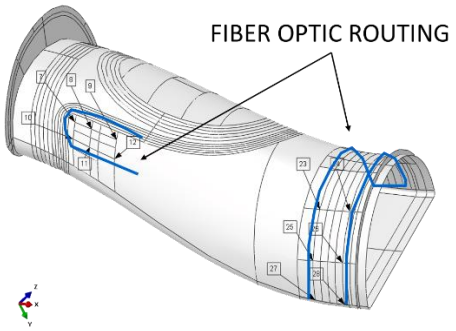

Fig. 3. Left air inlet with places of strain gauge and FBG sensors.

Two optical fibers with twenty FBG (Fiber Bragg Grating) sensors were installed on the surface of each inlet (see Fig. 3). The right inlet with installed sensors can be seen in Fig. 4. The load transmitted by the rods was monitored by strain gauges installed on their surfaces. The instrumented rods were calibrated on a universal testing machine with a conversion between the measured strains and the load forces. The temperature field around the strain gauge sensors was monitored with the six platinum resistance thermometer sensors. The sensors had to be installed before the inlet was assembled into the fuselage. Therefore, solder tabs had to be placed near access or inspection panels and the final cable connection was made after the air inlets were mounted in the fuselage.

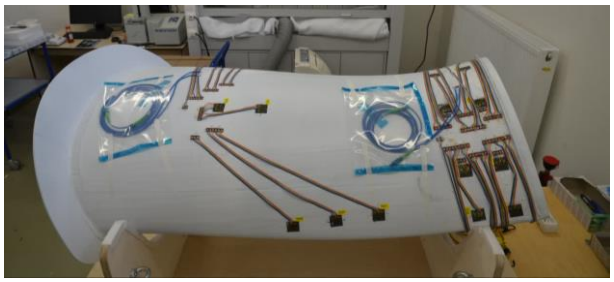

Fig. 4. Right air inlet with installed sensors.

Total number of the installed resistance strain gauges' grids was 186 which represented a large amount of connecting material and working time compared to installing four optical fibers with the 40 FBG sensors.

4. Engine ground run test

The large number of measurement channels was the reason for use of two independent strain gauge measurement systems and the need to perform measurement in parts. The first system contained 56 strain gauge channels with 25 kHz sampling frequency, the second system consisted of 36 channels with 19.2 kHz sampling. The optical interrogator measured at a sampling rate of 11.5 kHz when single fiber was connected. Based on the previous limitations, a test run of the engine has been proposed, where defined power levels have been maintained for some time. This successive loading was repeated after switching a set of other measuring channels. The situation during the test is shown in the Fig. 5.

Fig. 5. Engine ground run test.

5. Conclusions

During the test, a large amount of data was obtained, which will be used to verify numerical models mainly with regard to acoustic fatigue.

Acknowledgements

The authors would like to thank the Technology Agency of the Czech Republic for supporting this research with the project no. TE02000032.

References

[1] AERO Vodochody AEROSPACE a.s., L-39NG program remains a key priority to AERO. <http://www.aero.cz/en/media/news/l-39ng-program-remains-key-priority-aero/> Accessed August, 2019

[2] Kučera, J.: Composite air channel design for L-39NG aircraft, report, Aero Vodochody Aerospace a.s., Odolena Voda, TR-AV9954-0011, 2017

DELAMINATION DETECTION USING ELECTRICAL RESISTANCE CHANGE METHOD AND ITS RELIABILITY

Nikola SCHMIDOVÁ[1], Milan RŮŽIČKA[1], Karel DOUBRAVA[1] and Milan DVOŘÁK[1]

[1] Department of Mechanics, Biomechanics and Mechatronics, Faculty of Mechanical Engineering, Czech Technical University in Prague, Technická 4, 160 00, Praha, Czech Republic, E-mail: Nikola.Schmidova@fs.cvut.cz

1. Introduction

The reliability of delamination detection on Carbon Fiber Reinforced Polymer (CFRP) composites with thermoplastic matrices using Electrical Resistance Change Method (ERCM) was investigated. The ERCM is based on measuring electrical resistance change and it is used mainly for the CFRP composites or glass-fiber reinforced composites doped with conductive particles. The results measured using the ERCM are influenced by the contact configuration, nominal resistivity of the material, environmental conditions such as temperature and mechanical loading of the material. The method can serve for different purposes of Structural Health Monitoring (SHM). Several configurations of the electrical contacts have been proposed for various measurement/detection scenarios, such as an impact detection [1,2], delamination detection [3, 4] or detection of transverse cracks [5]. The ERCM method is most often studied in connection with the delamination detection. One of the typical application for which is the ERCM intended is the delamination detection after impact in an aircraft fuselage and wings area. For this particular application the configuration of the contacts has to be situated on one face, which is not the most effective contact configuration for the delamination detection. It was shown, that the contact configuration for through-thickness or oblique measurement is more convenient [1]. Although number of papers are dedicated to impact localization on a CFRP plate with electrical contacts on one face [2, 4], no such attention is paid to measurements with contacts located on both faces. This configuration could be successfully used for many other typical structural elements which can be also typically damaged by delamination such as curved components, skin stringers in an aircraft structure or components with ply drop. For these types of components there is also a need for reliable SHM and there is no problem with placing contacts on both sides of the material. The presented research is therefore focused on components, where contacts can be placed on both sides.

2. Material and Specimen Preparation

Delamination detection using ERCM was studied on the specimens made of carbon fabric with Polyphenylene Sulphide resin (CF-PPS), material sheet AIMS05-09-002. Six specimens with the dimensions 5 × 15 × 54 mm were cut from one sheet of the material. Surface of the specimens was slightly sanded at first with sandpaper P120 and P600 and then degreased. Electrical contacts were prepared using a CHO-BOND® 584-29 conductive epoxy and copper strips. To initialize the delamination, specimens were partly cut in the half of the thickness. Afterwards the delamination growth was forced mechanically. Experimental data measured during the delamination growth were compared to those obtained during the delamination growth on the specimens made of carbon fabric prepreg with thermoset polymer matrix (CF-epoxy). The configuration of the electrical contacts on the specimens are given in Fig. 1. The specimens made of CF-epoxy were loaded simultaneously by mode I and mode II loading (Mixed-Mode Bending - MMB specimens). Experimental results were already published in [6]. The MMB specimens were extracted from CFRP composite made of 16 layers. Dimensions of the specimens were 3.3 × 25 × 185 mm. A 25 mm long non-adhesive plastic foil sheet was inserted to the plate edge during manufacturing to the neutral axis to initiate the delamination.

3. Measurement Procedure

The measurement was performed using the HP E3631A current source and two Agilent 34461A multimeters. The change in electrical resistance was determined using the series comparison measurement method. The resolution of the measurement was ± 0.01 mΩ and the accuracy of

the measurement was ± 0.03 mΩ. Value of the measurement accuracy is the limit for the reliable measurement. The reliable detection of the delamination growth is limited by the minimal detectable resistivity change.

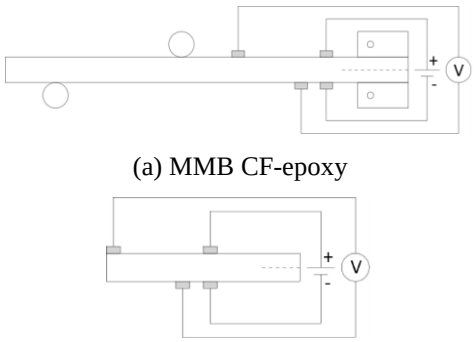

(a) MMB CF-epoxy

(b) DCB CF-PPS

Fig. 1. Measurement configuration of the electrical resistance measurement - configuration of duty current injection and voltage change measurement on the CF-epoxy specimen (a), CF-PPS specimen (b).

4. Experimental Results

The electrical resistance of each CF-PPS specimen was measured before an initialization of the delamination and after each delamination growth (increment). Delamination growth was recorded using a Nikon camera. Measured values of electrical resistivities were used in the numerical simulation of the delamination growth. Results of the experimental and numerical investigations are given in Fig. 2 as a relative change of measured electrical resistance.

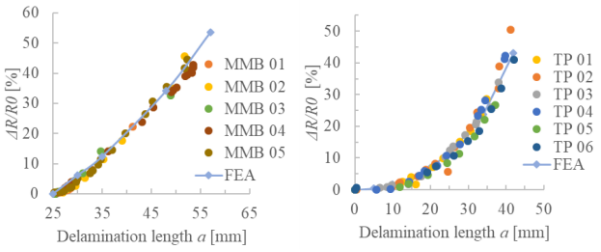

Fig. 2. Comparison of experimental results and numerical simulation results of delamination growth on the CF-epoxy specimen (left) and CF-PPS specimens (right).

The R_0 in the equation corresponds to the initial electrical resistance. For the MMB CF-epoxy specimen the initial resistance was measured before delamination growth, when the delamination was only 25 mm. For the DCB CF-PPS specimen the initial resistivity was determined on the specimen without delamination.

5. Conclusions

The experimental investigation and the numerical simulation of the delamination growth on the specimens made of CF-PPS and CF-epoxy resin were performed. Comparison of the numerical and the experimental results has shown good agreement. The influence of the temperature change, values of the nominal resistivity and distance of the electrical contacts was also studied using the finite element analysis.

Acknowledgements

The authors would like to thank the TACR for supporting this research with project no. TE02000032 and Grant Agency of the CTU in Prague for supporting this research with grant No. SGS18/175/OHK2/3T/12.

References

[1] Wang, S., D.D.L. Chung and J.H. Chung. 2005. "Impact damage of carbon fiber polymer-matrix composites, studied by electrical resistance measurement," *Composites*, 36:1707-1715.

[2] Baltopoulos, A, N. Polydoride, L. Pambaguian, A. Vavouliotis amd V. Kostopoulos. 2012. " Damage identification in carbon fiber reinforced polymer plates using electrical resistance tomography mapping," *Journal of Composite Materials*, 47:3285-3301

[3] Todoroki, A. 2001. "The effect of number of electrodes and diagnostic tool for the delamination of CFRP laminates by changes in electrical resistance," *Composite Science and Technology*, 61:1871-1880.

[4] Atsushi, I., and A. Todoroki. 2005. "Statistical evaluation of modified electrical resistance change method for delamination monitoring of CFRP plate," *Structural Health Monitoring* , 4(2):119-136.

[5] Selvakumaran, L., Q. Long, S. Prudhomme and G. Lubineau. 2015. " On the detectability of transverse cracks in laminated composites using electrical potential change measurement," *Composite Structures*, 121:237-246.

[6] Schmidova, N, M. Dvorak, M. Kadlec and M. Ruzicka. 2018. "Monitoring of delamination growth on the MMB specimens using FBG sensors and electrical resistance measurement," *Proceedings of 56th conference on experimental stress analysis EAN 2018*, Praha.

THE EFFECT OF LOW ENERGY IMPACT LOADS ON THE FLEXURAL STRENGTH OF A SANDWICH-STRUCTURED COMPOSITE WITH HEREX CORE

Andrzej KOMOREK[1], Paweł PRZYBYŁEK[1], Robert SZCZEPANIAK[1], Marek ROŚKOWICZ[2]

[1] The Polish Air Force University, 08-530 Dęblin, Dywizjonu 303 No. 35 Street,

E-mail: a.komorek@law.mil.pl, p.przybylek@law.mil.pl, r.szczepaniak@law.mil.pl

[2] Military University of Technology, Faculty of Mechatronics and Aviation, 2 Kaliskiego Street 01-479 Warsaw, Poland, E-mail: marek.roskowicz@wat.edu.pl

1. Introduction

Sandwich-type composites are usually made with two types of materials. The outer layers are made of materials with good mechanical properties, carry the load and determine the strength. The inner layer, called the core, is made of a material of lesser strength, stiffness and density in relation to the outer layers [1]. The middle layer separates the two covers (mostly in thin-walled structures) in order to increase the stiffness of the entire structure with a slight increase in weight.

The structures made up of core materials are characterized by much greater flexural strength in relation to materials made only with a solid material. The stresses caused by the bending moment are smaller in sandwich-type structures.

Due to a favourable weight ratio of the selected strength parameters, the core materials are used in the production of building walls, sports equipment and above all in the airline industry as a material for fuselages, beams, wing ribs, stabilizers.

However, composite structures may be exposed to mechanical damage caused by low energy loads acting perpendicular to the surface of the element. This type of damage adversely affects the strength of the layered composite [2]. The paper presents the results of research on the effect of low energy impact loads on the strength of the sandwich-structured composite. As a test to determine the change in the strength of the composite after impact, a three-support bending test was selected.

2. Experimental research

For testing, the authors prepared three sandwich-structured composite boards of different Herex density. The external layers consisted of one layer of a carbon fabric 160 g/m^2 in weight and one layer of glass fabric 250 g/m^2 in weight, while the core was Herex foam of the densities: 55 kg/m^3, 75 kg/m^3 and 90 kg/m^3 (Fig. 1). The matrix of the tested composites was epoxy resin LH385, with the hardener HG385.

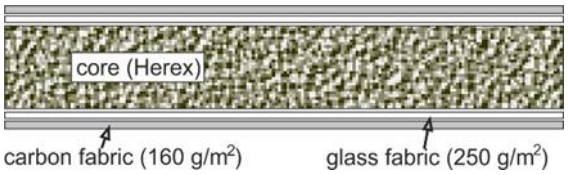

Fig. 1. Structure of the sandwich composite used in research.

The composite sheets were prepared by the contact method of manual lamination, using compression on both sides with glass plates at standard pressure. The fabrics in the layers were laid out with fibres parallel to one another. Next, they were cut down into samples square samples with dimensions 60x60 mm and the resulting thickness.

Fig. 2. Impact loaded surface of a sample loaded with 3 J energy.

The samples were divided into four parts. The first was intended for flexural strength tests. The remaining series of samples were subjected to impact loads with energies of 1, 3 and 5 J (Fig. 2).

Samples after impact loads were observed using a microscope, and next their flexural strength was tested, thus determining the residual strength.The bending strength test of the samples was performed using the three-support method on the Zwick / Roell Z100 machine, with the spacing of supports 50 mm. The results of the tests are presented in Figures 3 and 4.

The highest flexural strength for all impact loads characterized a composite with a Herex core of 90 kg/m3 density (Fig. 3).

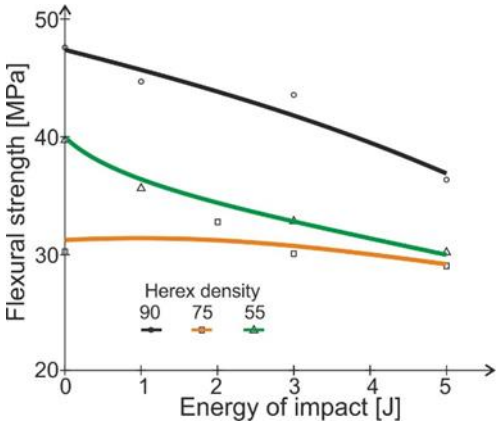

Fig. 3. Dependence of the composite's flexural strength on the energy of the impact load.

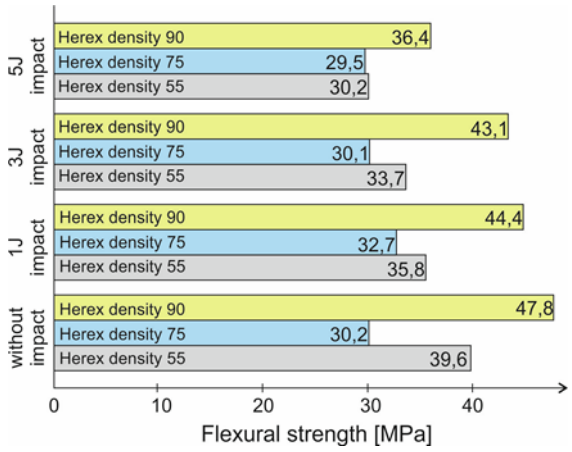

Fig. 4. Flexural strength of tested composites.

It was found that there is no correlation between the density of the core material of the composite and its flexural strength regardless of the value of impact loads (Fig. 4).

For all the impact loads used in the tests, similar damage to the samples was observed. Loads of 1 J caused a plastic deformation of the outer composite layer (approx. 0.2 mm) without matrix cracking and fiber damage. Loads of 3 J and 5 J caused cracks in the outer layer of the composite (Fig. 2), and at loads of 5 J additionally deformations of the lower layer of the composite were observed. We also tested samples of Herex foam, but they

breaks and splits into several parts when it was loaded with 1 J energy.

Observation of the top layer damage using an electron microscope allows perceiving broken reinforcement fibers (Fig. 5).

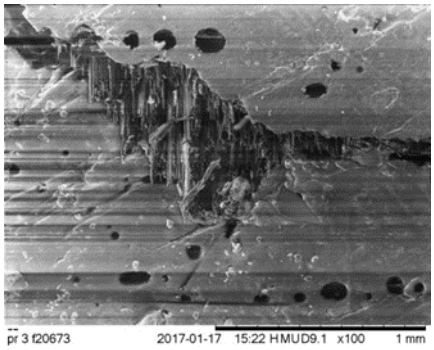

Fig. 5. Picture of damage in the composite loaded with 3 J energy (electron microscope - magnification x100).

3. Conclusions

Increasing energy resulted in an increase in the damage area of the top layer, and with 3 J energy, visual noticeable deformation of the backsheet of the composite was noticeable.

The flexural strength of a composite with a Herex core is dependent on the density of the core material, but higher density does not mean higher strength. Therefore, we are planning to conduct a series of additional tests with use of other Herex densities.

The Herex PVC foam core in the sandwich composite absorbs and dissipates the impactor's energy, which at low values of impact loads results in damage only the layer to which the load have been applied and Herex foam. The bottom layer of the composite remains intact, so repairing such an element is much easier than in classic layered composites without a core. It is worth considering using such materials (with a core) in structures exposed to low energy impact loads.

References

[1] Meunier M., Shenoi R.A.: J. Sound Vib., Vol. 263(1):131-151, 2003.
[2] Komorek A., Przybyłek P.: Eksploat. Niezawod. 14: 265-269, 2012.

EXPERIMENTAL INVESTIGATION OF FATIGUE BEHAVIOUR OF ADDITIVELY MANUFACTURED AIRCRAFT STRUCTURAL MATERIALS

Wyman ZHUANG[1]

[1] Aerospace Division, Defence Science and Technology, Melbourne, VIC, Australia

E-mail: wyman.zhuang@dst.defence.gov.au

Introduction

Additive manufacturing (AM) has demonstrated to have great potential for aerospace applications since it is able to optimise design freedom for fabricating more complex geometry and lightweight structures and components, and to achieve higher fuel efficiency and reduced lead-time and cost of ownership. Although AM has been successfully applied for many secondary structures or other non-critical applications, most aircraft fracture-critical components are currently still machined out of forged metal alloys [1]. This is mainly because of the confidence in aerospace industry in understanding the mechanical properties (specifically fatigue strength and fracture toughness) of forgings adequately and accurately [2]. Given this conventional manufacturing often resulted in typical buy-to-fly ratios more than 10:1 with lengthy lead times and high cost, there is a demand for further R&D to unlock the potential of AM especially for aircraft fracture-critical structures and parts.

Deep Surface Rolling of AMed Specimens

This paper firstly outlined the various technical challenges to be considered in the qualification of additively manufactured alloys for aerospace applications, focusing on critical load bearing components. Although, in recent years, extensive R&D efforts have been devoted to achieving lower cost fabrication of Ti-6Al-4V parts using AM, it has founded that the fatigue strength of additively manufactured Ti-6Al-4V published so far is equivalent to that of casting counterparts. Secondly, some promising post processing technologies to enhancing fatigue performance of additively manufactured Ti-6Al-4V alloys (Fig. 1) were experimentally investigated. The post processing technologies investigated include post heat-treatment, hot isostatic pressing, and surface enhancement technologies such as deep surface rolling as shown in Fig. 2.

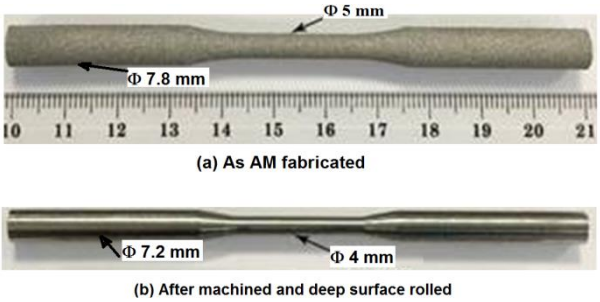

Fig. 1. (a) Additively manufactured Ti-6Al-4V and (b) The specimen after post machining.

Fig. 2. Deep surface rolling processing on the surface of additively manufactured specimen.

Experimental Results

Fatigue testing was performed at four stress levels for each group of the specimens, using a MTS testing machine (100 kN), at the stress ratio (R = min/max stress amplitudes) of 0.1 at the frequency of 10 Hz at room temperature, as listed in Table 1. Fig. 3 presents fatigue behaviours of additively manufactured Ti-6Al-4V with different post processing technologies. Finally, the mechanics and mechanisms of how these post

processes to enhance fatigue performance of additively manufactured alloys were discussed from a perspective of certification specifications and requirements in accordance with airworthiness standards.

Table 1. Fatigue testing matrix

Specimen ID	Stress Ratio R	Max Stress (MPA)
DSR-AM05	0.1	900
DSR-AM10	0.1	900
DSR-AM15	0.1	900
DSR-AM20	0.1	900
DSR-AM01	0.1	800
DSR-AM02	0.1	800
DSR-AM03	0.1	800
DSR-AM04	0.1	800
DSR-AM06	0.1	700
DSR-AM07	0.1	700
DSR-AM08	0.1	700
DSR-AM09	0.1	700
DSR-AM11	0.1	600
DSR-AM12	0.1	600
DSR-AM13	0.1	600
DSR-AM14	0.1	600
DSR-AM16	0.1	500
DSR-AM17	0.1	500
DSR-AM18	0.1	500
DSR-AM19	0.1	500

Conclusions

The recent experimental results clearly demonstrated that the deep surface rolling technology is able to considerably improve the fatigue strength of AMed Ti-6Al-4V specimens, compared with other common post processing technology such as HIP.

Additive manufacturing has not been found to be ready for aircraft flight-critical parts from the current literature in the public domain;

To unlock the potential of deep surface rolling on additive manufacturing for aircraft fracture-critical structures, it is recommended that further research on DSR induced beneficial residual stresses using synchrotron X-ray diffraction and associated surface nanocrystallization using scanning TEM should be conducted.

References

[1] Zhuang, W., Miller, J., Fatemi, A., Liu, Q. and Sharp, K., Fatigue Performance of Additive Manufactured Alloys: Challenges and Opportunities for Aerospace Applications, Keynote to *CAMS 2018 – Advancing Materials and Manufacturing*, Wollongong, NSW, Nov 27-29, 2018.

[2] Li, P., Warner, D.H., Fatemi, A., Phan, N., Critical assessment of the fatigue performance of additively manufactured Ti–6Al–4V and perspective for future research, *International Journal of Fatigue*, Vol. 85, pp. 130–143, 2016.

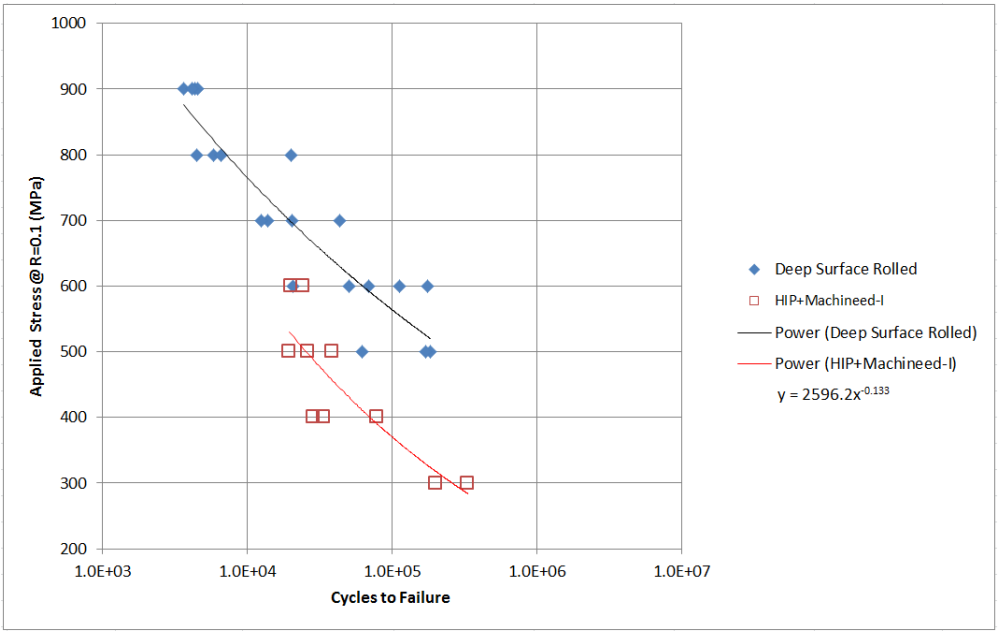

Fig. 3. Fatigue behaviours of additively manufactured Ti-6Al-4V with different post processing technologies

AUTHOR INDEX

Title: **36th Danubia Adria Symposium on Advances in Experimental Mechanics EXTENDED ABSTRACTS**

Editors: Robert Zemčík, Jan Krystek

Published by: University of West Bohemia,
Univerzitní 8, 301 00 Plzeň, Czech Republic

First edition, 2019

ISBN 978-80-261-0876-4